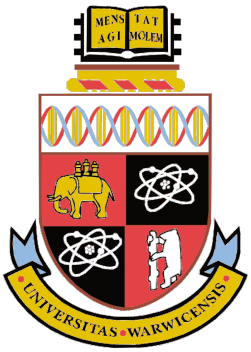


# Developing and Extending the Capabilities of the Scanning Ion Conductance Microscope

**by**

**David John Perry**

**Thesis**

Submitted to the University of Warwick

for the degree of

**Doctor of Philosophy**

Supervisors: Prof Patrick R. Unwin and Prof Bruno G. Frenguelli

MOAC Doctoral Training Centre

September 2016


*For*

*June and Arthur Perry*

*Betty and Jim Riley*

*The most loving and supporting grandparents I could ever have had*

# Contents

# List of Figures

# List of Tables

# Abbreviations

| | |
|---|---|
| SICM | Scanning Ion Conductance Microscopy |
| BM-SICM | Bias Modulated Scanning Ion Conductance Microscopy |
| DM-SICM | Distance Modulated Scanning Ion Conductance Microscopy |
| P-SICM | Potentiometric Scanning Ion Conductance Microscopy |
| FEM | Finite Element Method |
| I-V | Current-Voltage |
| SIR | Surface Induced Rectification |
| ICR | Ion Current Rectification |
| SECM | Scanning Electrochemical Microscopy |
| SECCM | Scanning Electrochemical Cell Microscopy |
| SPM | Scanning Probe Microscopy |
| SPR | Scanning Plasmon Resonance |
| SEM | Scanning Electron Microscopy |
| FE-SEM | Field Emission Scanning Electron Microscopy |
| TEM | Transmission Electron Microscopy |
| AFM | Atomic Force Microscopy |
| QRCE | Quasi Reference Counter Electrode |
| FPGA | Field Programmable Graphics Array |
| DDL | Diffuse Double Layer |
| AC | Alternating Current |
| DC | Direct Current |
| CV | Cyclic Voltammogram |
| UME | Ultra-microelectrode |
| PLL | Poly-L-Lysine |
| APTES | (3-Aminopropyl) triethoxysilane |
| DTC | Doctoral Training Centre |
| MOAC | Molecular Organisation and Assembly in Cells |

# Acknowledgements

Firstly, I would like to thank my supervisor Prof Patrick R. Unwin for all of his support, encouragement and enthusiasm throughout my PhD. I also would like to thank Prof Bruno G. Frenguelli and Dr Phil Young for their help with cell culturing and advice in the latter stages of my project.

Thank you to all of the people who have helped to establish the Warwick Electrochemical Platform without which my project would not have been as successful.

Next, thank you for everyone in the Warwick Electrochemistry and Interfaces Group who make it such a great place to work day to day and for all the help, expertise and advice that they have been able to provide. Thanks to Dmitry and Rehab for all of their advice and help and special thanks in the group to 'Team Cell' as Binoy, Ashley and honorary member Minkyung have been fantastic to work with over the last few years and have provided huge amounts of help.

My two hockey clubs, helped keep me sane throughout my many years at Warwick and were one of the biggest parts of my time here, thank you for all the friends I have made throughout my time and their support, especially to Toby and Bates for all the steak nights!

Without the love and support of my parents I would not have been able to achieve any of what I have done so far and I will always be grateful for all that you have done for me. Thank you also to my brother, Chris, whose constant calling me an idiot has spurred me on to this! Also to my Nanny, who has provided me with chocolate and beer throughout my student years, which has been much needed!

Finally, a huge thank you to Vikki, who has made these last few years so special and has supported me through all the highs and lows of my PhD and generally put up with me and all of my Pokémon talk at times! Though sometimes I may not be as grateful as I should, I appreciate all that you do for me and know I would not be where I am without you so thank you.

# Declaration

The work presented in this thesis is entirely original and my own work, except where acknowledged in the text. I confirm that this thesis has not been submitted for a degree at another University. This work is being submitted for thesis by publication.

Chapter 2 was published as:
**Surface Charge Mapping with a Nanopipette.** Kim McKelvey, Sophie L. Kinnear, **David Perry**, Dmitry Momotenko, and Patrick R. Unwin, *J. Am. Chem. Soc*. **2014**, *136*, 13735–13744. This manuscript also provided the basis of a chapter in Sophie L. Kinnear's thesis who jointly performed the experiments.

Chapter 3 was published as:
**Bias modulated scanning ion conductance microscopy**
Kim McKelvey, **David Perry**, Joshua C. Byers, Alexander W. Colburn, Patrick R. Unwin, *Anal. Chem.* **2014**, *86*, 3639-3646

Chapter 4 was published as:
**Simultaneous Nanoscale Surface Charge and Topographical Mapping**
**David Perry,** Rehab Al Botros, Dmitry Momotenko, Sophie L. Kinnear, and Patrick R. Unwin**,** *ACS Nano* **2015**, *9*, 7266–7276. Some sections also feature in the thesis of Rehab Al Botros, who performed much of the simulation work.

Chapter 5 was published as:

**Characterization of Nanopipettes**

**David Perry,** Dmitry Momotenko, Robert A. Lazenby, Minkyung Kang, and Patrick R. Unwin, *Anal. Chem.* **2016**, *88*, 5523–5530

Chapter 6 was published as:

**Surface Charge Visualization at Viable Living Cells**

**David Perry,** Binoy Paulose Nadappuram, Dmitry Momotenko, Philip D. Voyias, Ashley Page, Gyanendra Tripathi, Bruno G. Frenguelli, and Patrick R. Unwin,

*J. Am. Chem. Soc.* **2016**, *138*, 3152–3160

Chapter 7 was published as:

**Fast Nanoscale Surface Charge Mapping with Pulsed-Potential Scanning Ion Conductance Microscopy**

Ashley Page, **David Perry**, Philip Young, Daniel A Mitchell, Bruno G Frenguelli, and Patrick R Unwin, *Anal. Chem.* **2016**, *88*, 10854–10859

Chapter 8 was published as:

**Electrochemical Control of Calcium Carbonate Crystallization and Dissolution in Nanopipettes**

**David Perry**, Alexander S. Parker, Ashley Page, and Patrick R. Unwin, *ChemElectroChem* **2016**, 10.1002/celc.201600547

Additionally, I have contributed to the following papers whose results are not presented in this thesis:

**Time-Resolved Detection and Analysis of Single Nanoparticle Electrocatalytic Impacts**

Minkyung Kang, **David Perry**, Yang-Rae Kim, Alex W. Colburn, Robert A. Lazenby, and Patrick R. Unwin, *J. Am. Chem. Soc.*, **2015**, *137*, 10902–10905

**Single Molecule Electrochemical Detection in Aqueous Solutions and Ionic Liquids**

Joshua C. Byers, Binoy Paulose Nadappuram, **David Perry**, Kim McKelvey, Alex W. Colburn, and Patrick R. Unwin, *Anal. Chem.*, **2015**, *87*, 10450–10456

**Nucleation and Aggregative Growth of Palladium Nanoparticles on Carbon Electrodes: Experiment and Kinetic Model**

Yang-Rae Kim, Stanley C. S. Lai, Kim McKelvey, Guohui Zhang, **David Perry**, Thomas S. Miller, and Patrick R. Unwin, *J. Phys. Chem. C*, **2015**, *119*, 17389–17397

And a feature review article, which discusses much of the work published in this thesis and the above-mentioned studies:

**Frontiers in Nanoscale Electrochemical Imaging: Faster, Multifunctional, and Ultrasensitive**

Minkyung Kang, Dmitry Momotenko, Ashley Page, **David Perry**, and Patrick R. Unwin, *Langmuir*, **2016**, *32*, 7993–8008

# Abstract

This thesis presents advances made to the scanning ion conductance microscope (SICM), a tool predominantly used to date for topographical imaging of biological samples. This technique is demonstrated to be a powerful tool for non-invasive surface charge mapping as well, through probing of the diffuse double layer formed at charged interfaces. Surface charge mapping with SICM is demonstrated for a range of samples, including biological systems, and it is shown that through the use of a novel feedback technique, also introduced herein, and newly implemented scanning regimes, that the surface charge information can be elucidated unambiguously, together with topography.

Through adopting a characterisation protocol presented in this work, which helps provide a fuller understanding of the used nanopipette probe, the SICM response to charged interfaces and also in bulk solution can become quantitative, allowing for surface charge values for cell membranes and other substrates to be determined. This combination of: SICM experiments, complete probe characterisation and FEM simulations serves as a robust platform for investigating biological and other charged interfaces. The surface charge mapping protocols used allow for unseen surface charge heterogeneities, presented on cell membranes, to be identified and are amenable to future studies, performed in combination with other microscopy techniques, that could help correlate charged domains with physiological function.

Finally, the nanopipette probe is also used as a reaction centre for driving the crystallisation of calcium carbonate, as an exemplar system. Through partitioning the constituent ions of calcium carbonate, with calcium present in a bath solution, and carbonate ions in a nanopipette, a bias can subsequently be applied to drive the ions together, leading to the formation of a crystalline entity, which blocks the nanopipette. Changes in the nanopipette conductance can then provide information about the growth process or subsequently the dissolution as the applied bias is reversed. FEM simulations can allow for an understanding of the underlying mixing problem and the technique is shown to be powerful for the screening of growth additives.

# Chapter 1. Introduction

## 1.1 Aims of Thesis

This thesis is concerned with the development of scanning ion conductance microscopy (SICM), a scanning probe microscope technique (SPM), first introduced in 1989,[1] and how its capabilities can be developed, and its function extended to applications beyond topographical mapping, becoming in the process a more powerful tool for probing the structure and function of both living and non-living systems. The presented developments include the introduction of an improved feedback approach for positioning of the SICM probe above the substrate of interest. As a consequence of this new feedback approach, it also becomes possible to extract more functional information about the system being probed, specifically information about the presented surface charge which, when combined with a robust theoretical model of the probe and surface, becomes quantitative in nature.

Each chapter of this thesis contains the manuscript together with supporting information, where relevant, from work that has been published in peer reviewed journal articles. Chapter 2 describes initial work that demonstrates that the SICM response, used for feedback in a host of topographical studies of living systems, is inherently sensitive to the surface charge of a sample.[2] The implications of this, with regards to the accuracy of probe positioning, and the possible capabilities of the technique for mapping surface charge heterogeneities, are discussed. In light of these issues with probe positioning, chapter 3 introduces a new feedback type to the SICM.[3] Termed bias modulated (BM-) SICM, this approach generates an alternating current (AC) signal, through applying a small oscillation around 0 V between the two SICM quasi reference counter electrodes (QRCEs), which can then be used for feedback.

Chapter 4 utilises finite element method (FEM) simulations and experiments to demonstrate that BM-SICM can overcome the convolution of surface charge and topography through adopting a new scan regime.[4] The BM-SICM approach at no net bias is insensitive to surface charge allowing for truer topographical information to be collected. Following an initial approach using BM-SICM, the potential can then be

switched in order to obtain surface charge information. In all of these initial studies, the FEM simulations performed have served to validate, and inform, the technique, but failed to provide quantitative information about the surface charge of samples. This task requires a complete knowledge of the probe's geometric and surface charge properties, as these also affect the SICM response. Chapter 5 considers how best to characterise nanopipettes in order to overcome this problem.[5] Previous work has focussed on using scanning electron microscopy (SEM) or analytical approaches to characterise pipettes but this is shown to be insufficient and instead transmission electron microscopy (TEM) characterisation is shown to be necessary for providing a sufficient understanding of the nanopipette when combined with FEM simulations and voltammetric experiments.

Chapter 6 moves on to consider the limits of SICM as a tool for surface charge mapping and it is shown that these observations, and the ability to map heterogeneous surface charge, are not limited to low ionic strengths and inert samples. It is demonstrated that it is possible to observe surface charge heterogeneities, not previously seen or accessible with other techniques, on the surface of living cells in physiological electrolyte conditions.[6] Chapter 7 discusses some ways in which the resolution of this technique can be improved resulting in surface charge maps collected at much higher rates and with greater fidelity. Finally, using the same configuration as SICM experiments, chapter 8 considers the nanopipette itself and how it can be used as a reaction centre for forming crystal nuclei, growing crystals in the nanopipette. This methodology is then used as a tool for screening growth additives with high control and time resolution, allowing for their efficacy to be ranked. The final chapter will summarise and consider the implications of these studies and how SICM could be developed further still and the possible applications of these proof of concept studies going forward for the consideration of living and non-living systems.

## 1.2 Scanning Probe Microscopy

SPM is a diverse family of microscopic tools that involve using a physical probe in order to attain information about, or image, a substrate or other interface.[7] Each

SPM technique takes advantage of a specific type of interaction between the probe, which also varies between each SPM technique, and the interface in order to provide morphological or functional information about it. Some of the primary examples of SPM techniques include: atomic force microscopy (AFM),[8-9] scanning tunnelling microscopy (STM),[10-11] Scanning electrochemical microscopy (SECM)[12-14] and SICM[1, 15], which is the focus of this work. Each of these techniques finds application in different areas and each has their own merits and disadvantages. SECM, for example, has been used extensively for electrochemical mapping of electrodes and other interfaces[14, 16-20] as well as for detection of various ions and pH using functionalised electrodes,[21-24] but miniaturising the SECM probes is challenging and the topographical information that can be obtained from SECM experiments is often of poorer resolution than that possible with other SPM techniques.[25] Consequently, hybrid techniques such as SICM-SECM[25-28] and AFM-SECM[29-31] have become more common in recent years, combining the high-resolution topographical information that can be attained with SICM or AFM, with the electrochemical information provided by SECM. In doing so, this allows for a correlation of structure and function to be attained.

The resolution of SPM techniques is a key consideration in their usage as it determines the level of information that they can attain and is usually related to the type and size of the probe employed. Typically, SPM techniques span from the microscale, in the case of SECM, which use ultra-microelectrode (UME) probes,[25] down to the nanoscale for SICM, which uses a nanopipette probe,[15, 32-34] and can even obtain atomistic level information when STM[35-36] and AFM[37-38] are employed. SPMs can provide a wealth of information not accessible with other microscopic techniques and they are becoming increasingly valuable for answering key questions about a host of different interfaces.

### 1.3 Scanning Ion Conductance Microscopy

The SICM was first described in 1989[1] around the same time as the SECM.[13] Whilst SECM has been used widely since as a tool for functional electrochemical mapping of substrates, SICM has found limited functional applications to date and has

predominantly been used as a tool for topographical mapping of samples[33-34, 39-41] as well as some studies where it has been used to measure ionic conductance through porous substrates[1, 42-44] and for local delivery from, or patterning with, the nanopipette probe.[45-46]

### 1.3.1 Principles of Operation

SICM is used for probing an interface that is bathed in a conducting electrolyte solution. A single channel nanopipette probe is usually filled with a similar electrolyte solution along with a QRCE, with a second QRCE placed in bulk solution. Typically, a bias is applied between the two QRCEs to drive a current through the end of the nanopipette, which can be recorded, as depicted in Figure 1.1a. In bulk solution, with the probe positioned away from the substrate, the resistance of the nanopipette, together with the conductivity of the electrolyte solution, are what contribute most to determine the ionic current that flows. The majority of this resistance is accounted for by the narrowest region of the nanopipette, near the nanopipette opening. As the inner lumen of the pipette gets wider, the contribution to the overall pipette resistance goes down.[15]

As the nanopipette is brought towards a substrate of interest, it is expected, in conventional SICM experiments, that the ionic current will decrease, as the probe-substrate separation distance decreases to below one tip diameter. At these separation distances, the increased access resistance, caused by the narrowing gap between the pipette walls and the substrate, becomes comparable to the nanopipette resistance. Consequently, the overall system resistance increases, as shown in Figure 1.1b, and a measurable drop in the ionic current flowing through the pipette is recorded, as depicted in Figure 1.1c. Under a large range of imaging conditions this is what will be seen to happen and the drop off in the ionic current can be used to sense the surface of interest. It will be explored later on that sometimes the SICM ionic current response, on approach to charged interfaces in lower ionic strength solutions, is seen instead to increase due to the influence of the diffuse double layer (DDL) extending from the substrate.[2, 4, 6, 47]

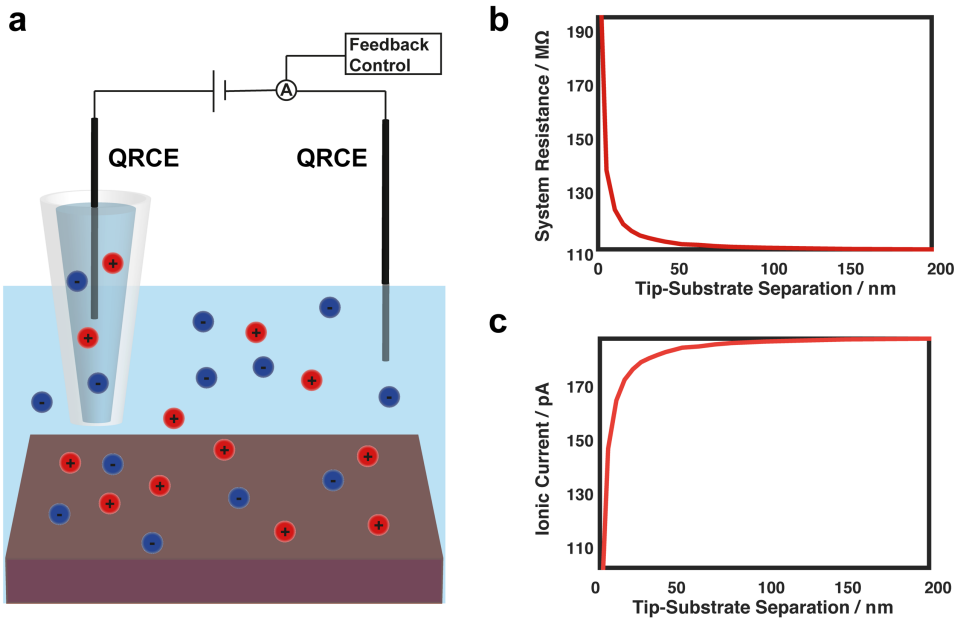


**Figure 1.1. a)** Schematic of the SICM setup with a nanopipette filled and bathed in electrolyte solution above the substrate of interest. A bias is applied between a QRCE in the nanopipette and one in bulk solution in order to generate an ionic current, which can sense the surface. **b)** Upon approaching within one tip diameter (100 nm) of the surface, an increase in the resistance is observed as a result of the reduced access of ions to the probe opening. **c)** A drop off in the recorded ionic current is observed as a consequence of the increased resistance.

### 1.3.2 Feedback Types and Scanning Regimes

As outlined above, on approach to a neutral, insulating substrate, or under conditions where surface charge plays a negligible role on the SICM response, the current is expected to decrease on approach to the surface.[13, 15, 33] Consequently, the ionic current can be used as a means of detecting when the SICM probe is near the substrate and hence be used for tracking the surface topography. If the probe is brought into the vicinity of the surface at different spatial locations until the same drop off of ionic current is observed, it would be expected that the separation distance between the probe and tip would be identical, and hence a topographical map can be built up from extracting the position at which the probe conductance reached this set point value.[1, 15, 33]

The probe position is often controlled by piezo electric positioners, which allow for sub-nm precision in moving the pipette vertically or laterally across the surface. These piezo electric positioners are controlled by applying a voltage, usually controlled via a computer interface, which leads to an expansion or contraction of the piezo material. A feedback loop can be setup such that the piezo electric positioners move the nanopipette probe towards the surface until the current drops below a certain value. The expansion of the piezo, in the *z* direction, at this point can then be extracted to infer on the nanopipette position and used to generate a topographical map of the sample. At this point, the probe can be scanned across the surface, with the piezo positioners adjusting the height of the nanopipette above the sample, aiming to maintain a constant current value. This current value should correspond to the same tip-substrate separation distance and this scanning mode is termed constant distant scanning and often is performed in a raster scan pattern.[1, 15, 33, 48] Alternatively, pixel wise measurements can be made, whereby once the set point current value is reached upon approach, the probe is then retracted away, moved laterally to a new location before repeating. This has advantages for mapping samples that have large height gradients, where a constant distance scan mode may not be able to track the steep changes accurately or quickly enough. This scan regime is known as a hopping or standing approach mode.[39, 41, 49-50] Whilst the constant distance mode has advantages in terms of being able to perform scans at a faster rate, hopping mode holds key advantages such as being able to make self-referencing measurements to bulk values at each pixel. This becomes particularly beneficial, as will be discussed in later chapters, for trying to elucidate surface properties other than topography using SICM, whereby the bulk properties of the nanopipette need to be subtracted to reveal the effects of the surface.

The utilisation of the raw ionic current as a means of feedback for topographical mapping is often termed the direct current (DC) feedback type in SICM experiments (Figure 1.2a).[15] In some studies it has proven beneficial to instead use a different feedback signal. The ionic current can be highly susceptible to drift between the two QRCE electrodes and for long scan times this can be particularly problematic and could lead to a failure to track surface topography accurately. This is particularly troublesome in constant distance scans, which do not self-reference

from a bulk value at each pixel. Even In hopping mode scans, if the ionic current is drifting too much, false approaches may occur whereby the SICM has not actually sensed the surface at all and so the produced topographical map may contain false height information. To avoid these affects, modulation techniques can be employed in order to generate an AC signal. Usually this is achieved through oscillating the nanopipette position up and down at an applied frequency, typically in the 100 Hz – 1000 Hz range. A lock-in amplifier can then be used to extract the ionic current response at the same frequency. This provides a signal that is much less noisy than the raw ionic current and is less susceptible to drift effects.[51-54]

Using this distance modulated (DM-) approach (Figure 1.2b), when the nanopipette is in bulk solution, more than one tip diameter away, no AC signal is expected because there would be little difference in the conductance state between when the nanopipette is furthest and closest to the surface, across an oscillation cycle. However, as the ionic current begins to respond to changes in the resistance, as the nanopipette approaches the substrate, there will subsequently be a variation in the conductance state throughout the oscillation period and as such there will be a resulting AC signal. This AC signal can be described by both its amplitude and a phase angle component, with respect to the applied modulation signal. Typically, in DM-SICM experiments, for example those presented in chapter 2 of this thesis, an increase in the AC amplitude is used for feedback. A threshold value of the AC amplitude can be set and upon reaching this value, the piezo electric positioners will cease to move the nanopipette further towards the substrate and the substrate height can be extracted.[15]

In chapter 3 of this work, an alternative modulation technique is described, whereby an AC signal is generated instead through oscillating the bias between the two QRCEs (Figure 1.2c).[3] This approach holds several advantages over the DM-SICM scheme, which will be explored later, but the most significant is that this allows for the detection of the substrate, even when there is no net bias applied. As is the focus of chapter 4, this will help render the SICM response insensitive to surface charge when desired, making the SICM a truer tool for topographical mapping.[4] Modulation techniques hold other advantages over the DC approach in SICM. Through the generation of an AC amplitude and phase signal in BM-SICM,

information can be obtained about the total system resistance and capacitance. The relative contribution of these two components to the SICM response can be explored through considering how the AC phase signal changes in an SICM experiment. In BM-SICM, where there is a measurable AC signal even when the probe is positioned far from the substrate, the bulk capacitive properties of the nanopipette can also be determined.

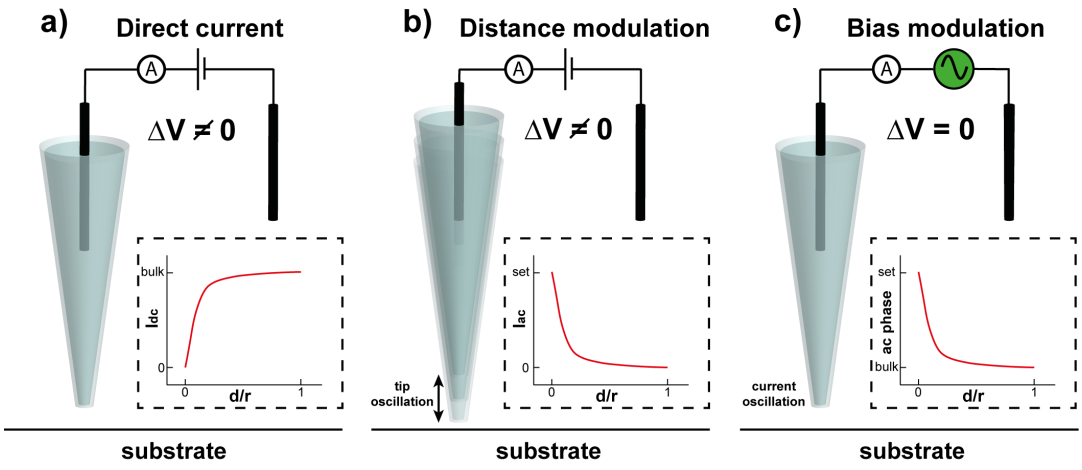


**Figure 1.2.** Schematic depiction of three SICM feedback types. **a**) In the DC approach a drop off in the ionic current is used to sense the substrate. **b**) In DM-SICM an oscillation is applied to the nanopipette probes *z* position generating an AC current, which is only significant when the nanopipette approaches the substrate. **c**) In BM-SICM an oscillation is instead applied to the bias between the QRCE in the nanopipette and outside generating an AC signal which is sensitive to the substrate even when no net bias is applied.

Whilst modulation techniques hold these notable advantages, they can suffer from longer scan times compared to experiments performed using the DC feedback type. The extraction of the AC signal using a lock-in amplifier, and its subsequent response time to changes in the conductance state of the SICM system is significantly greater than that of the unmodulated current signal. As a result of this, slower approach speeds are often used in modulation experiments, which lead to longer scan times. The response time of the DM- and BM- SICM experiments is directly related to the time constant of the lock-in amplifier used to extract the AC

signal and this time constant is chosen relative to the oscillation frequency applied.[55] For higher oscillation frequencies, where the oscillation period is less, a smaller time constant is required to extract the AC signal over. Typically, in order to get a clean AC signal, the time constant should be approximately 3-4 times the period of oscillation. If the time constant is smaller, the AC signal may be too noisy, but if the time constant is too great the response time will be too long. In unmodulated SICM approaches, the ionic current responds near instantaneously to changes in the conductance, depending on the current follower used, and so faster approach speeds can often be achieved, which is part of the focus of chapter 7 where a trade-off between faster imaging and more accurate surface charge and topographical information is explored.

### 1.3.3 The SICM Probe

SICM employs a single barrelled micropipette or nanopipette as its probe, which is usually fabricated from either a glass or quartz capillary. The capillary is heated in the centre using a laser puller, whilst a simultaneous pulling force is applied to each end of the capillary. Where the laser heats the capillary, it is melted and the pulling force distorts the glass, pulling it finer until the two halves of the capillary separate, yielding two similar halves, which have a fine taper at the end. The parameters used in the production of these nanopipettes can be varied to give a variety of geometries, depending on the desired application. Depending on the heat used, pulling force and material chosen it is possible for pipettes spanning the nanometre to micrometre scale to be fabricated.

The lateral resolution of SICM is inherently linked to the size of the probe used, and is typically stated to be around 3 times the opening radius of the nanopipette.[32, 56-57] With the smallest pipettes that are claimed to be used, this can give SICM a resolution of sub 15 nm[41, 58] which, whilst is not the atomistic level possible in some AFM studies, means that high-resolution topographical mapping is achievable with SICM.[59] It is important to note that the response of SICM is dependent on the nanopipette probe used, both in terms of its geometry and surface properties. As such, the characterisation of the nanopipette probe is an

important task and is the subject of chapter 5.[5] It is common practice to take one of several approaches to characterise the nanopipette used in SICM experiments. In order to get geometrical parameters of nanopipettes, scanning electron microscopy (SEM) is commonly used.[58, 60-62] SEM can provide some information useful for characterising nanopipettes allowing for estimates of the nanopipette opening size, as shown in Figure 1.3a as well as how the overall diameter of the nanopipette varies up its length. As chapter 5 explores, this is insufficient knowledge to interpret and capture the nanopipette response fully and techniques that provide information about the nanopipette lumen up the length of the nanopipette become necessary, which is only possible through using transmission electron microscopy (TEM), as exemplified in Figure 1.3b. An alternative strategy that is used, and is evaluated in chapter 5, is the use of analytical equations for estimating the nanopipette geometric parameters from the recorded SICM signal in bulk. Commonly used in other SPM techniques, this approach fails when the nanopipette deviates significantly from the assumed geometry, which is usually approximated as being conical in the most significant region for determining resistance. As will be discussed later, these approaches also suffer when the nanopipettes are operated in conditions where the surface chemistry of the nanopipette material also begins to influence its response.

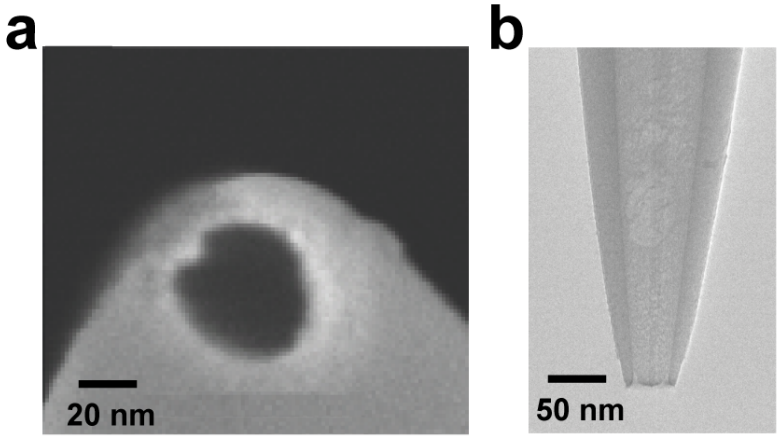


**Figure 1.3.** Nanopipettes can be fabricated to a variety of sizes with openings on the nanometre scale. To characterise them SEM **(a)** is often used but TEM **(b)** offers much more information about the nanopipette dimensions.

### 1.3.4 Morphological Studies of Live Cells

To date the majority of the applications of SICM have primarily been focussed around mapping the surface topography of non-conducting samples. The non-contact method of SICM feedback, established by either the DC or modulation based approach, makes SICM a comparably non-invasive technique in contrast to force/contact based probe techniques. This, combined with the wide range of possible imaging media available for use in SICM experiments, makes it particularly suitable for the consideration of living cells. As such, a large number of SICM studies have been carried out studying the morphology of a variety of living cells and biological systems, both in their natural state and also to observe their response to varying stimuli, which may be chemical or mechanical. Figure 1.4 shows an example topographical image obtained using DC mode SICM of a group of PC12 cells.

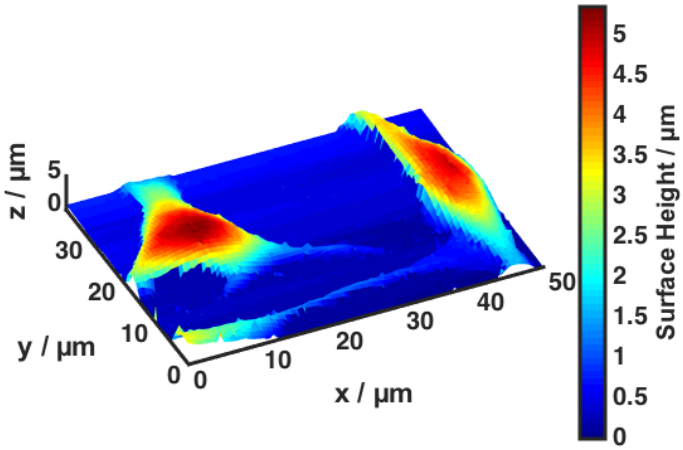


**Figure 1.4.** SICM topographical image of three PC12 pheochromocytoma cells in close proximity showing processes extending from the cell bodies.

The first studies of cell morphology using the SICM were conducted in 1997[33, 63] in work that demonstrated the benefits of its non-invasive nature, showing there was no damage caused to the cells studied as a result of the SICM scanning process. This initial work was demonstrated for cardiac myocytes, cells from the Caco-2 colon cancer cell line and the murine melan-b line and, since this work, many other cell types have been explored using SICM. Although there are non-contact modes of AFM, these still involve the probe being positioned within Angstroms of the

substrate so that damage, or perturbations to the cell's natural state, could occur. This means that SICM, which can probe a substrate from a distance of tens-hundreds of nanometres away is much less invasive, reducing the risk of perturbing cellular processes or damaging the cell.[59] Another advantage of the SICM over other techniques, for the study of cells, is that there is a minimal preparation required. They can be imaged in physiological buffers because of the high electrolyte composition present in them. Although not in the scope of the initial SICM study, the possibility of being able to simultaneously deliver drugs or other stimuli to the cell surface, using the SICM, were already proposed, as well as options for micromanipulation with the probe and using it for electrophysiological studies. Since its inception, there have been many more studies focussed on using SICM for probing and mapping other living systems, many of which are discussed below.

Through the acquisition of several topographical maps, it is possible to see how the volume and morphology of a cell varies over time.[48, 62, 63] Regulation of the cell volume is an important homeostatic mechanism, as there is a constant flux of material across the cell membrane, and studies using SICM have provided insights into how the volume of cells is controlled and varies in response to changes in osmolality.[48, 64] Because of the high spatial resolution achievable with SICM, it is then possible to see where the changes in volume are taking place across the cell from where the height maps differ between scans.

When high scan rates are employed in SICM experiments, it is possible to track the dynamics and behaviour of whole cells, or subcellular structures, over a long period of time. Using SICM, the cycle in the behaviour of microvilli on the surface of cells could be studied and it was demonstrated that these microvilli grow and then undergo a stationary phase before retracting.[65-66] Through collecting multiple scans, over a large region of a cell's surface, it becomes possible to visualise many such microvilli and a distribution of their state at each time point could be identified. Analysing consecutive scans performed using SICM, can also provide information about the motility of whole cells, their speed of movement and any preferential direction, as has been demonstrated in studies of oligodendrocyte cells. These measurements were able to distinguish between undifferentiated and mature cells and showed that the undifferentiated cells are much more mobile.[67] Repeated

scans performed over a long time period become possible thanks to the robustness of the SICM feedback, particularly when employed in a DM mode, and can help to identify the morphological changes that occur throughout the cell cycle and during cell division.[66] Other cellular processes, such as exocytosis, can also be studied, providing quantitative information about the subsequent changes in cell surface area that occur.[68]

SICM can allow for imaging on the single protein level, as has been demonstrated for immobilised proteins on a substrate, as well as for proteins presented on the surface of living cells.[58] As well as allowing for topographical imaging of processes and proteins present on the cell membrane, it is also possible to locally manipulate cells with the SICM, where in one study the probe could be used to guide and promote the development of neuronal growth cones protruding from them, changes which could be subsequently tracked with topographical scans.[69]

Whilst much of the early work studying living cells utilised a constant distance scanning approach, maintaining the SICM set point as the probe is scanned laterally across the surface, more recent work has focussed on the use of a hopping, or standing approach, protocol, whereby pixel-by-pixel maps of surface topography are built up through a repeated approach-extract height-retract-move laterally regime.[39, 41, 70] This mode introduced a more stable method for scanning living cells, where changes in surface height can be quite steep and hence there would be the risk of the probe and cell colliding with constant distance scanning. Additionally, hopping mode SICM allows for a self-referencing approach to be taken where at each pixel the SICM response can be considered relative to its bulk value. This makes the technique more robust to drifts in the ionic current caused by changes in the ionic composition, thus facilitating longer scan times.[70] Using this approach, finer cellular structure could be revealed with the SICM and it became possible, for example, to image and track the motion of stereocillia on murine hair cells and also to map neurites from neuronal type cells.[39] The total scan area and hopping distance can be tuned to achieve the desired resolution and scan time.

A great wealth of information can be obtained using the SICM for studies of cell pathology, as it is a powerful tool for identifying heterogeneities and phenotypic

differences between neighbouring cells. Through identifying morphological variations between individual cells it is possible to distinguish, and categorise, the different types present in a group of cells, or to identify abnormal, possibly diseased, cells. As an example, three different types of neuroblastoma cells studied were each seen to exhibit a characteristic height, width and length and from measurements, obtained using the SICM, they could be quickly screened and categorised.[71] SICM used in the study of cardiac tissue, could quickly identify damaged cells from the loss of T-tubules on the cell surface and a flattening process, where the Z-groove present on the cell membrane disappears.[72-73] From such phenotypic variations, it is thus possible to use SICM to identify unhealthy tissue from healthy tissue.

The response of the cell membrane to stimuli can also be observed using SICM; treatment of cardiac cells with formamide, for example, also results in a similar loss of T-tubules and reduction in the Z-groove dimensions.[72] Studies of cardiac tissue have considered the use of SICM for the study of other forms of cardio vascular diseases as well, considering how morphological changes in the cell and structural properties relate to arrhythmias, heart failure, atherosclerosis, hypertrophy and mechanical dysfunction of the heart.[74] It is even possible with SICM to track the contractions of cardiac cells, which can help distinguish cardiomyocytes amongst other cell types as well as to help identify anomalies with contractions.[75]

Pathological studies with SICM have not been solely focussed on cardiac disease, SICM has been used to provide insights with regards to Alzheimer's disease, allowing for high-resolution studies of the structure of individual amyloid fibres, which are believed to play a key role in the development of the disease, to be performed.[76] Renal cells have also been studied, providing information with regards to how the renal epithelial membrane maintains integrity in the presence of stress. This work demonstrated the formation of protective structures on the surface of the cell membrane, balloon-like features and also demonstrated a cooperative movement of cells following apoptosis.[77] SICM has also been used in the study of endothelial cells, comparing cells grown under different shear stress conditions and showing that they resultantly exhibited different morphologies. This information could then be related to the structure of cells taken from different regions of the aorta which experience different levels of stress as part of their natural function.[78]

Electrophysiological studies are also possible with the SICM probe employed in a smart patch clamp mode, where the nanopipette is used for both topographical measurements as well as patch clamp recordings.[50, 66, 79-81] The patch clamp is a technique that allows for the dynamics and mechanism of individual or small clusters of ion channels present on a cell membrane to be studied.[82-83] A glass nano- or micropipette is used to seal the area around an ion channel, as depicted in Figure 1.5, and, together with the application of suction, forms a high resistance seal of the order of gigaohms.[84] Subsequently the ion channels can be studied through recording the current that passes through them. The ion channels can also be stimulated from the nanopipette with ions or toxins, for example, and the response of the ion channels to these can be monitored.[80-81] Whereas in traditional patch clamp measurements, where optical microscopy is used to position the patch clamp probe near the region of the cell membrane to be studied, the combined SICM/patch clamp allows for SICM feedback to be used instead, allowing for a more automated procedure that also enables correlative topographical information to be extracted to guide and relate to the patch clamp measurements.[85] A host of different ion channels can be explored in this technique including $K^+$, $Na^+$, $Cl^-$, and $Ca^{2+}$ selective channels.[84]

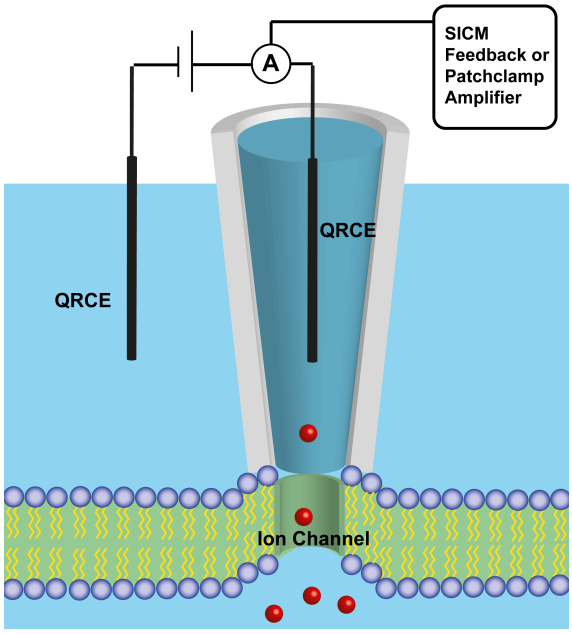


**Figure 1.5.** Schematic of combined patch clamp and SICM measurements. Nanopipette can be used to either provide topographical information or single ion channel recordings through positioning above channel.

Other studies of living cells using SICM have involved applying the technique for assessing the stiffness of living cells and measuring the elasticity of the cell membrane.[59, 62] Two approaches have been taken for this task. The first combines results from both AFM and SICM measurements, using the difference between the force based scan and non-contact measurement to inform on the stiffness.[59, 86] The second approach involves inducing a small pressure driven flow through the end of the nanopipette to perturb the cell membrane surface. Through measuring the height differences between SICM measurements with, and without, the flow present, information about the cell elasticity can be obtained.[62] These approaches are not limited to single measurements but can spatially resolve regions of the cell membrane that are more or less rigid, thus allowing for a correlation with other known cell function. As well as being used to measure stiffness of cells, pressure driven flow through a nanopipette has also been utilised as a tool for applying mechanical stimuli to neuronal cells over a small area. This approach is highly localised as it acts only over the footprint of the nanopipette probe, and thus can locally stimulate without perturbing the whole cell.[80] Using this approach, the response of mechanosensitive ion channels for example has been observed.[80]

### 1.3.5 Other Applications

SICM is a powerful tool for providing diagnostic information about living cells from their morphology, with a spatial resolution that can be comparable to AFM and other high-resolution microscopy techniques. However, the SICM has not been used exclusively for mapping living cells, and has not solely been used for studying topographical properties of samples. In the initial study where SICM was demonstrated, the capabilities of SICM for mapping surface topography were complemented by the ability to perform conductance measurements of porous membranes or substrates. Through scanning the SICM probe at fixed height above a substrate, regions of high conductance were indicative that the SICM probe was above a pore where the access of ions to the nanopipette would be less hindered, than when it was above a planar surface. This information could then be correlated to topographical scans performed subsequently using feedback.[1] Since this study,

SICM has been used in a similar manor for locating ion channels or pores on membranes and other surfaces. Using a DM-SICM approach for probe positioning, it has been demonstrated that the ionic current can detect changes in the ionic atmosphere present around a nanopore where an ion current has been induced through establishing a concentration gradient across it.[42, 87] The conductance information can be correlated to the topographical information of the SICM scan and the ionic transport through the nanopore can be well modelled.[43] The obtained information can provide diagnostic information about the nanopore itself with it being shown that the SICM can distinguish between conical and cylindrical nanopores from the measured resistance across the membrane.[88]

Further studies have explored the capabilities of SICM for imaging biological nanopores. Through imaging a membrane bathed in potassium free media and using the scanning nanopipette as a source of potassium ions, the location of ATP regulated potassium channels can be identified and their response observed using a second nanopipette, when the potassium containing probe is positioned above it.[79]

The example above highlights another potential application of the SICM probe as a tool for the local delivery of drugs, molecules or other stimuli to a surface of interest, as well as the possibility of patterning through depositing material from the nanopipette onto a surface.[45-46, 89-92] In these applications, the nanopipette probe can serve as a reservoir for a particular probe molecule of interest. Through controlling the potential applied to the QRCE in the nanopipette and considering the charge of the species it becomes possible to either capture it in the electric field present in the lowest region of the nanopipette or release it from the nanopipette via electrophoretic flow. This approach has been demonstrated for a variety of biomolecules including negatively charged DNA[46, 91] and positively charged immunoglobulin G (IgG).[91] Tuning the applied bias can allow for the controlled deposition or "writing" of the molecule onto a functionalised substrate, and the molecule can be fluorescently tagged for verification that it has been deposited. With this approach, either simple arrays, or more complex patterns, can be written onto a surface.[91] Not limited to biomolecules, a similar approach has been used for electroplating copper microarrays onto surfaces[92-93] as well as the deposition of silver.[94] Being able to deposit metal micro and nanostructures onto a surface with

high precision could find great applications in the manufacturing of electronic components.

Using nanopipettes, it becomes possible to deliver, with high accuracy, to very specific regions of the target substrate. This use of nanopipettes as “nanopens” has been demonstrated for the IgG antibody on both a functionalised glass substrate[95] as well as performing more targeted deposition where the antibody was deposited in nanoholes that were fabricated in a gold surface using a focussed ion beam.[96] In these cases, the nanopipette could subsequently be used to deliver anti-IgG molecules to the same areas, which had been targeted previously, and the selective deposition could be confirmed through using confocal microscopy as the IgG and anti-IgG were tagged with different fluorophores.

Controlled delivery from nanopipettes allows for specifically targeting of individual cells with a particular stimuli or drug and can be used to study complex cellular processes such as inter cellular communication. This has been demonstrated for $\alpha$-toxin, which is produced by a bacterium infection linked to the onset of cardiac arrests, where it was delivered specifically to one of a cluster of cardiac myocyte cells.[97] This led to the formation of large non-selective ion channels in the cell membrane. Before being targeted with the toxin, the observed contractions of the targeted, and nearby, cells, were synchronised and regular with baseline calcium levels present in all of the cells. However, as a result of the toxin, the perturbed cell exhibited much higher levels of intracellular calcium, that it could not recover, and this caused increased cellular contraction rates, which were seen to spread to surrounding cells. The contractions in the cluster lost all synchronicity and eventually they stopped contracting. This type of study could help unravel information with regards to how signals propagate, and how perturbing one cell can influence the neighbouring cells.

As well as delivering material to a substrate, nanopipettes, in an SICM configuration, can also be used to perform nanobiopsies on a cellular substrate,[98] extracting and capturing material using the electrowetting properties of the nanopipette. The extracted material can then be further analysed, for example by PCR analysis, in the case where mRNA has been extracted. Utilising SICM in this fashion allows for very precise probe positioning so that specific regions of the cell

can be targeted for extraction and this allows for correlation of the biopsy results with SICM topographical information. Very small volumes of cellular material can be extracted, minimising any damage to the cell and maintaining its viability.

Nanopipettes also can find great application as tools for electrospray analysis, where it has been shown that they function at much lower potentials than traditional electrospray methods, whilst exhibiting a high signal to noise.[99] Furthermore, these principles have been exploited in a novel scanning electrospray microscopy technique, where a distance dependence of the electrospray probe to a substrate is observed, allowing for it to be used for tracking surface topography.[61]

Local manipulation of substrates is also possible using the nanopipette in an SICM configuration. It has been demonstrated that the technique can be used to puncture targeted regions of a membrane suspended above a pore array at will. In doing so the nanopipette can produce lithographic patterns on the membrane at desired, targeted locations.[100] These membranes can subsequently be imaged using the SICM with feedback to validate the technique and to map the produced pattern.

As well as the above-mentioned applications, which have been focussed on using SICM for topographical measurements, pore conductance measurements, local delivery and manipulation, there have been limited studies, which have shown that SICM is capable of monitoring electrochemical reactions. One such study considered using SICM for studying lithium battery materials, showing that there was a correlation between topographical features present on the lithium based substrates and the ionic current signals recorded. Thus, SICM was able to spatially resolve heterogeneities in activity present on the surface, possibly informing on how the structure of the lithium material affects its capacitive and lifetime behaviour.[54] More recently, SICM was employed with the aim to unambiguously, but simultaneously, measure topography and interfacial reactivity at electrode surfaces as well as on catalytic nanoparticles. It was demonstrated that high-speed topographical information could be obtained, through adopting a spiral scan pattern, but also that the SICM ionic current was sensitive to faradaic processes occurring at the substrate interface, thus opening up exciting possibilities for electrochemical mapping with SICM.[101]

SICM is not confined for the study of solid-aqueous interfaces and there have been studies of using SICM to track and probe liquid-liquid interfaces as well. SICM has been used to probe the interface between water and nitrobenzene allowing for new information about the interface, including a precise measurement of its thickness to be obtained.[102] Information about the presented double layer at this interface was obtained through varying the electrolyte concentration and observing changes to the shape of the approach curves generated from moving the probe travelled through the solution.

### 1.3.6 Hybrid/SICM Based Techniques

SICM is capable of performing many important, fundamental and nanoscale tasks including being a powerful tool for generating high-resolution 3D topographical maps of living cells.[33-34, 48-49, 59, 70, 103] However, as some of the studies outlined above have alluded to, when SICM is employed in combination with other techniques, in a multi-microscopy approach, the capabilities and versatility can be extended further. Such an approach could, for example, combine the ability of SICM for local delivering or topographical mapping together with fluorescence based confocal microscopy. The laser source of the confocal microscope can be focussed on the region below the nanopipette tip, causing any species that are fluorescently active at the applied wavelength, to emit a fluorescence signal. This signal can provide additional functional and specific chemical information about where the labelled probe species or nanoparticle diffuses to and where it resides. As an example, this approach has been used to monitor calcium concentrations around contracting myocytes and allowed for correlation with the structural information obtained from SICM.[53]

In the same way that nanopipettes can be used to deliver material to a substrate, they also provide a means of trapping molecules such as DNA and proteins in the electric field present at the end of the nanopipette, localising and concentrating the species. These effects can be observed for fluorescently tagged molecules, using confocal microscopy to observe their location.[104]

The combination of using laser confocal microscopy together with SICM has also revealed new endocytic pathways, through studying the mechanism of clathrin

pit formations and closure.[105-106] Clathrin can be tagged with Green Fluorescent Protein, which can be excited and detected using confocal microscopy, whilst other proteins involved in the process could also be tagged and identified.[105] Endocytosis can also be studied through observing the interaction between fluorescently labelled nanoparticles, delivered from the nanopipette probe to targeted locations on the cell surface as demonstrated for lung epithelial cells in one study.[107] To summarise, confocal microscopy provides a means of confirming what has been released from the probe and also to provide information with regards to the dynamics of release from the nanopipette and the behaviour of the fluorescent species whilst in the nanopipette.[46, 91, 95, 108-109]

Similarly, there has been some effort to combine SICM with scanning near field optical microscopy (SNOM) through the insertion of an optical fibre into the SICM probe. The SICM response can be used to provide accurate topographical information, whilst SNOM can provide optical images taken under the same conditions the SICM scan was obtained. Using this technique on rabbit cardio myocytes, SICM topographical data was combined with optical images and it was shown that it was possible to identify features such as sarcomeric striations.[110]

Amalgamating separate SPM techniques can help increase the depth of information that can be obtained from them, for example SICM-SECM combines the two individual techniques into a single probe. In contrast to SICM, SECM uses an UME probe and can generate spatial electrochemical maps through monitoring electron transfer reactions of redox active mediators to give an electrochemical signal. SECM is capable of obtaining topographical information, as the availability of the redox species to the SECM probe will change, as the probe approaches a substrate of interest. However, in comparison to SICM, the topographical capabilities of SECM are poor and can suffer greatly from effects such as electrode fouling. This can be overcome through combining the two techniques, which is achieved by either using a theta, dual barrelled, capillary where one serves as the SICM barrel and the other contains serves as the UME SECM channel,[28, 111] or through using a ring configuration where metal is deposited on the walls of the SICM channel and is used for SECM imaging.[25-26, 112] SICM-SECM, as depicted in Figure 1.6, facilitates spatially

resolved electrochemical maps, which can be correlated with the topographical maps generated by the SICM channel.

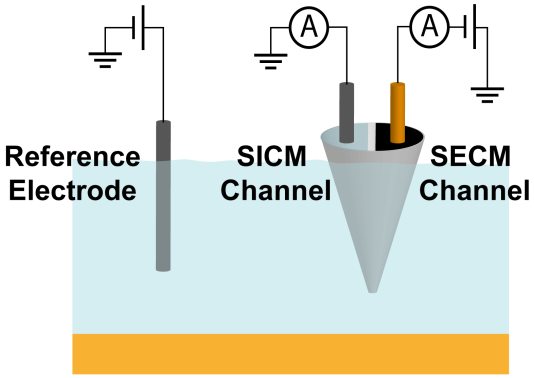


**Figure 1.6.** Schematic of SICM-SECM with a dual barrelled pipette, one barrel for SICM topographical measurements whilst the other barrel is filled with carbon (for example) and used to monitor electrochemical processes.

The SECM electrode can be functionalised to provide sensitivity and specificity to a wide range of analytes whilst the SICM channel can independently position the probe. SICM-SECM has been employed for pH sensing,[111-112] where the carbon or metal electrode is coated with iridium oxide or a polyalanine film for example, allowing potentiometric pH measurements to be undertaken. Functionalisation of a carbon electrode in the SICM-SECM setup with platinum also permits measurements of $O_2$[113-114] and $H_2O_2$[115] by amperometry. SICM-SECM has facilitated the studies of the electrochemical properties of a wide range of different substrates ranging from dissolving crystals[111] and single living cells[114] to electrocatalytic nanoparticles[28, 115] and electrode surfaces.[27]

In contrast to SICM-SECM experiments where the SICM channel is used to facilitate accurate probe positioning and hence improve the accuracy of the acquired topographical information, SICM-AFM instead uses the feedback of AFM to position the probe, independent of variations in the ion current, whilst allowing the SICM response to make conductance measurements. SICM-AFM uses a bent nanopipette probe to serve as both the AFM cantilever but still capable of making conductance measurements as it contains an open channel, as shown in Figure 1.7. This technique

has successfully mapped nanopores in a synthetic membrane in both a tapping mode and contact mode of feedback, providing maps of the pore structure, as well as making measurements of their ionic conductance.[116] However, since the introduction of modulated feedback types in SICM and the introduction of hopping self-referencing scan regimes, which facilitate mapping of topographic and conductance measurements concurrently, the use of SICM-AFM has been limited, although there have been some applications for performing force and topography measurements simultaneously.[69, 117]

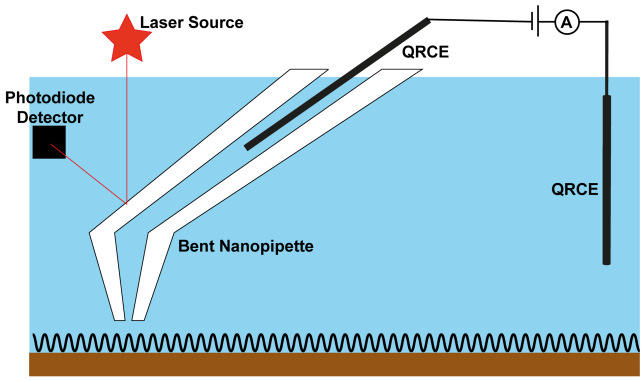


**Figure 1.7.** Representation of combined SICM-AFM with a bent nanopipette serving as both a cantilever for force measurements and an open channel containing an electrode for conductance measurements.

A further development to the SICM has been the introduction of potentiometric SICM (P-SICM), which utilises a dual barrelled pipette and has been applied for investigating transmembrane ionic conductance at biological and porous interfaces.[44, 118-119] In the P-SICM setup, one of the barrels contains a pipette electrode, which serves to measure the ionic current for probe positioning. The second barrel contains an electrode to measure the potential at the pipette tip with respect to a reference electrode in bulk solution. A potential difference across a porous membrane can be induced through applying a bias between the working electrode, located on one side of the membrane, with respect to a counter electrode on the other side. Using this approach, the effects of pore size and applied bias on the measured potential can be explored through the potentiometric measurements made at the nanopipette tip as it is scanned across the substrate.[118] Additionally, the technique allows for the differentiation of conductive pathways, showing a

significant difference in conductance between the cell bodies and cell junctions of renal cells.[119]

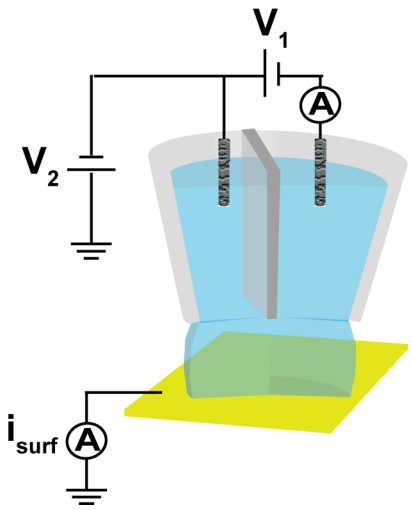


**Figure 1.8.** Schematic of the SECCM setup with a dual barrelled nanopipette filled with electrolyte solution. A bias is applied between the two QRCEs, one in each barrel to produce an ion conductance signal through the meniscus that can be used for feedback.

Based on similar principles to the SICM, SECCM is instead a droplet-based technique, which does not require the substrate of interest to be completely immersed in electrolyte solution.[120-122] In this configuration, a dual barrelled pipette is used, with both channels filled with electrolyte solution and a QRCE, as shown in Figure 1.8. A meniscus forms at the end of the pipette and, as a bias is applied between the two QRCEs, an ion conductance signal is produced and can be monitored. When the droplet contacts with a substrate, the meniscus will become compressed, changing shape and consequently exhibits a change in its conductance. Through recording the probe position required to maintain a constant conductance value, as the droplet is scanned across a substrate, SECCM can be used to map topography of insulating or conducting samples. Additionally, through the inclusion of redox active species in the SECCM barrels, the electron transfer between the probe molecule and a working substrate electrode can be studied in a highly localised manor.[123] In this way heterogeneities in surface activity can be identified

through variations in the faradaic current at the working electrode. SECCM has been used extensively in the study of carbon electrodes including: graphene,[120, 124-125] carbon nanotubes[126-127] and boron doped diamond[128] as well as for studying other electrode materials[129] and individual catalytic nanoparticles.[130-132] As with SICM, SECCM can allow for controlled deposition and delivery of material to a substrate allowing for complex patterning and formation of microstructures on an electrode or other substrate.[133-135]

## 1.4 Prospects for SICM as a Tool for Surface Charge Mapping

Whilst there are great advantages and potential applications for multifunctional imaging platforms that combine SICM with optical, or other SPM, techniques, the SICM can provide further functional information in its own right. Much of this thesis is concerned with first showing the potential of SICM for sensing surface charge heterogeneities of extended substrates, through sensing variation in the surrounding DDL. These concepts are then developed further, allowing SICM to be a robust and quantitative tool for unambiguous mapping of both surface topography and surface charge for a range of systems, both inert and living. Surface charge plays an important role in a diverse range of complex interfacial systems and so being able to probe the surface charge in a non-invasive way could find a great range of applications spanning the study of crystals and minerals,[136-140] colloidal science,[141-143] nanoscale analytical devices[144-146] and perhaps most significantly in living systems, where surface charge is known to play a key role in a range of living processes such as cellular growth and division,[147-148] adherence,[149-151] cellular uptake,[152-157] and communication.[158-160]

### 1.4.1 Surface Charge and the Diffuse Double Layer

Surface charge density refers to the distribution of charge across a solid interface. While many solids are neutral, in an aqueous environment, ions may interact with, and adsorb onto, the surface or, depending on the conditions, surface groups may become dissociated. Both of these effects can result in a nonzero net charge being present at the surface. When a charged surface is exposed into an electrolyte

solution, a DDL forms as ions are either attracted to the oppositely charged surface (Figure 1.9a, b), or repelled if they are the same charge, resulting in a depleted concentration (Figure 1.9c). The DDL can freely move and its structure, length and composition strongly depend on the magnitude of the surface charge, the ionic composition and concentration of the bulk fluid.

Understanding the structure of the DDL is of great importance in a range of systems including colloidal systems and plays a role in the electrochemical behaviour of electrodes. Much work has gone into developing a model for the structure and characteristics of the DDL at electrodes and other interfaces. Helmholtz was the first to attempt to describe the solid-solution interface, approximating it as a dielectric that stores charge linearly with applied voltage so that it could be described by a fixed capacitance. Gouy and Chapman independently showed that the capacitance was not constant, scaling instead with voltage and ionic concentration and proposed an electric potential that decays exponentially from the charged surface. In their description the relationship between surface charge and the surface potential was:[161]

$$\sigma_p = (8RT\varepsilon\varepsilon_0 c \times 10^3)^{1/2} \sinh(\frac{Z\psi_0 F}{2RT}) \qquad (1.1)$$

where *R* is the molar gas constant, *T* the absolute temperature, ε the relative dielectric constant of water, $\varepsilon_0$ the permittivity of free space, *c* the molar concentration and *Z* the ionic charge of the symmetrical electrolyte. With low potentials, this equation yields the Debye parameter:[161]

$$\kappa = \left(\frac{2F^2 I \times 10^3}{RT\varepsilon\varepsilon_0}\right)^{\frac{1}{2}} \qquad (1.2)$$

where *I* is the ionic strength of the electrolyte solution, and whose reciprocal is the characteristic DDL thickness. It is significant to note, as the value of *I* increases, the characteristic thickness of the DDL decreases as illustrated by comparing the simulated concentration profile in Figure 1.9a and b as well as seen from line profiles through the DDL in 1.9d and e.

The Gouy-Chapman model fails when the surface charge is too great and hence the surface potential is too high, resulting in unrealistic concentrations of ions present near the charged surface and so Stern proposed a new model that combined the Gouy-Chapman and Helmholtz models, proposing a fixed Helmholtz layer of ions adhered to the charged substrate with a surrounding Gouy-Chapman like diffuse layer.[161-162]

Further elaborations include those proposed by Grahame, who proposed the Helmholtz layer be split into two layers, one of ions adsorbed to the substrate with the other being a compact layer of fully solvated ions,[161-162] the BMD model proposed by Bockris, Müller and Devanthan[163] and a triple layer model, which expands the model of Sterne and Grahame, modified how adsorbed ions were viewed and included additional capacitances.[161]

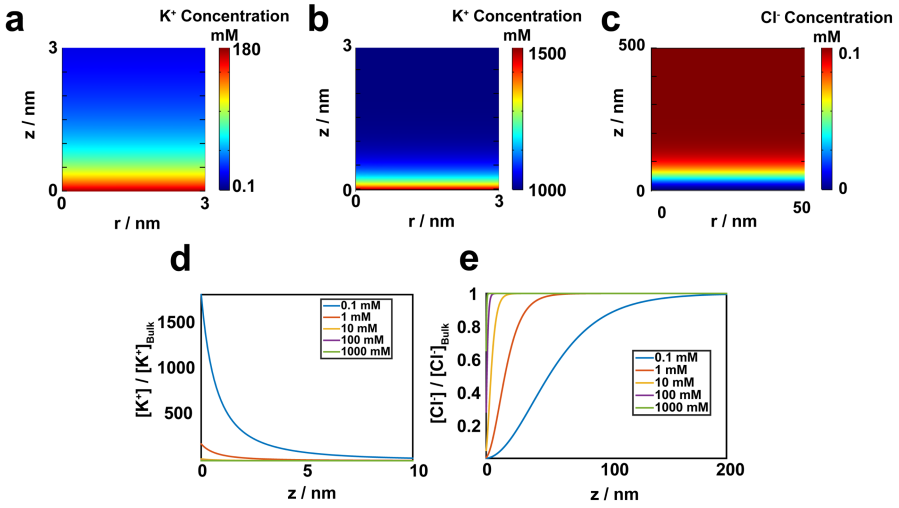


**Figure 1.9.** FEM simulations of a negatively charged interface (-25 mC $m^{-2}$) in KCl solution showing the $K^+$ concentration profiles in **(a)** 0.1 mM and **(b)** 1000 mM as well as the **(c)** $Cl^-$ concentration in 0.1 mM. The concentrations of $K^+$ and $Cl^-$ normalised to their bulk values are presented in **d** and **e** respectively with varying concentration.

### 1.4.2 Techniques for Mapping Surface Charge

Because surface charge is thought to play a key role in a range of important systems, being able to probe, measure and quantify surface charge, particularly of extended substrates such as living cells, could find great application in a range of fundamental

studies. However, currently there do not exist many robust techniques that are capable of doing so.

One of the most promising techniques that has found limited success is using force microscopy to provide some information about surface charge.[164-168] Surface charge mapping with force microscopy utilises a charged cantilever tip in order to probe the electrostatic interactions between the probe and the substrate. Whilst there have been studies that have used this technique to provide qualitative information about relative surface charges present on an extended substrate,[165] this technique has several drawbacks that limit its applicability, particularly in the study of living systems, where some of the most exciting uses of this technique might be found. Firstly, the technique relies on a charged cantilever to generate an electrostatic interaction that can be used to probe the substrate charge. This charge itself is usually unknown and may change throughout a scan depending on interaction between the tip and surface, wear and fouling. In order to provide quantitative information about the substrate charge, there first needs to be a way of knowing the charge present on the probe. Secondly, AFM force curves are complex and understanding the relative contributions of all of the various interactions that act on the AFM tip is a difficult task[169-170] and this means that quantifying the surface charge is unfeasible. Finally, under the magnitude of concentrations at which many living cells are maintained and viable, the range at which AFM is sensitive to surface charge is compressed to the order of one nm and this would make charge measurements without perturbing or damaging the sample particularly challenging.

A second technique that can be used for limited surface charge mapping is surface plasmon resonance (SPR).[171] SPR is very sensitive to local changes in refractive index near a metal solution interface.[172] It involves using polarised light aimed at the bottom surface of the thin metal film and measuring the angle at which the light is reflected. Commonly used to study the binding of ligands on metal surfaces, changes in the refractive index within 300 nm of the metal film can be distinguished. As such, the technique is sensitive to the height of objects, which could be macromolecules, cells or nanoparticles in this region, above the metal film. If these entities are charged, there will be a direct relationship between the charge of its surface, and their equilibrium height above a charged layer on the metal film. If

there is a strong electrostatic attraction, the particle will have an equilibrium height closer to the film whereas a repulsive force will increase the equilibrium distance. This technique can therefore be used in two ways. Either using particles of known charge and using them to probe the surface charge of the film on the metal or if the charge of the film is known, the technique could be used to give information about the particle surface charge. The technique does have some limitations though. The spatial resolution of the technique is limited by the size of the charged particles but can give submicron measurements. Additionally, in order to get a good SPR signal, a high surface coverage of particles is needed. In terms of quantifying the response, knowledge of either the particle surface charge or substrate surface charge is needed, which could therefore rely on other techniques. Other techniques include zeta potential measurements,[173-174] that are more focussed on colloidal systems in solution and also potentiometric titration methods[175-177] but these lack spatial resolution and instead provide information about the average surface charge of a substrate/entity as a whole.

### 1.4.3 Ion Current Rectification in Nanopipettes and Nanopores

Before discussing how the surface charge of substrates, and the DDL extending from them, may influence the SICM response, it is useful to first consider the behaviour of the nanopipette in bulk solution. As mentioned in section 1.3.3, the nanopipette probes used in SICM, as well as for other bulk measurements, are typically fabricated from either a glass material or quartz. Consequently, the surface chemistry of these materials means that the surface charge presented at the interface with electrolyte solutions depends heavily on the solution properties, such as pH.[178] The pKa for the dissociation of silanol groups is 7.5 and, as such, at neutral and physiological pH, these nanopipette materials present a negative surface charge.[178] This, combined with the conical geometry and asymmetric mass transport rates within, and outside, the nanopipette (or nanopore), results in the phenomena known as ion current rectification (ICR), where the current response to a varying applied bias between a QRCE in the nanopipette, and one in bulk solution, is no longer ohmic.[144, 179-184] Instead, depending on the surface charge of the glass and the ionic strength of the

electrolyte present in the nanopipette and bulk solution, as well as the nanopipette size and shape, an enhanced current is observed at one bias polarity and a diminished current at the other, when compared with what would be expected if the nanopipette were uncharged.[180-181, 184] This deviation from the linear current-voltage behaviour can be explained by considering the region at the charged interface as being perm-selective,[184] where the ability for the ions present in the solution to pass through the selective region depends on their polarity. In nanopipettes, where the lumen size is comparable to the size of the extending DDL, the negative charge at the walls of the nanopipette create a region where the positively charged cations can pass but the anions are hindered. When a negative bias is applied in the nanopipette with respect to outside, a build-up of cations is observed, as the diffusion of cations to the nanopipette is greater than the movement up the nanopipette because of the geometry. This results in an enhanced conductance in the nanopipette and a greater ionic current. When the polarity of the bias is reversed, a depletion zone is formed because movement of cations away from the nanopipette is greater than they can be replaced from further up the nanopipette.[5-6, 184] In the case of a positively charged nanopipette (possible where the nanopipette material is functionalised) these effects would reverse and the shape of a current-voltage curve would be reversed, as shown in Figure 1.10.

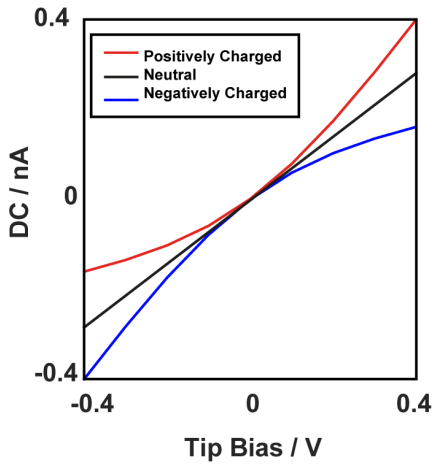


**Figure 1.10.** Whilst neutral nanopipettes exhibit an ohmic current-voltage response, charged nanopipettes experience an enhanced current at one bias polarity and diminution at the other depending on the polarity of the surface charge of the walls.

The level of ICR observed in nanopipette or nanopore systems is dependent on the shape and size of the nanopipette, for larger nanopipettes, the effects would be much less pronounced and a rectification ratio, the ratio between the currents at the equivalent magnitude but opposite polarity potentials, would be closer to unity. ICR is also more prominently seen when the concentration of the electrolyte in bulk solution and in the nanopipette decreases. At higher concentrations, the surface charge of the walls would be screened to a greater extent by the ions in solution, compressing the DDL, and resulting in a smaller influence of the charge. Electro-osmotic flow arising from the passage of current at charged interfaces can also contribute to this effect but several studies have shown that its effect is not as significant in the generally accepted perm-selective model for ICR.[184]

### 1.4.4 Surface Induced Rectification

Whilst the ICR phenomenon has been studied extensively over the last few decades,[180-181, 184] the impact of surface charge on ion conductance measurements has not been apparent until recently. The work presented in this thesis[2, 4-6] as well as some studies performed in other groups[47] have begun to show the exciting capabilities of SICM for being able to probe the DDL and hence provide information about the polarity and magnitude of the charge on extended substrates. As is the case for the walls of the nanopipette in bulk solution, depending on the solution and surface chemistry of the SICM substrate, it may also exhibit a surface charge, which will again lead to the formation of a DDL.[2, 4, 6, 47] It seems reasonable, and is confirmed by studies performed and presented herein, that the ion conductance response will be similarly influenced by the DDL extending from a substrate as the SICM probe approaches it. In fact, it will be revealed that the SICM is sensitive to the composition and structure of the DDL across a similar distance to which the standard SICM response is observed, around one tip diameter away. The response upon approach to a charged interface can differ greatly from that to an uncharged surface and, depending on the magnitude, and sign, of the applied bias and surface charge, as well as the nanopipette characteristics and ionic strength of the bulk solution, an increase in the ionic current can be observed. This is in contrast to what would be

expected as a result of the increased access resistance between the walls of the nanopipette and surface. This interesting result is attributed to the substrate surface charge and the interaction between this and the nanopipette, and raises the exciting new possibility for the SICM to be used as a novel tool for probing surface charge.

Surface charge mapping with SICM offers many advantages over the techniques mentioned above, such as AFM. As it will be shown, it becomes possible to uncouple the response of the nanopipette from the contribution of the substrate through making measurements in bulk solution as well as at the surface.[4-5] These measurements can allow for characterising the surface charge of the nanopipette walls itself, which subsequently means that the contribution of the substrate can be extracted through analysing the ionic current when the nanopipette is next to it. The observed response is seen to occur over a range that means that the nanopipette should not damage the substrate that is being probed. The lateral resolution for surface charge mapping is seen to be a similar size to that of the nanopipette used, with those used herein within the range 40-200 nm with scope for further improvements in future work. The ability to use FEM simulations in particular gives strength to this approach. These simulations allow for both the quantification of the bulk nanopipette properties as well as allowing for quantifying the surface charge of the substrate being probed in a robust manor. This technique is demonstrated in this thesis for a range of substrates including a polymer film, glass and a variety of living systems, both in low ionic strength media (~10 mM) and in physiological conditions. The ability to probe the surface charge in physiological conditions, where the DDL is highly compressed, is particularly advantageous, as probing surface charge in these conditions is highly challenging. Locating surface charge heterogeneities on viable cells in these conditions could help answer fundamental questions if they can be correlated to cellular function.

As well as showing potential new applications for SICM, the studies that are presented also raise questions about how care needs to be taken for SICM studies, particularly when attempting to produce highly accurate topographical maps. The surface charge of a sample affects the SICM response and hence can affect the tip-substrate separation distance in these experiments. This is demonstrated throughout and it is stressed that care needs to be taken with how SICM mapping is

performed. Minimising the effects of convolution is essential to ensure that the tip-substrate separation distance is constant and maintained across a scan. This can be done by either using a BM-SICM approach, so no net bias is applied, reducing the sensitivity to surface charge, or by simply using as small a bias as possible as to allow successful approaches to the substrate. The conclusions drawn from this work may have implications for past studies performed using SICM and shows that perhaps some care should be taken when analysing past results.

## 1.5 FEM Modelling and Quantifying the SICM Response

In order to fully understand the response of SPM techniques it becomes necessary to use theoretical methods. In the work presented in this thesis, a combination of established analytical equations, and computational modelling techniques, specifically finite element method (FEM) simulations, are used to inform and quantify the observed results.

As outlined above, the nanopipette properties, both geometrical and chemical, influence strongly on the SICM response.[5] Consequently, the characterisation of nanopipettes is an important task that first needs to be performed in order to allow for a meaningful understanding of experimental results. The assumption is commonly made that in the region of the nanopipette that contributes most significantly to the ionic current response, the geometry exhibited is conical. Whether this assumption is justified is explored in chapter 5 but what this assumption does allow is for analytical approaches to be applied. Through using equations for the resistance of a cone and knowledge about the electrolyte properties, in conditions where surface charge is not playing a role, and so the nanopipette exhibits an ohmic response, it becomes possible to predict the opening size of the nanopipette without the use of further microscopy tools. Furthermore, this assumption allows then for theoretical approach curves to insulating surfaces to be produced. For a well-defined, simple, conical geometry, there are analytical equations for how the access resistance would be expected to increase with a decreasing tip-substrate distance as in equation 1.3:[3, 15]

$$R_{tip} = R_{bulk} + \frac{\frac{3}{2}\log\frac{r_o}{r_i}}{\kappa.\pi.d} \quad (1.3)$$

where $r_o$ and $r_i$ are the outer and inner radii of the nanopipette at the opening respectively, $d$ is the separation distance and $\kappa$ is the solution conductivity. Such equations are useful approximations, but are limited in their applicability. If surface charge of either the nanopipette or substrate has a significant influence, as it would in aqueous environments of low ionic strength, or, if indeed the nanopipette geometry deviates greatly from the assumed conical geometry, such an approximation would no longer be valid.

FEM models provide an attractive alternative for giving a theoretical understanding to such systems. In FEM simulations, computational software, such as COMSOL Multiphysics, as used in the studies herein, use numerical methods to solve a specified set of partial differential equations across a defined geometry, subject to the initial conditions and boundary conditions chosen by the user. A typical FEM model first involves defining the desired geometry to closely match the experimental system and specifying the necessary properties of the materials that need to be captured such as viscosity, dielectric constants and density. This geometry can be in 1D, 2D or 3D with the higher dimensions often requiring more computational power to solve. Concentrations, charge numbers and diffusion coefficients are also required for each ionic species present in solution. Then the physical equations that are to be solved need to be chosen depending on the system that is being studied. In the case of the simulations performed herein, this includes the Nernst-Plank equation, to describe the flux of ions in solution:

$$\mathrm{J_i} = -\mathrm{D_i}\nabla \mathrm{c_i} - \mathrm{z_i}\frac{\mathrm{D_i}}{\mathrm{RT}}\mathrm{Fc_i}\nabla\phi + \mathrm{c_i u} \quad (1.4)$$

where $J_i$ is the total flux of species $i$, $D_i$ is the diffusion coefficient of species $i$, $R$ is the universal gas constant, $T$ is the temperature and $u$ is the fluid velocity, and the Poisson equation to describe the electric potential:

$$\nabla^2\phi = \frac{-F}{\varepsilon\varepsilon_0}\sum_i z_i c_i \qquad (1.5)$$

where *F* is the Faraday constant, $\varepsilon$ is the relative permittivity of the solution,[3] $\varepsilon_0$ is the vacuum permittivity, and $z_i$ is the charge on species *i*. Using the initial conditions as a first approximation, FEM simulations then estimate subsequent solutions until a calculated error has been minimised, giving the final steady-state solution. It is also possible for time-dependent simulations to be performed to study the transport processes involved, as will be used in chapter 8. FEM models find application in a great deal of systems including the study of mixing problems, crystal growth and dissolution,[185] heat transfer problems[186] and the study of electrode materials.[125]

In the studies presented herein, FEM simulations are predominantly used as a means of exploring the effects of surface charge of the sample and nanopipette, as well as to help characterise the nanopipette properties and validating a new protocol for nanopipette characterisation. Additionally, time-dependent FEM simulations form the basis of understanding and quantifying the mixing timescales required for driving crystallisation in a nanopipette, which is explored in chapter 8. In other studies, FEM simulations have helped provide insights into the limitations of SICM including the possible resolution achievable.[56-57] 3D simulations performed of the nanopipette over a cylindrical pipette showed that it was possible to clearly resolve features when they were separated by 3*r* where *r* is the radius of the nanopipette opening.[57] Whilst there are limitations with these simulations in that they assumed nanopipettes to exhibit a conical geometry, the simulation results help to understand the SICM response and the effect of various experimental parameters, such as the nanopipette size required to get the desired resolution and the separation distances that are needed to achieve this. There is some discrepancy between simulated and experimental studies of resolution in SICM,[32] which have suggested a resolution as low as 0.5*r*[32, 58] is possible, and this could be due to inaccurate characterisation of nanopipettes as well as different definitions of resolution being used, which varies from study to study.[32]

FEM simulations can also help understand how the nanopipette response changes with the slope of the sample being probed.[187] The change in resistance on

approach to a flat sample could be very different to that where the slope of the sample varies greatly over the scale of the nanopipette opening. Consequently, FEM simulations have been useful for implementing algorithms to deal with this and to give image-processing procedures to help correct for any discrepancy. This involves combining the initial topographical information extracted from SICM with FEM simulations of the nanopipette and using an iterative procedure to improve the final SICM topographical image based on this.[187]

## 1.6 Resistive Pulse Detection

A final use of nanopipettes considered here is that of using changes in the ionic current as an entity is present in the nanopipette orifice to provide diagnostic information about it. Nanopipettes and nanopores are being increasingly used as a means of detection for objects in solution.[188-195] As an entity passes through the orifice, there is a transient increase in the nanopipette resistance as the orifice is blocked and hence a drop off in the ionic current flowing through the end of the nanopipette is seen. The larger the entity is, the bigger the obstruction and the larger the drop off in ionic current, as depicted in Figure 1.11. Additionally, the duration of the blockages can provide information about the particles size, charge, shape as well as the speed of translocation.

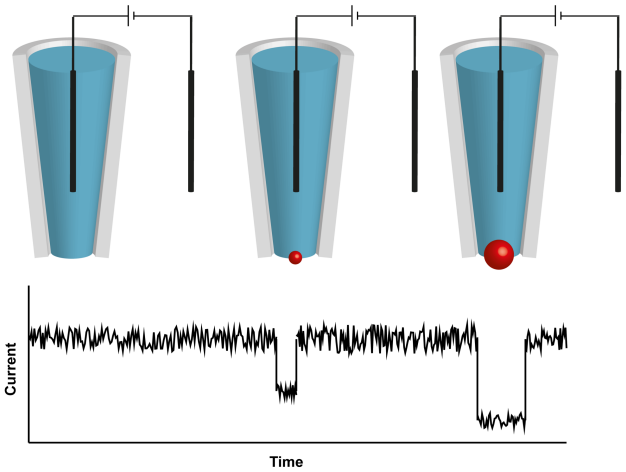


**Figure 1.11.** Nanopipettes can be used as resistive pulse sensors. The current flowing through the end of the nanopipette becomes hindered as an entity passes through the opening. This typically causes a drop off in the ionic current signal recorded.

Whilst this technique can be used simply as a Coulter counter to provide information about the quantity or size distribution of the entity being probed, further structural information can also be extracted. There are exciting advances in using nanopores and pipettes as a next generation platform for sequencing DNA.[196-198] The interactions between the walls of the nanopore, which can be bare or functionalised to enhance interactions, vary, depending on the DNA structure and base presented, and these interactions will result in subtle, but repeatable, changes in the observed current transient. There has also been work using this technique to provide information about the surface charge of particles in solution. As the entity passes through the opening, the surface charge present on the nanopipette/pore walls as well as on the entity can affect the speed at which the entity moves and hence how long a blockage event lasts.

Using the same principles, the current through a nanopipette is also sensitive to the growth of material in the nanopipette opening. Previous work has shown that it is possible to drive crystallisation processes in a nanopipette through having one of the constituent ions that forms the crystal present in the nanopipette with the other in bulk solution.[199] Through applying a bias of the necessary polarity, the two ionic species can be driven together at the end of the nanopipette causing a crystal to form. Chapter 8 of this thesis builds on this work using calcium carbonate as an exemplar system. Using FEM simulations, the mixing processes that take place in this experimental system can be explored and used to justify the experimental observations. Additionally, the approach allows for quick additive screening that is amenable to statistical analysis and can also be used to extract growth rates from the rate at which the current is seen to drop off as the crystal forms.

## 1.7 References

1. Hansma, P.; Drake, B.; Marti, O.; Gould, S.; Prater, C., *Science* **1989,** *243*, 641-643.

2. McKelvey, K.; Kinnear, S. L.; Perry, D.; Momotenko, D.; Unwin, P. R., *J. Am. Chem. Soc.* **2014,** *136*, 13735-13744.

3. McKelvey, K.; Perry, D.; Byers, J. C.; Colburn, A. W.; Unwin, P. R., *Anal. Chem.* **2014,** *86*, 3639-46.

4. Perry, D.; Al Botros, R.; Momotenko, D.; Kinnear, S. L.; Unwin, P. R., *ACS Nano* **2015,** *9*, 7266-76.

5. Perry, D.; Momotenko, D.; Lazenby, R. A.; Kang, M.; Unwin, P. R., *Anal. Chem.* **2016,** *88*, 5523-5530.

6. Perry, D.; Paulose Nadappuram, B.; Momotenko, D.; Voyias, P. D.; Page, A.; Tripathi, G.; Frenguelli, B. G.; Unwin, P. R., *J. Am. Chem. Soc.* **2016**, *138*, 3152–3160

7. Meyer, E.; Hug, H. J.; Bennewitz, R., *Scanning probe microscopy: the lab on a tip*. Springer Science & Business Media: 2013.

8. Binnig, G.; Quate, C. F.; Gerber, C., *Phys. Rev. Lett.* **1986,** *56*, 930.

9. Rugar, D.; Hansma, P., *Physics Today* **1990,** *43*, 23-30.

10. Binnig, G.; Rohrer, H., *Surf. Sci.* **1983,** *126*, 236-244.

11. Hansma, P. K.; Tersoff, J., *J. Appl. Phys.* **1987,** *61*, R1-R24.

12. Kwak, J.; Bard, A. J., *Anal. Chem.* **1989,** *61*, 1794-1799.

13. Bard, A. J.; Fan, F. R. F.; Kwak, J.; Lev, O., *Anal. Chem.* **1989,** *61*, 132-138.

14. Bard, A. J.; Mirkin, M. V., *Scanning electrochemical microscopy*. CRC Press: 2012.

15. Chen, C. C.; Zhou, Y.; Baker, L. A., *Annu. Rev. Anal. Chem.* **2012,** *5*, 207-28.

16. Lee, C. M.; Kwak, J. Y.; Bard, A. J., *Proc. Natl. Acad. Sci. U.S.A.* **1990,** *87*, 1740-1743.

17. Macpherson, J. V.; Unwin, P. R., *J. Phys. Chem.* **1995,** *99*, 14824-14831.

18. Amemiya, S.; Bard, A. J.; Fan, F.-R. F.; Mirkin, M. V.; Unwin, P. R., *Annu. Rev. Anal. Chem.* **2008,** *1*, 95-131.

19. Schulte, A.; Nebel, M.; Schuhmann, W., *Annu. Rev. Anal. Chem.* **2010,** *3*, 299-318.

20. Sun, T.; Yu, Y.; Zacher, B. J.; Mirkin, M. V., *Angew. Chem. Int. Ed.* **2014,** *53*, 14120-14123.

21. Izquierdo, J.; Nagy, L.; Varga, Á.; Bitter, I.; Nagy, G.; Souto, R. M., *Electrochim. Acta* **2012,** *59*, 398-403.

22. Shen, M.; Ishimatsu, R.; Kim, J.; Amemiya, S., *J. Am. Chem. Soc.* **2012,** *134*, 9856-9859.

23. Varga, Á.; Nagy, L.; Izquierdo, J.; Bitter, I.; Souto, R. M.; Nagy, G., *Anal. Lett.* **2011,** *44*, 2876-2886.

24. Kimmel, D. W.; LeBlanc, G.; Meschievitz, M. E.; Cliffel, D. E., *Anal. Chem.* **2011,** *84*, 685-707.

25. Takahashi, Y.; Shevchuk, A. I.; Novak, P.; Murakami, Y.; Shiku, H.; Korchev, Y. E.; Matsue, T., *J. Am. Chem. Soc.* **2010,** *132*, 10118-10126.

26. Morris, C. A.; Chen, C.-C.; Baker, L. A., *Analyst* **2012,** *137*, 2933-2938.

27. Comstock, D. J.; Elam, J. W.; Pellin, M. J.; Hersam, M. C., *Anal. Chem.* **2010,** *82*, 1270-1276.

28. O'Connell, M. A.; Wain, A. J., *Anal. Chem.* **2014,** *86*, 12100-12107.

29. Kranz, C.; Friedbacher, G.; Mizaikofft, B.; Lugstein, A.; Smoliner, J.; Bertagnolli, E., *Anal. Chem.* **2001,** *73*, 2491-2500.

30. Kueng, A.; Kranz, C.; Lugstein, A.; Bertagnolli, E.; Mizaikoff, B., *Angew. Chem. Int. Ed.* **2003,** *42*, 3238-3240.

31. Macpherson, J. V.; Unwin, P. R., *Anal. Chem.* **2000,** *72*, 276-285.

32. Weber, A. E.; Baker, L. A., *J. Electrochem. Soc.* **2014,** *161*, H924-H929.

33. Korchev, Y. E.; Bashford, C. L.; Milovanovic, M.; Vodyanoy, I.; Lab, M. J., *Biophys. J.* **1997,** *73*, 653-658.

34. Takahashi, Y.; Ito, K.; Wang, X.; Matsumae, Y.; Komaki, H.; Kumatani, A.; Ino, K.; Shiku, H.; Matsue, T., *Electrochemistry* **2014,** *82*, 331-334.

35. Baro, A.; Miranda, R.; Alaman, J.; Garcia, N.; Binnig, G.; Rohrer, H.; Gerber, C.; Carrascosa, J., **1985**, *315*, 253-254

36. Driscoll, R. J.; Youngquist, M. G.; Baldeschwieler, J. D., *Nature* **1990,** *346*, 294-296.

37. Giessibl, F. J., *Science* **1995,** *267*, 68-71.

38. Gross, L.; Mohn, F.; Moll, N.; Liljeroth, P.; Meyer, G., *Science* **2009,** *325*, 1110-1114.

39. Novak, P.; Li, C.; Shevchuk, A. I.; Stepanyan, R.; Caldwell, M.; Hughes, S.; Smart, T. G.; Gorelik, J.; Ostanin, V. P.; Lab, M. J., *Nat. Methods* **2009,** *6*, 279-281.

40. Shevchuk, A. I.; Frolenkov, G. I.; Sanchez, D.; James, P. S.; Freedman, N.; Lab, M. J.; Jones, R.; Klenerman, D.; Korchev, Y. E., *Angew. Chem. Int. Edit.* **2006,** *45*, 2212-6.

41. Takahashi, Y.; Murakami, Y.; Nagamine, K.; Shiku, H.; Aoyagi, S.; Yasukawa, T.; Kanzaki, M.; Matsue, T., *Phys. Chem. Chem. Phys.* **2010,** *12*, 10012-10017.

42. Chen, C.-C.; Derylo, M. A.; Baker, L. A., *Anal. Chem.* **2009,** *81*, 4742-4751.

43. Chen, C.-C.; Zhou, Y.; Baker, L. A., *ACS Nano* **2011,** *5*, 8404-8411.

44. Zhou, L.; Zhou, Y.; Baker, L. A., *Electrochem. Soc. Interface* **2014**, 47.

45. Ivanov, A. P.; Actis, P.; Jönsson, P.; Klenerman, D.; Korchev, Y.; Edel, J. B., *ACS Nano* **2015,** *9*, 3587-3595.

46. Ying, L.; Bruckbauer, A.; Rothery, A. M.; Korchev, Y. E.; Klenerman, D., *Anal. Chem.* **2002,** *74*, 1380-1385.

47. Sa, N.; Lan, W.-J.; Shi, W.; Baker, L. A., *ACS Nano* **2013,** *7*, 11272-11282.

48. Korchev, Y. E.; Gorelik, J.; Lab, M. J.; Sviderskaya, E. V.; Johnston, C. L.; Coombes, C. R.; Vodyanoy, I.; Edwards, C. R., *Biophys. J.* **2000,** *78*, 451-457.

49. Vélez-Ortega, A. C.; Belov, O.; Novak, P.; Rawashdeh, S. A.; Sinha, G. P.; Korchev, Y. E.; Frolenkov, G. I., *Biophys. J.* **2014,** *106*, 797a-798a.

50. Yang, X.; Liu, X.; Zhang, X.; Lu, H.; Zhang, J.; Zhang, Y., *Ultramicroscopy* **2011,** *111*, 1417-1422.

51. Chen, C.-C.; Baker, L. A., *Analyst* **2011,** *136*, 90-97.

52. Li, P.; Liu, L.; Yang, Y.; Zhou, L.; Wang, D.; Wang, Y.; Li, G., *J. Lab. Autom.* **2015**, *20*, 457-462

53. Shevchuk, A. I.; Gorelik, J.; Harding, S. E.; Lab, M. J.; Klenerman, D.; Korchev, Y. E., *Biophys. J.* **2001,** *81*, 1759-1764.

54. Lipson, A. L.; Ginder, R. S.; Hersam, M. C., *Adv. Mater.* **2011,** *23*, 5613-5617.

55. Kang, M.; Momotenko, D.; Page, A.; Perry, D.; Unwin, P. R., *Langmuir* **2016,** *32*, 7993-8008.

56. Edwards, M. A.; Williams, C. G.; Whitworth, A. L.; Unwin, P. R., *Anal. Chem.* **2009,** *81*, 4482-4492.

57. Rheinlaender, J.; Schäffer, T. E., *J. Appl. Phys.* **2009,** *105*, 094905.

58. Shevchuk, A. I.; Frolenkov, G. I.; Sánchez, D.; James, P. S.; Freedman, N.; Lab, M. J.; Jones, R.; Klenerman, D.; Korchev, Y. E., *Angew. Chem. Int. Ed.* **2006,** *118*, 2270-2274.

59. Rheinlaender, J.; Geisse, N. A.; Proksch, R.; Schäffer, T. E., *Langmuir* **2010,** *27*, 697-704.

60. Karhanek, M.; Kemp, J. T.; Pourmand, N.; Davis, R. W.; Webb, C. D., *Nano Lett.* **2005,** *5*, 403-407.

61. Yuill, E. M.; Shi, W.; Poehlman, J.; Baker, L. A., *Anal. Chem.* **2015**.

62. Rheinlaender, J.; Schäffer, T. E., *Soft Matter* **2013,** *9*, 3230-3236.

63. Korchev, Y.; Milovanovic, M.; Bashford, C.; Bennett, D.; Sviderskaya, E.; Vodyanoy, I.; Lab, M., *J. Microsc.* **1997,** *188*, 17-23.

64. Happel, P.; Hoffmann, G.; Mann, S.; Dietzel, I., *J. Microsc.* **2003,** *212*, 144-151.

65. Gorelik, J.; Shevchuk, A. I.; Frolenkov, G. I.; Diakonov, I. A.; Kros, C. J.; Richardson, G. P.; Vodyanoy, I.; Edwards, C. R.; Klenerman, D.; Korchev, Y. E., *Proc. Natl. Acad. Sci. U. S. A.* **2003,** *100*, 5819-5822.

66. Gorelik, J.; Zhang, Y.; Shevchuk, A. I.; Frolenkov, G. I.; Sánchez, D.; Lab, M. J.; Vodyanoy, I.; Edwards, C. R.; Klenerman, D.; Korchev, Y. E., *Mol. Cell. Endocrinol.* **2004,** *217*, 101-108.

67. Happel, P.; Wehner, F.; Dietzel, I. D., Scanning ion conductance microscopy-a tool to investigate electrolyte-nonconductor interfaces. In *Modern Research and Educational Topics in Microscopy, Vol. 2*, Formatex: 2007; pp 968-975.

68. Shin, W.; Gillis, K. D., *Biophys. J.* **2006,** *91*, L63-L65.

69. Pellegrino, M.; Orsini, P.; De Gregorio, F., *Neurosci. Res.* **2009,** *64*, 290-296.

70. Happel, P.; Dietzel, I. D., *J. Nanobiotechnology* **2009,** *7*, 1.

71. Liu, X.; Yang, X.; Zhang, B.; Zhang, X.; Lu, H.; Zhang, J.; Zhang, Y., *Brain Res.* **2011,** *1386*, 35-40.

72. Lyon, A. R.; MacLeod, K. T.; Zhang, Y.; Garcia, E.; Kanda, G. K.; Korchev, Y. E.; Harding, S. E.; Gorelik, J., *Proc. Natl. Acad. Sci. U. S. A.* **2009,** *106*, 6854-6859.

73. Gorelik, J.; Yang, L. Q.; Zhang, Y.; Korchev, Y.; Harding, S. E., *Cardiovasc. Res.* **2006,** *72*, 422-429.

74. Miragoli, M.; Moshkov, A.; Novak, P.; Shevchuk, A.; Nikolaev, V. O.; El-Hamamsy, I.; Potter, C. M.; Wright, P.; Kadir, S. S. A.; Lyon, A. R., *J. R. Soc. Interface* **2011,** *8*, 913-925.

75. Gorelik, J.; Ali, N. N.; Shevchuk, A. I.; Lab, M.; Williamson, C.; Harding, S. E.; Korchev, Y. E., *Tissue Eng.* **2006,** *12*, 657-664.

76. Zhang, S.; Cho, S.-J.; Busuttil, K.; Wang, C.; Besenbacher, F.; Dong, M., *Nanoscale* **2012,** *4*, 3105-3110.

77. Zhang, Y.; Gorelik, J.; Sanchez, D.; Shevchuk, A.; Lab, M.; Vodyanoy, I.; Klenerman, D.; Edwards, C.; Korchev, Y., *Kidney Int.* **2005,** *68*, 1071-1077.

78. Potter, C. M.; Schobesberger, S.; Lundberg, M. H.; Weinberg, P. D.; Mitchell, J. A.; Gorelik, J., *PloS one* **2012,** *7*, e31228.

79. Korchev, Y. E.; Negulyaev, Y. A.; Edwards, C. R.; Vodyanoy, I.; Lab, M. J., *Nat. Cell Biol.* **2000,** *2*, 616-619.

80. Sánchez, D.; Anand, U.; Gorelik, J.; Benham, C. D.; Bountra, C.; Lab, M.; Klenerman, D.; Birch, R.; Anand, P.; Korchev, Y., *J. Neurosci. Meth.* **2007,** *159*, 26-34.

81. Yang, X.; Liu, X.; Lu, H.; Zhang, X.; Ma, L.; Gao, R.; Zhang, Y., *Chem. Res. Toxicol.* **2012,** *25*, 297-304.

82. Sakmann, B.; Neher, E., *Annu. Rev. Physiol* **1984,** *46*, 455-472.

83. Sakmann, B., *Single-channel recording*. Springer Science & Business Media: 2013.

84. Jonas, E. A.; Knox, R. J.; Kaczmarek, L. K., *Neuron* **1997,** *19*, 7-13.

85. Novak, P.; Gorelik, J.; Vivekananda, U.; Shevchuk, A. I.; Ermolyuk, Y. S.; Bailey, R. J.; Bushby, A. J.; Moss, G. W.; Rusakov, D. A.; Klenerman, D., *Neuron* **2013,** *79*, 1067-1077.

86. Pellegrino, M.; Pellegrini, M.; Orsini, P.; Tognoni, E.; Ascoli, C.; Baschieri, P.; Dinelli, F., *Pflügers Arch.,EJP* **2012,** *464*, 307-316.

87. Pastré, D.; Iwamoto, H.; Liu, J.; Szabo, G.; Shao, Z., *Ultramicroscopy* **2001,** *90*, 13-19.

88. Zhou, Y.; Chen, C.-C.; Baker, L. A., *Anal. Chem.* **2012,** *84*, 3003-3009.

89. Babakinejad, B.; Jönsson, P.; López Córdoba, A.; Actis, P.; Novak, P.; Takahashi, Y.; Shevchuk, A.; Anand, U.; Anand, P.; Drews, A., *Anal. Chem.* **2013,** *85*, 9333-9342.

90. Shi, W.; Sa, N.; Thakar, R.; Baker, L. A., *Analyst* **2015,** *140*, 4835-4842.

91. Bruckbauer, A.; Ying, L.; Rothery, A. M.; Zhou, D.; Shevchuk, A. I.; Abell, C.; Korchev, Y. E.; Klenerman, D., *J. Am. Chem. Soc.* **2002,** *124*, 8810-8811.

92. Zhang, H.; Wu, L.; Huang, F., *J. Vac. Sci. Technol. B* **1999,** *17*, 269-272.

93. Momotenko, D.; Page, A.; Adobes-Vidal, M.; Unwin, P. R., *ACS Nano* **2016**, *10*, 8871–8878

94. Yatziv, Y.; Turyan, I.; Mandler, D., *J. Am. Chem. Soc.* **2002,** *124*, 5618-5619.

95. Bruckbauer, A.; Zhou, D.; Ying, L.; Korchev, Y. E.; Abell, C.; Klenerman, D., *J. Am. Chem. Soc.* **2003,** *125*, 9834-9839.

96. Bruckbauer, A.; Zhou, D.; Kang, D.-J.; Korchev, Y. E.; Abell, C.; Klenerman, D., *J. Am. Chem. Soc.* **2004,** *126*, 6508-6509.

97. Ying, L.; Bruckbauer, A.; Zhou, D.; Gorelik, J.; Shevchuk, A.; Korchev, Y.; Klenerman, D., *Phys. Chem. Chem. Phys.* **2005,** *7*, 2859-2866.

98. Actis, P.; Maalouf, M. M.; Kim, H. J.; Lohith, A.; Vilozny, B.; Seger, R. A.; Pourmand, N., *ACS Nano* **2013,** *8*, 546-553.

99. Yuill, E. M.; Sa, N.; Ray, S. J.; Hieftje, G. M.; Baker, L. A., *Anal. Chem.* **2013,** *85*, 8498-8502.

100. Böcker, M.; Muschter, S.; Schmitt, E. K.; Steinem, C.; Schäffer, T. E., *Langmuir* **2009,** *25*, 3022-3028.

101. Momotenko, D.; McKelvey, K.; Kang, M.; Meloni, G. N.; Unwin, P. R., *Anal. Chem.* **2016**, *88*, 2838–2846.

102. Ji, T.; Liang, Z.; Zhu, X.; Wang, L.; Liu, S.; Shao, Y., *Chem. Sci.* **2011,** *2*, 1523-1529.

103. Klenerman, D.; Korchev, Y. E.; Davis, S. J., *Curr. Opin. Chem. Biol.* **2011,** *15*, 696-703.

104. Clarke, R. W.; White, S. S.; Zhou, D.; Ying, L.; Klenerman, D., *Angew. Chem. Int. Ed.* **2005,** *44*, 3747-3750.

105. Shevchuk, A. I.; Novak, P.; Taylor, M.; Diakonov, I. A.; Ziyadeh-Isleem, A.; Bitoun, M.; Guicheney, P.; Gorelik, J.; Merrifield, C. J.; Klenerman, D., *J. Cell Biol.* **2012,** *197*, 499-508.

106. Shevchuk, A. I.; Hobson, P.; Klenerman, D.; Krauzewicz, N.; Korchev, Y. E., *Pflügers Arch.,EJP* **2008,** *456*, 227-235.

107. Novak, P.; Shevchuk, A.; Ruenraroengsak, P.; Miragoli, M.; Thorley, A. J.; Klenerman, D.; Lab, M. J.; Tetley, T. D.; Gorelik, J.; Korchev, Y. E., *Nano Lett.* **2014,** *14*, 1202-1207.

108. Bruckbauer, A.; Ying, L.; Rothery, A. M.; Korchev, Y. E.; Klenerman, D., *Anal. Chem.* **2002,** *74*, 2612-2616.

109. Bruckbauer, A.; James, P.; Zhou, D.; Yoon, J. W.; Excell, D.; Korchev, Y.; Jones, R.; Klenerman, D., *Biophys. J.* **2007,** *93*, 3120-3131.

110. Korchev, Y. E.; Raval, M.; Lab, M. J.; Gorelik, J.; Edwards, C. R.; Rayment, T.; Klenerman, D., *Biophys. J.* **2000,** *78*, 2675-2679.

111. Nadappuram, B. P.; McKelvey, K.; Al Botros, R.; Colburn, A. W.; Unwin, P. R., *Anal. Chem.* **2013,** *85*, 8070-8074.

112. Morris, C. A.; Chen, C.-C.; Ito, T.; Baker, L. A., *J. Electrochem. Soc.* **2013,** *160*, H430-H435.

113. Şen, M.; Takahashi, Y.; Matsumae, Y.; Horiguchi, Y.; Kumatani, A.; Ino, K.; Shiku, H.; Matsue, T., *Anal. Chem.* **2015,** *87*, 3484-3489.

114. Actis, P.; Tokar, S.; Clausmeyer, J.; Babakinejad, B.; Mikhaleva, S.; Cornut, R.; Takahashi, Y.; López Córdoba, A.; Novak, P.; Shevchuck, A. I., *ACS Nano* **2014,** *8*, 875-884.

115. O'Connell, M. A.; Lewis, J. R.; Wain, A. J., *Chem. Commun.* **2015,** *51*, 10314-10317.

116. Proksch, R.; Lal, R.; Hansma, P. K.; Morse, D.; Stucky, G., *Biophys. J.* **1996,** *71*, 2155-2157.

117. Pellegrino, M.; Orsini, P.; Pellegrini, M.; Baschieri, P.; Dinelli, F.; Petracchi, D.; Tognoni, E.; Ascoli, C., *Micro. Nano. Lett.* **2012,** *7*, 317-320.

118. Zhou, Y.; Chen, C.-C.; Weber, A. E.; Zhou, L.; Baker, L. A., *Langmuir* **2014,** *30*, 5669-5675.

119. Zhou, Y.; Chen, C.-C.; Weber, A. E.; Zhou, L.; Baker, L. A.; Hou, J., *Tissue Barriers* **2013,** *1*, e25585.

120. Ebejer, N.; Güell, A. G.; Lai, S. C. S.; McKelvey, K.; Snowden, M. E.; Unwin, P. R., *Annu. Rev. Anal. Chem.* **2013,** *6*, 329-351.

121. Aaronson, B. D. B.; Güell, A. G.; McKelvey, K.; Momotenko, D.; Unwin, P. R., Scanning Electrochemical Cell Microscopy: Mapping, Measuring, and Modifying Surfaces and Interfaces at the Nanoscale. In *Nanoelectrochemistry*, CRC Press: 2015; 655-694.

122. Snowden, M. E.; Güell, A. G.; Lai, S. C.; McKelvey, K.; Ebejer, N.; O'Connell, M. A.; Colburn, A. W.; Unwin, P. R., *Anal. Chem.* **2012,** *84*, 2483-2491.

123. Ebejer, N.; Schnippering, M.; Colburn, A. W.; Edwards, M. A.; Unwin, P. R., *Anal. Chem.* **2010,** *82*, 9141-9145.

124. Güell, A. G.; Cuharuc, A. S.; Kim, Y.-R.; Zhang, G.; Tan, S.-y.; Ebejer, N.; Unwin, P. R., *ACS Nano* **2015,** *9*, 3558-3571.

125. Güell, A. G.; Ebejer, N.; Snowden, M. E.; Macpherson, J. V.; Unwin, P. R., *J. Am. Chem. Soc.* **2012,** *134*, 7258-7261.

126. Güell, A. G.; Meadows, K. E.; Dudin, P. V.; Ebejer, N.; Macpherson, J. V.; Unwin, P. R., *Nano Lett.* **2014,** *14*, 220-224.

127. Byers, J. C.; Güell, A. G.; Unwin, P. R., *J. Am. Chem. Soc.* **2014,** *136*, 11252-11255.

128. Patten, H. V.; Lai, S. C.; Macpherson, J. V.; Unwin, P. R., *Anal. Chem.* **2012,** *84*, 5427-5432.

129. Chen, C.-H.; Jacobse, L.; McKelvey, K.; Lai, S. C.; Koper, M. T.; Unwin, P. R., *Anal. Chem.* **2015,** *87*, 5782-5789.

130. Kang, M.; Perry, D.; Kim, Y.-R.; Colburn, A. W.; Lazenby, R. A.; Unwin, P. R., *J. Am. Chem. Soc.* **2015,** *137*, 10902-10905.

131. Lai, S. C.; Lazenby, R. A.; Kirkman, P. M.; Unwin, P. R., *Chem. Sci.* **2015,** *6*, 1126-1138.

132. Kim, Y.-R.; Lai, S. C. S.; McKelvey, K.; Zhang, G.; Perry, D.; Miller, T. S.; Unwin, P. R., *J. Phys. Chem. C* **2015,** *119*, 17389-17397.

133. Patel, A. N.; McKelvey, K.; Unwin, P. R., *J. Am. Chem. Soc.* **2012,** *134*, 20246-20249.

134. Oseland, E. E.; Ayres, Z. J.; Basile, A.; Haddleton, D. M.; Wilson, P.; Unwin, P. R., *Chem. Commun.* **2016**, *52*, 9929-9932.

135. McKelvey, K.; O'Connell, M. A.; Unwin, P. R., *Chem. Commun.* **2013,** *49*, 2986-2988.

136. Sahın, Ö.; Nusret Bulutcu, A., *J. Cryst. Growth* **2002,** *241*, 471-480.

137. Lin, N. H.; Shih, W.-Y.; Lyster, E.; Cohen, Y., *J. Colloid Interface Sci.* **2011,** *356*, 790-797.

138. Bodhak, S.; Bose, S.; Bandyopadhyay, A., *Acta Biomater.* **2009,** *5*, 2178-2188.

139. Hellevang, H.; Miri, R.; Haile, B. G., *Cryst. Growth Des.* **2014,** *14*, 6451-6458.

140. Yanina, S. V.; Rosso, K. M., *Science* **2008,** *320*, 218-222.

141. Hirsch, V.; Kinnear, C.; Moniatte, M.; Rothen-Rutishauser, B.; Clift, M. J. D.; Fink, A., *Nanoscale* **2013,** *5*, 3723-3732.

142. Chan, D. Y.; Pashley, R. M.; White, L. R., *J. Colloid Interface Sci.* **1980,** *77*, 283-285.

143. Ohshima, H.; Healy, T. W.; White, L. R., *J. Colloid Interface Sci.* **1982,** *90*, 17-26.

144. Lan, W.-J.; Holden, D. A.; White, H. S., *J. Am. Chem. Soc.* **2011,** *133*, 13300-13303.

145. Guo, W.; Tian, Y.; Jiang, L., *Acc. Chem. Res.* **2013,** *46*, 2834-2846.

146. Armstrong, J. A.; Bernal, E. E. L. n.; Yaroshchuk, A.; Bruening, M. L., *Langmuir* **2013,** *29*, 10287-10296.

147. Haupt, A.; Campetelli, A.; Bonazzi, D.; Piel, M.; Chang, F.; Minc, N., *PLoS Biol.* **2014,** *12*, e1002029.

148. Wong, J. Y.; Langer, R.; Ingber, D. E., *Proc. Natl. Acad. Sci. U. S. A.* **1994,** *91*, 3201-3204.

149. Bakhti, M.; Snaidero, N.; Schneider, D.; Aggarwal, S.; Möbius, W.; Janshoff, A.; Eckhardt, M.; Nave, K.-A.; Simons, M., *Proc. Natl. Acad. Sci. U. S. A.* **2013,** *110*, 3143-3148.

150. Busscher, H. J.; van der Mei, H. C., *PLoS Pathog.* **2012,** *8*, e1002440-e1002440.

151. Terada, A.; Okuyama, K.; Nishikawa, M.; Tsuneda, S.; Hosomi, M., *Biotechnol. Bioeng.* **2012,** *109*, 1745-1754.

152. Gregory, P. J., *Plant roots: growth, activity and interactions with the soil*. John Wiley & Sons: 2008.

153. Tedja, R.; Lim, M.; Amal, R.; Marquis, C., *ACS Nano* **2012,** *6*, 4083-4093.

154. Barisik, M.; Atalay, S.; Beskok, A.; Qian, S., *J. Phys. Chem. C* **2014,** *118*, 1836-1842.

155. Kim, S. T.; Saha, K.; Kim, C.; Rotello, V. M., *Acc. Chem. Res.* **2013,** *46*, 681-691.

156. Rivera-Gil, P.; Jimenez De Aberasturi, D.; Wulf, V.; Pelaz, B.; Del Pino, P.; Zhao, Y.; De La Fuente, J. M.; Ruiz De Larramendi, I.; Rojo, T.; Liang, X.-J., *Acc. Chem. Res.* **2012,** *46*, 743-749.

157. Chung, T.-H.; Wu, S.-H.; Yao, M.; Lu, C.-W.; Lin, Y.-S.; Hung, Y.; Mou, C.-Y.; Chen, Y.-C.; Huang, D.-M., *Biomaterials* **2007,** *28*, 2959-2966.

158. Lee, K.-D.; Hong, K.; Papahadjopoulos, D., *Biochim. Biophys. Acta, Biomembr.* **1992,** *1103*, 185-197.

159. Christianson, H. C.; Svensson, K. J.; van Kuppevelt, T. H.; Li, J.-P.; Belting, M., *Proc. Natl. Acad. Sci. U. S. A.* **2013,** *110*, 17380-17385.

160. Shi, X.; Bi, Y.; Yang, W.; Guo, X.; Jiang, Y.; Wan, C.; Li, L.; Bai, Y.; Guo, J.; Wang, Y., *Nature* **2013,** *493*, 111-115.

161. Stumm, W.; Morgan, J. J., *Aquatic chemistry: chemical equilibria and rates in natural waters*. John Wiley & Sons: 2012; Vol. 126.

162. Westall, J.; Hohl, H., *Adv. Colloid Interface Sci.* **1980,** *12*, 265-294.

163. Bockris, J. M.; Devanathan, M.; Muller, K. In *On the structure of charged interfaces*, Proceedings of the Royal Society of London A: Mathematical, Physical and Engineering Sciences, The Royal Society: 1963; pp 55-79.

164. Xu, S.; Arnsdorf, M. F., *Proc. Natl. Acad. Sci. U. S. A.* **1995,** *92*, 10384-10388.

165. Heinz, W. F.; Hoh, J. H., *Biophys. J.* **1999,** *76*, 528-538.

166. Miyatani, T.; Okamoto, S.; Rosa, A.; Marti, O.; Fujihira, M., *Appl. Phys. A Mater. Sci. Process.* **1998,** *66*, S349-S352.

167. Almonte, L.; Lopez-Elvira, E.; Baró, A. M., *ChemPhysChem* **2014,** *15*, 2768-2773.

168. Zimmerman, B.; Chow, J.; Abbott, A. G.; Ellison, M. S.; Kennedy, M. S.; Dean, D., *J. Eng. Fibers Fabr.* **2011,** *6*, 61.

169. Sotres, J.; Baró, A., *Biophys. J.* **2010,** *98*, 1995-2004.

170. Sotres, J.; Baró, A., *Appl. Phys. Lett.* **2008,** *93*, 103903.

171. Shan, X.; Huang, X.; Foley, K. J.; Zhang, P.; Chen, K.; Wang, S.; Tao, N., *Anal. Chem.* **2009,** *82*, 234-240.

172. Pattnaik, P., *Biotechnol. Appl. Biochem.* **2005,** *126*, 79-92.

173. Sprycha, R., *J. Colloid Interface Sci.* **1989,** *127*, 1-11.

174. Arjmandi, N.; Van Roy, W.; Lagae, L.; Borghs, G., *Anal. Chem.* **2012,** *84*, 8490-8496.

175. Gibson, G. T. T.; Mohamed, M. F.; Neverov, A. A.; Brown, R. S., *Inorg. Chem.* **2006,** *45*, 7891-7902.

176. Szekeres, M.; Tombácz, E., *Colloids Surf., A* **2012,** *414*, 302-313.

177. Sabia, R.; Ukrainczyk, L., *J. Non-Cryst. Solids* **2000,** *277*, 1-9.

178. Behrens, S. H.; Grier, D. G., *J. Chem. Phys* **2001,** *115*, 6716-6721.

179. Siwy, Z.; Heins, E.; Harrell, C. C.; Kohli, P.; Martin, C. R., *J. Am. Chem. Soc.* **2004,** *126*, 10850-10851.

180. Wei, C.; Bard, A. J.; Feldberg, S. W., *Anal. Chem.* **1997,** *69*, 4627-4633.

181. White, H. S.; Bund, A., *Langmuir* **2008,** *24*, 2212-2218.

182. Rosentsvit, L.; Wang, W.; Schiffbauer, J.; Chang, H.-C.; Yossifon, G., *J. Chem. Phys* **2015,** *143*, 224706.

183. Yin, X.; Zhang, S.; Dong, Y.; Liu, S.; Gu, J.; Chen, Y.; Zhang, X.; Zhang, X.; Shao, Y., *Anal. Chem.* **2015,** *87*, 9070-9077.

184. Momotenko, D.; Cortes-Salazar, F.; Josserand, J.; Liu, S.; Shao, Y.; Girault, H. H., *Phys. Chem. Chem. Phys.* **2011,** *13*, 5430-5440.

185. Perry, A. R.; Lazenby, R. A.; Adobes-Vidal, M.; Peruffo, M.; McKelvey, K.; Snowden, M. E.; Unwin, P. R., *CrystEngComm* **2015,** *17*, 7835-7843.

186. Meng, L.; Iacobini, J. G.; Joseph, M. B.; Macpherson, J. V.; Newton, M. E., *Farad. Discuss.* **2014,** *172*, 421-438.

187. Thatenhorst, D.; Rheinlaender, J.; Schäffer, T. E.; Dietzel, I. D.; Happel, P., *Anal. Chem.* **2014,** *86*, 9838-9845.

188. Lan, W. J.; Holden, D. A.; Zhang, B.; White, H. S., *Anal. Chem.* **2011,** *83*, 3840-7.

189. Wang, Y.; Kececi, K.; Mirkin, M. V.; Mani, V.; Sardesai, N.; Rusling, J. F., *Chem. Sci.* **2013,** *4*, 655-663.

190. Edwards, M. A.; German, S. R.; Dick, J. E.; Bard, A. J.; White, H. S., *ACS Nano* **2015,** *9*, 12274-12282.

191. Bayley, H.; Martin, C. R., *Chem. Rev.* **2000,** *100*, 2575-2594.

192. Cai, H.; Wang, Y.; Yu, Y.; Mirkin, M. V.; Bhakta, S.; Bishop, G. W.; Joshi, A. A.; Rusling, J. F., *Anal. Chem.* **2015,** *87*, 6403-6410.

193. Fu, Y.; Tokuhisa, H.; Baker, L. A., *Chem.l Commun.* **2009**, 4877-4879.

194. Steinbock, L. J.; Otto, O.; Chimerel, C.; Gornall, J.; Keyser, U. F., *Nano Lett.* **2010,** *10*, 2493-2497.

195. Gong, X.; Patil, A. V.; Ivanov, A. P.; Kong, Q.; Gibb, T.; Dogan, F.; deMello, A. J.; Edel, J. B., *Anal. Chem.* **2014,** *86*, 835-841.

196. Howorka, S.; Cheley, S.; Bayley, H., *Nat. Biotechnol.* **2001,** *19*, 636-639.

197. Clarke, J.; Wu, H.-C.; Jayasinghe, L.; Patel, A.; Reid, S.; Bayley, H., *Nat. Nanotechnol.* **2009,** *4*, 265-270.

198. Wells, D. B.; Belkin, M.; Comer, J.; Aksimentiev, A., *Nano Lett.* **2012,** *12*, 4117-4123.

199. Vilozny, B.; Actis, P.; Seger, R. A.; Pourmand, N., *ACS Nano* **2011,** *5*, 3191-3197.

# Chapter 2. Surface Charge Mapping with a Nanopipette

To date, SICM has been predominantly used for topographical mapping of samples, most notably living systems. This chapter describes how the SICM response is not just sensitive to surface topography but also to the surface charge of the sample and explores the surface induced rectification (SIR) phenomena. Exploiting SIR, it is possible to use SICM to map heterogeneous surface charge across samples using either the direct current (DC) or alternating current (AC) components of the ionic conductance current. As well as this, the implications of these effects for existing studies are also considered, as the sensitivity to surface charge could have great implications on the accuracy of topographical imaging.

This chapter contains the manuscript and supporting information from an article published in *The Journal of the American Chemical Society* where the effects of surface charge on the SICM response are described. I was responsible for the collection of mapping data as well as some of the approach curves together with Sophie L. Kinnear in whose thesis this work has already been seen (Warwick 2015) as well as being jointly responsible for manuscript preparation. Kim McKelvey was a postdoctoral researcher supervising on this project and performed the FEM simulations in this chapter.

# Surface Charge Mapping with a Nanopipette

Kim McKelvey,[1] Sophie L. Kinnear,[1] David Perry,[1,2] Dmitry Momotenko[1] and Patrick R. Unwin[1,*]

[1]Department of Chemistry and [2]MOAC Doctoral Training Centre, University of Warwick, Coventry, UK, CV4 7AL.

*** Corresponding Author**

p.r.unwin@warwick.ac.uk

## 2.1 Abstract

Nanopipettes are emerging as simple, but powerful, tools for probing chemistry at the nanoscale. In this contribution, the use of nanopipettes for simultaneous surface charge mapping and topographical imaging is demonstrated, using a scanning ion conductance microscopy (SICM) format. When a nanopipette is positioned close to a surface in electrolyte solution the direct ion current (DC), driven by an applied bias between a quasi-reference counter electrode (QRCE) in the nanopipette and a second QRCE in the bulk solution is sensitive to surface charge. The charge sensitivity arises because the diffuse double layers at the nanopipette and the surface interact, creating a perm-selective region, which becomes increasingly significant at low ionic strengths (10 mM 1:1 aqueous electrolyte herein). This leads to a polarity-dependent ion current and surface-induced rectification as the bias is varied. Using distance-modulated SICM, which induces an alternating ion current component (AC) by periodically modulating the distance between the nanopipette and the surface, the effect of surface charge on the DC and AC is explored and rationalised. The impact of surface charge on the AC phase (with respect to the driving sinusoidal signal) is highlighted in particular; this quantity shows a shift that is highly sensitive to interfacial charge and provides the basis for visualising charge simultaneously with topography. The studies herein highlight the use of nanopipettes for functional imaging with applications from cell biology to materials characterisation where

understanding surface charge is of key importance. They also provide a framework for the design of SICM experiments, which may be convoluted by topographical and surface charge effects, especially for small nanopipettes.

## 2.2 Introduction

Electrochemical measurements with, and control of, nanopipettes filled with electrolyte solution provide a platform for nanoscience, with myriad applications spanning analytical science,[1–5] materials characterisation[6–9] and live cell studies.[10] Nanopipettes, used as the probe in scanning ion conductance microscopy (SICM), are particularly powerful as a means of imaging the local topography of substrates.[10–13] A bias is applied between a quasi-reference counter electrode (QRCE) in the nanopipette and another in the bulk of the solution to induce a direct ion current (DC) through the end of the nanopipette, as illustrated schematically in Figure 2.1. As the nanopipette-surface distance decreases, the solution resistance in the probe-surface gap increases which, in turn, reduces the ion current. This decrease in ion current is used as a non-contact signal to sense the nanopipette-surface distance and ultimately for topographical imaging,[14–16] proving particularly effective for soft samples.[10,12]

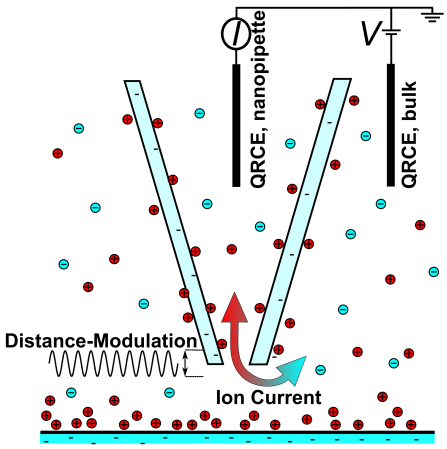


**Figure 2.1.** Schematic of an SICM probe, with one QRCE in a nanopipette and another in the bulk of the solution. A bias (*V*) is applied to the bulk QRCE and the ion current (*I*) is measured at the QRCE in the nanopipette. A distance-modulated technique is used where a sinusoidal modulation is applied to the position of the nanopipette.

SICM is typically operated in aqueous solutions with relatively high ionic strength. Under these conditions the diffuse double layer (DDL) that forms at interfaces in solution is compressed (usually down to a sub-nanometre level),[17] ensuring that the nanopipette response is relatively insensitive to surface charge effects and that the substrate topography is faithfully reproduced.[18] However, at lower electrolyte concentrations, the DDL characteristic length increases up to the several nanometre scale (in aqueous solutions), leading to surface charge effects such as ion current rectification (ICR) due to a polarity (bias) dependent conductivity of the nanopipette, as seen in simple nanopipette studies of bulk solutions.[19–22] At small separation distances between a nanopipette and a charged substrate, the interaction of the respective DDLs similarly leads to changes in the ion current signal (*surface-induced rectification*)[23] opening up the prospect of surface charge mapping using SICM, as described herein. This is an important advance because there are relatively few techniques for probing and visualising charge at interfaces. Although atomic force microscopy (AFM) can be used,[24–27] it employs a tip of (nominally) fixed charge that may change during a scan (*e.g.* by contamination or tip wear), and the force-distance characteristics are influenced by several forces, as well as the electrostatic forces. In contrast, as we highlight herein, the ion current through a nanopipette depends directly on the DDL at a charged surface and the applied potential can be tuned to optimise the response.

We use a nanopipette to investigate charged surfaces in electrolyte solutions at moderate aqueous ionic strength (10 mM 1:1 salt). We also take advantage of distance-modulated SICM,[28,29] where the probe-surface distance is oscillated with a small amplitude at a particular frequency to produce an alternating component (AC) in the ion current. We show that the ion current response (both DC and AC) is significantly affected by both substrate surface charge and the applied potential through approach curve measurements towards materials with different surface charge characteristics, namely glass, polystyrene and (3-aminopropyl) triethoxysilane (APTES). In particular, we highlight that the *AC phase*, which has largely been overlooked in the SICM community, can give considerable information on the charge state of the surface. Experimental data are shown to be well represented with

theoretical (finite element method) simulations. We use distance-modulated SICM to map the topography and surface charge simultaneously at model surfaces (polystyrene film with pinholes deposited on glass) and show that the phase signal, as well as the DC current, can distinguish between the two materials. We also demonstrate surface charge mapping of a soft positively charged polymer feature (poly-l-lysine), deposited as a small patch on a glass substrate. These model examples serve to illustrate the exciting possibility of using a nanopipette to map interfacial properties other than topography. We anticipate widespread applications in surface and interfacial science where knowledge of local surface charge would be hugely valuable for understanding interfacial processes.

## 2.3 Materials and Methods

### 2.3.1 Solutions

Milli-Q reagent grade water (resistivity ca. 18.2 MΩ cm at 25°C) was used for all solutions. 10 mM KCl (pH 6.6, Sigma-Aldrich) solutions were prepared for the SICM experiments. The pH values of electrolyte solutions were examined systematically before and after experiments to ensure stability, as pH could be a critical parameter controlling the charge properties of the interfaces, in particular those involving glass. Polystyrene (Sigma-Aldrich) was dissolved in chloroform (Fisher Scientific) at two different concentrations, one for creating a thick layer for SICM nanopipette approach tests (20 mg/ml) and one for dip-coating glass to create a thin (partial) film for imaging (0.66 mg/ml). A solution of (3-aminopropyl) triethoxysilane (APTES, Sigma Aldrich) and toluene (2 µl/ml) was used for glass surface modification with APTES. In order to protonate the amino groups and produce a positively charged surface, all experiments carried out on APTES samples were done in a slightly acidic solution of HCl (pH 3.4, Fisher Scientific) and KCl (9 mM). Consequently, the negative surface charge of the glass nanopipette in the studies at lower pH, would be diminished. To create 5 µm diameter dots of poly-l-lysine (PLL) on glass, a solution of 0.25 mg/ml PLL with a supporting electrolyte of 25 mM KCl was used.

### 2.3.2 Nanopipettes

60 nm radius nanopipettes with a half cone angle of 3° (dimensions measured with a Zeiss Supra55VP field emission scanning electron microscope, FE-SEM) were pulled from borosilicate glass capillaries (o.d. 1.2 mm, i.d. 0.69 mm, Harvard Apparatus) using a laser puller (P-2000, Sutter Instruments, Pulling Parameters: Line 1: Heat 350, Fil 3, Vel 30, Del 220, Pul -, Line 2: Heat 350, Fil 3, Vel 40, Del 180, Pul 120). Tips visualised by FE-SEM were sputter coated gold (10 nm thickness).

### 2.3.3 Substrates

Glass bottomed petri dishes with detachable cover slips (3512, WillcoWells) were used. Before use, the detachable cover slip was sonicated in acetone for 10 minutes followed by sonication in water for 10 minutes and plasma ashing for 1 minute at 100 W in oxygen. These were then used immediately as glass samples or functionalised with either polystyrene or APTES. The polystyrene samples were either thick films prepared by evaporation of a solution of polystyrene in chloroform onto the glass, used for the nanopipette approach curve measurements, or dip coated for 30 seconds in a less concentrated polystyrene solution (see above), to produce a heterogeneous thin film with holes that exposed the glass in small regions. This created a surface of both neutral polystyrene and slightly negatively charged glass under the condition of the measurements (aerated, unbuffered, 10 mM KCl).[21–23,30] Silanised substrates were fabricated from glass coverslips immersed in the APTES/toluene solution for 30 minutes and then sonicated in chloroform to form a monolayer.[31]

A substrate containing patches of positively charged PLL on a glass sample was created by taking a clean glass petri dish and depositing a spot of PLL for 3 minutes from a liquid meniscus formed in air at the end of a 5 µm diameter dual barrelled-pipette, using the fabrication capabilities of scanning electrochemical cell microscopy.[32] This sample was then washed with water and dried under ambient conditions.

### 2.3.4 Instrumentation

The basic instrumentation has been described previously.[33,34] Briefly, the SICM probe was mounted on a 38 µm piezoelectric positioning stage (P-753-3CD, Physik Instrumente) for movement normal to the substrate (*z*-direction), while the sample was mounted on a two axis piezoelectric positioner system (Nano-BioS300, Mad City Labs Inc.) for lateral movement. The current was measured using a custom current-to-voltage converter. A lock-in amplifier (SR830, Stanford Research Systems) was used to generate the driving signal for the oscillation of the probe position and to determine the magnitude and phase of the AC ion current. Data recording, as well as probe and voltage output control, was performed using a LabVIEW (2013, National Instruments) based program through a FPGA card (7852R, National Instruments). The lock-in amplifier phase calculation does not take into account the sign of the input signal, resulting in a 180 degree offset for negative current values compared to positive current values. Therefore, the phase at negative currents was translated by 180 degrees, allowing phases at both positive and negative currents to be compared.

The nanopipette probe was filled with KCl solution, and an Ag/AgCl quasi-reference counter electrode (QRCE) was inserted. This comprised an AgCl-coated Ag wire.[35] The end of the nanopipette was placed close to the surface of interest that was immersed in KCl solution. A second Ag/AgCl QRCE was placed in the bulk of the solution. The QRCE in the bulk solution was biased with respect to the QRCE in the probe, and the resulting ion current was measured at the QRCE in the probe. All potentials quoted herein refer to the potential of the QRCE in the nanopipette with respect to the bulk QRCE.

### 2.3.5 SICM Approach Curves

The ion current, as a function of the probe-substrate distance, was measured at different potential difference. To achieve this, the probe was oscillated at 288 Hz with 10 nm peak-to-peak amplitude and approached at 10 nm $s^{-1}$ towards the surface of interest with a bias of -0.2 V ($V_{QRCE,\ nanopipette} - V_{QRCE,\ bulk}$). Once the surface had been detected, through an increase in the AC current magnitude to 7 pA, the potential was switched to the potential of interest and the probe held stationary for

30 seconds for the ion current to stabilise. During this time the nanopipette-surface distance can change due to thermal expansion or retraction of the piezoelectric positioners (an effect called thermal drift).[36] However thermal drift is minimal for our experimental configuration (representing only 5 nm over 30 seconds) and so does not significantly affect the experimental results. The ion current response as the probe was moved away from the surface at 10 nm $s^{-1}$ was then recorded. For some approach curves over glass the tip (biased positively) was approached further towards the substrate, with the current observed to fall monotonically to low values before tip crash.

### 2.3.6 SICM Maps

Two dimensional maps of a surface were generated in a hopping mode.[12,17,37] The SICM probe was approached, at 300 nm $s^{-1}$, to the surface of interest until the surface was detected, as an increase in the AC ion current magnitude to 4 pA, at multiple different lateral positions over the sample. The ion current and *z*-piezoelectric position was recorded during these hops and the values at the closest approach to the surface were used to construct two-dimensional maps.

### 2.3.7 Atomic Force Microscopy

The height of the polystyrene/glass samples, as revealed by SICM, was compared to a section of the same sample imaged with atomic force microscopy (AFM) (Catalyst, Bruker-Nano) in contact mode using silicon tips on nitride lever (SNL-10, Veeco). AFM images were processed using the Scanning Probe Image Processor program (SPIP 6.0.14, Image Metrology).

### 2.3.8 Simulations

Two-dimensional finite element method (FEM) simulations of the end of a 60 nm radius, 3° half cone angle nanopipette in bulk and close to a charged surface were constructed to understand the theoretical basis of the ion current response. Simulations were constructed in Comsol Multiphysics using the Nernst-Plank and

electrostatics modules. Full details of the FEM simulations are available in the Supporting Information section 2.6.1.

## 2.4 Results and Discussion

The current-potential characteristics of a typical 60 nm radius nanopipette in bulk aqueous 10 mM KCl solution are shown in the Supporting Information, section 2.6.2, Figure 2.11. As expected, these nanopipettes show slight ICR due to the negative surface charge at the walls of the nanopipette,[21,22] with the current magnitude at positive values of the applied potential ($V_{QRCE,\ nanopipette}$ - $V_{QRCE,\ bulk}$) being less than the current magnitude at negative potential values, as discussed in some detail in the literature,[19,20,22,38,39] and briefly below. The additional effect of a charged surface on the DC and AC ion currents in SICM is investigated herein.

### 2.4.1 Approach Curves

The nanopipettes, operated in distance-modulation mode, were translated towards various surfaces in 10 mM KCl. The procedure outlined in the Methods and Materials section ensured that the nanopipette-surface distance was consistent at different potentials on a particular surface, with sets of curves obtained with one nanopipette. It should be noted, however, that the closest probe-surface distance is not the same for different surfaces due to the intrinsic charge characteristics of samples (*vide infra*). For convenience, probe-surface distances are assigned with respect to the point of closest approach, which can reasonably be expected to be within tens of nanometres of the surface itself, for all surfaces, as the ion current changes predominantly within a distance of a probe diameter from the substrate.[40] As could be expected, at a very small tip-to-substrate separation (data not shown) the drop of the ionic current was observed regardless the nature of the substrate.

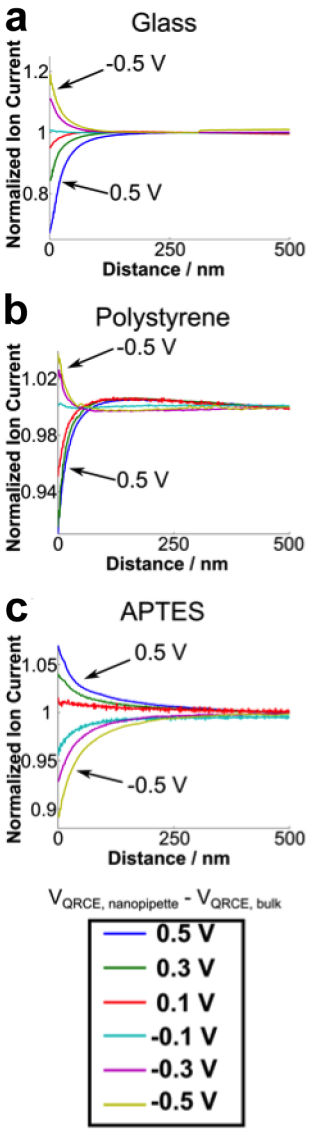


**Figure 2.2.** Normalised ion current as a function of probe-surface distance at different potentials over glass (**a**), polystyrene (**b**) and APTES (**c**) recorded in a 10 mM KCl solution with a 60 nm radius nanopipette, with an oscillation amplitude of 10 nm at 288 Hz.

The ion current, normalised with respect to the ion current in bulk, for approach curves towards glass, polystyrene and APTES are shown in Figure 2.2a-c, respectively. The glass provides a negatively charged surface (typically ca. -1 mC $m^{-2}$ in 10 mM KCl, or $-6\times10^{-3}$ *e* $nm^{-2}$, where *e* is the electric charge of a proton),[21,23,41] the polystyrene a neutral surface and APTES a positively charged surface.[42] Absolute values of a surface charge density depend on a number of factors: the particular type of substrate (*e.g.* different types of glass), the surface pre-treatment protocol

employed, surface cleanliness, sample ageing with time and the surface environment (*e.g.* electrolyte concentration, pH, etc.). In this work a moderate (and typical) surface charge among a wide range reported is chosen. On negatively charged glass (Figure 2.2a) the ion current shows an increase in magnitude as a function of decreasing nanopipette-surface distance at negative potential differences ($V_{QRCE,\ nanopipette}$ - $V_{QRCE,\ bulk}$), while there is a decrease in current with smaller nanopipette-surface distance at positive potential differences. This pattern is similar on the polystyrene surfaces (Figure 2.2b), although the changes in the ion current with distance are greatly diminished compared to the behaviour seen with the glass surface. Conversely, over the positively charged APTES surface (Figure 2.2c) an increase in ion current with decreasing nanopipette-surface distance is observed at positive ($V_{QRCE,\ nanopipette}$ - $V_{QRCE,\ bulk}$) potentials, while there is a decrease in ion current with nanopipette-surface distance at negative potentials. Thus, the trend in the current-distance curves with respect to potential is opposite to that seen with the negatively charged glass surface and neutral polystyrene-covered surface. The general observation is that the SICM ion current over charged interfaces depends on the bias polarity between the two QRCEs and the charge on the substrate, as recently reported, primarily through nanopore simulations.[23] In this contribution we describe surface-induced rectification at nanopipettes with a primary emphasis on high-resolution scanning to probe and map surface charge effects with high sensitivity using both the DC and AC components of ion current.

The origin of the surface-induced polarity-dependent ion current is the interaction between the DDL at the tip and the DDL at the substrate, combined with the asymmetry of mass transport inside and outside the nanopipette. In the case of a negatively charged glass or quartz nanopipette in bulk solution, the interaction of the DDLs formed at the side walls of the nanopipette create a perm-selective region at the end on the nanopipette in which the migration and diffusion of cations dominates. Mass transport inside the nanopipette is limited by the conical geometry, while the outer space near the tip provides much faster transport due to a larger access angle. At a positive bias cations are pushed from the nanopipette and the faster mass-transport rate outside the tip opening leads to the depletion of ion concentration inside the probe (as shown from FEM simulation results in Figure 2.9a

of the Supporting Information), giving rise to a low-conductance state and diminished ion current magnitude. At the opposite (negative) bias cations are pushed towards the nanopipette at higher rates than they are transported inside, resulting in ion accumulation within the nanopipette (Supporting Information, Figure 2.8b), yielding a high-conductance state and an enhancement of the ion current magnitude. This effect is subtle with this size nanopipette with 10 mM KCl (Supporting Information Figure 2.9), yet detectable (Supporting Information Figure 2.10).

With a nanopipette approaching the charged surface, the rectifying scenarios are seriously affected by the presence of DDLs at the substrate, which exhibit perm-selective behaviour towards cations or anions depending on the sign of the surface charge. It is therefore important to consider two coupled perm-selective regions: the one inside the nanopipette as in classical rectification and the one between the surface and the end of the nanopipette.

When the DDLs at the nanopipette and the surface consist of similar counter-ions (*e.g.* both the nanopipette and the substrate are negatively charged, Figure 2.3a, b), both the nanopipette and surface have similar perm-selective properties. In this case, cation-selectivity of the interface gives rise to a build-up of high- and low-conductance states in the nanopipette, at negative and positive nanopipette bias, in a very similar way to a classical ICR, but the accumulation/depletion of ions occurs not only inside the nanopipette but also in a perm-selective zone between the end of the nanopipette and the interface. Thus, ion concentration enhancement/depletion giving rise to the ICR effect is magnified (compare Figure 2.3 with Figure 2.8 in the Supporting Information). As a consequence, and as shown by the simulations, a surface-mediated enhancement of local ion concentration (and hence ion current) occurs at negative bias (Figure 2.3b), and a surface-mediated decrease of ion current is expected at positive bias on the basis of the ion concentration profile in Figure 2.3a for the glass nanopipette approaching a glass substrate.

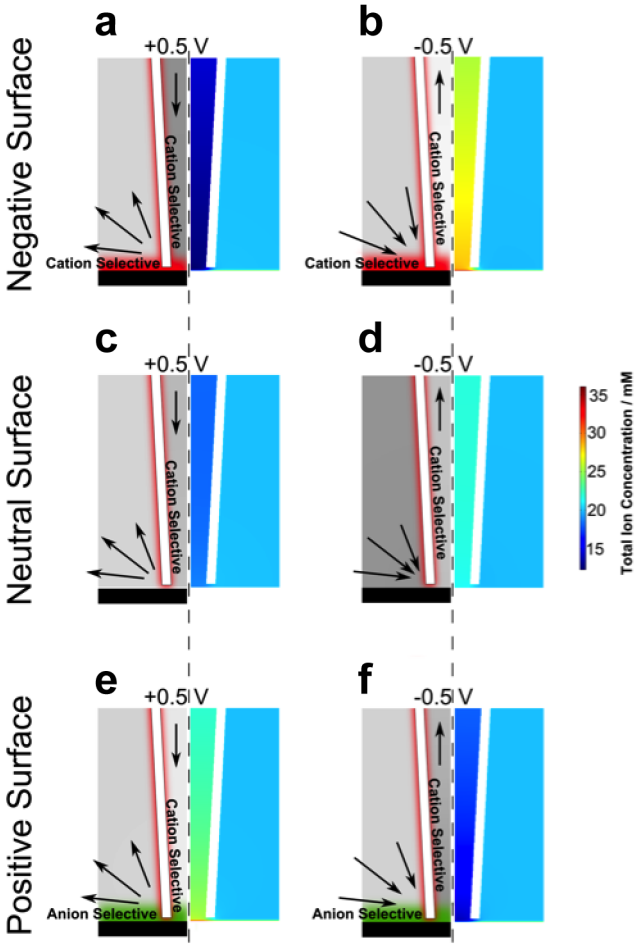


**Figure 2.3.** Schematics of cation mass transport flux (indicated by the arrows) and perm-selective regions (red, cation selective; green, anion selective) at the negatively charged nanopipette and substrates of different charge (on the left of each part) and FEM simulation results (on the right of each part) of the resulting ion concentrations near the end of a nanopipette at surfaces. The nanopipette walls were 30 nm thick and the nanopipette was 10 nm from the surface. Data are for: a negatively charged surface (-5 mC $m^{-2}$ or $-3\times10^{-2}$ *e* $nm^{-2}$) at applied potentials of 0.5 V **(a)**, and -0.5 V **(b)**, inside the nanopipette with respect to the bulk; a neutral surface at 0.5 V **(c),** and -0.5 V **(d)** inside the nanopipette with respect to the bulk; a positively charged (+5 mC $m^{-2}$ or $+3\times10^{-2}$ *e* $nm^{-2}$) surface at 0.5 V **(e)**, and -0.5 V **(f)**, inside the nanopipette with respect to the bulk.

Over uncharged substrates there is a similar effect, but of smaller magnitude. With charge solely on the nanopipette, there is only a weak cation-selective region between the probe and the substrate. As shown by FEM simulations, this causes the

formation of low-conductance (Figure 2.3c) and high-conductance (Figure 2.3d) states inside the nanopipette and between the nanopipette and the surface, but the intensity of the effect is significantly smaller (less perturbation of the total ion concentration from the bulk value) compared to a negatively charged interface.

The significant influence of the surface charge for determining the rectifying characteristics in SICM is demonstrated on Figure 2.3e and f, for the case of the nanopipette tip in the vicinity of a positively charged interface. This case is especially interesting because the nanopipette and the interface exhibit the opposite perm-selective behaviour, *i.e.* cation selectivity inside the nanopipette versus an anion selective DDL at the surface. The inversion of the rectifying properties with bias, as seen in Figure 2.2, can evidently be attributed to the inversion of the low- and high-conductance states in the nanopipette with respect to tip polarity. The anion-selective region at the surface plays the key role in this effect at this charge density (5 mC $m^{-2}$).

The simulation results (Figure 2.3) are in a good agreement with experimental results depicted on Figure 2.2 and with recent theoretical studies of surface-induced rectification which employed a simpler geometry and lower electrolyte concentration.[23] The agreement between experiment and the model is important because another recent report observing a polarity-dependent ion current signal over charged surfaces attributed the rectifying properties to the emergence of an electro-osmotic flow separation phenomenon.[43] The latter report described the surface-induced ion current enhancement at much higher electrolyte concentrations (150 mM NaCl), and even though the nanopipettes were smaller (15 nm radius) they would exhibit much weaker perm-selective properties. Our results (in electrolyte solutions of relatively low ionic strength) demonstrate that rectification is due to the presence of a surface charge and diffusion/electromigration effects, which are sufficient to explain the experimental observations. In fact, as described in Supporting Information, section 2.6.1, we further incorporated electro-osmotic flow into our finite element simulations, and found negligible effect on the ion current.[44,45] Thus, electro-osmotic effects play no part in surface-induced ICR phenomenon under the conditions of these experiments (tip size, bias, and electrolyte concentration).

Our studies now turn to the AC ion current components, induced by the oscillating probe, recorded in parallel with the ion current shown in Figure 2.2. As highlighted earlier, although distance modulated SICM is becoming a widely used technique,[10] these parameters (especially the phase) have not been studied or analysed in detail previously, but provide rich information on interfacial properties (*vide infra*). Irrespective of the surface, the AC current amplitude increases as the nanopipette-surface distance decreases (see Supporting Information, section 2.6.3 which shows the AC ion current magnitude (normalised with respect to the bulk DC ion current) on glass, polystyrene and APTES as a function of nanopipette-surface distance). The AC ion current magnitude at a particular distance represents the absolute change in ion current as the probe-surface distance is modulated (by 10 nm herein) at that distance, and is therefore related to the magnitude of the slope of the DC ion current, with respect to distance. The AC magnitude thus tends to increases as the nanopipette approaches a surface. This signal is typically used as a means of the nanopipette detecting a surface,[10] and any surface charge effects are evidently obscured. However, the phase of the AC ion current can also be recorded and we now show that this signal can be used to detect the surface charge with high sensitivity.

The periodic (time, $t$) change in the probe-surface distance, $z$ (with amplitude $A$ and frequency $f$) with respect to the interface,

$$z = A\sin(2\pi ft) \qquad (2.1)$$

leads to a harmonic oscillation in the ionic current, $I_{AC}$, (under the assumption of a small amplitude of distance modulation)

$$I_{AC} = kA\sin(2\pi ft + \varphi) \qquad (2.2)$$

where $k$ is the slope of the current-distance curve. Hence, the harmonic ion current signal would be expected to be in phase with the driving vertical position oscillation (phase shift $\varphi = 0°$) at positive $k$ (DC ion current drops in the vicinity of the substrate) or counterphase ($\varphi = 180°$) at negative $k$ (ion current increase near the substrate),

while at large separation distance, $k$ = 0, i.e. there is no AC amplitude or phase shift. However, the experimental phase shifts measured in parallel with the DC and AC ion currents for glass, polystyrene and APTES (as summarised in the polar plots in Figure 2.4a-c) are never strictly in phase or counterphase with respect to the driving oscillation and take intermediate values between 0° and 180°. Within the polar plots in Figure 2.4d-f each data point from an approach curve is displayed at a coordinate with its radius defined by the normalised AC ion current magnitude (the larger the current value, the closer the nanopipette is to the surface), and the angle with respect to the positive horizontal axis defines the phase shift, $\varphi$. These features are labelled in Figure 2.4. At relatively large nanopipette-to-substrate distances the AC ion current was negligible and so the traces were centred close to the origin (and largely contained experimental noise).

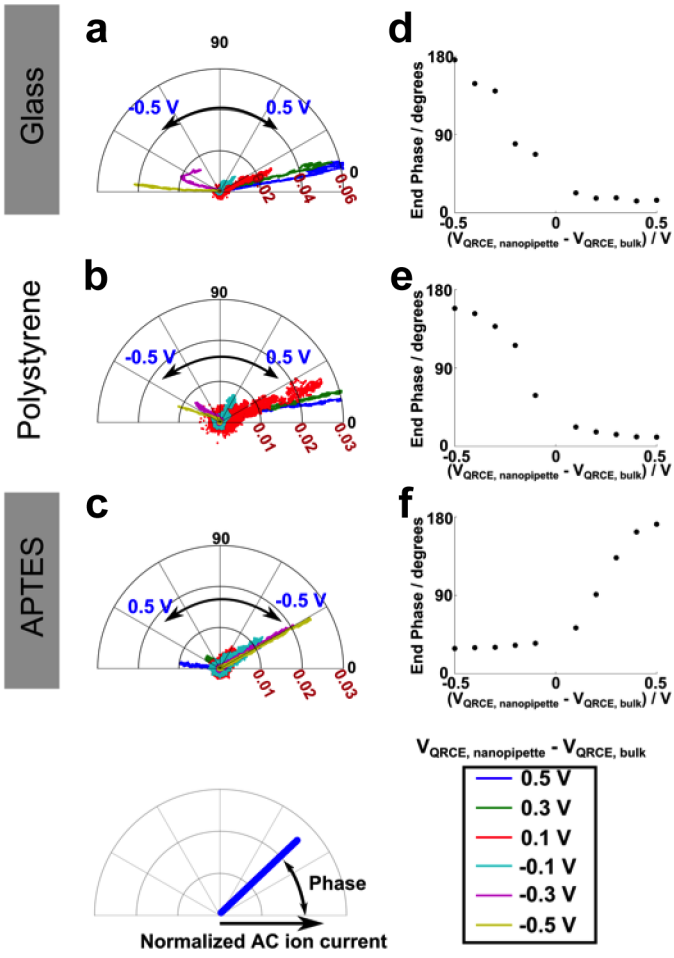


**Figure 2.4.** Polar plots, with the distance from the origin defined by the AC ion current magnitude normalised by the bulk DC ion current and angle defined by the ion current phase (as shown in the insert diagram at the bottom left) of the AC ion

current over glass (**a**), polystyrene (**b**) and APTES (**c**) substrates. Data obtained in 10 mM KCl solution with a 60 nm radius nanopipette oscillated with an amplitude of 10 nm at 288 Hz. The phase value at the smallest nanopipette-surface distance with respect to the applied bias on glass (**d**), polystyrene (**e**) and APTES (**f**).

Interestingly, at closer nanopipette-surface distances, where an appreciable AC ion current was generated, the phase shift over each of the three surfaces correlates with the respective ICR behaviour. Over all surfaces the phase was smallest (ca. 10 degrees over glass and polystyrene, and ca. 30 degrees over APTES) when the ion current magnitude decreased with decreasing nanopipette-surface distance ($V_{QRCE,\ nanopipette}$ - $V_{QRCE,\ bulk}$ = 0.5 V over glass and polystyrene and at -0.5 V over APTES), while the highest $\varphi$ values were associated with ion current enhancements at close nanopipette-surface distances, ($V_{QRCE,\ nanopipette}$ - $V_{QRCE,\ bulk}$ = -0.5 V over glass and polystyrene, and 0.5 V over APTES).

These experimental findings indicate that the phase shift is intrinsically sensitive to the interfacial charge and therefore ionic transport properties at selective biases. The reason is that distance modulation of the nanopipette, when in close surface proximity, results in a periodic interaction of the DLLs of the nanopipette and the surface. Based on the results in Figure 2.3 (discussed above), this would tend to give rise to a periodic change in the conductance strength inside the nanopipette, and in the probe-substrate region. The phase shift is then closely related to the time constant of ionic mass-transport required to change the conductance strength and is very bias sensitive.

It has recently been reported, by experiment and simulation of the bias-scan rate dependent ion current in a nanopore in bulk solution,[46,47] that the high- and low-conductance states take 1-10 ms to build up (for nanopipettes and conditions similar those herein). Close to a surface where ICR is magnified (as discussed above), this time constant would increase. Thus, as the vertical modulation of the SICM tip in our experiments was 10 nm at 288 Hz, with a time constant for the peak-to-peak nanopipette oscillation of *ca.* 1.74 ms, the formation of ion depletion and ion accumulation zones is not likely to reach steady-state and lags the periodic perturbation. The resulting AC ion current is therefore phase shifted with respect to

the driving oscillation, and this becomes especially significant when there is surface-induced charge accumulation in the nanopipette-surface region, (negative nanopipette bias on glass and polystyrene, and positive nanopipette bias at APTES).

### 2.4.2 Surface Charge Mapping

To demonstrate the newfound capabilities of distance-modulated SICM for high-resolution interfacial charge imaging, a surface consisting of a thin polystyrene film with holes revealing the glass substrate underneath was mapped in a hopping mode.[10,12] The nanopipette was repeatedly approached to the surface of the sample using the AC ion current amplitude with a set point of 4 pA (for positional feedback). Once the set point was reached, the nanopipette was retracted and then laterally moved by 250 nm to the next point, in this way forming a 5 µm by 5 µm image. The ion current (both DC and AC) was measured as a function of nanopipette vertical position during each approach and the last data point (closest to the surface) of each was used to construct two-dimensional maps. As shown above (Figure 2.2) both the glass and polystyrene substrates cause DC ion current enhancement at the same polarity (negative values of $V_{QRCE,\ nanopipette}$ - $V_{QRCE,\ bulk}$). Therefore, for imaging purposes, a fixed potential of -0.3 V was applied to the nanopipette, where the phase shift would be most sensitive to interfacial charge (*vide infra*).

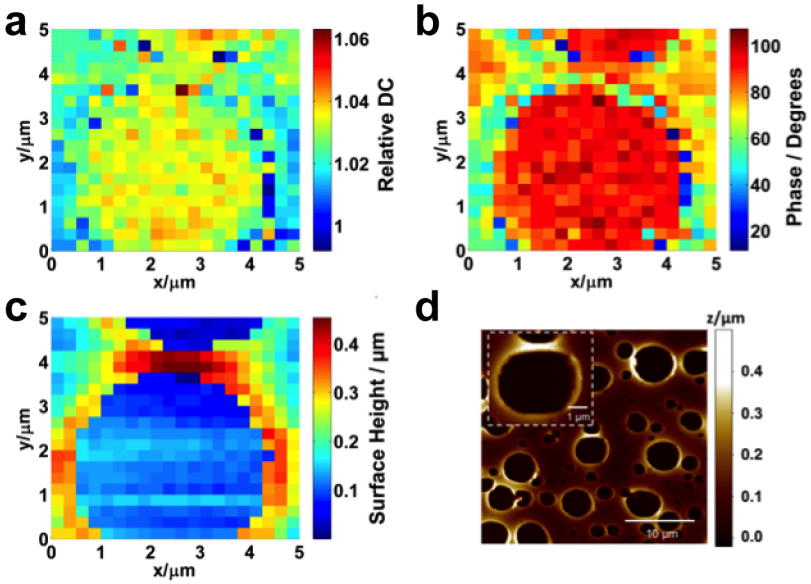


**Figure 2.5.** Two-dimensional hopping mode SICM images of a glass substrate partially covered with a thin polystyrene film. The images display the following ion

current components recorded simultaneously, with an applied bias of 0.3 V: **(a)** normalised (with respect to bulk) DC ion current; **(b)** phase; **(c)** topography. A topographical image of a typical surface as determined by AFM is shown in **(d)**.

Figure 2.5a-c shows typical results: a normalised DC ion current map, a phase map, and topography map (determined from the position at which the surface was detected) *recorded simultaneously*. The normalised ion current reveals the glass exposed by a pore in the film due to the subtle difference in the response of the ion current during the approaches to the two materials, with the glass producing slightly higher surface ion currents compared to the polystyrene, as expected based on the approach curves and simulations in Figure 2.2 and 2.3.

The phase map (Figure 2.5b) also clearly reveals the glass spot but having much higher contrast compared to the DC ion current components. The phase shift tends towards 100 degrees over glass, and is surrounded by the polystyrene, where the phase value is lower. This indicates higher negative surface charge density on the bare glass compared to the polystyrene-coated areas and demonstrates the efficiency of this approach to distinguish subtle surface charge heterogeneities at the nanoscale. A phase difference of > 20 degrees between the glass and polystyrene surfaces represents about 1 $mC/m^2$ (based on surface charge values assumed herein) with the surface charges assumed in this work. Given that phase shift can be detected with a resolution of at least 1 degree (and that this could be further improved), this gives an indication of the sensitivity with which surface charge can be detected via phase detection. Moreover, the phase image exhibits similar spatial resolution to the topography image. Any ICR effect seen over the polystyrene is due to the double layer on the glass nanopipette alone, while for the glass there is a surface-induced contribution leading to a noticeably higher phase.

The topography, shown in Figure 2.5c, shows the flat glass surface surrounded by an area of polystyrene. This topography was confirmed by AFM (Figure 2.5d) which is seen to be in good agreement. Taken together, the data in Figure 2.5 illustrate that substrate topography and charge can be visualised simultaneously. This is because, as a function of nanopipette-surface distance, the AC magnitude (used as a set point) is relatively surface independent, at least on the

scale of the topographical features in Figure 2.5. The ability to deconvolve surface charge and topography involves an interplay between the thickness of the double layer and the tip size. With decreasing tip size or ion concentration, as well as for substrates with extremely high surface charge density, the contribution of surface charge to the AC magnitude becomes more significant, resulting in a convolution of surface charge and topography. With a trend towards higher resolution imagining in SICM[12,14,17], this is an effect that needs careful consideration if SICM is to measure true surface topography. The approach in this chapter provides a framework for such an analysis and allows conditions to be identified where surface charge and topography can be resolved.

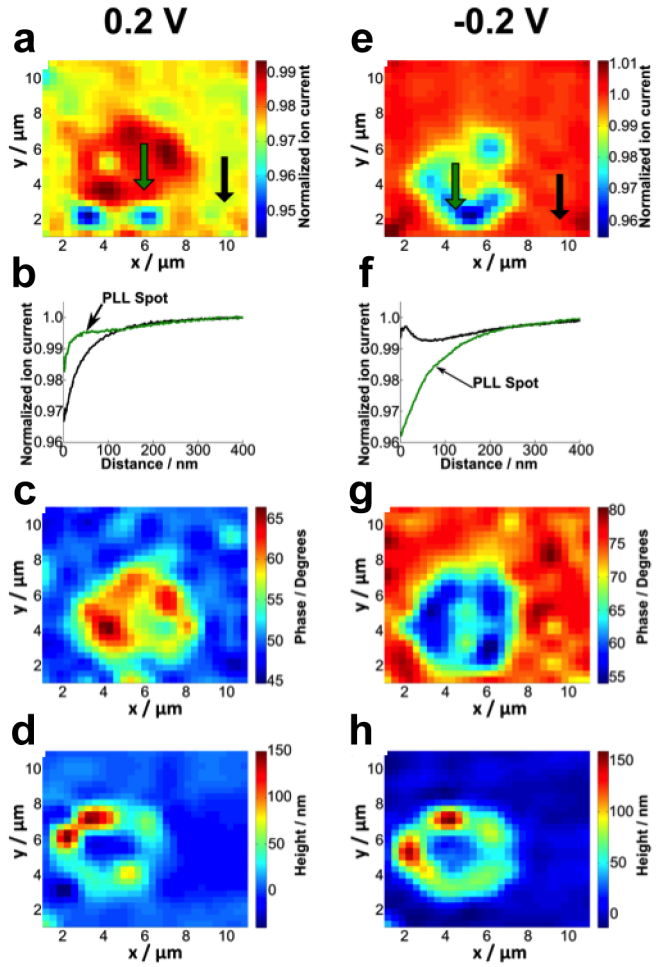


**Figure 2.6.** Hopping mode images, with 1 µm resolution, of a PLL spot (positively charged) on a glass substrate (negatively charged) with a bias of 0.2 V (left) and -0.2 V (right), applied to the QRCE in a 60 nm radius nanopipette with respect to a bulk QRCE in 10 mM KCl. The normalised ion current at the 2 different applied potentials is shown in **(a)** and **(e)**. Typical approach curves, at each potential, over the PLL spot

(green) and over glass (black) are shown in **(b)** and **(f)**. The arrows in **(a)** and **(e)** indicate the pixels at which the approach curves were extracted. Phase maps are shown in **(c)** and **(g)**. The surface topography, determined from the position that the surface was detected, are shown in **(d)** and **(h)**. Note that the 2D images are interpolated.

Finally, we mapped a soft polymeric spot with positive charge on a negatively charged background (glass with a 5 µm diameter spot of PLL) in a hopping mode, with a step size of 1 µm. Imaging was carried out twice with the same probe, first with a potential ($V_{QRCE,\ nanopipette}$ - $V_{QRCE,\ bulk}$) of 0.2 V and then with a potential of -0.2 V. Figure 2.6 shows the results of the two maps, with the PLL spot on a glass surface apparent in both the normalised ion current (a and e), phase (c and g) and topography (d and h) maps. Similar to the charge mapping above, the AC ion current magnitude (4 pA), not shown, was used as the feedback parameter to detect the surface.

The normalised ion current, Figure 2.6a and e for 0.2 V and -0.2 V, respectively, both reveal the PLL spot. At 0.2 V ($V_{QRCE,\ nanopipette}$ - $V_{QRCE,\ bulk}$) the DC ion current is higher over the PLL spot than the glass, but at -0.2 V this is reversed, as expected due to the polarity dependence of the ion current response over the positively charged PLL and negatively charged glass surface. Typical approach curves over the PLL spot, and over the glass, at the two bias values are shown in Figure 2.6b and f. These approaches were taken at the marked positions in Figure 2.6a and e. At a bias of 0.2 V ($V_{QRCE,\ nanopipette}$ - $V_{QRCE,\ bulk}$) the approaches over both glass and PLL decrease, but over PLL the current is higher. In contrast at -0.2 V ($V_{QRCE,\ nanopipette}$ - $V_{QRCE,\ bulk}$) the ion current is higher over glass.

The phase shift of the ion current also shows the PLL spot very clearly. The difference in AC phase over the positively charged spot, compared to the surrounding negatively charged glass, is *ca*. 20 degrees in both maps, but the sign of the change is bias-dependent. This makes the AC phase an especially sensitive and useful parameter for nanoscale surface charge measurements.

The topography, determined from the position that the surface was detected, is largely consistent at each bias (Figure 2.6d and f). This reveals that the

PLL has deposited from the 5 µm diameter droplet in a 'coffee' ring format.[48] The consistency of the topography at difference bias, together with the bias dependent phase (in particular) and ion current response, again highlights the capabilities of SICM for simultaneous topographical and charge mapping.

## 2.5 Conclusions

In solutions of moderate to low electrolyte concentration, the ion current (and alternating ion current) through a nanopipette is surface and potential dependent. This is primarily due to the creation of a perm-selective region between the nanopipette and the surface due to the interactions of the diffuse double layers at the substrate and the nanopipette, coupled with an asymmetry in mass-transport rates inside and outside the nanopipette. The ion current depends on the polarity. Indeed, the ion current can increase as the probe-surface distance decreases: at negative biases ($V_{QRCE,\ nanopipette} - V_{QRCE,\ bulk} < 0$) over negatively charged substrates and at positive biases ($V_{QRCE,\ nanopipette} - V_{QRCE,\ bulk} > 0$) over positively charged substrates. Significantly, for distance-modulation SICM there is a significant phase shift of the AC ion current component, which is highly sensitive to the diffuse double layer of the substrate surface.

Aided by these findings, we have shown that nanopipettes can be used to map the charge at solid-liquid interfaces in electrolyte solutions with the possibility of performing topographical and functional (surface charge heterogeneity) analysis simultaneously. This expands SICM beyond its main application of non-contact mapping of substrate topography and brings new multifunctional capability. In addition, our work has the implications for the capability of SICM to map true surface topography, especially with very small tips. The analysis in this chapter provides a guide for the design and execution of optimal SICM experiments, depending on the application and information sought. In this chapter we have highlighted the ability of a nanopipette to detect surface charge variations semi-quantitatively for surfaces and interfaces with rather modest charge densities. With further simulations it should be possible to extract quantitative surface charge values with good precision and further optimise the technique. Practically, an

important feature of the approach described is that the nanopipette in bulk solution can be checked regularly during a scan (especially in hopping mode where pixel level calibration is possible). The ability to check the probe and measure its charge characteristics in this way is particularly advantageous compared to other techniques for surface charge mapping such as AFM.

## 2.6 Supporting Information

### 2.6.1 FEM simulations

A two dimensional FEM simulation was constructed with the geometry (not to scale) shown in Figure 2.7a to support the experimental data. The inner radius of the pipette was set to 60 nm, the half-cone angle was 3 degrees and the glass wall of the nanopipette was set to be 30 nm thick. The distance between the pipette and the surface was varied. The external domain representing solution bulk was 5 µm high and 10 µm wide, while the domain within the pipette was 20 µm high, which is sufficient to capture the ICR response.[23] A high (1 nm) mesh size was used on the nanopipette walls and the surface.

In the domain of interest the electric potential ($\phi$) and the molar concentration ($c_i$) of $K^+$ and $Cl^-$ were simulated. The electric potential was described by the Poisson equation:

$$\nabla^2\phi = \frac{-F}{\varepsilon\varepsilon_0}\sum_i z_i c_i \qquad (2.3)$$

where $F$ is the Faraday constant, $\varepsilon$ is the relative permittivity of water (which was set to 80),[3] $\varepsilon_0$ is the vacuum permittivity, and $z_i$ is the charge on species $i$ (+1 for $K^+$ and -1 for $Cl^-$). The Nernst-Plank equation (2.2) describes ion transport:

$$J_i = -D_i\nabla c_i - z_i\frac{D_i}{RT}Fc_i\nabla\phi + c_i u \qquad (2.4)$$

where $J_i$ is the total flux of species $i$, $D_i$ is the diffusion coefficient of species $i$ (which was set to $1.95 \times 10^{-5}$ cm$^2$ s$^{-1}$ for $K^+$ and $2.03 \times 10^{-5}$ cm$^2$ s$^{-1}$ for $Cl^-$), $R$ is the universal

gas constant, $T$ is the temperature (which was set to 293.15 K) and $u$ is the fluid velocity. The fluid velocity was first set to zero assuming absence of convective fluxes due to electro-osmosis, although the incorporation of electro-osmosis is explored briefly below. The two governing equations (2.3 and 2.4) are coupled, with the electric potential depending on the molar concentrations and vice versa, and so are solved in parallel. The coupling of the two governing equations results in the formation of a diffuse double layer at charged surfaces.

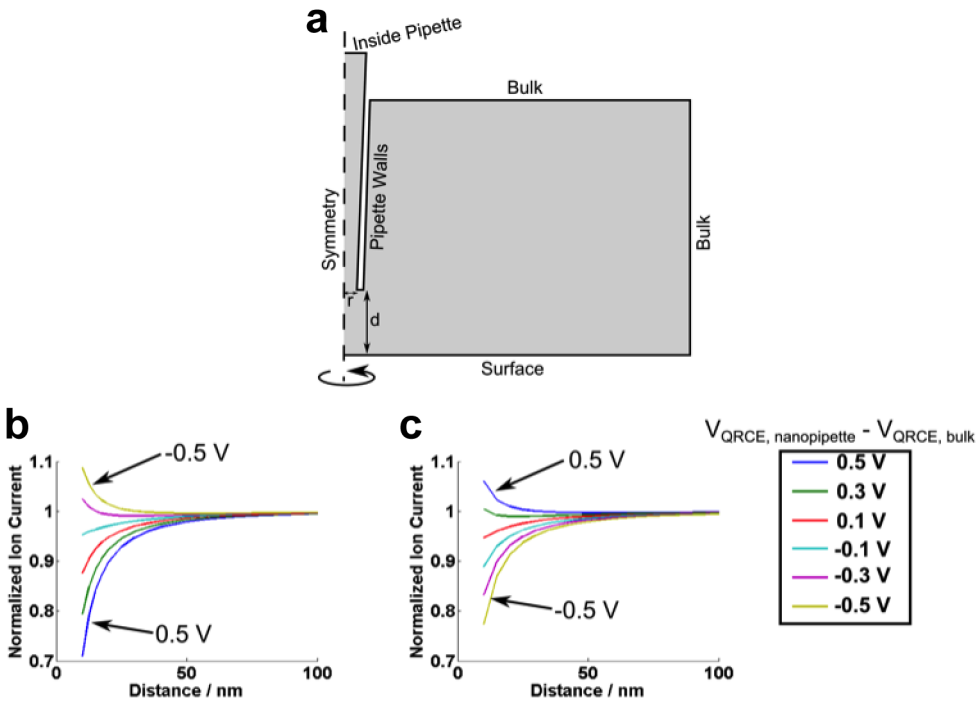


**Figure 2.7. a)** Schematic (not to scale) of the two-dimensional axisymmetric cylindrical domain used for the FEM simulations. Simulated ion current response as a function of nanopipette-surface distance to **(b)** a - 5 mC $m^{-2}$ and **(c)** a +5 mC $m^{-2}$ charged surfaces at different applied bias.

The steady-state electric potential and concentration were simulated subject to the following boundary conditions ($n$ is the surface normal): the pipette walls had a surface charge density of -1.125 mC $m^{-2}$ (or $6.75\times10^{-3}$ $e$ $nm^{-2}$, where $e$ is the electric charge of a proton)[41] and no flux in the ion concentration ($n.J_i$ = 0); at the bulk boundaries the concentration of both ion species was set to 10 mM ($c_i$ = 10 mM) and the potential was varied; at the solution boundary inside the pipette (labelled as 'Inside Pipette' in Figure 2.7a) the ion concentration of both species was set to 10

mM ($c_i$ = 10 mM) and the potential was set to zero ($\phi$ = 0). At the substrate surface the ion flux was set to zero ($n.J_i$ = 0) and the charge was set to either ± 5 mC $m^{-2}$ (or $\pm 3\times10^{-2}$ $e$ $nm^{-2}$). The FEM simulation was performed using COMSOL Multiphysics (v 4.3b) on a 64 bit Windows 7 PC with 16 GB of RAM. The ion current was calculated as the integral of the total charge passing a boundary spanning the inside of the nanopipette.

As displayed in Figure 2.7b and c, the FEM simulations resemble the experimental data in the main text (Figure 2.2), showing the bias-dependent normalised ion current as a function of nanopipette-surface distance for positively and negatively charged surfaces. This highlights that the experimental observations are well-grounded in terms of the electrostatic and mass transport characteristics of this system.

The total ion concentration in the negatively charged nanopipette at a bias of +0.5 V and -0.5 V in a bulk solution is shown in Figure 2.8. This shows the decrease and increase in the local concentration at positive and negative biases, respectively, that results in a corresponding decrease and increase in the ion conductance current through the nanopipette.

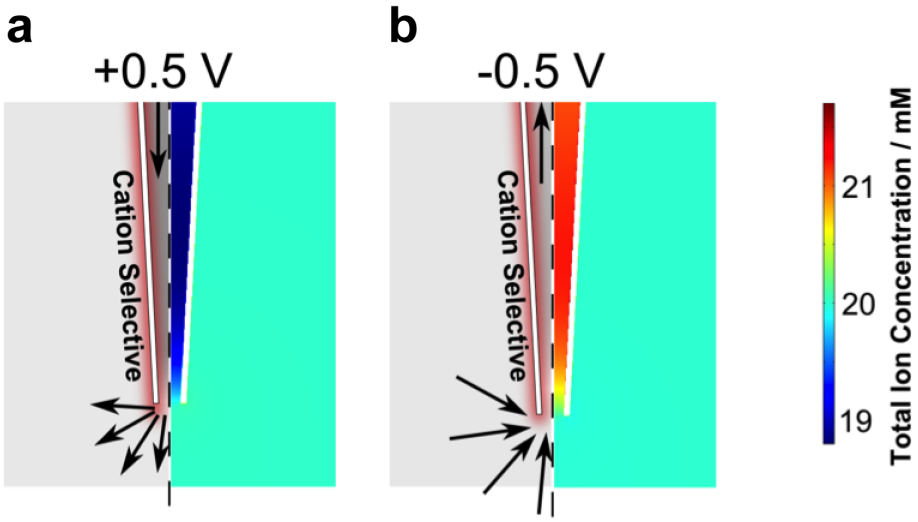


**Figure 2.8.** Schematic of the DDL and direction of cation transport (on the left of each subsection, mass-transport of cations is denoted with arrows) and FEM simulation total ion concentration profile (on the right of each subsection) showing the low **(a)**, bias of +0.5 V) and high **(b)**, bias of -0.5 V) conductance states of a nanopipette in a bulk solution of 10 mM KCl (total ion concentration 20 mM).

In addition, the influence of fluid movement due to electro-osmotic flow was incorporated and solved in parallel. The fluid velocity term, $u$, was described by incompressible Navier-Stokes flow:

$$u\nabla u = \frac{1}{\rho}(-\nabla p + \mu\nabla^2 u - F(\sum_i z_i c_i)\nabla\phi) \quad (2.5)$$

$$\rho\nabla u = 0 \quad (2.6)$$

where $\rho$ is the density of the solution (set to 1000 kg $m^{-3}$), $\mu$ is the viscosity of the solution (set to 0.001 Pa $s^{-1}$) as reasonable values for aqueous solution at ambient temperature, and $p$ is pressure. The boundary conditions for the fluid velocity were set as non-slip ($u$=0) for the nanopipette walls and the substrate surface, while the bulk boundaries and the inner nanopipette boundaries were set as open boundaries (($-p+\mu\nabla^2 u$).$n$=0).

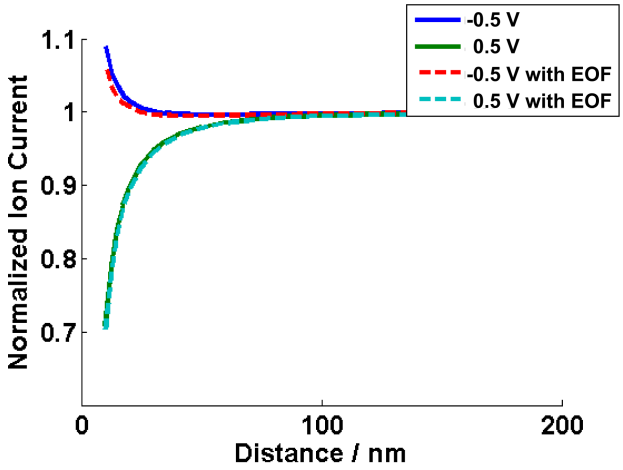


**Figure 2.9.** Simulated SICM ion current (normalised to the value in the bulk) approach curves to a surface with applied charge of +5 mC $m^{-2}$, with, and without, electro-osmotic flow (EOF). The stated potential is that of the QRCEs in the nanopipette with respect to Ag QRCE in bulk.

At the highest applied bias magnitude, 0.5 V and -0.5 V, where electro-osmotic flow would be largest, the ion current with and without electro-osmotic flow was simulated as a function of nanopipette-surface distance over a +5 mC $m^{-2}$ charged surface, and this is presented in Figure 2.9. This shows that electro-osmosis

contributes negligibly to the ion current even at ±0.5 V, in contrast to the electro-osmotic flow separation phenomenon, as described by Clarke.[43] The small effect of electro-osmosis on the ion current gives us confidence that such effects are not important in these systems.

### 2.6.2 Current-voltage characteristics of 60 nm radius pipette probes

In solutions containing relatively small electrolyte concentrations, nanopipette probes demonstrate slight rectifying behaviour (see Figure 2.10), with a classical diode-like characteristic of the pipette with the ion current magnitude at positive potentials ($V_{QRCE,\ nanopipette} - V_{QRCE,\ bulk}$) less than at negative potentials, as shown on Figure 2.10, and explained in details elsewhere[19,22,39] and summarised in the main text.

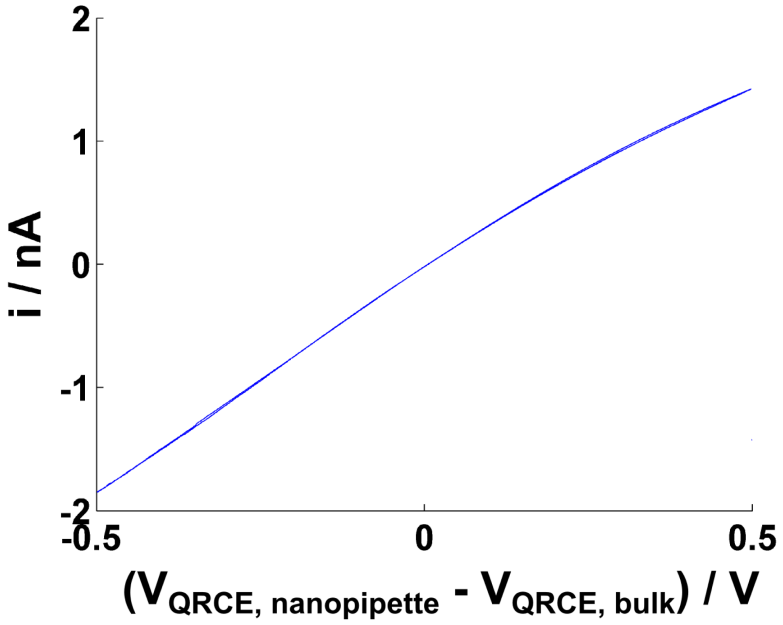


**Figure 2.10.** Typical current-potential response of a nanopipette of 60 nm radius in a 10 mM KCl solution.

### 2.6.3 AC current magnitude approach curves

Normalised AC ion current magnitude approach curves (AC magnitude normalised by the DC ion current value in bulk) to different substrates at different bias values are shown on Figure 2.11.

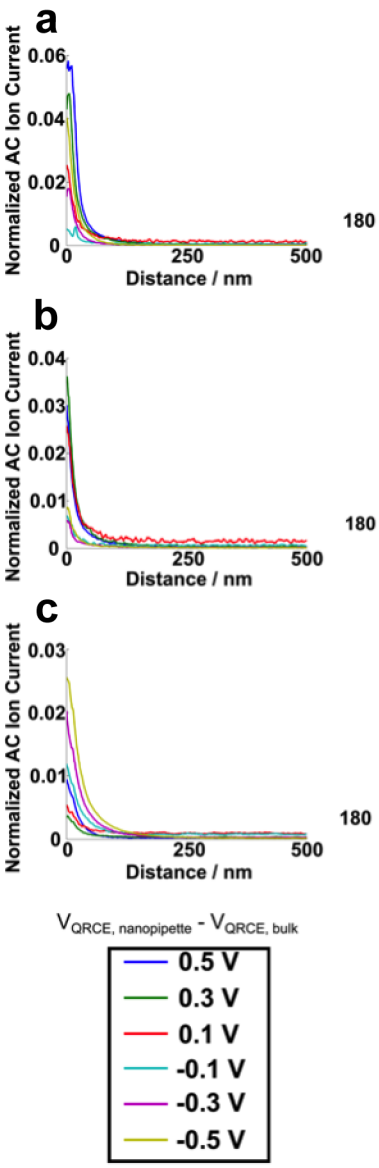


**Figure 2.11.** Normalised AC ion current magnitude (normalised with respect to the DC ion current, shown in Figure 2.11) as a function of probe-surface distance and potential, recorded concurrently with the data in Figure 2.2, over glass **(a)**, polystyrene **(b)** and APTES **(c)** recorded in a 10 mM KCl solution with a 60 nm radius nanopipette oscillated 10 nm at 288 Hz.

## 2.7 References


1. Sa, N.; Baker, L. A. *J. Am. Chem. Soc.* **2011**, *133*, 10398–10401.
2. Luo, L.; Holden, D. A.; White, H. S. *ACS Nano* **2014**, *8*, 3023–3030.
3. Davenport, M.; Healy, K.; Pevarnik, M.; Teslich, N.; Cabrini, S.; Morrison, A. P.; Siwy, Z. S.; Létant, S. E. *ACS Nano* **2012**, *6*, 8366–8380.

4. Morris, C. A.; Friedman, A. K.; Baker, L. A. *Analyst* **2010**, *135*, 2190–2202.
5. Shen, M.; Ishimatsu, R.; Kim, J.; Amemiya, S. *J. Am. Chem. Soc.* **2012**, *134*, 9856–9859.
6. Piper, J. D.; Li, C.; Lo, C.; Berry, R.; Korchev, Y.; Ying, L.; Klenerman, D. *J. Am. Chem. Soc.* **2008**, *130*, 10386–10393.
7. Laslau, C.; Williams, D. E.; Travas-Sejdic, J. *Prog. Polym. Sci.* **2012**, *37*, 1177–1191.
8. Ebejer, N.; Güell, A. G.; Lai, S. C. S.; McKelvey, K.; Snowden, M. E.; Unwin, P. R. *Ann. Rev. Anal. Chem.* **2013**, *6*, 329–351.
9. Lai, S. C. S.; Macpherson, J. V.; Unwin, P. R. *MRS Bull.* **2012**, *37*, 668–674.
10. Chen, C.; Zhou, Y.; Baker, L. A. *Ann. Rev. Anal. Chem.* **2012**, *5*, 207–228.
11. Hansma, P. K.; Drake, B.; Marti, O.; Gould, S. A. C.; Prater, C. B. *Science.* **1989**, *243*, 641–643.
12. Novak, P.; Li, C.; Shevchuk, A. I.; Stepanyan, R.; Caldwell, M.; Hughes, S.; Smart, T. G.; Gorelik, J.; Ostanin, V. P.; Lab, M. J.; Moss, G. W. J.; Frolenkov, G. I.; Klenerman, D.; Korchev, Y. E. *Nat. Methods* **2009**, *6*, 279–281.
13. Chen, C.-C.; Zhou, Y.; Baker, L. A. *ACS Nano* **2011**, *5*, 8404–8411.
14. Gorelik, J.; Shevchuk, A. I.; Frolenkov, G. I.; Diakonov, I. A.; Lab, M. J.; Kros, C. J.; Richardson, G. P.; Vodyanoy, I.; Edwards, C. R. W.; Klenerman, D.; Korchev, Y. E. *Proc. Natl. Acad. Sci. U. S. A.* **2003**, *100*, 5819–5822.
15. Nikolaev, V. O.; Moshkov, A.; Lyon, A. R.; Miragoli, M.; Novak, P.; Paur, H.; Lohse, M. J.; Korchev, Y. E.; Harding, S. E.; Gorelik, J. *Science* **2010**, *327*, 1653–1657.
16. Korchev, Y. E.; Bashford, C. L.; Milovanovic, M.; Vodyanoy, I.; Lab, M. J. *Biophys. J.* **1997**, *73*, 653–658.
17. Klenerman, D.; Korchev, Y. E.; Davis, S. J. *Curr. Opin. Chem. Biol.* **2011**, *15*, 1–8.
18. Rheinlaender, J.; Geisse, N. A.; Proksch, R.; Schäffer, T. E. *Langmuir* **2011**, *27*, 697–704.
19. Wei, C.; Bard, A. J.; Feldberg, S. W. *Anal. Chem.* **1997**, *69*, 4627–4633.
20. Siwy, Z.; Heins, E.; Harrell, C. C.; Kohli, P.; Martin, C. R. *J. Am. Chem. Soc.* **2004**, *126*, 10850–10851.

21. Momotenko, D.; Cortés-Salazar, F.; Josserand, J.; Liu, S.; Shao, Y.; Girault, H. H. *Phys. Chem. Chem. Phys.* **2011**, *13*, 5430–5440.
22. White, H. S.; Bund, A. *Langmuir* **2008**, *24*, 2212–2218.
23. Sa, N.; Lan, W.; Shi, W.; Baker, L. A. *ACS Nano* **2013**, *7*, 11272–11282.
24. Manne, S.; Cleveland, J. P.; Gaub, H. E.; Stucky, G. D.; Hansma, P. K. *Langmuir* **1994**, *10*, 4409–4413.
25. Heinz, W. F.; Hoh, J. H. *Biophys. J.* **1999**, *76*, 528–538.
26. Miyatani, T.; Okamoto, S.; Rosa, A.; Marti, O.; Fujihira, M. *Appl. Phys. A* **1998**, *66*, S349–S352.
27. Hillier, A. C.; Kim, S.; Bard, A. J. *J. Phys. Chem.* **1996**, *100*, 18808–18817.
28. Shevchuk, A. I.; Gorelik, J.; Harding, S. E.; Lab, M. J.; Klenerman, D.; Korchev, Y. E. *Biophys. J.* **2001**, *81*, 1759–1764.
29. Chen, C.; Baker, L. A. *Analyst* **2011**, *136*, 90–97.
30. Powell, H. V; Schnippering, M.; Mazurenka, M.; Macpherson, J. V; Mackenzie, S. R.; Unwin, P. R. *Langmuir* **2009**, *25*, 248–255.
31. Chauhan, A. K.; Aswal, D. K.; Koiry, S. P.; Gupta, S. K.; Yakhmi, J. V.; Sürgers, C.; Guerin, D.; Lenfant, S.; Vuillaume, D. *Appl. Phys. A* **2007**, *90*, 581–589.
32. McKelvey, K.; O'Connell, M. A.; Unwin, P. R. *Chem. Comm.* **2013**, *49*, 2986–2988.
33. Nadappuram, B. P.; McKelvey, K.; Al Botros, R.; Colburn, A. W.; Unwin, P. R. *Anal. Chem.* **2013**, *85*, 8070–8074.
34. McKelvey, K.; Perry, D.; Byers, J. C.; Colburn, A. W.; Unwin, P. R. *Anal. Chem.* **2014**, *86*, 3639–3646.
35. Snowden, M. E.; Güell, A. G.; Lai, S. C. S.; McKelvey, K.; Ebejer, N.; O'Connell, M. A.; Colburn, A. W.; Unwin, P. R. *Anal. Chem.* **2012**, *84*, 2483–2491.
36. Kim, J.; Shen, M.; Nioradze, N.; Amemiya, S. *Anal. Chem.* **2012**, *84*, 3489–3492.
37. Takahashi, Y.; Murakami, Y.; Nagamine, K.; Shiku, H.; Aoyagi, S.; Yasukawa, T.; Kanzaki, M.; Matsue, T. *Phys. Chem. Chem. Phys.* **2010**, *12*, 10012–10017.
38. Umehara, S.; Pourmand, N.; Webb, C. D.; Davis, R. W.; Yasuda, K.; Karhanek, M. *Nano Lett.* **2006**, *6*, 2486–2492.
39. Kovarik, M. L.; Zhou, K.; Jacobson, S. C. *J Phys. Chem. B* **2009**, *113*, 15960–15966.

40. Edwards, M. A.; Williams, C. G.; Whitworth, A. L.; Unwin, P. R. *Anal. Chem.* **2009**, *81*, 4482–4492.
41. Behrens, S. H.; Grier, D. G. *J. Chem. Phy.* **2001**, *115*, 6716–6721.
42. Van der Maaden, K.; Sliedregt, K.; Kros, A.; Jiskoot, W.; Bouwstra, J. *Langmuir* **2012**, *28*, 3403–3411.
43. Clarke, R. W.; Zhukov, A.; Richards, O.; Johnson, N.; Ostanin, V.; Klenerman, D. *J. Am. Chem. Soc.* **2013**, *135*, 322–329.
44. Wang, D.; Liu, J.; Kvetny, M.; Li, Y.; Brown, W.; Wang, G. *Chem. Sci.* **2014**, *5*, 1827.
45. Powell, M. R.; Sa, N.; Davenport, M.; Healy, K.; Vlassiouk, I.; Létant, S. E.; Baker, L. A.; Siwy, Z. S. *J. Phys. Chem. C* **2011**, *115*, 8775–8783.
46. Guerrette, J. P.; Zhang, B. *J. Am. Chem. Soc.* **2010**, *132*, 17088–17091.
47. Momotenko, D.; Girault, H. H. *J. Am. Chem. Soc.* **2011**, *133*, 14496–14499.
48. Yunker, P. J.; Still, T.; Lohr, M. A.; Yodh, A. G. *Nature* **2011**, *476*, 308–311.

# Chapter 3. Bias Modulated Scanning Ion Conductance Microscopy

In SICM experiments, a feedback loop is required in order to follow and map surface topography. This feedback can be directly based on the ionic current flowing between the nanopipette QRCE and the one in bulk solution. This “DC” mode typically uses a decrease in the ionic current, which is expected in the absence of surface charge effects, in order to sense the substrate and a percentage drop off from the bulk response can be used as a feedback signal to track the topography. Modulation modes have also been employed with the aim of reducing the effects of ionic current drift, for example, and typically this approach involves the *z* position of the nanopipette being modulated in order to generate alternating current (AC) signals which are instead used for topographical mapping. These AC components can be extracted using a lock-in amplifier at the applied frequency as described in chapter 2 where it was also shown that the AC components also exhibited a sensitivity to surface charge.

This chapter was published as an article in *Analytical Chemistry* and describes an alternative mode of SICM feedback, termed bias modulated (BM-) SICM wherein an AC signal is instead generated using an oscillation applied to the bias between the two QRCEs. This has several advantages over the distance modulated (DM-) approach. As will be discussed it allows for sensing the surface with no net bias beyond the oscillation, which will be explored further in chapter 4, it allows accessing to a wider range of oscillation frequencies and removes the effects a physical oscillation may have on the solution or sample. In this work all experimental work and theoretical work was performed by myself and the manuscript was prepared by myself under the supervision of Kim McKelvey, my postdoctoral supervisor for this work.

# Bias Modulated Scanning Ion Conductance Microscopy

Kim McKelvey,[1] David Perry,[1,2] Joshua C. Byers,[1] Alex W. Colburn[1] and Patrick R. Unwin[1,*]

[1]Department of Chemistry and [2]MOAC Doctoral Training Centre, University of Warwick, Coventry, UK, CV4 7AL.

***Corresponding Author**

p.r.unwin@warwick.ac.uk

## 3.1 Abstract

Nanopipettes are versatile tools for nanoscience, particularly when used in scanning ion conductance microscopy (SICM) to determine, in a non-contact manner, the topography of a sample. We present a new method, applying an oscillating bias between a quasi-reference counter electrode (QRCE) in the SICM nanopipette probe and a second QRCE in the bulk solution, to generate a feedback signal to control the distance between the end of a nanopipette and a surface. Both the amplitude and phase of the oscillating ion current, induced by the oscillating bias and extracted using a phase-sensitive detector, are shown to be sensitive to the probe-surface distance and are used to provide stable feedback signals. The phase signal is particularly sensitive at high frequencies of the oscillating bias (up to 30 kHz herein). This development eliminates the need to physically oscillate the probe to generate an oscillating ion current feedback signal, as needed for conventional SICM modes. Moreover, bias modulation allows a feedback signal to be generated without any net ion current flow, ensuring that any polarisation of the quasi reference counter electrodes, electro-osmotic effects and perturbations of the supporting electrolyte composition are minimised. Both feedback signals, magnitude and phase, are analysed through approach curve measurements to different surfaces at a range of

distinct frequencies and via impedance measurements at different distances from a surface. The bias modulated response is readily understood via a simple equivalent circuit model. Bias modulated (BM)-SICM is compared to conventional SICM imaging through measurements of substrates with distinct topographical features and yields equivalent results. Finally, BM-SICM with both amplitude and phase feedback is used for topographical imaging of subtle etch features in a calcite crystal surface. The 2 modes yield similar results, but phase-detection opens up the prospect of faster imaging.

## 3.2 Introduction

Scanning ion conductance microscopy (SICM) is a versatile, solution phase technique that uses a nanopipette immersed in, and filled with, an electrolyte solution to interrogate the properties of a sample surface, most commonly the topography.[1–3] An ion current flows through the end of the nanopipette by applying a bias between a quasi-reference counter electrode (QRCE) in the nanopipette and another QRCE in the bulk of the solution, as illustrated in Figure 3.1. The ion current depends primarily on the solution resistance in the nanopipette and, critically, the solution resistance in the gap between the end of the nanopipette and the sample surface.[2,3] As a nanopipette approaches a surface (typically when the probe-surface distance is less than the nanopipette diameter)[4] the gap resistance increases, which leads to a drop in the ion current. Importantly, this change in current means that the nanopipette detects the surface without ever making physical contact, so that SICM is a rather powerful, non-contact, imaging technique.[2] SICM has thus proven particularly effective for mapping the local topography of very delicate samples such as living cells,[3,5–7] by using constant distance,[8–11] hopping/backstep/standing approach,[5,12–14] or hybrid[15] modes to move the nanopipette over the sample. SICM has also been used to investigate ion flow through nanopores,[11,16] and as a tool for mapping the mechanical properties of live cells.[17,18]

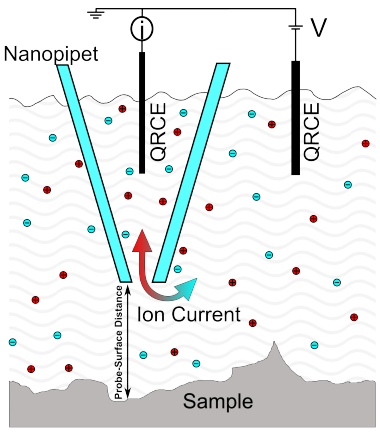


**Figure 3.1.** The SICM configuration, with one QRCE in the nanopipette and another in the bulk of the solution. A bias (V) is applied to the bulk QRCE and the ion current (i) is measured at the QRCE in the nanopipette. The ion current depends on the probe-surface distance. In BM-SICM an oscillating bias (V) is applied between the two QRCEs.

The initial implementations of SICM used the direct ion current between the QRCEs as a feedback signal to regulate the nanopipette-sample distance.[1] Typically, the surface was detected by the probe when the ion current value dropped by 0.2% - 3 % from the bulk ion current.[10] However, the ion current is susceptible to changes in the bulk solution resistance (*e.g.* due to thermal fluctuations), partial blockages of the nanopipette and changes in the polarised QRCEs, all of which can cause the ion current to change, reducing the stability of the feedback response.

A distance-modulated approach was introduced to improve the stability of the feedback response and is now commonly used.[2,3,6,9,19–23] The distance between the nanopipette and the surface is modulated which induces an alternating component of the ion current (AC), in addition to the direct ion current, when the tip is close to the surface. There is usually an increase in the magnitude of the alternating ion current with decreasing nanopipette-surface separation.[19,20] The AC is detected with a lock-in amplifier at the same frequency as the driving oscillation, reducing noise and improving the sensitivity of the surface detection. However, the need to physically oscillate the probe can induce convective fluid movement around the tip and also reduces the response time of the feedback signal (as it is now limited by the oscillation frequency of the probe).

An alternative method, pulse mode SICM,[24,25] applies a current pulse between the QRCEs and the change in potential needed to drive this pulse is measured. As mentioned above, as the probe approaches a surface the resistance generally increases and therefore the potential needed to drive the current pulse increases. Thus, the probe is first moved a small increment towards a surface, a current pulse is generated and the potential measured. Depending on the signal, the probe is moved another increment towards the surface until a desired (potential) set point is reached, when the probe position is measured.[24] In this way, a topographical map of the surface can be built up pixel by pixel, although the process is rather lengthy and the approach has not been widely adopted.

Herein, we explore an alternative mechanism to generate a feedback response in SICM, via bias modulation (BM). An oscillating bias is applied between the QRCEs, eliminating the need to physically oscillate the probe, and a phase-sensitive detector (a lock-in amplifier) is used to extract the amplitude and phase of the oscillating ion current. We show that this produces a stable feedback parameter (amplitude or phase) for SICM over a wide range of frequencies (from 200 Hz to 30 kHz herein). We explore the frequency dependent response using impedance measurements at different distances from a surface. Oscillating the bias between the QRCEs about 0 V ensures that there is no net ion current flow, in contrast to all other implementations of SICM. This ensures that any polarisation of the QRCEs and perturbation of the supporting electrolyte concentration in and around the probe are minimised, and that fluid movement induced by electro-osmotic effects through the end of the nanopipette is minimised. We note that preliminary limited measurements of this type were reported recently but were of a low-resolution, at limited frequencies and neglected to use any phase-sensitive detection of the AC ion current.[26] We demonstrate the use of this feedback mechanism for topographical imaging by mapping well defined structures, including gold bands on glass and subtle etch features on a calcite crystal surface using both the magnitude and the phase of the AC response as feedback parameters. These examples serve to highlight the future prospects for the use of this new mode of SICM.

## 3.3 Materials and Methods

### 3.3.1 Solutions

Milli-Q reagent grade water (resistivity of ca. 18.2 MΩ cm at 25°C) was used for all solutions. 100 mM KCl (Sigma-Aldrich) was typically used as an electrolyte solution for the SICM measurements, except for experiments to explore supporting electrolyte concentration effects, where the concentration was varied in the range 0.01 mM – 100 mM. For the studies of calcite, a 10 mM $CaCl_2$ (Sigma-Aldrich) solution was used. A 3 mM maleic acid (Sigma-Aldrich) solution was used to etch the calcite surface before imaging.[27]

### 3.3.2 Nanopipettes

60 nm radius nanopipettes were fabricated from borosilicate glass capillaries (o.d. 1.2 mm, i.d. 0.69 mm, Harvard Apparatus) using a laser puller (P-2000, Sutter Instruments, pulling parameters: Line 1: Heat 350, Fil 3, Vel 30, Del 220, Pul _, Line 2: Heat 350, Fil 3, Vel 40, Del 180, Pul 120). Each nanopipette used was filled with the same electrolyte solution as employed for the bulk solution and an Ag/AgCl QRCE was inserted. The nanopipette was then mounted on a piezoelectric positioner (see below) and placed in solution close to the sample. A second Ag/AgCl QRCE was placed in the bulk of the solution.

### 3.3.3 Substrates

Glass bottomed petri dishes (3512, WillcoWells), gold band structures on glass (fabricated using the lift off lithography method to produce 700 nm high and 50 µm wide gold features) and calcite (Iceland Spar, Richard Tayler Minerals, Surrey, UK; cleaved and etched for 5 minutes in 3 mM maleic acid solution that was constantly stirred, resulting in the formation of etch pits) were used as substrates.

### 3.3.4 Instrumentation

As described previously,[28] a 38 µm piezoelectric positioner (P-753-3CD, Physik Instrumente) was used for movement of the nanopipette normal to the sample (Figure 3.1). The sample was moved laterally under the tip with a two axis

piezoelectric positioner system (Nano-BioS300, Mad City Labs Inc.). A bias (V) was applied directly to the QRCE in the bulk of solution and the current was measured at the QRCE in the nanopipette using a custom wideband current-to-voltage converter (DC – 300 kHz (-3 dB)). A lock-in amplifier (SR830, Stanford Research Systems) was used to generate an oscillating bias that was applied directly to the bulk QRCE. Some conventional distance-modulated SICM measurements[9] were also made, for comparison, and in this case the bias voltage was added to the control signal for the 38 µm piezoelectric positioner so as to modulate the nanopipette position normal to the sample. The lock-in amplifier was used to detect the oscillating components (the magnitude and phase) of the ion current. The instrument was controlled, and data collected, through a FPGA card (7852R, National Instruments) that was programmed using LabVIEW (2013, National Instruments). Impedance measurements were made using a Gamry Femtostat (FAS2-38039), with spectra acquired using Gamry Framework Data Acquisition Software (6.04).

### 3.3.5 Bias Modulated SICM Procedure

An oscillating bias (10 mV r.m.s. amplitude), with a frequency between 200 Hz and 30 kHz, was applied. For the initial approach and for the approach curve measurements, the nanopipette was moved towards the surface at a rate of 100 nm $s^{-1}$ until the surface was detected as a change in either the magnitude or the phase of the oscillating component of the ion current (*vide infra*).

Maps and line traces of the local topography of substrates of interest were generated in a hopping mode, where a series of nanopipette approaches were made at different lateral positions (in a defined grid pattern) over the surface. At each position, the nanopipette was approached to the surface at a speed of 1 µm $s^{-1}$ until the surface was detected as the amplitude or phase reaching a desired user defined set point. The nanopipette was then retracted 1 µm, and then moved laterally to a new position where the process was repeated. The position of the piezoelectric positioners when the desired set point was attained was used to generate the maps (and line traces) of the local topography.

### 3.3.6 Distance Modulated SICM

The tip was oscillated normal to the surface using the oscillating potential generated by the lock-in amplifier, at a frequency of 230 Hz with 10 nm peak-to-peak amplitude. The QRCE in the bulk solution was biased at 0.3 V.

Maps of the local topography were generated in a hopping mode, as described above, except that the oscillating ion current was generated through the oscillating motion of the probe normal to the surface.[9]

### 3.3.7 Impedance Measurements

A nanopipette was positioned close to a glass surface and the Gamry Femtostat was connected to the QRCEs. The probe was moved in steps towards the surface and at each step an impedance measurement (between 1 Hz and 100 kHz with 9 points per decade and 10 mV r.m.s.) was taken. Before each impedance measurement the potential was allowed to equilibrate for 10 seconds, and a series of measurements at each point took ca. 90 seconds. Equivalent circuit models were fitted using a simplex method with 300 iterations using Gamry Echem Analyst software.

## 3.4 Results and Discussion

### 3.4.1 Approach Curves

Nanopipettes (60 nm in radius) were approached at a velocity of 100 nm $s^{-1}$ in 100 mM KCl to both an insulating glass bottomed petri dish and an unbiased conducting gold surface. The electrolyte concentration ensured that the ion current through the nanopipette showed ohmic behaviour without any rectification phenomena.[29] Note that the absolute nanopipette-surface distance was estimated from the point of inflection in the amplitude and phase response, which we assign to the nanopipette making physical contact with the surface. Thus, each approach curve was made with a separate tip. Typical BM-SICM approach curves at a range of frequencies are presented in Figure 3.2.

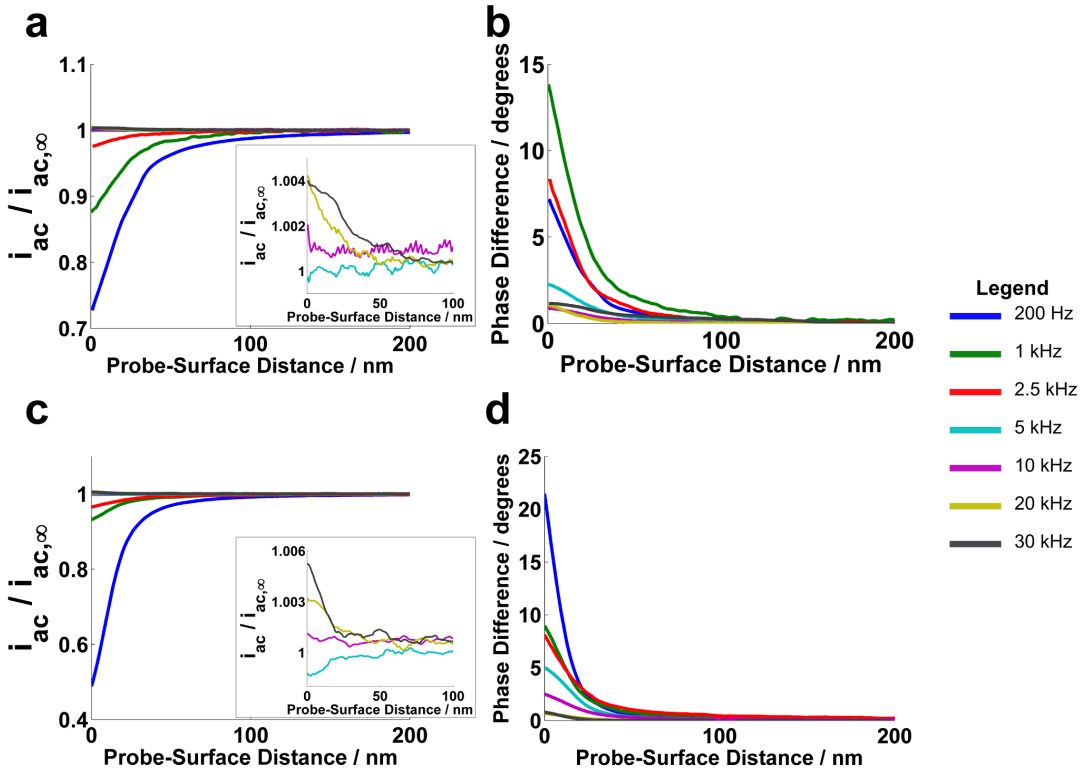


**Figure 3.2.** Approach curves, each with a separate pipette (60 nm radius, 10 mV r.m.s. bias oscillation in 100 mM KCl) to an insulating glass surface and a non-biased conducting gold surface over a range of frequencies. **a)** Normalised magnitude of the oscillating ion current over a glass surface. **b)** Phase difference magnitude compared to the bulk of the oscillating ion current over a glass surface. **c)** Normalised magnitude of the oscillating ion current over an unbiased gold surface. **d)** Phase difference magnitude compared to the bulk of the oscillating ion current over an unbiased gold surface.

In the bulk, far from the surface, the magnitude and phase of the oscillating ion current were constant at stable finite values. The absolute values of each depended on the bias modulation frequency as described in the impedance measurements section below (and shown as the bulk data in Figure 3.4a-c). These values were maintained until the nanopipette approached within (approximately) a tip diameter (or less) of the surface, when the magnitude and phase of the oscillating ion current changed (as shown in Figure 3.2), with both the insulating and unbiased conducting surfaces showing a fairly similar response. At low frequencies

the amplitude drops with probe-surface distance, but this effect was diminished with increasing frequency until at frequencies above 10 kHz the amplitude actually increased very slightly with the decrease in probe-surface distance (see inserts in Figure 3.2a and c). The phase difference magnitude always increased with a decrease in probe-surface distance, although the extent of the increase depends on the frequency and at close distances to some extent the substrate. Importantly, these data show that modulating the bias enables the surface to be sensed readily through changes in the oscillation ion current magnitude and phase, making this an attractive feedback signal for SICM imaging.

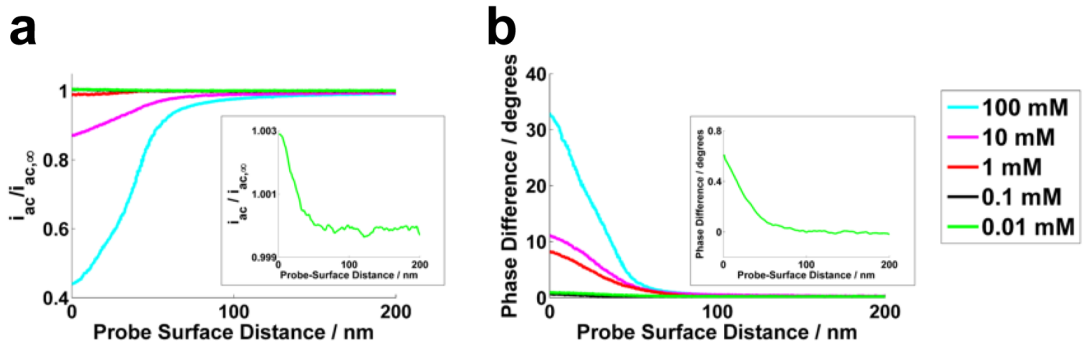


**Figure 3.3.** Approach curves (for a 60 nm radius pipet with a 10 mV r.m.s. bias oscillation at 200 Hz) to an insulating glass surface in a range of supporting electrolyte (KCl) concentrations. **a)** Normalised magnitude of the oscillating current. **b**) Phase difference magnitude compared to the bulk of the oscillating current.

While SICM usually employs relatively high electrolyte concentrations,[2] which is thus the main focus of the chapter, we also explored the effect of electrolyte concentration. The approach curve response was found to depend on the supporting electrolyte concentration, as shown in Figure 3.3a and b. These data are for a fixed oscillation frequency of 200 Hz to a glass substrate in various concentrations of KCl in the range 100 mM to 0.01 mM. In general, as the supporting electrolyte concentration decreases, there is a smaller amplitude and phase response as the probe approaches the surface. At low (0.1 mM and below) electrolyte concentrations, as shown in the inserts in Figure 3.3a and b, the amplitude of the oscillation actually increases very slightly (by just 0.3 %) with a decrease in the

nanopipette-surface distance, while the phase difference magnitude continues to increase as the probe approaches the surface, although by just 0.5°. These data highlight the sensitivity with which BM-SICM measurements can be made, and that a wide range of electrolyte concentrations should be employable. The impedance measurements and model that follow provide some rationalisation of the approach curve data. Moreover, as we show below, these responses can be explained and predicted using a simple physical model.

### 3.4.2 Impedance Measurements

To further explore the response of BM-SICM, we carried out impedance measurements (in 100 mM KCl) with a 60 nm radius nanopipette at different distances from a surface. Experiments were carried out at an insulating glass surface, which presented a smoother surface. The probe was moved in increments towards the surface and at each height an impedance measurement was made. The probe was held stationary for 90 seconds during the impedance measurement, however, in principle, thermal drift could change the probe-surface distance during this time.[30] We estimate from repeat approaches and measurements of a nanopipette to a surface that thermal drift would be no more than a maximum of 15 nm over this time period (data not presented), a distance that should not significantly influence the main features of our results. The low degree of thermal drift is consistent with other SICM measurements we have recently reported.[28]

Impedance measurements in bulk solution and at distances of approximately 200 nm, 100 nm and 50 nm from a glass surface are shown as a Nyquist plot in Figure 3.4a. The impedance data create a hemispherical curve in the upper right quadrant of the complex plane, with the low frequency data points on the real axis and the hemispherical curve traced out as the frequency increases. This response is typical for a nanopipette in a bulk solution with high electrolyte concentrations and no bias offset.[31] As the nanopipette nears the surface, the low frequency response moves to the right, corresponding to an increase in resistance, as would be expected based on conventional SICM.[1,4,10] However, the general shape of the impedance curves is maintained.

The impedance data can also be represented as a function of frequency in the format of a Bode plot, as shown in Figure 3.4b and c, which allows the range of frequencies over which the main changes in the amplitude or phase occur to be identified. At frequencies below ca. 100 Hz there is a clear and pronounced change in the amplitude response with probe-surface distance (decrease in amplitude with decreasing distance as discussed above), but this becomes attenuated at the higher frequencies. Above 500 Hz the changes are predominantly confined to the phase response. In fact, a window for observing changes in the phase with frequency at finite distances from the surface is apparent between ca. 10 Hz and 20 kHz. The upper limit opens up the possibility of fast imaging in the future.

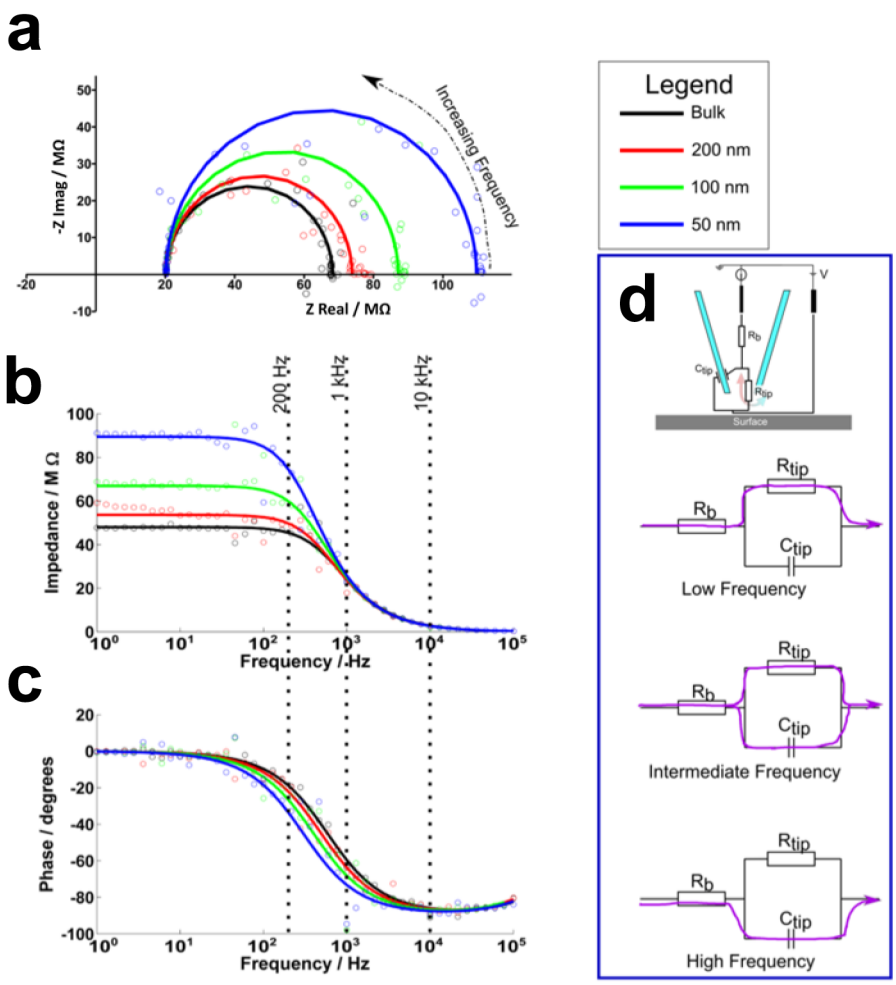


**Figure 3.4. a)** Nyquist plot showing the impedance in bulk, at 200 nm, 100 nm and 50 nm from a glass surface for a 60 nm radius nanopipette in 100 mM KCl. **b)** Impedance magnitude at the different probe-surface distance as a function of frequency. **c)** Phase as a function of frequency. In each case the points are data and

the solid lines are a fit to a simple equivalent circuit. **d)** Schematic of the equivalent electrical circuit (a parallel RC component in series with a resistor), with the current flow paths at low, intermediate and high frequencies, where $R_b$ is the bulk resistance of the solution, $R_{tip}$ is the resistance in the end of the pipet and in the probe-surface gap, and $C_{tip}$ is the capacitance across the glass walls of the nanopipette.

The approach curves, shown in Figure 3.2a and b, were carried out at constant frequency and the positions of the 200 Hz, 1 kHz and 10 kHz values are indicated on Figure 3.4b and c. For a frequency of 200 Hz both the frequency and phase of the approach curves change with distance. At a frequency of 1 kHz the phase change is significant while the change in amplitude is severely attenuated. With a frequency of 10 kHz there is no significant change in amplitude with probe-surface separation, but the change in the phase with distance is still detectable.

The impedance response in 100 mM KCl can be described by a simple equivalent electrical circuit, a parallel RC component in series with a second resistor as is shown in Figure 3.4d. The bulk resistance of the solution (both inside and outside the nanopipette) is described by the resistor, $R_b$, while the end of the tip (including the tip-surface gap) is described, in simplest terms, by a resistor and capacitor in parallel ($R_{tip}$ and $C_{tip}$), where $R_{tip}$ represents the resistance at the end of the tip (including the tip-surface gap) and $C_{tip}$ represents the capacitance across the glass walls of the nanopipette. Although the RC component at the end of the probe could be broken down into multiple sub-components, this is the simplest representation that effectively captures the nature of the response, as evident from the close agreement between experiment and the model. The values of the components of the simple equivalent electrical circuit were determined by fitting the simple model to the impedance data, and are shown in Table 1. Note that this model describes the nanopipette response in high electrolyte solution, which is most commonly used. In low electrolyte solutions ion current rectification due to inadequate screening of the charge on the walls of the nanopipette (and surface) becomes apparent, and this influences the impedance response.[31]

The resistance in the end of the tip (and tip-substrate gap), $R_{tip}$, is much larger than the resistance in the rest of the solution, as for conventional SICM.[2] As

the nanopipette approaches the surface, $R_{tip}$ increases, as also expected for conventional SICM.[2] The capacitance stays fairly constant (ca. 6 pF) with the change of probe-surface distance.

At low frequencies (below ca. 100 Hz) the current flows predominantly through the resistor of the parallel RC component, as shown schematically in Figure 3.4d. At intermediate frequencies (between ca. 100 Hz and 500 Hz), the current flows through both the resistor $R_{tip}$ and capacitor $C_{tip}$, while at high frequencies (above ca. 500 Hz) the current flows predominantly through the capacitor, as is also shown schematically in Figure 3.4d. Only the resistance, $R_{tip}$, changes significantly with the probe-surface distance, and therefore the frequency dependent response can easily be understood using the equivalent circuit model.

Using the well-known expression for the resistance between the end of a nanopipette and surface,[2] the simple equivalent model can further be used to predict the approach curves for high electrolyte solution. The tip resistance is equivalent to the access resistance plus the bulk resistance.

$$R_{tip} = R_{bulk} + \frac{\frac{3}{2}\log\frac{r_o}{r_i}}{\kappa.\pi.d} \qquad (3.1)$$

where $r_o$ and $r_i$ are the outer and inner tip radii, $\kappa$ is the solution conductivity and $d$ is the tip-substrate separation distance and $R_{bulk}$ is the fitted tip resistance in bulk solution (see Table 3.1), where the effects of the surface are not detectable. This expression was substituted into the equivalent circuit model, and the predicted approach curves at a range of frequencies are shown in Figure 3.5. These curves are a reasonable approximation to the data presented in Figure 3.2a and b.

**Table 3.1.** Parameters used to fit the impedance data in Figures 3.4a-c.

| **Distance** | **$R_b$ / Ω** | **$R_{tip}$ / Ω** | **$C_{tip}$ / F** |
|---|---|---|---|
| Bulk | $3.5 \times 10^4$ | $4.8 \times 10^7$ | $5.7\times 10^{-12}$ |
| 200 nm | $4.0 \times 10^4$ | $5.4 \times 10^7$ | $6.0\times 10^{-12}$ |
| 100 nm | $4.2 \times 10^4$ | $6.7 \times 10^7$ | $6.0\times 10^{-12}$ |
| 50 nm | $3.6 \times 10^4$ | $8.9 \times 10^7$ | $5.9\times 10^{-12}$ |

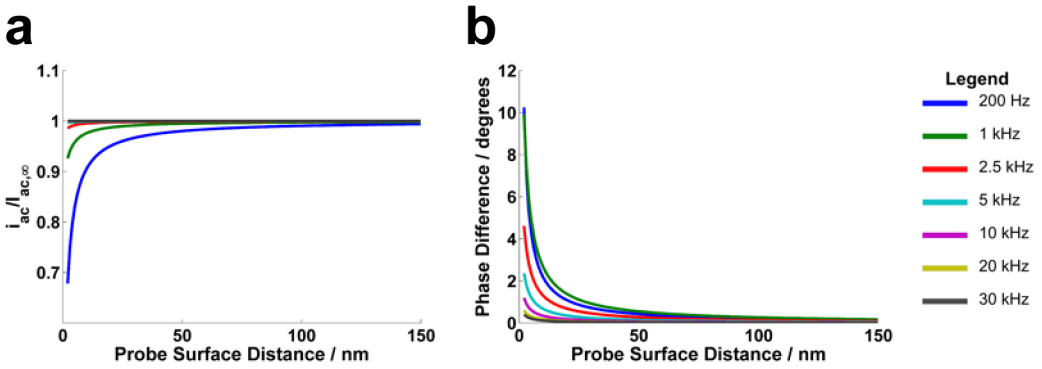


**Figure 3.5.** Theoretical approach curves (see text for details) for a 60 nm radius nanopipette in 100 mM KCl at a range of BM frequencies. **a)** The normalised magnitude of the oscillating current. **b)** The phase difference magnitude of the oscillating current.

For future implementations it could be advantageous to increase the frequency at which a significant surface response is observed, as this would reduce the time constant of the feedback response, and therefore allow the nanopipette to be moved at a greater lateral speed over a surface. This can be achieved by decreasing the resistance in our simple model, which can be achieved experimentally by increasing the concentration of the supporting electrolyte and/or by changing the shape (for instance the cone angle) or size of the nanopipette. The resolution of SICM is governed by the size of the nanopipette, with smaller nanopipettes providing

higher resolution images. Herein we have only considered 60 nm radius nanopipettes. However different sized nanopipettes will continue to exhibit a bias modulated response, with the magnitude and frequency range of the response, naturally, scaling with the nanopipette size. Based on our impedance model smaller nanopipettes (which have a higher resistance) should show a response over a smaller range of frequencies. In addition, smaller nanopipettes can exhibit an ion current rectification response that will also affect the magnitude of the response (in fact the 60 nm nanopipettes used in lower electrolyte concentrations, as shown in Figure 3.3, exhibited an ion current rectification response and provided a bias modulated response on approach to a surface). Interestingly at frequencies above 10 kHz we observe a very small increase in the amplitude of the oscillating current as the probe approaches the surface (as is shown in the inserts in Figure 3.2a and c). These responses are not captured in our impedance data as the probe was not placed closer than 50 nm from the surface and so is not captured in our simple equivalent circuit model above. We also observed a similar small increase in the amplitude at close distances, at a lower frequency (200 Hz), at low electrolyte concentrations (Figure 3.3a). This suggests the current flow between the nanopipette and bulk interacts with the diffuse double layer that forms at the glass substrate surface, where there is both a higher ion concentration and where there may also be consequentially an ion current rectification phenomena between the end of the nanopipette and the surface.[32] This is an interesting observation, and one that BM-SICM could play a significant role in elucidating in the future.

### 3.4.3 Mapping Topography

Initially we compared the topography generated by distance-modulated SICM,[19,20] the predominant SICM technique, to that of BM-SICM using an amplitude set point of 0.983 times the bulk value. Figure 3.6a shows line profiles of the topography of a sample with unbiased gold features (conducting) on a glass (insulating) surface that was imaged with both modes in 100 mM KCl. An oscillating frequency of 200 Hz was used for both the bias and distance modulation. The line profiles are practically identical for the two techniques, confirming that BM-SICM produces the same

topography as distance-modulated SICM but without the need to physically oscillate the nanopipette or generate a net ion current. These data confirm that BM-SICM is not affected by the nature of the substrate when the tip images at or about a radius from the surface (i.e. has a small set point) consistent with the approach curve data presented herein. A topographical map of a gold band edge is shown in Figure 3.6b generated using BM-SICM (with a bias oscillation of 1 kHz and 10 mV r.m.s.) and using the alternative phase signal for feedback with set point 1°. The image shows a sharp, straight edge at the gold-glass interface and a height of 100 nm as expected.

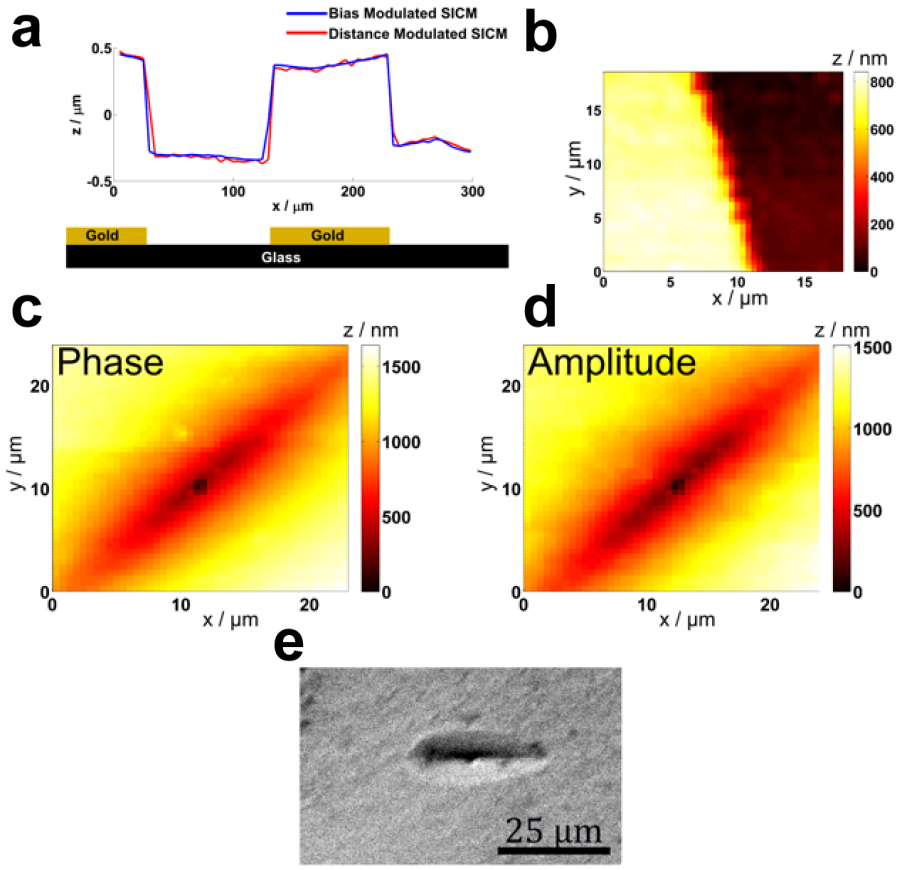


**Figure 3.6. a)** Line scan across glass surface with gold bands in both conventional distance-modulated SICM and BM-SICM. **b)** Topography map of the edge of a gold band feature on glass imaged using BM-SICM at 1 kHz using phase as the feedback with a set point of 1°. **c)** Topography of a calcite etch pit determined using BM-SICM at 1 kHz using phase as the feedback with a set point of 1°. **d)** Topography of the same calcite etch pit determined using BM-SICM at 1 kHz using the AC amplitude as feedback with a set point of 0.995. **e)** Optical image of a typical calcite etch pit.

Finally, we imaged etch pits in calcite using BM-SICM with both amplitude and phase set points. The etch pits were formed by dissolving the calcite in maleic acid for 5 minutes, which creates distinct oval shaped pits in the surface. The dissolution was stopped by removing the maleic acid solution and replacing it with 10 mM $CaCl_2$, in which the SICM mapping was conducted. Etch pits in calcite are oval depressions in the surface, as shown in the optical image in Figure 3.6e. The local topography was imaged in BM-SICM (with a bias oscillation of 1 kHz and 10 mV r.m.s.) in a hopping mode (1 μm separation between hops) with a 60 nm nanopipette. The topography of a single etch pit is shown in Figure 3.6 using the phase signal, with set point 1° (c), and AC amplitude, with set point 0.995 (d), as feedback parameters respectively. The etch pit is clearly resolved, and corresponds to typical etch pits as observed by optical microscopy (e). This demonstrates that BM-SICM can be used to determine the topography of interesting practical samples. In the future, the capability of BM-SICM to be carried out at higher frequencies should allow dynamic surfaces to be followed with good time resolution.

## 3.5 Conclusions

Modulating the bias between the QRCEs in SICM allows the probe-surface distance to be detected through the amplitude and phase components of the oscillation ion current, detected with a lock-in amplifier. This provides a simple, stable method to detect the probe-substrate distance that does not require the physical movement of a probe or the application of a net ion current. This reduces both convective and electro-osmotic fluid movement, detrimental effects from extensive polarisation of the QRCEs and changes of the supporting electrolyte composition within the nanopipette that can be problematic with conventional SICM.

The frequency dependence of the probe-surface distance response can be readily understood using a simple equivalent circuit model that we developed for an inert surface and was elucidated through impedance measurements at different probe-surface distances. This has allowed us to identify a window in which either the magnitude (up to ca. 500 Hz) or phase (between ca. 100 Hz and 30 kHz) of the oscillation ion current can be used to sense the probe-surface distance. Interestingly,

at very close pipette-surface distances (at frequencies above 10 kHz in 100 mM KCl or at lower frequencies in lower supporting electrolyte concentrations) there is a subtle effect of the surface which is likely due to the nanopipette ion flow interacting with the diffuse double layer at the surface. The sensitivity of this technique in detecting these subtle responses indicates that BM-SICM is not only a topographical tool, but could prove to be a powerful method for investigating other properties of surfaces and interfaces.

To illustrate the capability of BM-SICM for imaging, we have measured substrate topography, the dominant use of SICM. The topography obtained using BM-SICM (in a hopping mode) was equivalent to that generated by conventional distance-modulated SICM over both insulating and non-biased conducting substrates, confirming the validity of the technique. An interesting sample of an etched calcite surface was imaged using both the amplitude and phase of the oscillating ion current as feedback parameters. In both cases, similar images were obtained and the topography of an individual subtle etch pit in the surface was easily identified. These data provide a platform for the future use of BM-SICM for imaging surface processes and dynamics.

## 3.6 References


1. Hansma, P. K.; Drake, B.; Marti, O.; Gould, S. A. C.; Prater, C. B. *Science* **1989**, *243*, 641–643.
2. Chen, C.; Zhou, Y.; Baker, L. A. *Ann. Rev. Anal. Chem.* **2012**, *5*, 207–228.
3. Happel, P.; Thatenhorst, D.; Dietzel, I. D. *Sensors* **2012**, *12*, 14983–15008.
4. Edwards, M. A.; Williams, C. G.; Whitworth, A. L.; Unwin, P. R. *Anal. Chem.* **2009**, *81*, 4482–4492.
5. Yang, X.; Liu, X.; Zhang, X.; Lu, H.; Zhang, J.; Zhang, Y. *Ultramicroscopy* **2011**, *111*, 1417–1422.
6. Ushiki, T.; Nakajima, M.; Choi, M.; Cho, S.-J.; Iwata, F. *Micron* **2012**, *43*, 1390–1398.
7. Klenerman, D.; Korchev, Y. E.; Davis, S. J. *Curr. Opin. Chem. Biol.* **2011**, *15*, 1–8.

8. Shevchuk, A. I.; Frolenkov, G. I.; Sánchez, D.; James, P. S.; Freedman, N.; Lab, M. J.; Jones, R.; Klenerman, D.; Korchev, Y. E. *Angew. Chem. Int. Ed.* **2006**, *45*, 2212–2216.
9. Shevchuk, A. I.; Gorelik, J.; Harding, S. E.; Lab, M. J.; Klenerman, D.; Korchev, Y. E. *Biophys. J.* **2001**, *81*, 1759–1764.
10. Korchev, Y. E.; Bashford, C. L.; Milovanovic, M.; Vodyanoy, I.; Lab, M. J. *Biophys. J.* **1997**, *73*, 653–658.
11. Chen, C.-C.; Derylo, M. A.; Baker, L. A. *Anal. Chem.* **2009**, *81*, 4742–4751.
12. Novak, P.; Li, C.; Shevchuk, A. I.; Stepanyan, R.; Caldwell, M.; Hughes, S.; Smart, T. G.; Gorelik, J.; Ostanin, V. P.; Lab, M. J.; Moss, G. W. J.; Frolenkov, G. I.; Klenerman, D.; Korchev, Y. E. *Nat. Methods* **2009**, *6*, 279–281.
13. Happel, P.; Dietzel, I. D. *J. Nanobiotechnology* **2009**, *7*, 7.
14. Takahashi, Y.; Murakami, Y.; Nagamine, K.; Shiku, H.; Aoyagi, S.; Yasukawa, T.; Kanzaki, M.; Matsue, T. *Phys. Chem. Chem. Phys.* **2010**, *12*, 10012–10017.
15. Zhukov, A.; Richards, O.; Ostanin, V.; Korchev, Y.; Klenerman, D. *Ultramicroscopy* **2012**, *121*, 1–7.
16. Chen, C.-C.; Zhou, Y.; Baker, L. A. *ACS Nano* **2011**, *5*, 8404–8411.
17. Schäffer, T. E. *Anal. Chem.* **2013**, *85*, 6988–6994.
18. Rheinlaender, J.; Schäffer, T. E. *Soft Matter* **2013**, *9*, 3230–3236.
19. Li, C.; Johnson, N.; Ostanin, V.; Shevchuk, A.; Ying, L.; Korchev, Y.; Klenerman, D. *Prog. Nat. Sci.* **2008**, *18*, 671–677.
20. Pastré, D.; Iwamoto, H.; Liu, J.; Szabo, G.; Shao, Z. *Ultramicroscopy* **2001**, *90*, 13–9.
21. Rheinlaender, J.; Geisse, N. A.; Proksch, R.; Schäffer, T. E. *Langmuir* **2011**, *27*, 697–704.
22. Chen, C.; Baker, L. A. *Analyst* **2011**, *136*, 90–97.
23. Zhou, Y.; Chen, C.-C.; Baker, L. A. *Anal. Chem.* **2012**, *84*, 3003–3009.
24. Mann, S. A.; Hoffmann, G.; Hengstenberg, A.; Schuhmann, W.; Dietzel, I. D. *J. Neurosci. Methods* **2002**, *116*, 113–117.
25. Happel, P.; Hoffmann, G.; Mann, S. A.; Dietzel, I. D. *J. Microsc.* **2003**, *212*, 144–151.

26. Kawashima, T.; Matsugase, T.; Tanaka, K.; Nagai, M.; Shibata, T.; Mineta, T.; Makino, E. *Microelectron. Eng.* **2012**, *98*, 663–667.
27. Compton, R. G.; Pritchard, K. L.; Unwin, P. R.; Grigg, G.; Silvester, P.; Lees, M.; House, W. A. *J. Chem. Soc. Faraday Trans. 1* **1989**, *85*, 4335–4366.
28. Nadappuram, B. P.; McKelvey, K.; Al Botros, R.; Colburn, A. W.; Unwin, P. R.; Unwin, R. *Anal. Chem.* **2013**, *85*, 8070–8074.
29. Wei, C.; Bard, A. J.; Feldberg, S. W. *Anal. Chem.* **1997**, *69*, 4627–4633.
30. Kim, J.; Shen, M.; Nioradze, N.; Amemiya, S. *Anal. Chem.* **2012**, *84*, 3489–3492.
31. Feng, J.; Liu, J.; Wu, B.; Wang, G. *Anal. Chem.* **2010**, *82*, 4520–4528.
32. Sa, N.; Lan, W.; Shi, W.; Baker, L. A. *ACS Nano* **2013**, *7*, 11272–11282.

# Chapter 4. Simultaneous Nanoscale Surface Charge and Topographical Mapping

Chapter 2 explored how the SICM response can be influenced by surface charge and the implications for the accuracy of topographical mapping in the presence of these effects. A strong relationship between the applied bias and response to surface charge was observed. In chapter 3 it was shown that a new feedback type allowed for SICM topographical mapping, even with no net bias applied, just a small harmonic oscillation applied between the two SICM QRCEs. In this chapter the possibility of deconvolving surface charge and topography through a new scan regime and utilising the BM-SICM feedback is explored. This new approach developed herein eliminates the effects of heterogeneous surface charge on the feedback signal used to map topography and subsequently allows for the surface charge mapping through applying a bias between the SICM QRCEs.

This chapter was published as an article in *ACS Nano*. All of the experimental work was carried out by myself as well as the manuscript preparation. FEM simulations used herein were performed by Rehab Al Botros and are also present in her thesis (Warwick 2016). Supervisory help was provided by Dmitry Momotenko for some of this work.

# Simultaneous Nanoscale Surface Charge and Topographical Mapping

*David Perry,[1,2,†] Rehab Al Botros,[1,†] Dmitry Momotenko,[1,†] Sophie L. Kinnear[1] and Patrick R. Unwin[1,*]*

[1]Department of Chemistry and [2]MOAC Doctoral Training Centre, University of Warwick, Coventry, CV4 7AL, United Kingdom.† These authors contributed equally.

***Corresponding Author**

p.r.unwin@warwick.ac.uk

## 4.1 Abstract

Nanopipettes are playing an increasingly prominent role in nanoscience, for sizing, sequencing, delivery, detection and mapping interfacial properties. Herein, the question of how to best resolve topography and surface charge effects when using a nanopipette as a probe for mapping in scanning ion conductance microscopy (SICM) is addressed. It is shown that using a bias modulated (BM) SICM scheme it is possible to map the topography faithfully, while also allowing surface charge to be estimated. This is achieved by applying zero net bias between the electrode in the SICM tip and the one in bulk solution for topographical mapping, with just a small harmonic perturbation of the potential to create an AC current for tip positioning. Then a net bias is applied, whereupon the ion conductance current becomes sensitive to surface charge. Practically this is optimally implemented in a hopping-cyclic voltammetry mode where the probe is approached at zero net bias at a series of pixels across the surface to reach a defined separation, and then a triangular potential waveform is applied and the current response is recorded. Underpinned with theoretical analysis, including finite element modelling of the DC and AC components of the ionic current flowing through the nanopipette tip, the powerful capabilities of this approach are demonstrated with the probing of interfacial acid-base equilibria and high-resolution imaging of surface charge heterogeneities, simultaneously with topography, on modified substrates.

## 4.2 Introduction

Surface charge density plays an important role in interfacial processes and properties, and being able to probe surface charge in a simple, robust manner could find great application in mineralogy,[1-3] colloidal science,[4-7] materials science, including the study of electrode surfaces,[8] and in living systems[4, 9-16] where surface charge is known to play a key role. While zeta potential measurements[17, 18] and potentiometric titrations[19-21] give important information on the charge of colloids in solutions, the charge on extended surfaces is more difficult to probe, with relatively few techniques available. Since surfaces are often characterised by both heterogeneous charge distributions and topographical features, scanning probe microscopes (SPMs), such as force microscopy (FM)[22-26] and scanning ion conductance microscopy (SICM),[27-32] are potentially attractive as a means of probing local surface charge. At the same time, because the response of these techniques depends on both topography and surface charge (and other properties) there is a wider consideration about the operation of these SPMs, and the extent to which these different effects are convoluted in the response.

This chapter describes how SICM can be used to (i) measure topography largely free from surface charge effects and (ii) how the corresponding charge on the surface can be probed semi-quantitatively. SICM uses a positionable nanopipette to examine electrolyte-substrate interfaces without requiring a direct mechanical contact with the substrate itself, making it a powerful approach for the investigation of soft (biological) samples.[27, 32, 33] Traditionally in SICM, a bias is applied between a quasi-reference counter electrode (QRCE) in the nanopipette tip and a second QRCE in bulk solution to generate a direct ionic current (DC). Away from the surface, the total resistance of this conductimetric cell is dominated by the contribution from the narrow tip opening. As the tip approaches the surface to within a tip diameter, the resistance contribution from the tip-to-substrate gap increases and causes the value of ionic current to drop.[27] This provides a means of monitoring the surface topography, using various schemes such as distance modulation (DM)[27, 28, 30, 34] and the hopping (backstep) mode[32, 35, 36] in which a specific tip current value is used to

maintain a fixed tip-surface separation during scanning. In DM-SICM, a harmonic oscillation to the vertical (*z* axis) position is applied and an alternating current signal (AC) is induced, the amplitude of which can be used for positionable feedback.[27, 28, 30, 34] Typically, under high electrolyte conditions any double layer formed at charged interfaces is considered to be compressed to an undetectable level[37] and so it has been argued that surface charge does not convolute recorded signals, enabling topography to be faithfully reproduced[29] within the framework of traditional SICM experiments.

For lower electrolyte conditions (most prominently below 10 mM) the diffuse double layer (DDL) at charged interfaces expands further into solution, with a Debye length of a few nanometres, and even more in media with lower dielectric constants and/or lower ionic strength.[38] This effect leads to ion current rectification phenomena at nanopipette tips in bulk solution[39-41] as well as surface induced rectification,[42, 43] once a nanopipette approaches towards a charged surface. Indeed, near a surface, there is a polarity-dependent current enhancement or diminution, due to the double layer at the surface modulating the transport of ions travelling through the nanopipette opening,[42, 44] in contrast to the expectations of the operation of conventional SICM.[27] This phenomenon has recently been explored and used to map surface charge heterogeneities using a classical DM-SICM setup.[44] However, there are a number of issues with this technique. The mechanical oscillation of the tip in DM-SICM, limits the range of working distances achievable with the nanopipette and consequently the sensitivity and resolution. Furthermore, the high-speed motion of the probe and fluid exerts mechanical forces on the sample, which may influence its response, for example when living cells are studied. The requirement of a large bias between the two QRCEs has also been suggested to lead to fluidic instabilities which impact on the surface.[43] Finally, for smaller probes, it becomes especially difficult to separate topography and surface charge.[44]

We have recently proposed an alternative approach for positionable feedback control of nanopipettes in SICM, whereby the tip-to-substrate separation is controlled through the application of an oscillating bias between the two QRCEs to generate an AC signal.[45] It has been demonstrated that at high electrolyte concentrations, bias modulated (BM)-SICM provides a stable feedback for tracking

surface topography with oscillation around 0 V between the two QRCEs, at a range of frequencies using either the AC amplitude or AC phase signals. In this chapter, we reveal the capabilities of BM-SICM for accurate tracing of the surface topography at charged substrates, at low electrolyte concentrations, by minimising (virtually eliminating) polarity dependent effects of surface charge in the conductimetric response. Moreover, we further highlight the possibility of probing and mapping unevenly distributed charge at interfaces by sensing of the local ionic environment within a double layer. This is achieved through the use of a *hopping approach* and *CV measurement* at each pixel in an image, with certain biases between the two QRCEs shown to highlight surface charge in a sensitive manner while, for others, the current response is insensitive to the surface charge, thus revealing only the topography with high precision. With the aid of finite element method (FEM) modelling, we verify the experimental observations and demonstrate the sensitivity of the AC voltammetric response to the double layer and charge at target surfaces. As well as independent and simultaneous topographical and surface charge imaging, this work provides a robust platform for future local nanoscale impedance experiments.

## 4.3 Materials and Methods

### 4.3.1 Solutions

Milli-Q reagent grade water (resistivity ca. 18.2 MΩ cm at 25°C) was used for all solutions. For the BM-SICM approach curve measurements to glass, impedance studies and BM-SICM imaging, 10 mM KCl (Sigma-Aldrich, pH 6.5) solutions were prepared. To produce the polystyrene-glass substrate for imaging, polystyrene (Sigma-Aldrich) was dissolved in chloroform (Fisher Scientific) giving a solution (0.66 mg/ml) into which a glass slide was dip-coated (30 s) to create a polystyrene film. A solution of 3-aminopropyl triethoxysilane (APTES, Sigma Aldrich) in toluene (2 µl/ml) was used for glass surface modification for some experiments (dip-coated for 5 min). All impedance measurements and approach curve studies carried out on APTES samples were done in a slightly acidic solution of HCl (pH 3.4, Fisher Scientific) and KCl (9 mM). Solutions with varying ratios of KCl to HCl (keeping 10 mM constant ionic strength) were used to explore the effect of pH on the surface charge of glass.

Approach curve measurements were also carried out towards glass in 1 – 100 mM KCl solutions to test the limits at which surface charge effects could be observed.

### 4.3.2 Nanopipettes

Nanopipettes (~75 nm radius, inner taper angle 2.5 – 3.5°, dimensions measured with a Zeiss Supra55VP field emission scanning electron microscope) were pulled from borosilicate glass capillaries (o.d. 1.2 mm, i.d. 0.69 mm, Harvard Apparatus) using a laser puller (P-2000, Sutter Instruments; pulling parameters: Line 1: Heat 330, Fil 3, Vel 30, Del 220, Pul -, Line 2: Heat 330, Fil 3, Vel 40, Del 180, Pul 120). We deliberately chose to use a relatively large tip to produce a well-defined probe that was easily characterized. Although surface charge effects would be expected to be less prominent than on smaller tips;[42, 44] they are still shown to be significant with major implications for nanoscale SICM imaging as we discuss herein.

### 4.3.3 Substrates

Glass bottomed petri dishes with detachable cover slips (3512, WillcoWells) were used as glass samples, either as received, after sonication in acetone (10 min), sonication in water (10 min) and plasma ashing in oxygen (1 min, 100 W), or after functionalisation with either polystyrene or APTES. The polystyrene samples were dip coated to produce a heterogeneous thin neutral polystyrene film with exposed negatively charged glass regions, under the condition of the measurements (aerated, unbuffered, 10 mM KCl, pH 6.5).

### 4.3.4 Instrumentation

The basic instrumentation has been described elsewhere.[45, 67] Briefly, movement of the SICM probe in the direction normal to the substrate was controlled using a piezoelectric positioning stage of range 38 µm (P-753-3CD, Physik Instrumente) with lateral movement of the substrate controlled using a two-axis piezoelectric positioning system with a range of 300 µm (Nano-BioS300, Mad City Labs Inc.) The current-to-voltage converter used to measure currents was custom built. A lock-in amplifier (SR830, Stanford Research Systems) was used to generate the oscillating

signal for BM-SICM approaches and to extract the phase and amplitude of the AC ion current. Data recording, as well as the probe position and voltage output control, was performed using a custom written LabVIEW (2013, National Instruments) program through an FPGA card (7852R, National Instruments). Impedance measurements were carried out using a Gamry Femtostat (FAS2-38039), with spectra acquired using Gamry Framework Data Acquisition Software (6.04).

### 4.3.5 Bias Modulated-Scanning Ion Conductance Microscopy Approaches

An oscillating bias (10 mV r.m.s. amplitude, 270 Hz) was applied between the two QRCEs about mean biases of -0.3 V, 0 V and 0.3 V. All potentials quoted herein refer to the potential of the QRCE inside of the nanopipette with respect to the bulk QRCE. Nanopipettes were approached towards glass and APTES-coated substrates at 10 nm $s^{-1}$ and the DC, AC phase and AC amplitude of the ionic current were recorded simultaneously. Approaches towards glass were also carried out in 10 mM electrolyte concentration with the pH varying between 2.1 (10 mM HCl) and 6.5 (10 mM KCl) to vary the surface charge on the glass substrate.

### 4.3.6 Bias Modulated-Scanning Ion Conductance Microscopy Imaging

BM-SICM images were acquired with a positionable nanopipette in a hopping mode, while applying a small oscillation to the bias (10 mV r.m.s. amplitude, 270 Hz) about 0 V. In this mode, the probe was translated towards the surface at each image pixel at 700 nm $s^{-1}$ until the surface was detected through a 0.5° increase in the AC phase signal. The piezo height at this point was used to generate topographical maps (as under these conditions the SICM response was relatively insensitive to surface charge effects; *vide infra*). The bias between the QRCEs was then swept linearly down to -0.4 V, reversed to 0.4 V, and finally returned to 0 V at a rate of 1 V $s^{-1}$, and the AC phase and DC recorded, enabling polarity-dependent surface charge mapping. As well as movies of SICM response *vs*. applied potential (presented over the range -0.4 V to 0.4 V), representative maps at specific potentials as an average of

several maps over potentials within ±5 mV of the stated bias value were extracted, by taking average values of the AC and DC response for each pixel in the map.

### 4.3.7 FEM Simulations

A two-dimensional axisymmetric finite element method (FEM) model was constructed to mimic a nanopipette in bulk and in the vicinity of a charged surface (with a varying tip-to-substrate separation distance). Simulations were constructed in Comsol Multiphysics (version 4.4), using the transport of diluted species and electrostatics modules, using harmonic bias perturbation boundary conditions to simulate the AC behaviour of the BM-SICM setup (for more details see Supporting Information 4.6.1).

### 4.3.8 Impedance Measurements

The Gamry Femtostat was connected between the two QRCEs: one in the nanopipette and one in bulk solution. Impedance spectra were collected at a set of frequencies between 1 Hz and 100 kHz, with 9 points per decade. Impedance measurements were performed with a 10 mV r.m.s. oscillation with 0 V mean bias.

### 4.3.9 Atomic Force Microscopy

Contact mode atomic force microscopy (AFM) (Catalyst, Bruker-Nano), using silicon tips on a nitride lever (SNL-10, Veeco), was employed for the analysis of sample substrates.

## 4.4 Results and Discussion

### 4.4.1 Bias Modulated-SICM as an Ion-Sensing Probe of Double Layers

An uncompensated surface charge in electrolyte solutions leads to the formation of a diffuse double layer, consisting of co- and counterions that balance the charge. The approach herein is to probe the ionic atmosphere of the double layer electrochemically (conductimetrically) with a nanopipette and derive surface charge information. At low electrolyte concentrations, glass (or quartz) nanopipettes with small tip openings exhibit perm-selectivity[39, 40] towards counter ions of the DDL, that

have enhanced concentration near the charged nanopipette walls. In combination with asymmetric mass-transport rates inside and outside nanopipettes (taking into account the geometrical configuration of the probe) the absolute value of ionic current driven through the opening becomes polarity dependent and this diode-like behaviour is known as ion current rectification (ICR).[39-41, 46, 47]

When a nanopipette approaches a charged surface, the rectifying characteristics of the probe can be modified due to the presence of the DDL at the surface.[42, 44] As a result, the surface-induced rectification contributes significantly to the overall mass-transport properties of the nanopipette and, in principle, this effect can be employed for probing and mapping surface charge.[44] However, as mentioned in the introduction, the DC or AC components of ionic current, are also distance-dependent and this presents a conundrum as to how to separate charge and distance effects in the conventional DM-SICM scheme. Essentially in DM-SICM the ionic current driven through the nanopipette cannot necessarily be reliably employed for either task – probing the surface charge or tracking the topography.[44] For surfaces with large topographical features and relatively low surface charge densities, the implications of this may not be noticeable,[44] but as the resolution of the technique is advanced with smaller nanopipettes being utilised and smaller topographical features being probed,[36, 48] the resulting effects of surface charge heterogeneities on the DM-SICM feedback, may become much more apparent.

Herein, we present an elegant way to resolve both surface topography and charge by using BM-SICM (Figure 4.1a). In a BM-SICM configuration, a small harmonic oscillation of potential is applied to induce an AC ionic current component, which can be used for vertical probe positioning even in the absence of mean bias applied between two QRCEs.[45] Additionally, by applying an additional bias, $\Delta V$, we show herein that one can control the extent to which the SICM current response is sensitive (or not) to surface charge. In essence for $\Delta V = 0$, the BM-SICM response faithfully maps topography (Figure 4.1b), due to minimal surface induced rectification about 0 V, while for $\Delta V \neq 0$ the SICM response becomes surface charge sensitive. Note that by maintaining $\Delta V = 0$ on approach for *topographical imaging* in this work, the scenario of traditional SICM experiments is avoided where, based on

recent work,[42, 44] an applied bias upon approach to heterogeneously charged substrates, may result in a non-constant working distance and hence distorted topography (Figure 4.1c).

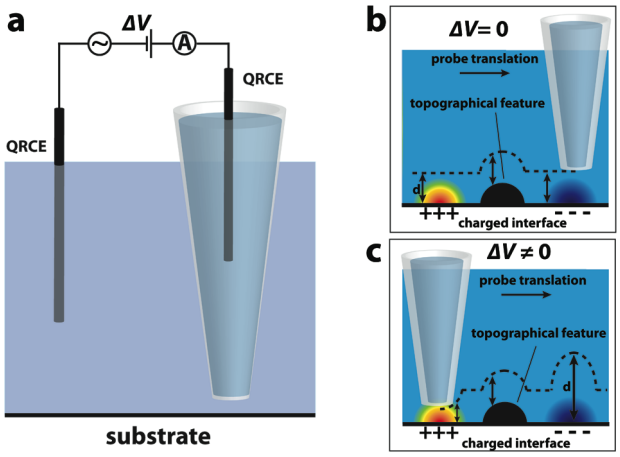


**Figure 4.1.** Concept of simultaneous topographical and charge mapping with a positionable nanopipette. **a)** Schematic representation of the bias-modulation SICM (BM-SICM) setup. Graphical representation (not to scale) demonstrating deconvoluted **(b)** and hypothetically convoluted **(c)** scanning over a sample containing topographical (shown in black) and charge features (double layer over positively and negatively charged areas are shown in rainbow and blue gradients, respectively). The possible probe trajectory for a fixed set point (target distance, *d*) is shown as a dashed line.

To demonstrate the efficacy of BM-SICM for probe positioning near a surface, independent of surface functionality, a series of nanopipette approaches towards positively (APTES) and negatively (glass) charged substrates were carried out at different nanopipette biases, applied to the probe. Here the distance, *d*, was defined with respect to the distance of closest approach, ca. 25 nm or less. For simulations, *d* is the absolute tip-substrate distance. These approach curves, and all experimental and simulation studies herein, were performed using an oscillation frequency of 270 Hz. This frequency was selected based on our recent work[45] and impedance studies performed herein (see Supporting Information, section 4.6.2) that highlights a frequency domain where the AC phase is most sensitive to changes in both system

capacitance and resistance. This region is where the slope of the Bode plot of AC phase against frequency is greatest, which can be seen to exist between 100 Hz and 1 kHz, for the experimental conditions of the experiments herein (Supporting Information, Figure 4.7). Below this frequency range, the phase is zero, as the current solely passes through the resistive component of the system. Above this frequency range the current is dominated by the capacitive component of the system.

As expected, based on recent DM-SICM studies,[42, 44] at close probe-substrate separations in BM-SICM surface-induced rectification influences the mass-transport of ions, leading to surface-enhanced or diminished ion current values, compared to the bulk to which currents are normalised (Figure 4.2a and b), depending on the substrate charge and the SICM bias polarity. The AC phase shift (which we define throughout as the distance-dependent phase with respect to that with the nanopipette in bulk) is particularly sensitive to the presence of surface charge at the substrate when $\Delta V \neq 0$ (see Figure 4.2c and d), an aspect we explore further below with FEM simulations. The AC amplitude also exhibits a dependence on the substrate surface charge, albeit weaker, seen to be enhanced under the same conditions as the DC enhancement and diminished with decreasing DC values (see Supporting Information, 4.6.3 for AC amplitude approach curves recorded simultaneously with the data in Figure 4.2). Interestingly, although these effects are manifested at low ionic strength, for reasons outlined in the introduction, they can be seen at relatively high ionic strength, up to 0.1 M, even though the magnitude of the effect decreases with increasing concentrations (see Supporting Information 4.6.4 for data). These data have important implications for how topographical SICM experiments are designed (to avoid charge effects), but could also be exploited to allow for the probing of the double layer at biological samples *in vivo*, which require a physiological environment (relatively high ionic strength) for viability. Note that the data are especially significant as we have used a relatively large SICM tip for these studies, and the effects seen at high ionic strength would be magnified with smaller tip sizes deployed at closer sample distances.

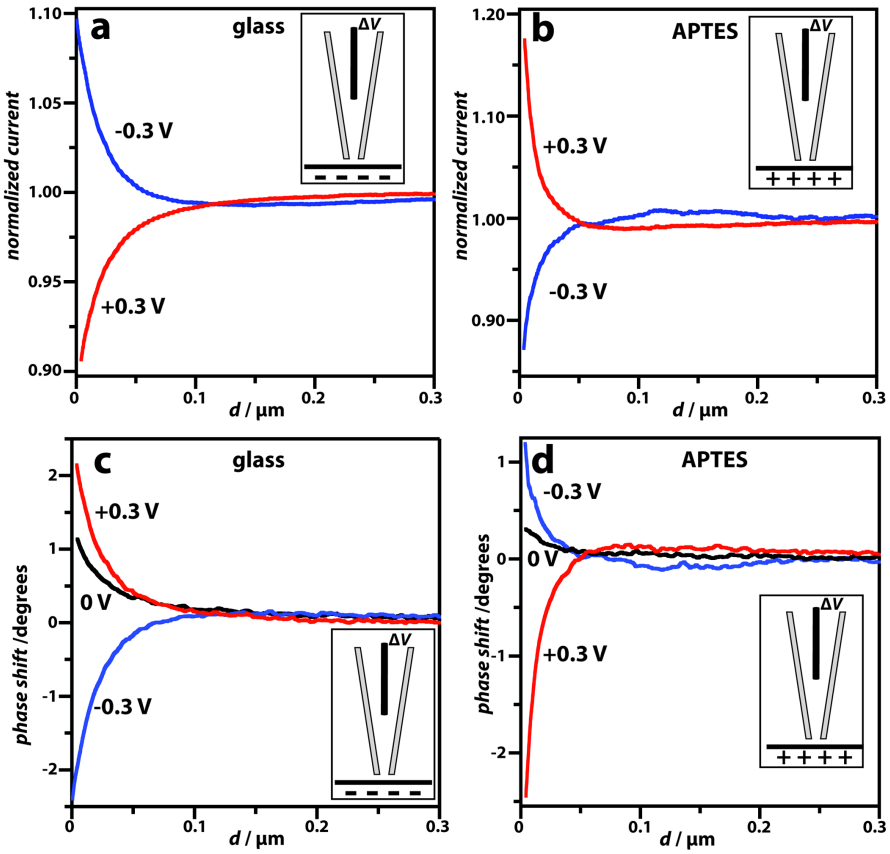


**Figure 4.2.** Experimental approach curves depicting: normalised DC ion current **(a)** and **(b)**; and phase shift **(c)** and **(d)** behaviour as a function of the probe-to-substrate distance, *d*, recorded with *ca.* 75 nm radius nanopipette over negatively charged glass and positively charged APTES substrates at 0.3 V (red lines), -0.3 V (blue lines) and 0 V (black lines) bias offset ($\Delta V$) values. Schematic illustrations, as insets, depict the nanopipette approaching variously charged substrates for the corresponding plots. The DC ionic currents are normalised to the respective values at solution bulk, while the phase shifts are reported with respect to the corresponding bulk values. The DC data at 0 V are not presented, as there is no significant ion flow.

A major observation in Figure 4.2 is that with no mean bias ($\Delta V$ = 0, with just a small amplitude oscillation of the bias between the QRCEs) the phase shift is intrinsically a distance-dependent quantity and is relatively insensitive to surface charge. The phase of the AC current (with respect to the bulk response) shifts slightly positive over both the negatively charged glass substrate and positively charged APTES functionalised substrate (Figure 4.2c and d). In order to account for these AC effects, and to assess BM-SICM for topographical and charge mapping, finite

element simulations were used to study the AC and DC SICM response towards a harmonic perturbation of the electric potential.

### 4.4.2 Theory and Simulations

The simulation of the harmonic perturbation of the DDL due to an applied alternating potential is a complicated task, especially in a nanopore or nanopipette configuration, and a typical treatment of this problem is performed in terms of equivalent electrical circuits.[45, 49] Here, we adopt a more general approach by studying the ionic transport and ion distributions, from which we can derive the resulting impedance response, using finite element method modelling.

Ions are considered as point charges, while ionic transport is assumed to follow the classical Nernst-Planck relationship, where the flux $J_i$ of species, *i,* is given as:

$$J_i = -D_i \nabla c_i - z_i \frac{F}{RT} D_i c_i \nabla \phi \qquad (4.1)$$

while the Poisson equation describes the electrical potential $\phi$:

$$\nabla^2 \phi = -\frac{F}{\varepsilon \varepsilon_0} \sum_i z_i c_i \qquad (4.2)$$

Here $c_i$ denotes the species concentration, while $D_i$, $z_i$, $F$, $R$, $T$, $\varepsilon$ and $\varepsilon_0$ specify constants: system diffusion coefficient of *i*, its charge number, the Faraday constant, gas constant, temperature, relative permittivity and vacuum permittivity, respectively.

Throughout this work a surface charge density on the nanopipette tip was assumed to be -1.125 mC $m^{-2}$ (140 $nm^2$ per ionised site), consistent with previously reported simulations.[40-42, 50, 51] However, the actual density of ionisable sites strongly depends on the nature of the material and could vary within the range of

microcoulombs to a few hundreds of millicoulombs per squared meter of a surface.[42, 52-55]

The system of differential equations (4.1) and (4.2) was solved with appropriate boundary conditions (see section 4.6.1 and Table 4.1, Supporting Information), for a particular $\Delta V$ and assuming flux conservation in a first step (eq. 4.3)

$$\nabla J_i = 0 \tag{4.3}$$

Then, for AC analysis, a harmonic bias modulation was applied between the two QRCEs in the form of a linearised perturbation in the frequency domain

$$\nabla J_i = j\omega c_i \tag{4.4}$$

where $j$ is the imaginary unit and $\omega$ is the angular frequency (full details of the FEM simulations are given in section 4.6.1, Supporting Information).

This approach provides a powerful framework to study the impedance response both in bulk (see for example Figure 4.7, supporting information 4.6.2) and with a nanopipette positioned at different separations from a charged or uncharged substrate. As highlighted earlier in Figure 4.2, the experimental phase shift with zero net bias, $\Delta V = 0$, as a function of distance appeared relatively insensitive to the surface charge, while for an applied bias ($\Delta V \neq 0$) there was a surface-charge dependent phase shift.

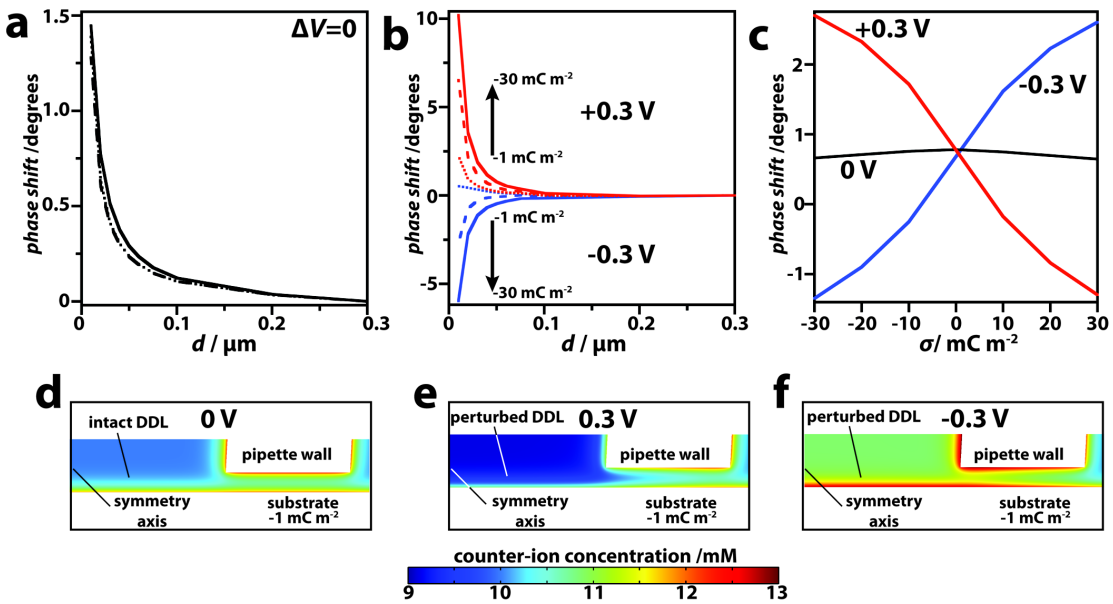


**Figure 4.3. a)** Simulated BM-SICM approach curves in the absence of mean bias offset ($\Delta V$ = 0) at 270 Hz, 10 mV r.m.s. amplitude bias modulation over a substrate carrying surface charge densities, $\sigma$, of 0 (solid), -30 (dotted) and +30 (dashed) mC m$^{-2}$. **b)** A series of simulated approaches towards a negatively charged surface ($\sigma$ values -30 (solid), -10 (dashed) and -1 (dotted) mC m$^{-2}$ with the arrows indicating an increase of the absolute magnitude of the surface charge density) at bias values of +0.3 V (red lines) and -0.3 V (blue lines). **c)** Theoretically predicted values of the phase shift of the ion current passing through a 75 nm radius nanopipette positioned at 25 nm from a charged surface at 0 V, -0.3 V and +0.3 V bias (black, blue and red lines, respectively). **d-f)** Calculated steady-state concentration profiles of DDL counter-ion, for a DC bias only, near a nanopipette tip positioned 10 nm above a charged interface ($\sigma$ = -1 mC m$^{-2}$) at d) 0 V, e) +0.3 V and f) -0.3 V bias. Note that only half of the symmetric nanopipette cross-section is shown.

Figure 4.3a shows simulated approach curves towards substrates with applied surface charge of ± 30 mC m$^{-2}$ (5 nm$^2$ per ionised site) and 0 mC m$^{-2}$. It can be seen that the model predicts the phase shift of the induced harmonic ion current to be almost independent of surface charge when there is no DC bias offset between the QRCEs, similar to the experimental observations in Figure 4.2c and d. This effect has a very important consequence for careful (and accurate) probe positioning over a sample surface, as the phase shift value is an intrinsically sensitive quantity that

evidently depends predominantly on the tip-to-substrate distance when $\Delta V$ = 0. Under these conditions, Figure 4.3a (and Figures 4.2c and 4.2d) make it clear that with $\Delta V$ = 0, the phase shift can be used as a set point for determining topography and being able to position the probe at close tip-to-substrate separations, which is important for enhancing the resolution of SICM.[56, 57]

In a similar way to the experimental approaches at non-zero bias (Figure 4.2), the model predicts a dramatic change of the phase-distance behaviour for $\Delta V \neq 0$. Figure 4.3b depicts theoretically predicted approach curves that demonstrate the sensitivity of the AC phase to surface charge. The AC phase shift can be seen to be negative under conditions when an enhanced ionic current is observed, that is when negative $\Delta V$ is applied to the tip QRCE with a negatively charged substrate. In this case the system resistance, upon approaching the substrate, decreases and so more current flows through the resistive component of the system, resulting in the phase tending more towards 0 degrees, thus explaining the negative phase shift from the bulk value, which is between 0 and 90 degrees (Supporting Information 4.6.2, Figure 4.7). It can further be seen that the magnitude of the effect scales with the surface charge density, as would be expected. As the polarity of the bias is reversed, so that the nanopipette QRCE is positive, the negatively charged substrate now induces a diminution of the ionic current and a positive shift in the phase is observed. In this case, the system resistance increases as the tip approaches, so more current flows through the capacitive component of the system and the phase tends to increase towards 90 degrees. Thus, a positive phase shift from that with the nanopipette in bulk is observed. The simulated DC signal mirrors this behaviour (Supporting Information 4.6.5, Figure 4.10) with the DC current increasing compared to the bulk at close tip-substrate distances (negatively charged substrate) with positive bias on the nanopipette QRCE, but decreasing at negative bias.

From these data it is clear that even a relatively small surface charge (down to 1 mC $m^{-2}$, equivalent to 160 $nm^2$ per ionised site) leads to strong variation of the phase shift with bias, that is particularly noticeable when the probe is brought in close proximity to a substrate (especially, at distances below one tip radius, $d < r_{tip}$). This effect, revealed with an applied bias, can therefore be employed for

mapping surface charge with the nanopipette held at a constant distance above the specimen during scanning, as considered below.

Figure 4.3c shows the phase shift with a 75 nm radius nanopipette positioned 25 nm above a charged substrate, as a function of surface charge density for 3 biases, $\Delta V$ = +0.3 V, 0 V and -0.3 V. The plots clearly illustrate the sensitivity of the technique, at a constant probe-to-substrate distance, to distinguish between values of surface charge. Importantly, at 0 V bias, a wide range of surface charges have little influence on the phase, making this condition ideal for detecting surface topography, as discussed above. The sensitivity (magnitude) of the phase to a particular surface charge is similar at both positive and negative bias polarities, although the technique offers slightly higher sensitivity in cases when surface-induced rectification acts to enhance the ionic current (*e.g.* at negative tip bias over a positively charged surface or at positive tip bias over a negatively charged surface).

The reasons for the striking effect of bias on the phase response (Figures 4.3) and DC current response of BM-SICM (Figure 4.2) with charged surfaces becomes apparent from the distribution of electrical potential and ion concentrations near the tip opening (when held in the proximity of a surface). With a 0 V bias offset there is almost no perturbation of the DDL at the substrate, which remains intact. The application of bias, however, is known to lead to ICR inside the nanopipette itself[39-41] (when it is freely suspended in bulk) and a surface-induced rectification.[44] This causes a drastic change in the nanopipette conductance state depending on bias polarity and surface charge due to a significant change of ionic conductivities (and therefore, the overall resistance) within and near the tip opening (see Figure 4.3e and f for $\Delta V$ values of +0.3 V and -0.3 V, respectively). In turn, the AC ion current components, particularly the phase shift, which are highly sensitive to the overall resistance, as explained above, also demonstrate a strong dependence to the nature of the charged interface.

### 4.4.3 Probing Acid-Base Equilibria at Interfaces

To illustrate the capabilities of BM-SICM for sensing variations of surface charge, a series of approaches towards glass substrates was carried out as a function of bulk pH (surface titration experiments).

The electrostatic charge on glass and silica surfaces is typically attributed to the presence of silanol groups (SiOH) due to the following acid-base equilibrium:

$$\text{-SiOH} \rightleftarrows \text{-SiO}^- + \text{H}^+ \tag{4.5}$$

The dissociation process, however, is rather complicated and depends on the particular type of silica and any surface treatment. In a first approximation, the degree of dissociation depends on the inherent properties of the glass-electrolyte interface (given by the intrinsic dissociation constant, $K_{\text{int}}$) as well as the electrostatic potential on the surface, $\psi_0$:[58]

$$\frac{[H^+]\Gamma_{SiO^-}}{\Gamma_{SiOH}} = K_{\text{int}} \exp\left[\frac{F\psi_0}{RT}\right] \tag{4.6}$$

A broad range of silica interfaces show a p$K_{\text{int}}$ in the range 7 – 7.5[52, 54] and the surface charge density, $\sigma$, can be estimated, using equation (6) along with mass-conservation, which defines the surface concentrations of protonated and deprotonated sites ($\Gamma_{\text{SiOH}}$ and $\Gamma_{\text{SiO-}}$, respectively)

$$\sigma = -e\Gamma_{SiO^-} = -e\Gamma_{total}\frac{K_{\text{int}}10^{pH}\exp\left[\frac{F\psi_0}{RT}\right]}{1+K_{\text{int}}10^{pH}\exp\left[\frac{F\psi_0}{RT}\right]} \tag{4.7}$$

where $\Gamma_{total}$ represents the total number of silanol groups per unit area and $e$ is the elementary charge. The surface potential can be calculated from the Grahame equation (for monovalent electrolyte ions present at $c_0$ bulk concentration):[58]

$$\sigma = \left(8RT\varepsilon\varepsilon_0 c_0\right)^{1/2} \sinh\left[\frac{F\psi_0}{2RT}\right] \qquad (4.8)$$

Solution of equations (4.7) and (4.8) provides the self-consistent surface charge density value. However, surface acid-base equilibria on other types of silica are characterised by two dissociation constants[53, 59] with corresponding p$K_a$ of 4.5 and 8.5. These values are associated with two different types of titratable silanol groups, present at the surface at 19% and 81% of the total number of ionised sites, respectively.[53, 59] The total surface charge density is therefore given through both contributions.

It follows that under ambient conditions (pH ~ 7) a small fraction of silanol groups are ionised, resulting in a negatively charged surface. The experimental approaches of phase shift *vs*. tip to surface distance, *d*, shown in Figure 4.4 for an applied bias $\Delta V$ = -0.3 V to the nanopipette (and the DC data in Figure 4.11, Supporting Information 4.6.6) confirm the presence of a negative surface charge under these conditions, as surface-enhanced rectification induces a significant decrease of the AC phase value (and increase in the DC value, Figure 4.11, Supporting Information 4.6.6), when the nanopipette is brought into the vicinity of the substrate.

In more acidic solutions, increasing protonation of the silanol groups leads to an overall decrease of (absolute) surface charge density. Experimental phase shift-distance approach curves (Figure 4.4) under these conditions (pH = 2.1 – 4.3), reveal a smaller surface-enhanced rectification at lower pH. At pH values around 2.1 – 2.5 the AC phase shift-distance curves approach the behaviour expected at an uncharged interface, in good agreement with a point of zero charge found on most of silica materials (typically, in the pH range 2 – 4).[60] Approach curves shown in Figure 4.4 evidence an almost linear variation of near-surface phase shift with pH over the range studied. Based on our simulations presented above (Figure 4.3c), this behaviour suggests a linear-like titration of surface charges with pH. Dedicated modelling in the future could provide further insight into the protonation of this type of surface, although it needs to be recognised that other processes can complicate the analysis and interpretation. Although the electric field from the SICM probe is in

the kV $cm^{-1}$ range, a field of this magnitude is unlikely to induce changes in the local acid disassociation constants, as the Wein effect occurs at hundreds of kV $cm^{-1}$.[61-63] However local ion mobilities, particularly of protons at surfaces,[64, 65] maybe high and would need to be taken into account, with the tip-induced field possibly altering local pH values.

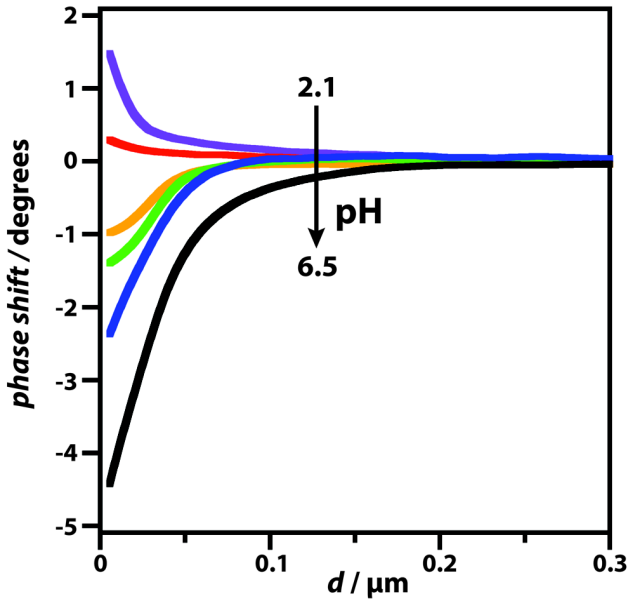


**Figure 4.4.** Experimental approach curves recorded with *ca.* 75 nm radius nanopipettes over a glass substrate at different solution pH (2.1, 2.5, 3.3, 3.7, 4.3 and 6.5 for purple, red, orange, green, blue and black lines, respectively) performed with a bias, $\Delta V$ = -0.3 V applied to the nanopipette QRCE with respect to that in bulk solution. The arrow indicates an increase of the solution pH.

### 4.4.4 Surface Charge Mapping

Simultaneous mapping of surface charge distributions along with independent recording of surface topography is a particular advantage of the SICM technique described herein: an AC phase shift at 0 V mean bias can be used for a positionable feedback control, whereas measurements at $\Delta V \neq 0$ allow the detection of surface charge. We implemented this concept using a hopping voltammetric scan strategy, where the nanopipette was approached towards the substrate until a set value of a feedback parameter (phase shift, 0.5° used herein) was reached, followed by the recording of a cyclic voltammogram at that position (for which we present the linear part between -0.4 and 0.4 V) to sense the charge. The probe was then moved away

from the surface and to the next pixel such that a spatial array of voltammograms was recorded. At each pixel, a voltammogram was recorded when the probe was away from the surface ($d$ = 500 nm) and this response was subtracted from the surface voltammogram to reveal only the surface ICR. Examples of bias-dependent phase responses close to glass, polystyrene and in bulk are given in Supporting Information, section 4.6.7.

The capability of this approach was validated for a partial polystyrene film on a glass substrate, comprising heterogeneously distributed pinholes (exposing the glass) in the polystyrene layer. This substrate thus comprised both negatively charged glass regions, in 10 mM KCl solution, and neutral areas (uncharged polymer film). The topography recorded from the initial approaches to the substrate at $\Delta V = 0$ is shown in Figure 4.5a. This matches well to the typical topography recorded using AFM (Figure 4.5b). Taking into account the working distance (given by the set point value, corresponding to *ca*. 25 nm), SICM allows careful examination of substrate topography independently of surface charge. Even the smaller nanoscale pits in the film are apparent in the BM-SICM topography, an advance on our recent DM-SICM studies[44] in terms of resolution.

Significantly, the protocol used produces voltammetric data that can be represented as 81 image frames (phase and DC as a function of x, y position) at a set of different bias values at 10 mV intervals. Maps of the DC current at the surface, normalised by that in bulk, and AC phase shift at the surface with respect to bulk (subtracted) at -0.3 V and 0.3 V are presented in Figure 4.5c – f. These images, free from topographical effects, are highly revealing of the charge distribution across the surface, which is evidently very heterogeneous, from both the DC current and phase maps. In particular, it can be seen that there is an increase in the ion current magnitude, when a higher conductance state is formed. That is, with a negative tip bias applied to the nanopipette over negatively charged regions (Figure 4.5c), where the normalised current magnitude ratio attains values between 1.1 and 1.2; or current diminution with positive tip bias in negatively charged regions where the normalised current attains values <0.8 (Figure 4.5e).

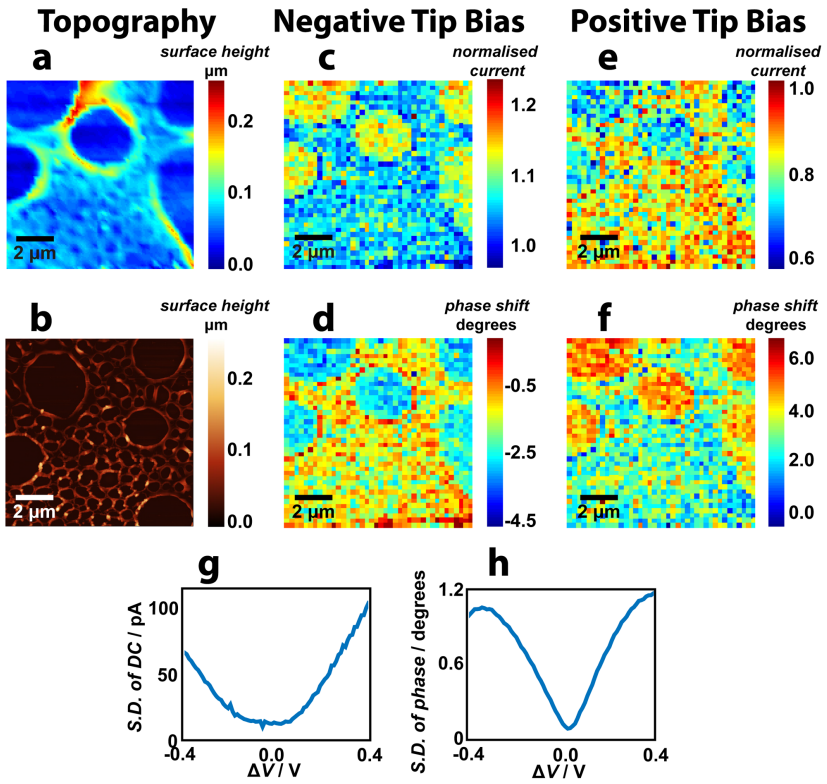


**Figure 4.5.** Simultaneous surface charge and topographical mapping over a non-uniform polystyrene film on glass. **a)** Topography image recorded with a ~75 nm radius nanopipette operated in a hopping mode at 0 V bias offset and **b)** an AFM image of a similar area of a substrate. **c)**-**f)** Example images of the normalised DC component and AC phase shift (with the response in bulk subtracted) of the ion current at -0.3 V and +0.3 V mean bias values. Standard deviation of **g)** ion currents and **h)** bulk-corrected AC phase shift calculated across each image in a set of image frames acquired at 81 equally spaced bias values over the linear region scanned between -0.4 and +0.4 V.

The corresponding phase behaviour (Figures 4.5d and f) shows the interfacial charge effect with stronger contrast due to the fact that any change in the resistance is detected as a change in the ratio between the capacitive and resistive behaviour of the nanopipette (and better signal to noise due to measurement with the lock-in amplifier). When the nanopipette experiences a low conductance state, the capacitance provides a larger contribution, which ideally has 90 degrees phase shift

with respect to the driving voltage, while at a high conductance state a nanopipette acts more like as a resistor (0 degrees phase shift for resistor circuit component).

The change of the conductance state of the nanopipette is also seen in voltammograms recorded at each pixel during imaging. As follows from the image sequences (see Supporting Information Figure 4.12), the AC phase shift flips from negative to positive as the bias ($\Delta V$) is scanned from negative to positive values through 0 V. With the bias ca. 0 V, however, the phase signal across both the glass and polystyrene regions of the sample is close to the set point value because of the insensitivity of the phase to surface charge when $\Delta V$ = 0, a key feature of this technique that we have described.

These data allow the standard deviation of every pixel value of each DC and phase image in the sequence to be calculated, with results shown in Figures 4.5g and h. It is clear that around $\Delta V$ = 0, the images are relatively featureless (small standard deviation), but increase with a higher magnitude of applied potential, consistent with the greater contrast between the heterogeneously charged regions seen at ± 0.3 V. Interestingly, the region where the standard deviation attains a minimum is relatively broad (-0.2 V – 0.1 V) for the DC signal, highlighting the lower sensitivity of the DC signal (Figure 4.5g) towards surface charge compared to the AC phase signal (Figure 4.5h), where the minimum of the standard deviation *vs*. potential plot is much sharper.

## 4.5 Conclusions

This work provides a robust framework for nanoscale mapping of surface charge variations at substrates through sensing the ionic atmosphere of the diffuse double layers formed at interfaces with a simple nanopipette approach. We have explored the versatility of bias-modulated SICM for independent and accurate characterisation of the topographical and charge properties of surfaces, using the capability of BM-SICM for performing experiments in the absence of a mean applied bias. In this situation, the nanopipette can be carefully positioned over the sample at a desired distance, using a set point value of the AC phase shift of the ionic current,

which is shown to be a distance-dependent quantity, essentially unaffected by surface charge that makes it ideal for topographical mapping.

At non-zero bias, however, BM-SICM becomes an extremely sensitive tool for probing surface charge *via* surface-induced rectification. Our experimental findings, supported by finite element simulations, suggest that AC components of the ionic current, and, in particular, the phase shift are very responsive to the local resistance and, correspondingly, variations in surface charge. The possibility of imaging heterogeneities of surface charge makes this technique indispensable for surface science, to unravel structure-functional relationships and to provide insights on interfacial processes and adsorption equilibria that modify the charge. Here, we have been able to resolve topography, free from surface-charge effects, and obtain semi-quantitative insights into surface charge. Further quantitative analysis will require extremely detailed characterisation of tip geometry and charge (which is often not the precise conical shape assumed in this and other work), and the charge/ICR characteristics of the nanopipette itself, as well as considerations of changes in ion mobility near surfaces. For future studies, transmission electron microscopy of glass nanopipettes[66] should allow better understanding of the probe geometry and, in perspective, this nanopipette approach should offer detailed quantification of surface charges.

## 4.6 Supporting Information

### 4.6.1 FEM model details

A schematic representation (not to scale) of the two-dimensional axisymmetric (FEM) model is depicted in Figure 4.6a, showing the tip of a nanopipette, with $r_0$ = 75 nm radius, with a half-cone angle $\alpha = 2.3^{o}$ and wall thickness $w$ = 50 nm (similar to that used herein) for all simulations. The geometrical parameters of the nanopipette probe were extracted from corresponding SEM images (see Figure 4.6b). In order to eliminate effects of the domain size on the numerical results, a relatively large section of the pipette (200 μm long) was simulated in a square domain (160 μm × 160 μm) of the axisymmetric geometry representing solution bulk.

The numerical model was constructed in the Comsol Multiphysics (v4.4) software package, using the "Transport of diluted species" and "Electrostatics" modules. Electrical properties of the bulk materials, water and borosilicate glass, were simulated through their respective dielectric constants (78 and 4.7, respectively). The electrostatic charge on the pipette walls was assumed to be constant in the simulations, with a surface charge density value of -1.125 mC $m^{-2}$ as in previous work,[40,42,44] while the charge on the substrate was varied. The set of boundary conditions is summarised in Table 4.1.

**Table 4.1.** Summarised boundary conditions for the FEM model.

| **Boundary** | **Concentration condition** | **Potential/charge condition** |
|---|---|---|
| **B1** | $c_i = c_{0,i}$ | $V = V_{DC} + V_{AC}$ |
| **B2** | $J_i = 0$ | $V = 0$ |
| **B3** | $c_i = c_{0,i}$ | $V = 0$ |
| **B4** | $J_i = 0$ | $\sigma$ = -1.125 mC $m^{-2}$ |
| **B5** | $J_i = 0$ | $\sigma = \sigma_{substrate}$ |

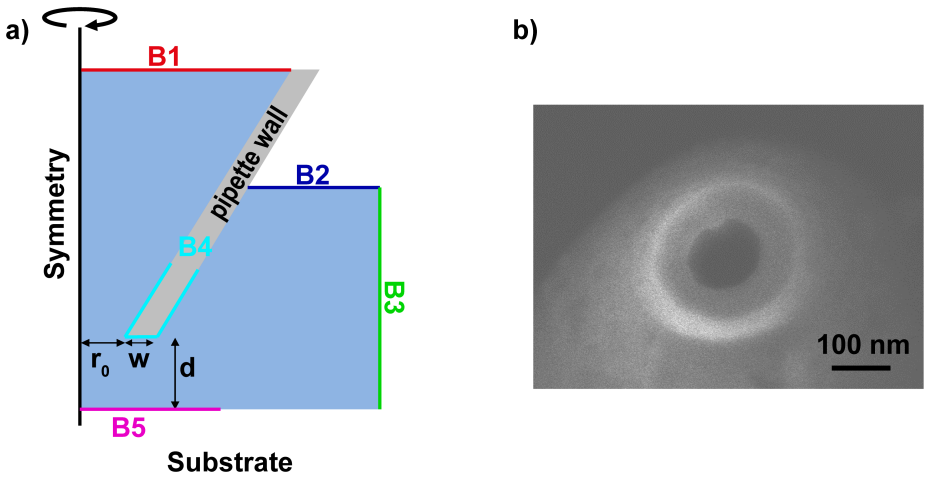


**Figure 4.6. a)** Representation of the 2D axisymmetric FEM model of a nanopipette at a distance, *d*, from a substrate. **b)** SEM micrograph showing the end of a typical nanopipette probe.

### 4.6.2 Impedance measurements

To ensure adequacy of the numerical description of both the DC and AC characteristics of the system, the simulation results were compared to experimental impedance measurements of the nanopipette suspended in bulk solution.

Impedance spectra at different frequencies (0.1 Hz – 100 kHz) were acquired in 10 mM KCl solutions in a two-electrode cell configuration. As evident from Figure 4.7a and b, depicting experimental and theoretical Nyquist and Bode plots, experimental measurements are very well correlated with predictions from numerical modelling.

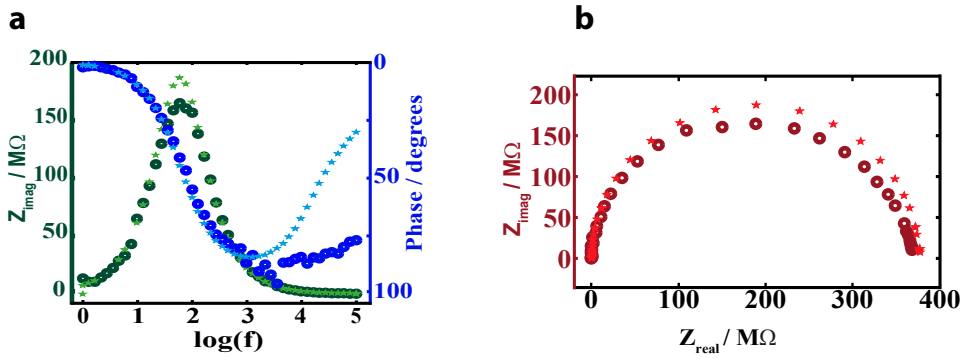


**Figure 4.7.** Comparison between experimental (stars) and FEM calculated impedance response of the nanopipette (circles), in the form of Bode **(a)** and Nyquist **(b)** plots. Note that the axes in **(a)** are coloured on the graph on the Bode plots in accordance with the graph line colours.

### 4.6.3 Typical AC amplitude approach curves

The amplitude of AC current is recorded along with the AC phase shift and DC ion current components. The ionic current is quite sensitive to the presence of surface charge, but the magnitude of AC current is relatively small due to the small driving voltage oscillation. Typical AC amplitude approach curves to glass, corresponding with the DC and AC phase data presented in Figure 4.2a and c (in the main manuscript) are presented in Figure 4.8. The shape of these approaches can be seen to correlate with the shape of the DC approach curves, increasing with negative tip bias and decreasing at positive tip bias, upon approach to a negatively charged substrate such as glass.

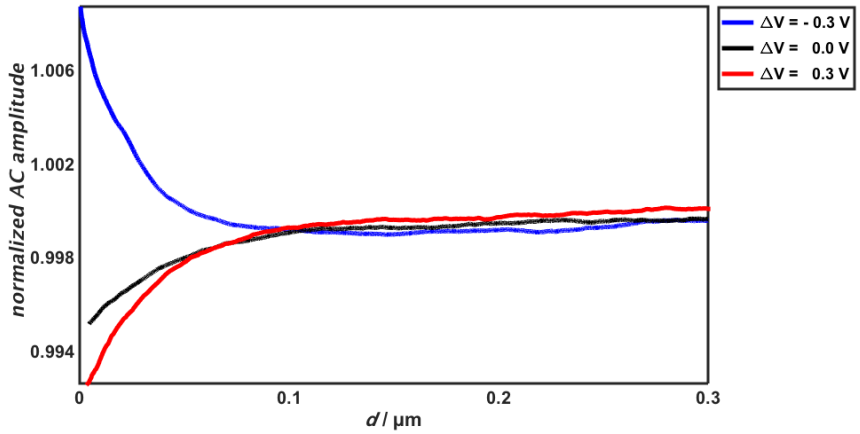


**Figure 4.8.** Typical BM-SICM AC amplitude approach curve to negatively charged glass substrate at different potentials (-0.3, 0 and +0.3 V bias for blue, black and red lines, respectively).

### 4.6.4 Approach curves in electrolytes of high ionic strength

Approaches performed at electrolyte with higher salt concentration, with negative tip bias towards a negatively charged glass substrate, show that even at 100 mM (Figure 4.9), at very small tip-substrate separations, the DC and AC ion components are still sensitive to surface charge. This indicates that special care has to be taken when SICM is implemented for recording substrate topography as it can be potentially convoluted with the surface charge. This may particularly be the case for nanoscale pipettes (*e.g.* <30 nm diameter)[32,48] where charge effects will be magnified. As discussed in the main text, whilst this may be a problem in a traditional SICM arrangement, when the surface is approached at 0 V net bias, using BM-SICM, this effect is minimised and the topography can be accurately tracked.

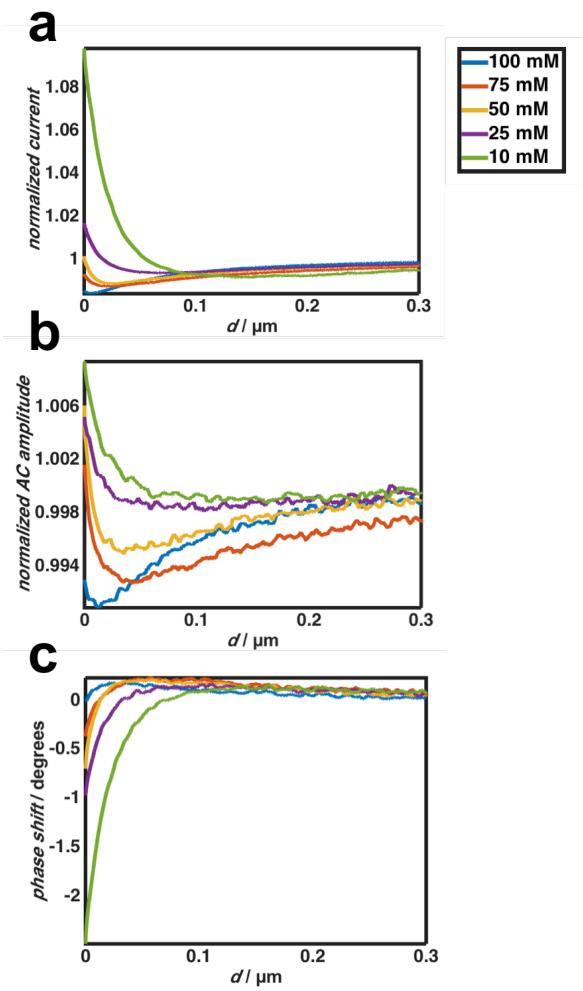


**Figure 4.9. a)** Normalised DC ion current, **(b)** normalised AC amplitude and **(c)** relative phase shift acquired with ca. 75 nm radius nanopipette probe during BM-SICM approaches to a negatively charged glass substrate with -0.3 V tip bias and varying supporting electrolyte concentrations. Green, purple, yellow, red and blue curves correspond to 10, 25, 50, 75 and 100 mM KCl (see also the legend on the figure).

### 4.6.5 Theoretical DC approach curves

Theoretical AC phase shift approach curves have been presented in the main text (Figure 4.3). The corresponding DC approach curves are presented here (Figure 4.10). These show enhanced current in the conditions where the AC phase was seen to decrease and agree with the trends observed in the experimental DC approach data, presented in this work (Figure 4.2 of main text). The DC ionic current is also sensitive to the presence of the DDL on the tip and substrate, resulting in an

enhanced current upon approach to a significantly negatively charged substrate with a negative tip bias.

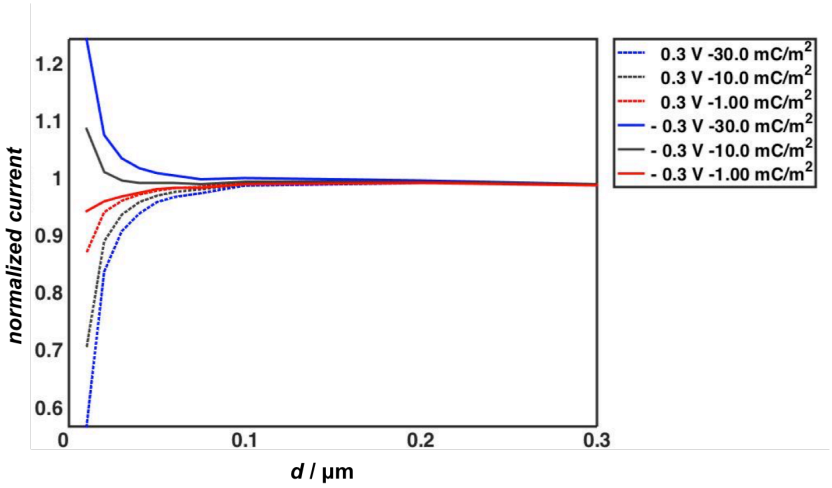


**Figure 4.10.** Simulated DC approach curves to negatively charged substrates at positive and negative tip bias (see the legend for the description of colour code).

### 4.6.6 Approach curves at varying pH

Sensing surface charge at varying pH conditions is described in the main manuscript (Figure 4.5). Here the DC and AC components of the theoretical and experimental data are shown (Figure 4.11).

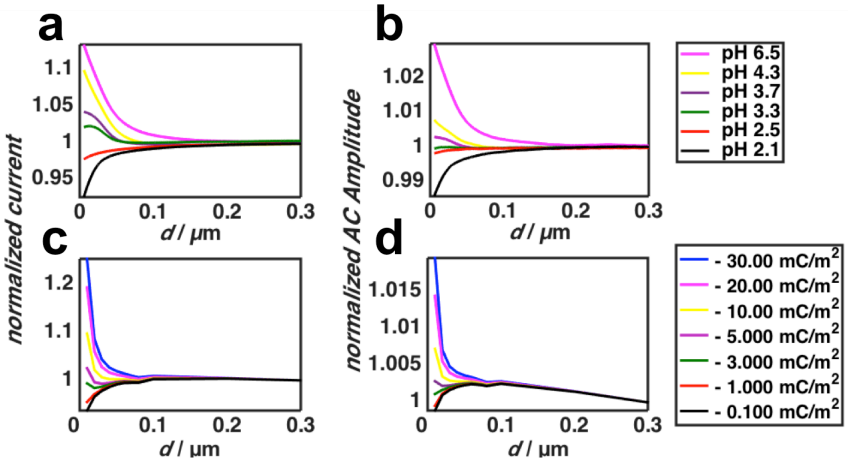


**Figure 4.11.** Experimental DC **(a)** and AC amplitude **(b)** and theoretical DC **(c)** and AC amplitude **(d)** approach curves to a glass substrate bathed in solutions of varying pH (see the legend for the colour code on the graphs).

### 4.6.7 Experimental phase-voltage curves

Rectification of the AC current, particularly the phase, appears to be very beneficial for ion sensing within the DDL of a surface. Phase-bias curves shown on Figure 4.12a can provide a "fingerprint" of surface-induced rectification in a similar way that current-voltage curves are used to characterise ICR in nanostructures.[40,41,51] The charge state of the substrate clearly plays a key role in the rectifying characteristics. The curves for bulk solution and over an uncharged polystyrene film are very similar, proving the absence of surface charge on a polystyrene surface. The intrinsic rectifying properties of the glass nanopipette lead to slight rectification (as manifested in the phase shift change with $\Delta V$) but this is independent of the tip-substrate separation over polystyrene. In contrast, there is considerable surface-induced rectification with the nanopipette over glass, consistent with the presence of negative charge (see main text).

Recorded voltammograms in bulk solution allow for the subtraction of the rectifying behaviour of the probe itself from the measurement at surface proximity (as used to present the imaging data). As evident from Figure 4.12b, in such a case, the neutral polystyrene substrate exhibits almost no surface-driven ICR. In the case of a charged surface, *e.g.* glass, the effect of the surface-induced rectification is clear in the phase-bias response.

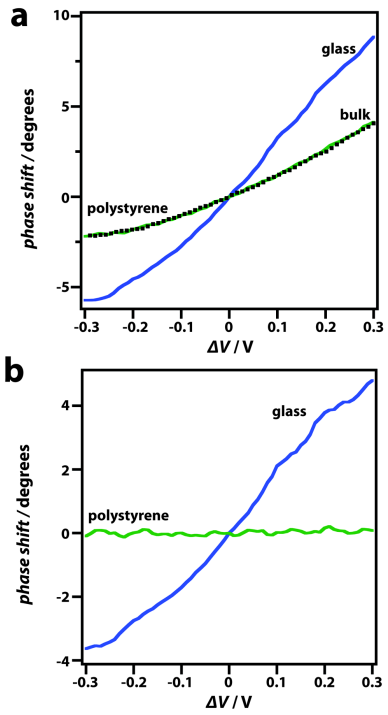


**Figure 4.12. a)** Experimental phase shift-voltage characteristics of a nanopipette (75 nm radius) in a bulk solution (black dotted line), and positioned over an uncharged polystyrene film (green solid line) and negatively charged glass (blue solid line). **b)** Phase shift – voltage curves near polystyrene and glass with bulk data subtracted.

## 4.7 References


1. Sahın, Ö.; Nusret Bulutcu, A. *J. Cryst. Growth* **2002**, *241*, 471-480.
2. Lin, N. H.; Shih, W.-Y.; Lyster, E.; Cohen, Y. *J. Colloid Interface Sci.* **2011**, *356*, 790-797.
3. Bodhak, S.; Bose, S.; Bandyopadhyay, A. *Acta Biomater.* **2009**, *5*, 2178-2188.
4. Hirsch, V.; Kinnear, C.; Moniatte, M.; Rothen-Rutishauser, B.; Clift, M. J. D.; Fink, A. *Nanoscale* **2013**, *5*, 3723-3732.
5. Chan, D. Y.; Pashley, R. M.; White, L. R. *J. Colloid Interface Sci.* **1980**, *77*, 283-285.
6. Ohshima, H.; Healy, T. W.; White, L. R. *J. Colloid Interface Sci.* **1982**, *90*, 17-26.
7. Tufenkji, N.; Elimelech, M. *Langmuir* **2005**, *21*, 841-852.
8. Cuesta, A. *Surf. Sci.* **2004**, *572*, 11-22.
9. Manzini, M. C.; Perez, K. R.; Riske, K. A.; Bozelli Jr, J. C.; Santos, T. L.; da Silva, M. A.; Saraiva, G. K. V.; Politi, M. J.; Valente, A. P.; Almeida, F. C. L.*, et al*. *Biochim. Biophys. Acta, Biomembr.* **2014**, *1838*, 1985-1999.

10. Chen, L.; Mccrate, J. M.; Lee, J. C.; Li, H. *Nanotechnology* **2011**, *22*, 105708.

11. Chung, T.-H.; Wu, S.-H.; Yao, M.; Lu, C.-W.; Lin, Y.-S.; Hung, Y.; Mou, C.-Y.; Chen, Y.-C.; Huang, D.-M. *Biomaterials* **2007**, *28*, 2959-2966.

12. Xiao, K.; Li, Y.; Luo, J.; Lee, J. S.; Xiao, W.; Gonik, A. M.; Agarwal, R. G.; Lam, K. S. *Biomaterials* **2011**, *32*, 3435-3446.

13. Dobrovolskaia, M. A.; Patri, A. K.; Simak, J.; Hall, J. B.; Semberova, J.; De Paoli Lacerda, S. H.; McNeil, S. E. *Mol. Pharmaceutics* **2011**, *9*, 382-393.

14. Asati, A.; Santra, S.; Kaittanis, C.; Perez, J. M. *ACS Nano* **2010**, *4*, 5321-5331.

15. Ghosh, P. S.; Kim, C.-K.; Han, G.; Forbes, N. S.; Rotello, V. M. *ACS Nano* **2008**, *2*, 2213-2218.

16. Bakhti, M.; Snaidero, N.; Schneider, D.; Aggarwal, S.; Möbius, W.; Janshoff, A.; Eckhardt, M.; Nave, K.-A.; Simons, M. *Proc. Natl. Acad. Sci. U. S. A.* **2013**, *110*, 3143-3148.

17. Arjmandi, N.; Van Roy, W.; Lagae, L.; Borghs, G. *Anal. Chem.* **2012**, *84*, 8490-8496.

18. Sprycha, R. *J. Colloid Interface Sci.* **1989**, *127*, 1-11.

19. Szekeres, M.; Tombácz, E. *Colloids Surf., A* **2012**, *414*, 302-313.

20. Gibson, G. T. T.; Mohamed, M. F.; Neverov, A. A.; Brown, R. S. *Inorg. Chem.* **2006**, *45*, 7891-7902.

21. Sánchez, J.; del Valle, M. *Crit. Rev. Anal. Chem.* **2005**, *35*, 15-29.

22. Heinz, W. F.; Hoh, J. H. *Biophys. J.* **1999**, *76*, 528-538.

23. Miyatani, T.; Okamoto, S.; Rosa, A.; Marti, O.; Fujihira, M. *Appl. Phys. A Mater. Sci. Process.* **1998**, *66*, S349-S352.

24. Miyatani, T.; Horii, M.; Rosa, A.; Fujihira, M.; Marti, O. *Appl. Phys. Lett.* **1997**, *71*, 2632-2634.

25. Hillier, A. C.; Kim, S.; Bard, A. J. *J. Phys. Chem.* **1996**, *100*, 18808-18817.

26. Manne, S.; Cleveland, J.; Gaub, H.; Stucky, G.; Hansma, P. *Langmuir* **1994**, *10*, 4409-4413.

27. Chen, C. C.; Zhou, Y.; Baker, L. A. *Annu. Rev. Anal. Chem.* **2012**, *5*, 207-28.

28. Happel, P.; Thatenhorst, D.; Dietzel, I. D. *Sensors* **2012**, *12*, 14983.

29. Rheinlaender, J.; Geisse, N. A.; Proksch, R.; Schäffer, T. E. *Langmuir* **2010**, *27*, 697-704.

30. Shevchuk, A. I.; Gorelik, J.; Harding, S. E.; Lab, M. J.; Klenerman, D.; Korchev, Y. E. *Biophys. J.* **2001**, *81*, 1759-1764.

31. Hansma, P.; Drake, B.; Marti, O.; Gould, S.; Prater, C. *Science* **1989**, *243*, 641-643.

32. Novak, P.; Li, C.; Shevchuk, A. I.; Stepanyan, R.; Caldwell, M.; Hughes, S.; Smart, T. G.; Gorelik, J.; Ostanin, V. P.; Lab, M. J. *Nat. Methods* **2009**, *6*, 279-281.

33. Korchev, Y.; Milovanovic, M.; Bashford, C.; Bennett, D.; Sviderskaya, E.; Vodyanoy, I.; Lab, M. *J. Microsc.* **1997**, *188*, 17-23.

34. Ushiki, T.; Nakajima, M.; Choi, M.; Cho, S.-J.; Iwata, F. *Micron* **2012**, *43*, 1390-1398.

35. Yang, X.; Liu, X.; Zhang, X.; Lu, H.; Zhang, J.; Zhang, Y. *Ultramicroscopy* **2011**, *111*, 1417-1422.

36. Takahashi, Y.; Murakami, Y.; Nagamine, K.; Shiku, H.; Aoyagi, S.; Yasukawa, T.; Kanzaki, M.; Matsue, T. *Phys. Chem. Chem. Phys.* **2010**, *12*, 10012-10017.

37. Klenerman, D.; Korchev, Y. E.; Davis, S. J. *Curr. Opin. Chem. Biol.* **2011**, *15*, 696-703.

38. Bard, A. J.; Faulkner, L. R. *Electrochemical Methods: Fundamentals and Applications*. Wiley New York: 1980; Vol. 2.

39. Wei, C.; Bard, A. J.; Feldberg, S. W. *Anal. Chem.* **1997**, *69*, 4627-4633.

40. Momotenko, D.; Cortes-Salazar, F.; Josserand, J.; Liu, S.; Shao, Y.; Girault, H. H. Ion *Phys. Chem. Chem. Phys.* **2011**, *13*, 5430-5440.

41. White, H. S.; Bund, A. *Langmuir* **2008**, *24*, 2212-2218.

42. Sa, N.; Lan, W.-J.; Shi, W.; Baker, L. A. *ACS Nano* **2013**, *7*, 11272-11282.

43. Clarke, R. W.; Zhukov, A.; Richards, O.; Johnson, N.; Ostanin, V.; Klenerman, D. *J. Am. Chem. Soc.* **2013**, *135*, 322-9.

44. McKelvey, K.; Kinnear, S. L.; Perry, D.; Momotenko, D.; Unwin, P. R. *J. Am. Chem. Soc.* **2014**,*136*, 13735-44.

45. McKelvey, K.; Perry, D.; Byers, J. C.; Colburn, A. W.; Unwin, P. R. *Anal. Chem.* **2014**, *86*, 3639-46.

46. Sa, N.; Baker, L. A. *J. Am. Chem. Soc.* **2011**, *133*, 10398-10401.

47. Siwy, Z.; Heins, E.; Harrell, C. C.; Kohli, P.; Martin, C. R. *J. Am. Chem. Soc.* **2004**, *126*, 10850-10851.

48. Shevchuk, A. I.; Frolenkov, G. I.; Sánchez, D.; James, P. S.; Freedman, N.; Lab, M. J.; Jones, R.; Klenerman, D.; Korchev, Y. E. *Angew. Chem. Int. Ed.* **2006**, *118*, 2270-2274.

49. Feng, J.; Liu, J.; Wu, B.; Wang, G. *Anal. Chem.* **2010**, *82*, 4520-4528.

50. Sa, N.; Baker, L. A. *J. Electrochem. Soc.* **2013**, *160*, H376-H381.

51. Kubeil, C.; Bund, A. *J. Phys. Chem. C* **2011**, *115*, 7866-7873.

52. Behrens, S. H.; Grier, D. G. *J. Chem. Phys* **2001**, *115*, 6716-6721.

53. Fisk, J. D.; Batten, R.; Jones, G.; O'Reill, J. P.; Shaw, A. M. *J. Phys. Chem. B* **2005**, *109*, 14475-14480.

54. Sabia, R.; Ukrainczyk, L. *J. Non-Cryst. Solids* **2000**, *277*, 1-9.

55. Zhuravlev, L. *Langmuir* **1987**, *3*, 316-318.

56. Weber, A. E.; Baker, L. A. *J. Electrochem. Soc.* **2014**, *161*, H924-H929.

57. Edwards, M. A.; Williams, C. G.; Whitworth, A. L.; Unwin, P. R. *Anal. Chem.* **2009**, *81*, 4482-4492.

58. Stumm, W.; Morgan, J. J. *Aquatic Chemistry: Chemical Equilibria and Rates in Natural Waters*. John Wiley & Sons: 2012; Vol. 126.

59. Powell, H. V.; Schnippering, M.; Mazurenka, M.; Macpherson, J. V.; Mackenzie, S. R.; Unwin, P. R. *Langmuir* **2008**, *25*, 248-255.

60. Papirer, E. *Adsorption on Silica Surfaces*. CRC Press: 2000.

61. Eckstrom, H. C.; Schmelzer, C. *Chem. Rev.* **1939**, *24*, 367-414.

62. Onsager, L.; Kim, S. K. *J. Phys. Chem.* **1957**, *61*, 198-215.

63. Onsager, L. *J. Chem. Phys* **1934**, *2*, 599-615.

64. Slevin, C. J.; Unwin, P. R. *J. Am. Chem. Soc.* **2000**, *122*, 2597-2602.

65. Lockwood, G. K.; Garofalini, S. H. *J. Phys. Chem. C* **2014,** *118*, 29750-29759.

66. Zhou, L.; Zhou, Y.; Baker, L. A. *Electrochemical Soc. Interface* **2014**, *27*, 47-52.

67. Nadappuram, B. P.; McKelvey, K.; Al Botros, R.; Colburn, A. W.; Unwin, P. R. *Anal. Chem.* **2013**, *85*, 8070-8074.

# Chapter 5. Characterisation of Nanopipettes

In the previous chapters, the capability of SICM for performing surface charge mapping was revealed with both experiments and FEM simulations revealing that SICM is well equipped for mapping heterogeneous surface charge on substrates as well as unambiguously mapping surface topography. Whilst FEM simulations performed thus far have shown that SICM is sensitive to surface charge with an applied bias and insensitive when no net bias is applied, quantification of surface charges and the SICM response to date has been challenging. As outlined above, the characterisation of the nanopipette geometry has not proven sufficient. In order to use FEM simulations to quantify the surface charge of the substrate, the geometrical and surface properties of the nanopipette itself must first be known.

This chapter contains the article published in *Analytical Chemistry* that outlines a new protocol for the characterisation of nanopipettes used in the SICM configuration that allows for FEM simulations to model the nanopipette probe more fully, thus allowing for the SICM response to be quantified both in bulk and in the presence of a charged substrate. Briefly this involves using transmission electron microscopy to obtain the geometric properties of the nanopipette before using FEM simulations to obtain the surface charge of the nanopipette walls required to match the bulk nanopipette current-voltage response. Furthermore, it is then shown that by achieving this, it becomes possible to quantify the surface charge of substrates. In this work all experiments, analytical calculations and FEM simulations were performed by myself as well as all of the manuscript preparation. Robert A. Lazenby and Minkyung Kang were responsible for obtaining the TEM images which were analysed by myself.

# Characterization of Nanopipettes

David Perry,[1,2] Dmitry Momotenko,[1] Robert A. Lazenby,[1] Minkyung Kang[1] and Patrick R. Unwin[1,*]

[1]Department of Chemistry, [2]MOAC Doctoral Training Centre, University of Warwick, Coventry, CV4 7AL, United Kingdom

***Corresponding Author**

p.r.unwin@warwick.ac.uk

## 5.1 Abstract

Nanopipettes are widely used in electrochemical and analytical techniques as tools for sizing, sequencing, sensing, delivery and imaging. For all of these applications, the response of a nanopipette is strongly affected by its geometry and surface chemistry. As the size of nanopipettes becomes smaller, precise geometric characterisation is increasingly important, especially if nanopipette probes are to be used for quantitative studies and analysis. This contribution highlights the combination of data from voltage-scanning ion conductivity experiments, transmission electron microscopy (TEM) and finite element method (FEM) simulations to fully characterise nanopipette geometry and surface charge characteristics, with an accuracy not achievable using existing approaches. Indeed, it is shown that presently used methods for nanopipette characterisation can lead to highly erroneous information on nanopipettes. The new approach to characterisation further facilitates high-level quantification of the behaviour of nanopipettes in electrochemical systems, as demonstrated herein for a scanning ion conductance microscope (SICM) setup.

## 5.2 Introduction

Nanopipettes are becoming increasingly important tools across nanoscience for their functional versatility and ease of fabrication.[1] Typically fabricated from glass (*e.g.* borosilicate) or quartz capillaries, nanopipettes are produced through the application of heat whilst a pulling force is applied to each end of the capillary. By adjusting the pulling parameters, the probe geometry can be finely tuned and it is possible to produce probes with opening diameters as low as tens of nanometers.[2, 3] While the simplest nanopipettes contain just a single channel, multichannel devices are also possible, which increases the versatility of nanopipettes for nanoscience applications.[4, 5] The channels can be open[5, 6] (filled with electrolyte and a control electrode) or functionalised with deposited carbon, for example, to produce ultramicroelectrodes (UMEs)[7, 8] that can also be further functionalised[9-11] to tune the sensory properties. Nanoelectrodes can also be fabricated by electrochemically plating nanopipettes with a variety of different metals.[12]

Applications of nanopipettes include as tools for sizing, counting,[13-17] and sequencing of single particles or molecules.[18-20] These applications use the changes in ionic current through the end of the nanopipette (with an applied bias), as a single entity passes through the end of the probe, to provide diagnostic information. Furthermore, these probes constitute powerful tools for the delivery of molecules, including drugs and other stimuli,[16, 21, 22] to surfaces and interfaces. Nanopipettes have also been used as chemical sensors, detecting, for example, pH,[9] sodium,[23] potassium[24] and other ions as well as dopamine[25] and DNA molecules.[16, 18, 26] Recently, the capability of using functionalised nanopipettes for single molecule electrochemical detection has been revealed.[27] Beyond electroanalysis, nanopipettes are finding novel applications as devices for electrospray mass-spectrometry.[28, 29]

Nanopipette probes, employed in different types of scanning probe microscopy (SPM) techniques,[5, 11, 30] are used increasingly for the study of interfacial properties across a range of materials including electrodes and living cells.[3, 31, 32] Examples of SPM techniques that can employ nanopipettes include scanning electrochemical microscopy (SECM),[30, 33] scanning ion conductance microscopy (SICM),[31, 34-38] SICM-SECM[9, 39] and scanning electrochemical cell microscopy

(SECCM).[5, 40] Beyond the surface or interface being investigated, the size, shape and surface properties of the nanopipette may also strongly influence the SPM response, such that robust theoretical models, underpinned by a complete knowledge of the nanopipette characteristics, are needed for quantitative analysis.

This work concerns the procedure for the characterisation of nanopipettes filled with electrolyte solution, which is the main configuration for the wide range of applications above. Although the focus is on single barrelled nanopipettes, and their use in bulk solution and SICM, the approach described could be extended to multi-barrelled nanopipettes[4, 10] and other SPM configurations.[5, 9] For SPM applications, it is important to know the geometry of a nanopipette, specifically the aperture size, the inner pipette half cone angle and the thickness of the glass, because this plays a significant role in the probe response. In particular, the size of the nanopipette opening typically determines the image resolution (estimated to be about $3r_o$ where $r_o$ is the radius of the pipette opening),[35, 41] whilst the thickness of the nanopipette walls at the opening can affect how the nanopipette responds upon approach to interfaces of different topographies.[35, 42] Herein, we utilise transmission electron microscopy (TEM) to obtain the nanopipette geometry with high precision and complementary finite element method (FEM) simulations allow us to match ionic current signals under an applied bias with theory. This provides information on the mass transport characteristics with high accuracy. Experimental measurements and FEM simulations further allow the characterisation of nanopipette surface charge, which is integral to quantitative surface charge mapping using SICM,[43-46] and is expected to be important in sizing applications.[47, 48]

## 5.3 Materials and Methods

### 5.3.1 Nanopipette Probes

Nanopipettes were pulled from either quartz capillaries (o.d. 1 mm, i.d. 0.5 mm, Friedrich & Dimmock, pulling parameters: Line 1: Heat 750, Fil 4, Vel 30, Del 150, Pul 80, Line 2: Heat 650, Fil 3, Vel 40, Del 135, Pul 150) or borosilicate glass capillaries (o.d. 1.2 mm, i.d. 0.69 mm, Harvard Apparatus, pulling parameters: Line 1: Heat 330, Fil 3, Vel 30, Del 220, Pul -, Line 2: Heat 330, Fil 3, Vel 40, Del 180, Pul 120) using a

laser puller (P-2000, Sutter Instruments. Dimensions of the individual nanopipettes used in experiments in this work were measured after experiments through a combination of TEM and optical microscopy. Typically, quartz nanopipettes presented an aperture diameter of 30-60 nm whilst borosilicate nanopipettes had a diameter of 150-200 nm (measured accurately).

### 5.3.2 Solutions

Milli-Q reagent grade water (resistivity ca. 18.2 MΩ cm at 25°C) was used for all solutions. 1 mM, 10 mM and 500 mM $KNO_3$ (Sigma-Aldrich) solutions were prepared and used for the SICM cyclic voltammetry (CV) experiments. $KNO_3$ was used as a typical 1:1 electrolyte, although in principle any electrolyte could be used for these studies.

### 5.3.3 Instrumentation

The instrumentation used has been described elsewhere.[38, 43, 44] The current-to-voltage converter used to measure currents was custom built. Data recording, as well as the probe position and voltage output control, was performed using a custom written LabVIEW (2013, National Instruments) program through an FPGA card. The SICM probe movement normal to the substrate was controlled using a piezoelectric positioning stage with a travel range of 38 μm (P-753-3CD, Physik Instrumente). A lock-in amplifier (SR830, Stanford Research Systems) was used to apply the oscillating bias in the BM-SICM setup and to extract the AC ion current amplitude and phase used for surface charge mapping and SICM feedback.

### 5.3.4 Nanopipette Voltammetry

Nanopipettes were bathed in, and filled with, the aqueous solution of interest, and one Ag/AgCl QRCE was inserted into the nanopipette and another similar electrode was placed in bulk solution. This electrode maintains a stable potential in a wide range of aqueous media, including $KNO_3$, because although AgCl is only sparingly soluble, its dissolution kinetics are fast,[49] so that the wire is bathed in saturated AgCl solution. The potential applied to the QRCE in the nanopipette was swept between -

0.4 V and 0.4 V, with respect to the bulk QRCE, at a rate of 50 mV/s and the current recorded at the QRCE in bulk solution.

### 5.3.5 Optical Microscopy

Optical images were taken of the nanopipette taper and were analysed using Adobe Illustrator (CC 2015) to provide estimates of the inner and outer diameter at lengths 20 μm to 300 μm from the nanopipette tip for use in FEM simulations.

### 5.3.6 TEM Imaging of Nanopipettes

Before TEM imaging, solution was removed from a nanopipette that had been used for current-voltage (*I*-*V*) measurements, and the nanopipette was then placed in a deionised water bath overnight to remove as much remaining salt residue from the end of the nanopipette as possible before being left to dry for 1 day. A JEOL 2000FX microscope operating at 200 kV accelerating voltage, equipped with a GATAN ORIUS 11-megapixel digital camera, was used for TEM tip characterisation. Adobe Illustrator CC 2015 graphics software was used to obtain nanopipette dimensions with pixel level (<1 nm at the highest magnification) precision.

### 5.3.7 FEM Simulations of Nanopipettes in Bulk Solution

A two-dimensional axisymmetric FEM model was constructed to calculate the *I*-*V* characteristics of a nanopipette in bulk solution of high (500 mM) and low (10 mM or 1 mM) ionic strength. Simulations were constructed in Comsol Multiphysics (version 4.4), using the transport of diluted species and electrostatics modules. Dimensions of the nanopipettes at various distances up the pipette, from the opening, were obtained from TEM and optical images. This ensured that the geometry of nanopipettes was reproduced faithfully in the simulations. Data for the nanopipettes, whose *I*-*V* characteristics are discussed in this work, are given in Supporting Information, Table 5.1.

The simulation was as outlined previously,[43] with details given in Supporting Information, section 5.8.1. A bulk domain of 160 μm × 160 μm was implemented

and a nanopipette length of 300 μm was used at which point the nanopipette inner diameter was in all cases larger than 10 μm and so the resistance contribution from the remainder of the nanopipette would be minimal. A surface charge was included on the lowest 20 μm of the nanopipette where the mesh size was also smallest (maximum 0.5 nm). The bias between the bulk of the nanopipette with respect to the solution bulk was changed between 0.4 V and -0.4 V as in the experimental CVs reported below and the current extracted, in order to generate *I-V* curves. For simulations performed in 10 mM and 1 mM, the surface charge applied to the nanopipette was adjusted (as the only variable) until matching with experimental data to give a value for the pipette surface charge.

### 5.3.8 BM-SICM Surface Charge Mapping of Glass Substrate

Surface charge mapping was performed as described in previous work.[43, 45] A quartz nanopipette was translated towards a glass substrate (glass bottomed Petri dish with detachable coverslip, WillcoWells), with no net bias applied between the 2 QRCEs, rather just a small harmonic oscillation of the bias (270 Hz, 28 mV r.m.s. amplitude about 0 V). Upon detection of the surface through a 0.5° increase in the recorded AC phase (see below for method of distance determination), probe translation stopped automatically and a CV was performed from 0 V to 0.4 V to -0.4 V and back to 0 V, for surface charge detection, at a rate of 0.2 V/s. The nanopipette was then retracted 500 nm (~10 tip radii) and the same CV profile performed in bulk for characterisation of the nanopipette probe surface charge. For the tips used herein, 500 nm corresponded to be around 10 tip diameters and was sufficiently far away from the surface to represent the bulk SICM response, which is typically seen around 1 tip diameter away from the substrate.[36] No observable difference was seen between CVs performed at greater separation distances than this.

### 5.3.9 Quantification of Surface Charge

For quantification of substrate surface charge, the surface charge of the nanopipette was obtained in the same way as above using the analysis of the bulk CV. A working distance for the near-surface experimental measurement was obtained by first

calculating the system differential capacitance at no net applied bias according to:[50]

$$C = \frac{\tan \theta}{2\pi f R} \quad (5.1)$$

where $\theta$ is the AC phase signal recorded experimentally, $f$ is the AC oscillation frequency and *R* is the system resistance around 0 V, obtainable from an *I-V* curve in bulk solution. A circuit diagram representing the components of the BM-SICM setup is presented in Supporting Information, Figure 5.9. A FEM simulated approach curve was then calculated at a range of tip-substrate separations to obtain the distance-dependent system resistance. We could then use equation 5.1 to calculate θ at each separation distance, because simulations showed that the capacitance did not change with distance (i.e. is dominated by the nanopipette itself). The resulting working curve of θ against tip-substrate separation allowed the evaluation of the separation at which the surface measurement was made. Once the working distance was known, the surface charge of the substrate was varied in the simulation until the simulated *I-V* curve matched that obtained experimentally, with the smallest residual error. Care should be taken in this approach, ensuring that the nanopipette is aligned perpendicular to the sample of interest, as a slope of the sample could affect the working distance and hence surface charge values obtained. If the slope of the sample was known or minimal over the dimensions of the nanopipette opening, the effects could be modelled or would be negligible.[42]

## 5.4 Results and Discussion

### 5.4.1 Evaluation of Existing Methods for Nanopipette Characterisation

Scanning electron microscopy (SEM) of nanopipette openings has commonly been used to extract an estimate for the aperture radius and the glass thickness at the opening.[3, 26, 29, 51] However, for nanopipettes that have openings less than 50 nm in diameter, the resolution of SEM is insufficient. The characterisation of nanopipettes using SEM also becomes more difficult at this scale as it requires the nanopipette to be sputtered with a conducting metal, which affects the nanopipette dimensions. SEM has other limitations as a tool for characterising nanopipettes of this size, as it

provides little information about the nanopipette lumen size beyond at the opening. The nanopipette resistance properties are dependent on the nanopipette inner angle and how the lumen size varies with distance into the nanopipette. Full characterisation of nanopipettes requires that these dimensions are obtained.

Hitherto, two approaches are commonly taken in order to characterise nanopipettes in the absence of more direct tools. Method 1 assumes that the ratio between the outer and inner diameter of a nanopipette remains constant to that at the nanopipette opening,[13, 41, 52] and, as such, the inner nanopipette angle can be calculated by using the relationship:

$$\tan\alpha_{inner} = \frac{\tan\alpha_{outer}}{r_{OI}} \tag{5.2}$$

where $\alpha_{outer}$ is the outer nanopipette angle, estimated from SEM images and $r_{OI}$ is the ratio between the outer and inner pipette radii at the nanopipette opening.

Method 2 involves approximating the nanopipette as a truncated hollow cone[13, 31, 41, 53-57] in order to model its resistive properties. The resistance then depends on the inner cone angle and aperture radius according to:[53, 54]

$$R_p = \frac{1}{\kappa\pi r_i \tan\beta} + R_{access} \approx \frac{1}{\kappa\pi r_i \tan\beta} + \frac{1}{4\kappa r_i} \tag{5.3}$$

or equivalent equations, where $R_p$ is the nanopipette resistance, $r_i$ the inner pipette radius, $\kappa$ is the solution conductivity and $\beta$ is the inner nanopipette half cone angle. Using such equations, the resistive properties can be estimated given knowledge of the nanopipette radius and cone angle estimate, or the nanopipette radius can be back-calculated from experimental resistance values and some input value for the inner cone angle. These approaches are widely used[31, 52-54, 56] but require an estimate for the nanopipette inner angle, which cannot be obtained directly near the nanopipette opening using SEM, and to date has usually been estimated from the outer pipette angle obtained in SEM images.[55, 57-59] Evidently, this approach fails if the assumption about a constant inner angle does not hold. Method 1 and 2 will

both be examined below to evaluate their suitability in nanopipette characterisation and modelling, and compared to the method that we develop herein.

The surface charge density of a nanopipette also strongly influences the resulting *I-V* characteristics.[22, 60-63] Glass and quartz both exhibit negatively charged surface charge under typical experimental conditions (neutral pH, aqueous solutions) owing to the presence of silanol groups that dissociate ($pK_a$ 7.5).[64] Ion current rectification phenomena (ICR) are manifest when the Debye length is even a small fraction of the dimension of the nanopipette opening,[60] resulting in a diminished ionic current with positive tip bias applied and an enhanced current when the polarity is reversed, compared to expectations if the nanopipette were uncharged.[43, 45, 60, 62]

Analytical approaches, such as utilising equation 5.3 or similar equations for calculating the nanopipette radius or resistive properties, often at a fixed applied bias,[55, 56] may evidently become inaccurate under these conditions, as the surface charge of the nanopipette is not generally considered. While there has been much work on the study and simulation of the ICR phenomena at nanopipettes in low ionic strength,[60, 62, 63] quantification of the nanopipette surface charge and understanding the nanopipette current response is a difficult task owing to a lack of more complete tip characterisation methods.

Recently it has been shown that TEM offers an attractive means for visualising nanopipettes.[65, 66] Here, we show that by combining TEM and optical microscopy of nanopipettes with data from ion conductance experiments, it is possible to obtain the most precise representation of the nanopipette geometry and properties, which provides a platform for a wide range of quantitative applications.

### 5.4.2 Characterisation of Nanopipettes in High Ionic Strength Media

Example TEM images of one of each of the quartz and borosilicate nanopipettes characterised in this work by *I-V* measurements are shown in Figure 5.1a and 5.1b, respectively. A full example sequence of TEM images of a quartz nanopipette at each magnification utilised is provided in Supporting Information, Figure 5.7. These nanopipettes did not exhibit a purely conical geometry and the inner angle of the

nanopipettes used in this work was seen to change significantly (2 —12°) up the length of the nanopipette taper as shown in Figure 5.1c, with the greatest change in the 500 nm nearest to the nanopipette opening. Further data are given in Table 5.1 in Supporting Information.

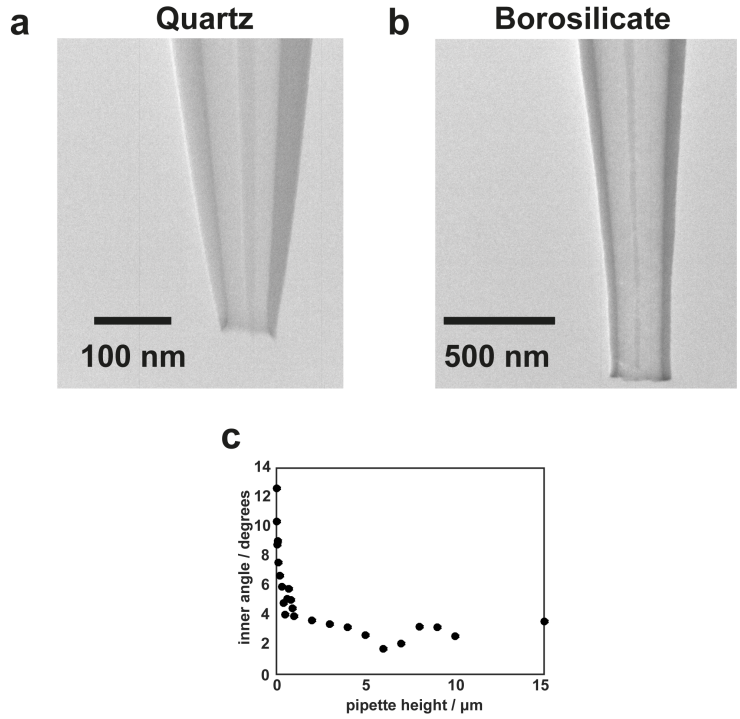


**Figure 5.1.** Typical TEM micrographs of quartz **(a)** and borosilicate **(b)** nanopipettes characterised after CV experiments had been performed. Dimensions were extracted from images with pixel (nm) level precision. The filament of the nanopipette, which aids their filling, can be seen down the centre of the TEM images, but has a negligible effect on the voltammetric characteristics. **c)** Plot of how the inner angle of Tip 1 varies up the length of the nanopipette. These data allow FEM models to faithfully reproduce the nanopipettes for ion conductance studies.

Typical SICM experiments are performed in moderate[19] to high ionic strengths (>100 mM),[3, 31, 32, 45, 67, 68] as are many pipette measurements.[14, 15, 18, 19] Under these conditions, the diffuse double layer is expected to be compressed to a sub-nanometre scale, and therefore undetectable, level according to:[50]

$$\frac{1}{\kappa} = \left( \frac{\varepsilon \varepsilon_0 k_B T}{2 n^0 z^2 e^2} \right)^{0.5} \qquad (5.4)$$

for a *z*:*z* electrolyte where $1/\kappa$ is the Debye length, $\varepsilon$ and $\varepsilon_0$ are the dielectric constants of the bulk material and vacuum, respectively, *T* is the temperature, $k_B$ is the Boltzmann constant, *z* is the charge of the monovalent electrolyte ion and $n^0$ is the number concentration of each ion in the solution.

The voltammetric characteristics for two nanopipettes, Tip 1 and Tip 2, are presented in Figure 5.2 and both exhibit almost ideal ohmic response with minimal nanopipette charge effects on the ionic current, as would be expected under these conditions.[60] Employing a nanopipette geometry with dimensions extracted from TEM data, in the simulation gives excellent agreement to experimental data (red lines) for both of the nanopipettes, with no adjustable parameters. Note that for the simulations, concentration dependent diffusion coefficients were used, calculated from:[69]

$$D_i = D_i^{\infty}[1 + C_i(\frac{\partial \ln \gamma_i}{\partial C_i})] \qquad (5.5)$$

where $D_i^{\infty}$ is the infinitely dilute diffusion coefficient of species *i*, $C_i$ is its concentration and $\gamma_i$ its activity coefficient. For $KNO_3$ at an ionic strength of 500 mM this yielded diffusion coefficients of $1.45 \times 10^{-5}$ $cm^2/s$ and $1.41 \times 10^{-5}$ $cm^2/s$ for $K^+$ and $NO_3^-$ respectively. Whilst the approaches outlined here have been demonstrated for single-barrelled nanopipettes, the principles could naturally be extended for the consideration of dual or multi-barrelled nanopipettes. By performing TEM imaging of a nanopipette from different angles, accurate dimensions could be obtained regardless of whether the nanopipette exhibited axial symmetry and this could be incorporated into a 3D FEM model for quantitative analysis of voltammetric properties.

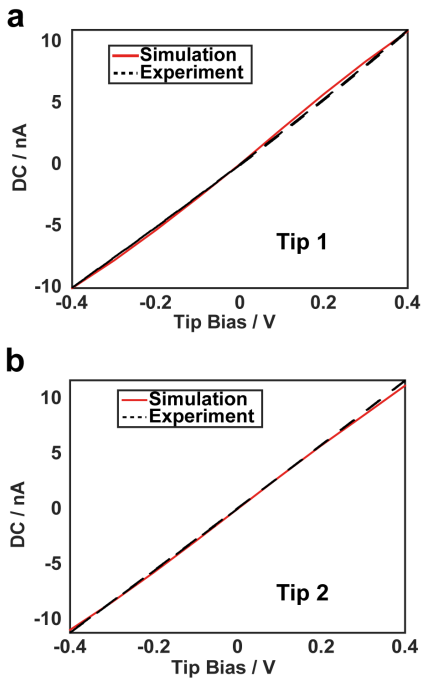


**Figure 5.2.** The *I-V* characteristics of Tip 1 **(a)** and Tip 2 **(b)** in high electrolyte conditions (500 mM $KNO_3$). An ohmic ion current-voltage response is seen and there is strong agreement between experiment (black) and the simulated response (red) based on the nanopipette dimensions extracted using TEM, with no adjustable parameters.

Having shown that TEM characterisation of nanopipettes results in excellent agreement between experiment and simulated conductivity data, Method 1 and Method 2 are now evaluated using Tip 1 as an example. Firstly in Method 1, if the assumption was made that the ratio of the inner to outer dimensions of the nanopipette remained constant up the nanopipette taper length, as is commonly done,[13,31,52,70] the result is a significant underestimation of the nanopipettes resistive properties. A FEM simulation was performed using the varying outer angle of the nanopipette up its length, which might be reasonably obtained from SEM data, to estimate the inner angle and hence dimensions, according to equation 5.2, keeping $r_{oi}$ constant as calculated at the nanopipette opening ($r_{oi}$ =1.47 for Tip 1 from TEM data). From the resulting *I-V* curve depicted in Figure 5.3a, it can be seen that the match to the experimental data is now rather poor (contrasting with Figure 5.2a where TEM data were used). This more simplistic analysis to estimate the inner geometry of the nanopipette greatly underestimates the inner tip dimensions and

hence the resistance properties of the nanopipette by around 50% at the extreme potentials of the *I-V* curve. This error could be even greater if a constant outer (and hence inner angle) was assumed, as is sometimes done in this field.

Next, Method 2 is considered which, as mentioned above, assumes a conical nanopipette geometry, and is often utilised to model the nanopipette resistance properties, or deduce the nanopipette radius.[31, 52-54, 56] Such an approach is very sensitive to the inner half cone angle chosen (equation 5.3). It has already been seen that the angle can change along the length of the nanopipette (Figure 5.1c) and will vary depending on the pulling parameters used for nanopipette fabrication. Quoted values for inner half cone angles range greatly, from 1.5° – 13° for different nanopipettes,[52, 55, 58, 71] and it has even been estimated to vary by as much as 2.5° between the same type of nanopipette.[59] However, it is important to point out that in all of these cases the estimate was not obtained using a suitable technique, as discussed above.

The black line in Figure 5.3b shows the effect of varying inner half cone angle on the predicted ionic current in 500 mM $KNO_3$ according to equation 5.3 at a tip bias of 0.4 V, assuming the nanopipette radius to be that obtained for Tip 1 from TEM data ($R_i$ = 25 nm). It can be seen that even small variations of the inner angle result in a large change in the nanopipette current response. The red line in Figure 5.3b utilises the observed *I-V* characteristics of Tip 1 to consider how the choice of inner half cone angle would affect the prediction for the nanopipette opening size, according to equation 5.3, again with $R_i$ = 25 nm. It can be seen that even a small variation of the inner cone angle assumed has a significant impact on the resulting nanopipette radius estimate.

Tip 1 has a measured radius of 25 nm, at the very end, and with this knowledge Method 2, yields an inner half cone angle of 3.7°, which should be compared with the actual profile in Figure 5.1c.

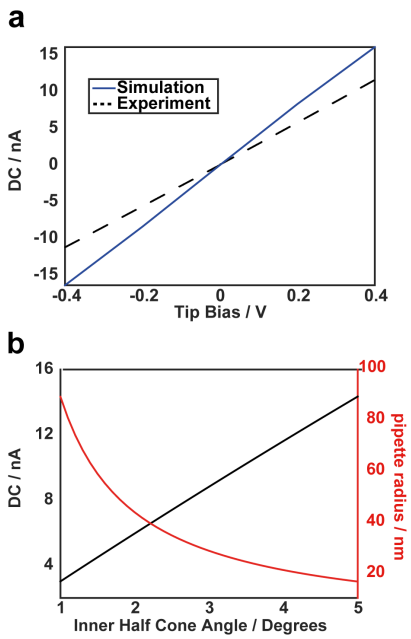


**Figure 5.3. a)** Simulation (blue), assuming that the ratio, $r_{oi}$, of the outer to inner wall thickness for Tip 1 remains the same as at the nanopipette opening ($r_{oi}$ = 1.47), calculating inner dimensions relative to the measured outer dimensions from TEM (which could be obtainable using SEM) alongside the experimental data from Figure 2a. **b)** FEM calculation of the ionic current at 0.4 V tip bias as a function of the inner half cone angle for the measured pipette radius for Tip 1 (25 nm) from TEM (black), together with calculated nanopipette radius as a function of inner half cone angle using the experimental resistance calculated from Figure 2a (red).

### 5.4.3 Quantifying Nanopipette Surface Charge in Low Ionic Strength

The charge on nanopipettes can also have a major impact on applications in sizing,[47] delivery and detection[18, 26] as well as imaging.[43, 45, 46] Furthermore, when deployed in SICM, nanopipettes are very promising for surface charge mapping. [43, 44] If the resistance is used to estimate the conical dimensions (equation 5.3) of a nanopipette, it is important to point out that such an approach is likely to fail in low ionic strength media, where the Debye length is longer, according to equation 5.4, especially if single potential measurements are made, which do not reveal surface charge effects. The *I-V* characteristics for quartz nanopipettes that were filled and bathed in 10 mM (Tip 3, Figure 5.4a) and 1 mM (Tip 5, Figure 5.4b) $KNO_3$ solutions exhibited an ICR response, which manifests more strongly at 1 mM, resulting in a

greater rectification ratio, the ratio between the currents at the positive and negative extreme potential limits of the *I-V* curve.[60, 61] ICR was also seen at borosilicate glass nanopipettes, as in Figure 5.4c, in 10 mM $KNO_3$. More examples for each of these conditions are presented in Supporting Information, Figure 5.8. These characteristics, where the current is smaller at positive tip bias than at negative tip bias indicate that the nanopipette is negatively charged.[61]

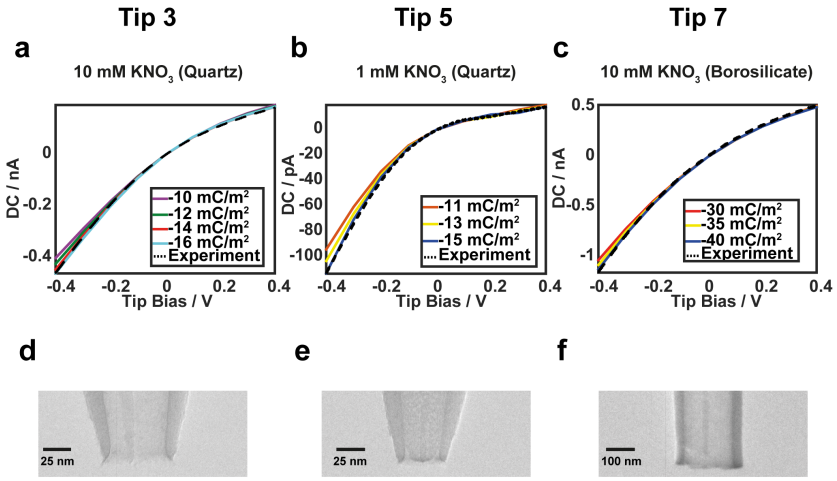


**Figure 5.4.** *I-V* characteristics of quartz nanopipettes at low ionic strength reveal ion current rectification in 10 mM $KNO_3$ (**a**), which is seen more strongly as the ionic strength decreases further to 1 mM $KNO_3$ (**b**). Larger borosilicate nanopipettes also exhibit ion current rectification **(c)** and a correspondingly larger nanopipette surface charge is required to match the experimental response. The noise level for these experiments was 3 pA (peak-to-peak). Corresponding TEM images for each tip are shown (**d**-**f**). Note that the surface charge on the nanopipette is the only variable in the simulation to fit to the experimental data. The simulation results for different charges are shown as the coloured lines.

Because the nanopipette geometry is known with high accuracy from TEM, the surface charge on the nanopipette is the only adjustable parameter in FEM simulations to match to *I-V* experiments under these conditions. For the quartz nanopipettes used in this work, the surface charge was between -14 $mC/m^2$ and -16 $mC/m^2$ (at pH 6.2), a narrow range of values where the simulated *I-V* curves closely matched the experimental voltammograms (Figure 5.4). The noise level in these

voltammetric experiments was 3 pA (peak-to-peak), which was much smaller than the difference between the currents at the extreme potentials of the simulated CVs (-0.4 V) with different surface charges depicted in Figure 5.4, (*e.g.* approximately 10 pA in the case of Figure 5.4a and b). This highlights the accuracy with which the surface charge could be determined (i.e. to better than 1 $mC/m^2$).

Importantly, there was no significant difference between the surface charges obtained in 10 mM (Figure 5.4a) and 1 mM $KNO_3$ (Figure 5.4b) solutions, giving confidence in this result. For the borosilicate glass nanopipettes studied, experimental and simulated *I-V* curves, presented in Figure 5.4c indicate a pipette wall surface charge of between -30 $mC/m^2$ and -40 $mC/m^2$. This higher charge on the borosilicate glass explains why it is possible to observe the effects of ICR, even with relatively large nanopipette sizes.[60-62]

There is much debate about the charge on glass nanopipettes and glass substrates, owing to a lack of techniques to robustly probe the surface charge of extended substrates. Consequently, a wide range of values have been quoted for the surface charge from -0.0001 $mC/m^2$ – -240 $mC/m^2$.[46] Some, but not all, of this variation in the surface charge of glass can be due to the fact that these measurements are made at a range of pH values.[64] The characterisation methods advocated herein provide a means of unambiguously quantifying the surface charge of typical nanopipettes.

### 5.4.4 Quantitative Surface Charge Mapping of Extended Substrates

The more precise nanopipette probe characterisation method is particularly beneficial for SICM studies. To this end, single barrelled quartz nanopipettes were approached to a glass substrate in a BM-SICM scheme, as described previously.[43] Upon detecting the surface through an increase in the AC phase of 0.5° (corresponding to a distance of 10 ± 3 nm, see Figure 5.5a and Supporting Information, Figure 5.8), a CV measurement was performed with the net bias between the two QRCEs varied from 0 V, the approach bias, to +0.4 V to -0.4 V and back to 0 V.

It has been demonstrated previously that the BM-SICM technique is insensitive to substrate surface charge and the phase or current amplitude only depends on distance when no net bias is applied.[43] ICR was seen at the quartz nanopipette in bulk solution (diminished current at positive tip bias compared to negative tip bias), which was magnified when the tip was near the surface. This can be seen in Figure 5.5b for Tip 4 whose surface charge was determined in bulk to be -16 mC/m$^2$ (Supporting Information, Figure 5.8a).

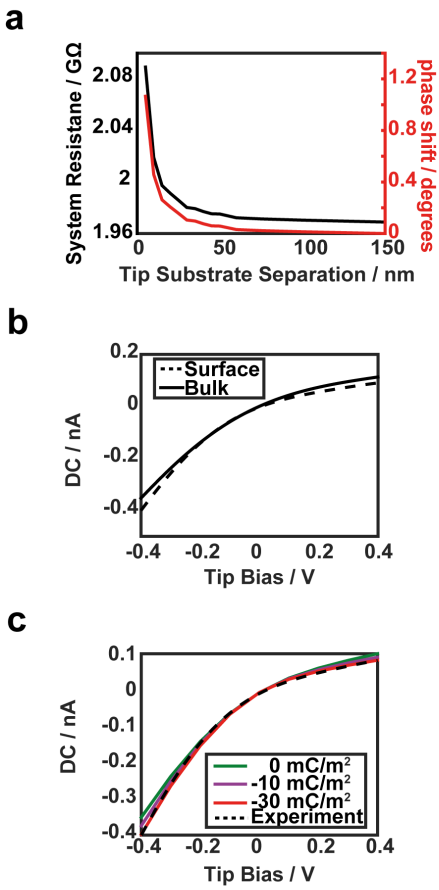


**Figure 5.5. a)** FEM simulations allow calculation of the system resistance for Tip 4 (black) as a function of tip-substrate separation at 0 V net bias from which the phase shift, as a function of distance, can be calculated (red), which can be used to estimate the working distance for surface charge experiments. **b)** *I-V* curves of Tip 4 in bulk solution and near (10 nm) from a glass surface in 10 mM $KNO_3$. **c)** Fits to the near-surface *I-V* curve with the charge on the substrate the only variable and the tip charge fixed at -16 mC/m$^2$ as measured in bulk solution (Supporting Information, Figure 5.8a).

A FEM simulation was performed, with the nanopipette at the determined working distance (10 nm). The surface charge density applied to the substrate in the simulation was then varied (as the only adjustable parameter), yielding surface *I-V* curves presented in Figure 5.5c. The best fit was obtained with a surface charge density of around -30 mC/m$^2$, similar to the borosilicate glass nanopipettes.

## 5.5 Conclusions

It has been demonstrated that visualisation of nanopipettes by TEM and optical microscopy, in combination with data for *I-V* measurements and FEM simulations, provides an holistic view of the geometry, properties and response of nanopipettes under electrochemical bias. Simulations of ion transport at high ionic strength, with the nanopipette geometry obtained precisely from TEM micrographs, results in strong agreement between simulated *I-V* curves and experimental data that can be trusted owing to no other assumptions being made about the nanopipette geometry or electrolyte properties, i.e. there are no adjustable parameters in the modelling. It is particularly important to note that in this work we have shown that the probe can easily be characterised by TEM after a set of *I-V* measurements or SICM experiments, and the inner dimensions of the nanopipette can be obtained with high accuracy.

The new approach we propose contrasts with methods used hitherto, which rely on the use of analytical equations to model *I-V* curves with a highly idealised geometry. In these methods, the nanopipette opening that is obtained is strongly dependent on the choice of inner angle chosen to represent the nanopipette geometry. Our work shows that nanopipettes do not necessarily have a conical shape and also that the outer and inner angles are very different, and vary with height along the nanopipette.

Through the use of FEM simulations, it also becomes possible to further characterise nanopipettes in terms of their surface charge, as exemplified in our work for both quartz and borosilicate nanopipettes, for which robust values over small ranges have been obtained. Finally, by characterising the nanopipette geometry and surface charge fully, it then becomes possible to quantify the surface charge of extended substrates in an SICM format, enhancing the SICM technique and

its capability for functional mapping.

## 5.7 Supporting Information

### 5.7.1 FEM Model Equations and Boundary Conditions

The equations and boundary conditions solved in the FEM simulations were as in previous work[43,45] but with an improved tip geometry obtained using TEM data, as described in the manuscript. Briefly, ionic transport is reasonably assumed to follow the classical Nernst-Planck relationship, where the flux $J_i$ of species, *i,* is given as:

$$J_i = -D_i \nabla c_i - z_i \frac{F}{RT} D_i c_i \nabla \phi \tag{5.6}$$

and the Poisson equation describes the electrical potential $\phi$:

$$\nabla^2 \phi = -\frac{F}{\varepsilon \varepsilon_0} \sum_i z_i c_i \tag{5.7}$$

where $c_i$ denotes the species concentration, while $D_i$, $z_i$, $F$, $R$, $T$, $\varepsilon$ and $\varepsilon_0$ specify constants: system diffusion coefficient of *i*, its charge number, the Faraday constant, gas constant, temperature, relative permittivity and vacuum permittivity, respectively.

The above differential equations were solved with the boundary conditions as follows and shown in the schematic in Figure 5.6. A fixed concentration, $C_{bulk}$ (1 mM-500 mM) was applied at the bulk nanopipette and bulk domain boundary. The bias, $V_{DC}$, was applied to the bulk nanopipette domain. There was a no flux condition at the walls of the nanopipette and bulk domain boundary. In some simulations a varying surface charge density was applied to the bottom 10 μm of the inner and outer nanopipette wall. For surface charge quantification of extended substrates a charge was applied to a 5 μm region of the surface, extending out from the symmetry axis.

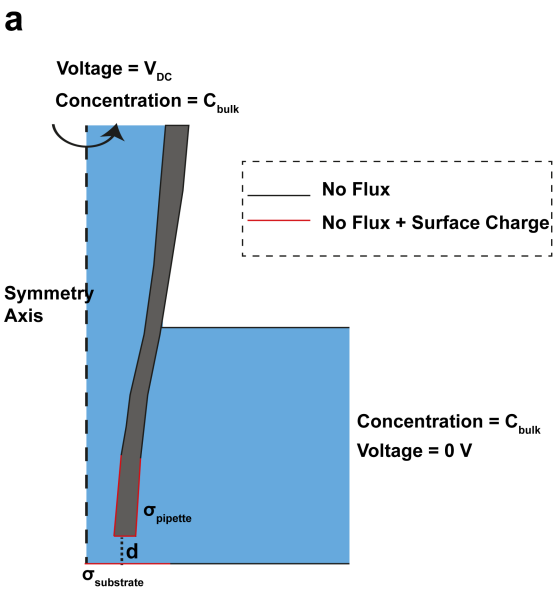


**Figure 5.6.** Schematic of the FEM simulation boundary conditions for the nanopipette geometry with no flux applied to the nanopipette walls and bulk boundaries. The concentration at the rightmost bulk boundary and the nanopipette top was held at $C_{bulk}$ 1 mM, 10 mM or 500 mM $KNO_3$. The tip potential $V_{DC}$ was applied to the top nanopipette boundary with respect to the bulk boundary.

### 5.7.2 Full Magnification Range of TEM

As discussed in the manuscript, accurate characterisation of the nanopipette inner geometry was achievable using TEM. For each characterised nanopipette, TEM images were taken at magnifications ranging from ×1000 to ×40000, as depicted in Figure 5.7, in the region of the nanopipette, that contributes most significantly to the pipette resistance (at the opening). Higher magnifications were achievable but this was not necessary for this study. Despite the cleaning of the nanopipettes, as described in the manuscript, some salt residue was often seen to remain in the nanopipettes but this did not affect the ability to make sufficiently quantitative measurements.

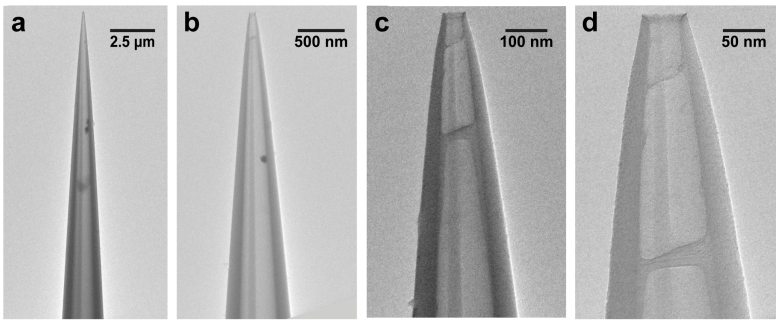


**Figure 5.7.** Examples of a sequence of TEM images that were used after experiments to extract geometry of nanopipettes (Tip 4 in this case) with magnifications of **(a)** ×1000, **(b)** ×5000, **(c)** ×20000 and **(d)** ×40000. In each case the inner lumen is clearly distinct. Some salt residues are observable, leftover from the ion conductance (*I-V*) experiments.

### 5.7.3 Table of Dimensions

**Table 5.1.** Dimensions of quartz and borosilicate nanopipettes characterised

| | Tip 1 | | Tip 2 | | Tip 3 | | Tip 4 | | Tip 5 | | Tip 6 | | Tip 7 | | Tip 8 | |
|---|---|---|---|---|---|---|---|---|---|---|---|---|---|---|---|---|
| | Quartz | | | | | | | | | | | | Borosilicate | | | |
| | 500 mM | | | | 10 mM | | | | 1 mM | | | | 10 mM | | | |
| Height | I.D. | O.D. | I.D. | O.D. | I.D. | O.D. | I.D. | O.D. | I.D. | O.D. | I.D. | O.D. | I.D. | O.D. | I.D. | O.D. |
| nm | nm | | | | nm | | | | nm | | | | nm | | | |
| **0** | 51 | 75 | 56 | 70 | 60 | 72 | 43 | 55 | 33 | 43 | 38 | 49 | 182 | 243 | 187 | 237 |
| **25** | 60 | 91 | 53 | 84 | 55 | 83 | 45 | 68 | 34 | 59 | 40 | 59 | 182 | 240 | 188 | 231 |
| **50** | 65 | 102 | 57 | 95 | 59 | 97 | 47 | 74 | 41 | 67 | 43 | 70 | 175 | 231 | 189 | 240 |
| **75** | 69 | 114 | 64 | 107 | 65 | 108 | 53 | 79 | 47 | 77 | 46 | 80 | 181 | 229 | 190 | 240 |
| **100** | 75 | 125 | 69 | 117 | 71 | 119 | 58 | 94 | 51 | 85 | 52 | 91 | 182 | 229 | 192 | 244 |
| **200** | 95 | 163 | 88 | 152 | 91 | 151 | 73 | 130 | 67 | 116 | 67 | 121 | 189 | 237 | 196 | 259 |
| **300** | 114 | 194 | 105 | 183 | 109 | 181 | 86 | 156 | 80 | 141 | 78 | 146 | 193 | 247 | 200 | 276 |
| **400** | 130 | 224 | 123 | 211 | 119 | 209 | 105 | 184 | 99 | 168 | 96 | 170 | 196 | 292 | 215 | 306 |
| **500** | 144 | 243 | 137 | 238 | 133 | 235 | 118 | 207 | 110 | 186 | 104 | 191 | 200 | 316 | 240 | 328 |
| **600** | 161 | 265 | 148 | 261 | 151 | 260 | 126 | 229 | 124 | 212 | 122 | 210 | 208 | 333 | 251 | 349 |
| **700** | 176 | 296 | 163 | 285 | 163 | 281 | 136 | 271 | 132 | 237 | 136 | 231 | 215 | 357 | 261 | 378 |
| **800** | 186 | 325 | 178 | 309 | 171 | 309 | 148 | 296 | 147 | 254 | 150 | 251 | 223 | 381 | 273 | 397 |
| **900** | 203 | 347 | 185 | 327 | 181 | 332 | 164 | 289 | 171 | 288 | 174 | 263 | 254 | 401 | 283 | 416 |
| **1000** | 214 | 371 | 198 | 349 | 190 | 357 | 176 | 315 | 185 | 322 | 197 | 280 | 278 | 426 | 306 | 434 |
| **2000** | 321 | 570 | 298 | 535 | 287 | 558 | 282 | 497 | 252 | 462 | 259 | 453 | 377 | 619 | 452 | 637 |
| **3000** | 430 | 746 | 392 | 712 | 388 | 732 | 369 | 671 | 357 | 629 | 348 | 632 | 501 | 767 | 569 | 804 |
| **4000** | 506 | 918 | 478 | 889 | 489 | 913 | 464 | 829 | 464 | 817 | 420 | 743 | 582 | 928 | 718 | 959 |
| **5000** | 610 | 1075 | 572 | 1039 | 572 | 1087 | 517 | 1124 | 588 | 972 | 519 | 873 | 693 | 1058 | 817 | 1083 |
| **6000** | 655 | 1188 | 637 | 1138 | 625 | 1174 | 587 | 1236 | 631 | 1083 | 575 | 990 | 767 | 1188 | 885 | 1207 |
| **7000** | 702 | 1251 | 714 | 1306 | 719 | 1373 | 675 | 1410 | 668 | 1231 | 631 | 1101 | 829 | 1293 | 1015 | 1330 |
| **8000** | 749 | 1400 | 808 | 1437 | 819 | 1466 | 890 | 1528 | 718 | 1324 | 736 | 1256 | 947 | 1448 | 1114 | 1467 |
| **9000** | 787 | 1580 | 861 | 1586 | 884 | 1553 | 972 | 1683 | 786 | 1454 | 785 | 1405 | 1021 | 1553 | 1194 | 1559 |
| **10000** | 841 | 1728 | 932 | 1723 | 996 | 1708 | 1061 | 1888 | 811 | 1553 | 829 | 1510 | 1126 | 1696 | 1287 | 1696 |
| **15000** | 1109 | 2379 | 1221 | 2394 | 1273 | 2236 | 1467 | 2553 | 1108 | 2160 | 1232 | 2104 | 1559 | 2302 | 1652 | 2333 |
| **20000** | 1301 | 3565 | 1386 | 3571 | 1517 | 3102 | 1686 | 3554 | 1302 | 2784 | 1599 | 3102 | 1876 | 3102 | 1941 | 3156 |
| **25000** | 1606 | 4781 | 1525 | 4156 | 1870 | 4055 | 2069 | 4362 | 1603 | 3765 | 1970 | 4055 | 2188 | 3893 | 2204 | 3932 |
| **30000** | 1836 | 5267 | 1694 | 4432 | 2376 | 4443 | 2452 | 4871 | 1894 | 4520 | 2504 | 4443 | 2874 | 4498 | 2934 | 4564 |
| **35000** | 2008 | 5430 | 1925 | 5325 | 2713 | 5008 | 2759 | 5856 | 2389 | 5320 | 2859 | 5008 | 3122 | 5237 | 3312 | 5352 |
| **40000** | 2372 | 6483 | 2156 | 5844 | 3096 | 5832 | 3065 | 6543 | 2734 | 6324 | 3263 | 5831 | 3424 | 6010 | 3567 | 6128 |
| **45000** | 2448 | 7374 | 2510 | 6250 | 3433 | 6284 | 3391 | 6947 | 3392 | 6738 | 3618 | 6284 | 3978 | 6560 | 4019 | 6673 |
| **50000** | 2639 | 8831 | 2895 | 6834 | 3694 | 6931 | 3755 | 7290 | 3810 | 7034 | 3893 | 6930 | 4295 | 7201 | 4451 | 7409 |
| **100000** | 3901 | 11143 | 4235 | 10471 | 5563 | 10258 | 5901 | 11632 | 5604 | 10245 | 5864 | 10258 | 6159 | 11087 | 6324 | 12196 |
| **150000** | 5738 | 12150 | 5650 | 12419 | 6973 | 12359 | 6583 | 14286 | 6201 | 14033 | 7350 | 12358 | 9724 | 14467 | 9878 | 15382 |

For each nanopipette characterised in this work, dimensions were extracted from TEM and optical micrographs at varying height up the nanopipette, with the dimensions presented in Table 5.1, along with the salt concentration in which they were used, and the type of nanopipette material. Simulations and experiments for Tip 1, Tip 2, Tip 3, Tip 5 and Tip 7 are presented in the main manuscript whilst data for the remaining tips (4, 6 and 8) is shown in this Supporting Information 5.8.3, Figure 5.8

### 5.7.4 Data from Tips 4, 6 and 8

For the lower electrolyte conditions investigated in the main manuscript, data were also obtained on other tips and analysed to validate the approach taken. Example *I-V* curves are shown in Figure 5.8 for 3 different tips. Each of these measurements yielded surface charge values, similar to those obtained in the main manuscript. For quartz, this was around -16 mC/m$^2$ and for borosilicate in the region -30 to -40mC/m$^2$.

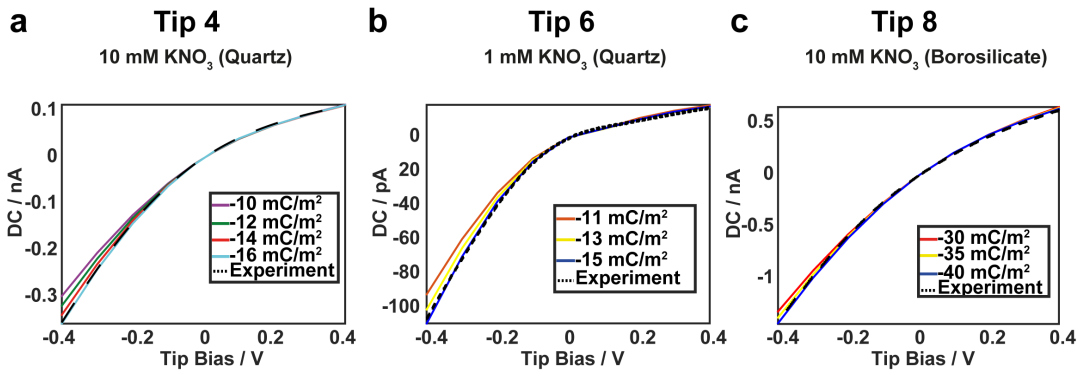


**Figure 5.8.** Experimental and simulated *I-V* curves for **(a)** Tip 4, **(b)** Tip 6 and **(c)** Tip 8. Surface charge was again varied in the simulation (the only variable) on the nanopipette walls until the simulated curve matched best to that seen experimentally.

### 5.7.5 Circuit Diagram of BM-SICM Setup

Figure 5.9 depicts a circuit model for a nanopipette in BM-SICM, with the end of the nanopipette modelled as a resistor and capacitor in parallel. This model allows for

the use of equation 1 in the main manuscript for the evaluation of the system capacitance and, later, the phase shift. The resistance at the end of the nanopipette has a contribution from both the access resistance between the substrate and the nanopipette, as well as from the highly resistive region of the nanopipette itself. The main contribution to the capacitance is from the walls of the nanopipette.

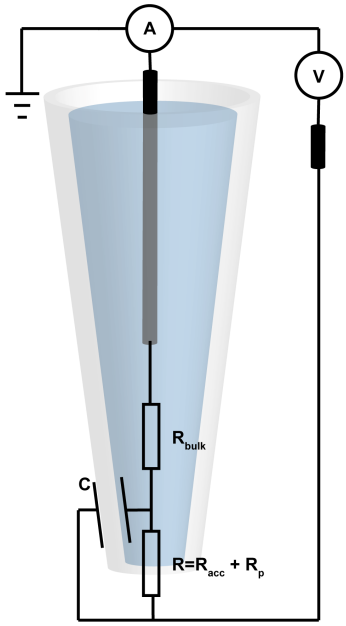


**Figure 5.9.** Circuit diagram of the Bias Modulated SICM setup in relation to the nanopipette. The most significant region is at the end of the nanopipette, which is modelled as a resistor and capacitor in parallel. The resistance is attributed to the high nanopipette resistance in this region and the access resistance, which increases as the nanopipette is approached to a substrate. There is a small contribution from $R_{bulk}$, the solution resistance in the rest of the nanopipette and bulk solution, but this is negligible compared to the resistance at the end of the nanopipette.

### 5.7.6 AC Phase Approach Curve

As described in the manuscript, the working distance at which surface charge measurements were performed was obtained from phase-shift measurements as a function of tip-substrate separation. It can be seen in Figure 5.10 that the experimental and simulated approach curves match well, allowing the distance at which measurements were made to be determined with high accuracy (± 3 nm of the stipulated distance, 10 nm).

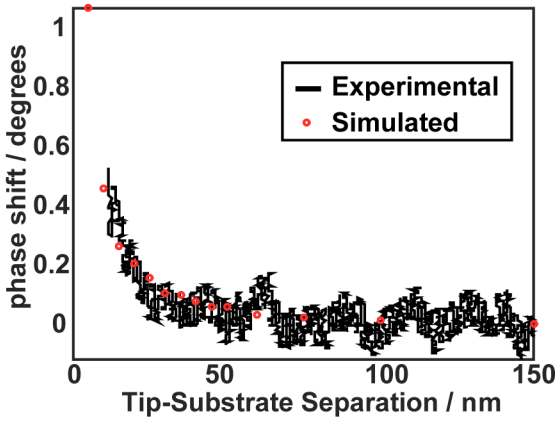


**Figure 5.10.** Theoretical (red) and experimental (black) AC phase shift approach curve on approach of a nanopipette (Tip 4) to a glass substrate with no net applied bias (BM-SICM).

## 5.8 References


1. Morris, C. A.; Friedman, A. K.; Baker, L. A. *Analyst* **2010**, *135*, 2190-2202.

2. Takahashi, Y.; Murakami, Y.; Nagamine, K.; Shiku, H.; Aoyagi, S.; Yasukawa, T.; Kanzaki, M.; Matsue, T. *Phys. Chem. Chem. Phys.* **2010**, *12*, 10012-10017.

3. Shevchuk, A. I.; Frolenkov, G. I.; Sánchez, D.; James, P. S.; Freedman, N.; Lab, M. J.; Jones, R.; Klenerman, D.; Korchev, Y. E. *Angew. Chem. Int. Ed.* **2006**, *118*, 2270-2274.

4. Paulose Nadappuram, B.; McKelvey, K.; Byers, J. C.; Güell, A. G.; Colburn, A. W.; Lazenby, R. A.; Unwin, P. R. *Anal. Chem.* **2015,** *87*, 3566–3573.

5. Ebejer, N.; Güell, A. G.; Lai, S. C. S.; McKelvey, K.; Snowden, M. E.; Unwin, P. R. Annu. Rev. *Anal. Chem.* **2013**, *6*, 329-351.

6. Li, Q.; Xie, S.; Liang, Z.; Meng, X.; Liu, S.; Girault, H. H.; Shao, Y. A*ngew. Chem. Int. Ed.* **2009**, *48*, 8010-8013.

7. Schrlau, M. G.; Dun, N. J.; Bau, H. H. *ACS Nano* **2009**, *3*, 563-568.

8. Takahashi, Y.; Shevchuk, A. I.; Novak, P.; Zhang, Y.; Ebejer, N.; Macpherson, J. V.; Unwin, P. R.; Pollard, A. J.; Roy, D.; Clifford, C. A.*, et al. Angew. Chem. Int. Ed.* **2011**, *50*, 9638-9642.

9. Nadappuram, B. P.; McKelvey, K.; Al Botros, R.; Colburn, A. W.; Unwin, P. R. *Anal. Chem.* **2013**, *85*, 8070-8074.

10. Takahashi, Y.; Shevchuk, A. I.; Novak, P.; Murakami, Y.; Shiku, H.; Korchev, Y. E.; Matsue, T. *J. Am. Chem. Soc.* **2010**, *132*, 10118-10126.

11. O'Connell, M. A.; Wain, A. J. *Anal. Chem.* **2014**, *86*, 12100-12107.

12. Hao, R.; Zhang, B. *Anal. Chem.* **2015**, *88*, 614-620.

13. Terejánszky, P.; Makra, I.; Fürjes, P.; Gyurcsányi, R. E. *Anal. Chem.* **2014**, *86*, 4688-4697.

14. Wang, Y.; Kececi, K.; Mirkin, M. V.; Mani, V.; Sardesai, N.; Rusling, J. F. *Chem. Sci.* **2013**, *4*, 655-663.

15. Edwards, M. A.; German, S. R.; Dick, J. E.; Bard, A. J.; White, H. S. *ACS Nano* **2015**, *9*, 12274-12282.

16. Ivanov, A. P.; Actis, P.; Jönsson, P.; Klenerman, D.; Korchev, Y.; Edel, J. B. *ACS Nano* **2015**, *9*, 3587-3595.

17. Liu, Y.; Yobas, L. *Biosens. Bioelectron.* **2013**, *50*, 78-83.

18. Steinbock, L. J.; Otto, O.; Chimerel, C.; Gornall, J.; Keyser, U. F. *Nano Lett.* **2010**, *10*, 2493-2497.

19. Gong, X.; Patil, A. V.; Ivanov, A. P.; Kong, Q.; Gibb, T.; Dogan, F.; deMello, A. J.; Edel, J. B. *Anal. Chem*. **2014**, *86*, 835-841.

20. Fu, Y.; Tokuhisa, H.; Baker, L. A. *Chem. Commun.* **2009**, *32*, 4877-4879.

21. Babakinejad, B.; Jönsson, P.; López Córdoba, A.; Actis, P.; Novak, P.; Takahashi, Y.; Shevchuk, A.; Anand, U.; Anand, P.; Drews, A. *Anal. Chem.* **2013**, *85*, 9333-9342.

22. Shi, W.; Sa, N.; Thakar, R.; Baker, L. A. *Analyst* **2015**, *140*, 4835-4842.

23. Piper, J. D.; Clarke, R. W.; Korchev, Y. E.; Ying, L.; Klenerman, D. *J. Am. Chem. Soc.* **2006**, *128*, 16462-16463.

24. Takami, T.; Iwata, F.; Yamazaki, K.; Son, J. W.; Lee, J.-K.; Park, B. H.; Kawai, T. *J. Appl. Phys.* **2012**, *111*, 044702.

25. Rees, H. R.; Anderson, S. E.; Privman, E.; Bau, H. H.; Venton, B. J. *Anal. Chem.* **2015**, *87*, 3849-3855.

26. Karhanek, M.; Kemp, J. T.; Pourmand, N.; Davis, R. W.; Webb, C. D. *Nano Lett.* **2005**, *5*, 403-407.

27. Byers, J. C.; Paulose Nadappuram, B.; Perry, D.; McKelvey, K.; Colburn, A. W.; Unwin, P. R. *Anal. Chem.* **2015**, *87*, 10450-10456.

28. Yuill, E. M.; Sa, N.; Ray, S. J.; Hieftje, G. M.; Baker, L. A. *Anal. Chem.* **2013**, *85*, 8498-8502.

29. Yuill, E. M.; Shi, W.; Poehlman, J.; Baker, L. A. *Anal. Chem.* **2015**.

30. Schulte, A.; Nebel, M.; Schuhmann, W. *Annu. Rev. Anal. Chem.* **2010**, *3*, 299-318.

31. Korchev, Y.; Milovanovic, M.; Bashford, C.; Bennett, D.; Sviderskaya, E.; Vodyanoy, I.; Lab, M. *J. Microsc.* **1997**, *188*, 17-23.

32. Shevchuk, A. I.; Gorelik, J.; Harding, S. E.; Lab, M. J.; Klenerman, D.; Korchev, Y. E. *Biophys. J.* **2001**, *81*, 1759-1764.

33. Amemiya, S.; Bard, A. J.; Fan, F.-R. F.; Mirkin, M. V.; Unwin, P. R. *Annu. Rev. Anal. Chem.* **2008**, *1*, 95-131.

34. Hansma, P.; Drake, B.; Marti, O.; Gould, S.; Prater, C. *Science* **1989**, *243*, 641-643.

35. Edwards, M. A.; Williams, C. G.; Whitworth, A. L.; Unwin, P. R. *Anal. Chem.* **2009**, *81*, 4482-4492.

36. Chen, C. C.; Zhou, Y.; Baker, L. A. *Annu. Rev. Anal. Chem.* **2012**, *5*, 207-28.

37. Happel, P.; Thatenhorst, D.; Dietzel, I. D. *Sensors* **2012**, *12*, 14983.

38. McKelvey, K.; Perry, D.; Byers, J. C.; Colburn, A. W.; Unwin, P. R. *Anal. Chem.* **2014**, *86*, 3639-46.

39. Morris, C. A.; Chen, C.-C.; Baker, L. A. *Analyst* **2012**, *137*, 2933-2938.

40. Ebejer, N.; Schnippering, M.; Colburn, A. W.; Edwards, M. A.; Unwin, P. R. *Anal. Chem.* **2010**, *82*, 9141-9145.

41. Rheinlaender, J.; Schäffer, T. E. *J. Appl. Phys.* **2009**, *105*, 094905.

42. Thatenhorst, D.; Rheinlaender, J.; Schäffer, T. E.; Dietzel, I. D.; Happel, P. *Anal. Chem.* **2014**, *86*, 9838-9845.

43. Perry, D.; Al Botros, R.; Momotenko, D.; Kinnear, S. L.; Unwin, P. R. *ACS Nano* **2015**, *9*, 7266-76.

44. McKelvey, K.; Kinnear, S. L.; Perry, D.; Momotenko, D.; Unwin, P. R. *J. Am. Chem. Soc.* **2014**, *136*, 13735-13744.

45. Perry, D.; Paulose Nadappuram, B.; Momotenko, D.; Voyias, P. D.; Page, A.; Tripathi, G.; Frenguelli, B. G.; Unwin, P. R. J. *Am. Chem. Soc.* **2016**, *138*, 3152–3160

46. Sa, N.; Lan, W.-J.; Shi, W.; Baker, L. A. *ACS Nano* **2013**, *7*, 11272-11282.

47. Lan, W.-J.; Kubeil, C.; Xiong, J.-W.; Bund, A.; White, H. S. *J. Phys. Chem. C* **2014**, *118*, 2726-2734.

48. Henriquez, R. R.; Ito, T.; Sun, L.; Crooks, R. M. *Analyst* **2004**, *129*, 478-482.

49. Macpherson, J. V.; Unwin, P. R. *J. Phys. Chem.* **1995**, *99*, 14824-14831.

50. Bard, A. J.; Faulkner, L. R. Electrochemical Methods: Fundamentals and Applications; Wiley New York, 1980; Vol. 2.

51. Rheinlaender, J.; Schäffer, T. E. *Soft Matter* **2013**, *9*, 3230-3236.

52. Takahashi, Y.; Ito, K.; Wang, X.; Matsumae, Y.; Komaki, H.; Kumatani, A.; Ino, K.; Shiku, H.; Matsue, T. *Electrochemistry* **2014**, *82*, 331-334.

53. Actis, P.; Mak, A. C.; Pourmand, N. *Bioanal. Rev.* **2010**, *1*, 177-185.

54. Del Linz, S.; Willman, E.; Caldwell, M.; Klenerman, D.; Fernández, A.; Moss, G. *Anal. Chem.* **2014**, *86*, 2353-2360.

55. Ying, L.; White, S. S.; Bruckbauer, A.; Meadows, L.; Korchev, Y. E.; Klenerman, D. *Biophys. J.* **2004**, *86*, 1018-1027.

56. Caldwell, M.; Del Linz, S. J.; Smart, T. G.; Moss, G. W. *Anal. Chem.* **2012**, *84*, 8980-8984.

57. Sánchez, D.; Johnson, N.; Li, C.; Novak, P.; Rheinlaender, J.; Zhang, Y.; Anand, U.; Anand, P.; Gorelik, J.; Frolenkov, G. I. *Biophys. J.* **2008**, *95*, 3017-3027.

58. Chen, C.-C.; Derylo, M. A.; Baker, L. A. *Anal. Chem.* **2009**, *81*, 4742-4751.

59. Chen, C.-C.; Baker, L. A. *Analyst* **2011**, *136*, 90-97.

60. Wei, C.; Bard, A. J.; Feldberg, S. W. *Anal. Chem.* **1997**, 69, 4627-4633.

61. White, H. S.; Bund, A. *Langmuir* **2008**, *24*, 2212-2218.

62. Momotenko, D.; Cortes-Salazar, F.; Josserand, J.; Liu, S.; Shao, Y.; Girault, H. H. *Phys. Chem. Chem. Phys.* **2011**, *13*, 5430-5440.

63. Kubeil, C.; Bund, A. *J. Phys. Chem. C* **2011**, *115*, 7866-7873.

64. Behrens, S. H.; Grier, D. G. *J. Chem. Phys* **2001**, *115*, 6716-6721.

65. Zhou, L.; Zhou, Y.; Baker, L. A. *Electrochem. Soc. Interface* **2014**, *23*, 47-52.

66. Cai, H.; Wang, Y.; Yu, Y.; Mirkin, M. V.; Bhakta, S.; Bishop, G. W.; Joshi, A. A.; Rusling, J. F. *Anal. Chem.* **2015**, *87*, 6403-6410.

67. Klenerman, D.; Korchev, Y. E.; Davis, S. *J. Curr. Opin. Chem. Biol.* **2011**, *15*, 696-703.

68. Gorelik, J.; Shevchuk, A. I.; Frolenkov, G. I.; Diakonov, I. A.; Kros, C. J.; Richardson, G. P.; Vodyanoy, I.; Edwards, C. R.; Klenerman, D.; Korchev, Y. E. *Proc. Natl. Acad. Sci. U. S. A.* **2003**, *100*, 5819-5822.

69. Girault, H. H. Analytical and Physical Electrochemistry; CRC Press, 2004.

70. Rodgers, P. J.; Amemiya, S.; Wang, Y.; Mirkin, M. V. *Anal. Chem.* **2009**, *82*, 84-90.

71. Clarke, R. W.; Zhukov, A.; Richards, O.; Johnson, N.; Ostanin, V.; Klenerman, D. *J. Am. Chem. Soc.* **2013**, *135*, 322-329.

# Chapter 6. Surface Charge Visualisation at Viable Living Cells

The capabilities of SICM for surface charge mapping have thus far been demonstrated in the previous chapters for model substrates in low ionic strength. In this chapter, the possibility of surface charge mapping in physiological conditions is highlighted with viable living cells used as the substrate. SICM has been widely used for morphological studies of living systems. Herein it is demonstrated that the sensitivity of SICM for surface charge mapping extends to higher electrolyte concentrations, making it a powerful technique for answering fundamental questions about the relationship between the surface charge of the cell membrane and heterogeneities and their function. Chapter 5 revealed how with a full characterisation of the nanopipette, FEM simulations can allow SICM to be a quantitative tool for surface charge mapping and this is built upon in this chapter for revealing quantitative estimates of the surface charge of living cells both in low ionic strength and physiological conditions.

This chapter was published as an article in *The Journal of the American Chemical Society*. In this work all experiments and simulations were performed by myself. Cell culturing and preparation was performed by Binoy Paulose Nadappuram and Philip D. Voyias.

# Surface Charge Visualization at Viable Living Cells

David Perry[1,2], Binoy Paulose Nadappuram[1], Dmitry Momotenko[1], Philip D. Voyias[3], Ashley Page[1,2], Gyanendra Tripathi[3], Bruno G. Frenguelli[4] and Patrick R. Unwin[1,*]

[1]Department of Chemistry, [2]MOAC Doctoral Training Centre, [3]Division of Metabolic and Vascular Health, Warwick Medical School and [4] School of Life Sciences, University of Warwick, Coventry, CV4 7AL, United Kingdom.

***Corresponding Author**

p.r.unwin@warwick.ac.uk

## 6.1 Abstract

Scanning ion conductance microscopy (SICM) is demonstrated to be a powerful technique for quantitative nanoscale surface charge mapping of living cells. Utilising a bias modulated (BM) scheme, in which the potential between a quasi-reference counter electrode (QRCE) in an electrolyte-filled nanopipette and a QRCE in bulk solution is modulated, it is shown that both the cell topography and the surface charge present at cellular interfaces can be measured simultaneously at high special resolution using dynamic potential measurements. Surface charge is elucidated by probing the properties of the diffuse double layer (DDL) at the cellular interface and the technique is sensitive at both low ionic strength and under typical physiological (high ionic strength) conditions. The combination of experiments that incorporate pixel-level self-referencing (calibration) with a robust theoretical model, allows for the analysis of local surface charge variations across cellular interfaces, as demonstrated on two important living systems. First, charge mapping at *zea mays* root hairs shows that there is a high negative surface charge at the tip of the cell. Second, it is shown that there are distinct surface charge distributions across the surface of human adipocyte cells, whose role is the storage and regulation of lipids in

mammalian systems. These are new features, not previously recognised, and their implications for the functioning of these cells are highlighted.

## 6.2 Introduction

Surface charge is known to play a key role in a host of different dynamic interfacial processes and equilibria,[1] from the stability of colloids[2,3] and crystal growth/dissolution[4,5] to nanoscale analytical devices[6-8] and biological systems, where it determines structure and function at levels ranging from biomolecular assemblies[9] to complex life forms such as living cells and organisms.[10-13] Interfacial charge is thought to influence cellular communication,[14-16] cell adherence to surfaces,[17-19] the uptake of nutrients,[20] molecules and particles,[21-24] and cell growth and division,[25,26] among other processes. The ability to visualise local surface charge, and also to identify charge heterogeneities on living cell surfaces, would thus be hugely beneficial in unravelling fundamental questions of cell function.

Probing surface charge, however, remains a difficult task owing to a lack of robust techniques capable of measurements at the micro- and nanoscale in complex (relevant) environments. This is particularly the case for studies of living systems, where physiological conditions are usually required to maintain cell viability. Typically, physiological media require aqueous electrolyte solutions of high ionic strength (~150 mM), and under these conditions the diffuse double layer (DDL) is compressed to a sub-nanometre scale.[27,28] In such cases, mapping surface charges by probing the DDL around viable cells becomes troublesome, since the surface charge is well screened by electrolyte ions. This difficulty is compounded by the fact that living cells are intrinsically soft, fragile and sensitive to external perturbation/stimulation. While atomic force microscopy (AFM) has been used extensively for mapping the surface properties of living cells,[29-33] as well as being used for the study of double layer characteristics of inert and living systems,[34-40] AFM force-distance curves are not easily analysed because various forces can act on the probe.[41,42] Moreover, at high electrolyte concentrations (physiological conditions), the tip-substrate distance over which AFM becomes sensitive to surface charge

becomes extremely compressed to a nm, or less, making charge measurements particularly challenging.

In this work we describe how the surface charge at living cells can be imaged, probed and analysed through the use of local ion-conductance measurements. Scanning ion conductance microscopy (SICM),[27,43-46] involves the use of a nanopipette filled with electrolyte positioned above a substrate that is also bathed in electrolyte. A potential is typically applied between a quasi-reference counter electrode (QRCE) in the nanopipette and one in bulk solution to generate an ionic current.[47,48] Changes in resistance as the probe approaches an interface (sample) allows the ionic current to be used for positional feedback for high-resolution topographical imaging.[43,44,49,50] For improved stability, a vertical oscillation of pipette position[51] or bias modulation[52] (BM) is applied to generate alternating components of the ionic current (AC) as the feedback signal.

The capabilities of SICM have recently been expanded to embrace the imaging and probing of charge distributions on a variety of model substrates semi-quantitatively via surface induced rectification (SIR) of the ion current.[53-56] SICM does not probe the surface charge itself, but the ionic atmosphere around a charged interface,[52] making the technique less invasive compared to other methods (*e.g.* atomic force microscopy, AFM) to the substrate, which is desirable for the study of living cells in their natural state. Herein, using a combination of BM-SICM and finite element method (FEM) simulations, we demonstrate that even in solutions of high salt concentration (ionic strength 150 mM) it is possible to quantify simultaneously the surface charge at living cells and cell topography, as well as to identify heterogeneously distributed features across cellular membrane surfaces. Our studies are exemplified through studies of: *zea mays* (common corn) root hair cells at low electrolyte concentrations, where knowledge of cell charge would aid in understanding the absorption mechanisms important in this system,[57] and human adipocytes under physiological conditions, where the cell surface charge plays a great role in cell uptake properties.[58]

## 6.3 Materials and Methods

### 6.3.1 Solutions

Milli-Q reagent grade water (resistivity ca. 18.2 MΩ cm at 25°C) was used for all solutions. 10 mM KCl (Sigma-Aldrich) solution was prepared and used for the SICM experiments involving root hair cells. Preadipocyte cells were grown to confluence in Dulbecco's Modified Eagle Medium (DMEM)/Ham's F-12 phenol-free medium (Invitrogen, UK) containing 10% FCS, penicillin (100 U/ml), streptomycin (100 μg/ml), and transferrin (5 μg/ ml). Differentiation media (Promocell, Germany) for the preadipocytes contained biotin (8 μg/ml), insulin (500 ng/ml), Dexamethasone (400 ng/ml), 3-isobutyl-1-methylxanthine (IBMX, 44 μg/ml), L-Thyroxin (9 ng/ml) and Ciglitazone (3 μg/ml). The adipocytes were then grown in nutrition media (NM) containing DMEM/Ham's F-12, 3% FCS, D-biotin (8 μg/ml), insulin (500 ng/ml) and dexamethasone (400 ng/ml). Adipocyte cells were imaged in DMEM/F-12 media (Invitrogen) containing 1 Adipocyte Nutrition Medium Supplement Pack (Promocell).

### 6.3.2 Cell Culturing and Preparation

Human Abdominal Subcutaneous (AbSc) adipose tissue (AT) was digested with collagenase to isolate preadipocytes, which were cultured in tissue culture flasks until confluent and then trypsinised to obtain cells used in this work. The preadipocytes from the same passage were then grown to confluence in the above-specified growth media. At confluence, preadipocytes were differentiated in differentiation media for 72 h. After this period, the differentiating cells were grown in nutrition media until fully differentiated (14–18 days) and the viability of adipocytes was assessed using the trypan blue dye exclusion method[59] (Sigma–Aldrich).

*Zea mays* seeds (Avenir, Syngenta) were germinated between two layers of damp paper at 25 °C for four days. This provided a root of approximately 20 mm in length with a dense layer of root hair cells. At this stage of development, all nutrients for the corn growth are still provided by the seed.

### 6.3.3 Imaging Substrates

AbSc cells were adhered to a collagen-coated petri dish in order to keep them stationary for imaging purposes without impacting their viability. The corn roots were attached away from the point of imaging to a glass bottomed petri dish (3512, WillcoWells) using SPM adhesive tabs (Agar Scientific).

### 6.3.4 Nanopipette Fabrication

For most BM-SICM experiments, nanopipettes (~90 nm radius at the opening, dimensions measured using a JEOL 2000FX transmission electron microscope (TEM)), were pulled from borosilicate glass capillaries (o.d. 1.2 mm, i.d. 0.69 mm, Harvard Apparatus) using a laser puller (P-2000, Sutter Instruments; pulling parameters: Line 1: Heat 330, Fil 3, Vel 30, Del 220, Pul -, Line 2: Heat 330, Fil 3, Vel 40, Del 180, Pul 120). For the high-resolution scans of root hair cells, nanopipettes (~20 nm radius at the opening) were pulled from quartz capillaries (o.d. 1 mm, i.d 0.5 mm, Friedrich & Dimmock, pulling parameters: Line 1: Heat 750, Fil 4, Vel 30, Del 150, Pul 80, Line 2: Heat 650, Fil 3, Vel 40, Del 135, Pul 150). Typical TEM images of a borosilicate and of a quartz SICM probe, as used herein, are shown in Supporting Information 6.6.1, Figure 6.7.

### 6.3.5 Instrumentation

The SICM probe movement normal to the substrate was controlled using a piezoelectric positioning stage with a travel range of 38 µm (P-753-3CD, Physik Instrumente) whilst lateral movement of the substrate for XY positioning was achieved using a two-axis piezoelectric positioning system (Nano-BioS300, Mad City Labs, Inc.). A lock-in amplifier (SR830, Stanford Research Systems) was used to apply the oscillating bias in the BM-SICM setup and to extract the AC ion current amplitude and phase used for surface charge mapping and SICM feedback. The control of instrumentation and data collection was achieved using a custom written LabVIEW (2013, National Instruments) program through an FPGA card (NI PCIe-7852R, National Instruments) on the Warwick Electrochemical-Scanning Probe Microscopy platform.

### 6.3.6 Topographical and Surface Charge Mapping

The BM-SICM setup was built on the stage of an inverted optical microscope (Axiovert 40 CFL, Zeiss). To generate topographical and surface charge maps of the living cells, the probe was approached towards the surface at a rate of 500 nm $s^{-1}$ for the lower resolution scans and 100 nm $s^{-1}$ for the higher resolution root hair scan, while applying a small oscillation to the bias (10 mV r.m.s. amplitude, 270 Hz) about 0 V (so that SICM was a topographical probe)[54] until an increase in the AC phase signal was observed (0.5°for the lower resolution scans, 0.25° for high-resolution imaging with smaller nanopipettes). The vertical position of the piezoelectric actuator at this point was used to generate topographical maps of cells.[52] The tip potential was then linearly swept from 0 V to -0.4 V and then to 0.4 V and back to 0 V (all with respect to Ag/AgCl QRCE in solution bulk) at a rate of 800 mV $s^{-1}$ and the AC phase and DC signal recorded for polarity-dependent surface charge mapping.[54] The tip was then retracted from the point of closest approach by a set distance (7 μm in the case of the root cells, 1 μm in the case of adipocyte cells), to prevent contact between the nanopipette and cell during the lateral movement as the probe was translated over the support-cell boundary, and the voltage sweep was again performed in order to obtain a bulk response for the normalisation of ionic currents. The probe was then translated to the next pixel and the sequence was repeated. This approach is not only powerful in revealing both surface charge and topography unambiguously, but is a pixel-level self-referencing technique enabling ultra-sensitive surface charge measurements.

### 6.3.7 FEM Simulations

A 2D axisymmetric FEM simulation was performed in COMSOL Multiphysics (v4.4) using the transport of diluted species and electrostatics modules for a 90 nm radius glass nanopipette (geometrical arrangement of the probe determined from TEM) in both 10 mM KCl and 150 mM NaCl solution, which were the major components of the imaging media used for the root hair and adipocyte experiments, respectively. The tip was positioned at 30 nm (root hair) and 40 nm (adipocyte) above a substrate

to which a varying surface charge density was applied (mimicking the experiments). A bias of +/- 0.4 V was applied to the nanopipette with respect to bulk. A surface charge of -1.125 mC $m^{-2}$ was applied at the glass walls of a nanopipette probe, as used in previous work.[53-55,60] FEM simulations were also performed of a 40 nm diameter quartz nanopipette above a charged substrate in 10 mM electrolyte at a working distance of 15 nm to allow further quantification of the high-resolution root hair scan. For more details of the FEM model see Supporting Information 6.6.1.

## 6.4 Results and Discussion

### 6.4.1 Principles of Surface Charge Mapping with a Nanopipette

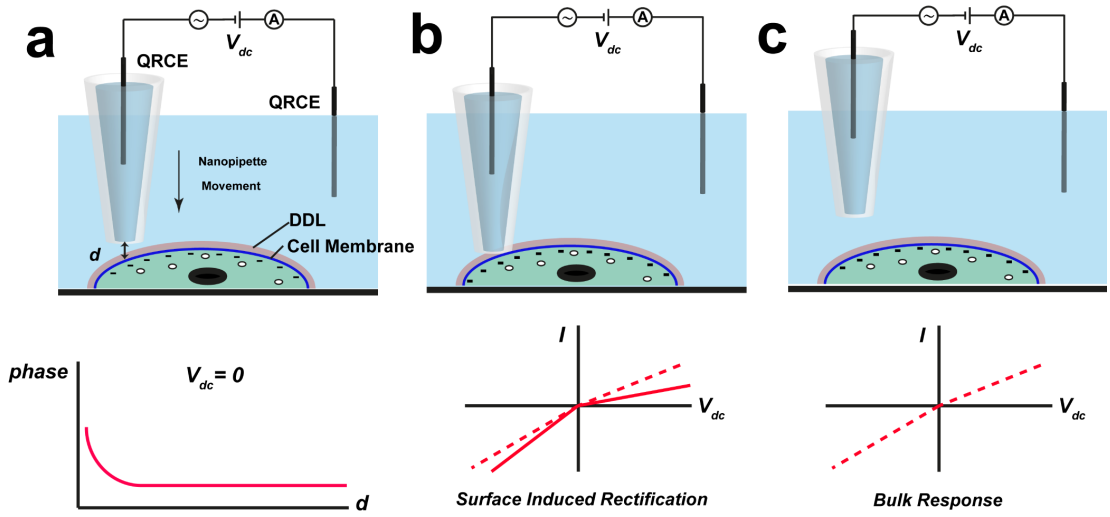


**Figure 6.1.** Schematic of the BM-SICM approach for non-covoluted surface charge/topographical imaging. A typical scan routine at each image pixel involves: **(a)** approaching the interface at 0 V ($V_{dc}$) net bias for determination of the topography with the AC phase due to the bias modulation used for accurate positioning (feedback) at tip to surface distance, *d*; **(b)** recording a voltammogram with the tip near the surface (distance defined by AC phase set point) by sweeping the pipette bias, $V_{dc}$ (between the 2 QRCEs), and measuring the corresponding DC current, *I*, as indicated by the solid line; and **(c)** retracting the probe into bulk, followed by a voltammetric scan to obtain data for normalisation of surface responses (dashed line).

The basic concept for independent mapping of the topography and surface charge of cells is illustrated in Figure 6.1. The double layer at the surface has increasing effect on the nanopipette current at larger driving bias ($V_{dc}$), where surface induced rectification can considerably modify net ionic transport to and from the nanopipette.[54] In contrast, probe positioning is most accurate when surface charge effects are minimised, *i.e.* with no net nanopipette bias, where the effects of SIR are negligible.[54] Mapping of surface charge independently from topography can thus be performed by approaching the surface at 0 V net bias (using the AC phase signal from BM for feedback) to achieve a desired tip to surface distance, as shown on Figure 6.1a. A voltammogram is then run with the nanopipette situated at this desired position near the surface (Figure 6.1b). This response is compared with the current-voltage scan with the nanopipette in solution bulk (i.e. at distances larger than a few tip diameters, Figure 6.1c), in a self-referencing format at each pixel in an image.

Figure 6.2 depicts the principles of surface charge mapping using SICM. In bulk solutions, nanopipettes may exhibit an ion current rectification (ICR)[60-62] response depending on the charge and the opening size of a nanopipette with respect to the Debye length (which, in turn, depends on the ionic strength).[60,62] This arises because there is generally a cation-selective region (double layer) near the walls of the nanopipette, due to the negative surface charge at nanopipettes (glass or quartz) in aqueous solution, at neutral and higher pH,[63] coupled with asymmetric mass transport of ions from outside of the nanopipette (high mass transport rates due to hemispherical ion flow) and more restricted ion flow inside the nanopipette. As a result, when a negative tip bias is applied with respect to bulk (Figure 6.2a), cations accumulate in the nanopipette as they enter the nanopipette at a faster rate than they can migrate up the nanopipette, resulting in a high conductance state. Then, when the nanopipette is brought towards a negatively charged substrate (Figure 6.2b) the flux of cations to the nanopipette increases further because of the high cation concentration in the diffuse double layer at the interface. This manifests as SIR and an enhanced current.[53,55] In the case where the nanopipette is brought towards a positively charged interface (Figure 6.2c), where there is an anion

selective region, the migration of cations to the nanopipette opening is hindered, resulting in a smaller current magnitude at negative tip bias.

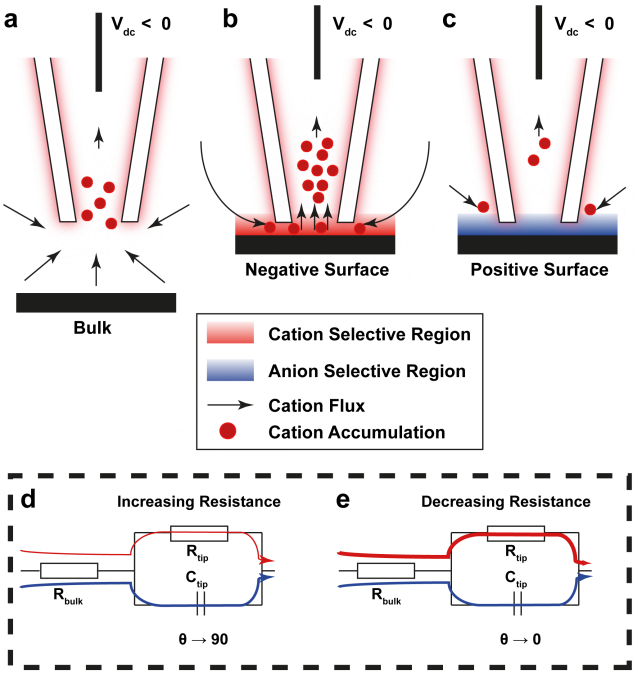


**Figure 6.2.** Cartoons (not to scale) demonstrating the charge distribution around a negatively charged nanopipette in bulk **(a)**, near a negatively charged surface **(b)** and near a positively charged surface **(c)** and mass transport of cations (as an example) to the nanopipette with the internal solution biased negatively with respect to an exterior electrode. Circuit diagrams representing the nanopipette tip as an RC circuit for which there is a reduced current through the nanopipette opening when near a surface, (for example, as compared to when in bulk) for which $R_{tip}$ increases, resulting in a positive phase shift of AC currents, θ, towards 90 degrees,[54] i.e. towards the ideal capacitive behaviour **(d)** and when there is enhanced current through the end of the nanopipette opening (*e.g.* near a surface) so that $R_{tip}$ decreases, resulting in a negative phase shift of AC current, θ, towards 0 degrees, i.e. towards the ideal resistor behaviour **(e)**.

When the tip bias is reversed (so that the tip electrode is positive with respect to the bulk), the mass transport scenario inverts, so that the more positive (less negative) the surface charge, the lower the resistance and the higher the current. The effect of the pipette conductance state on the AC response can be

estimated using an RC circuit diagram, representing the pipette tip region, as shown in Figure 6.2d and Figure 6.2e. As the conductance state of the pipette changes near the charged interface, the AC current through the capacitive element will either increase or decrease, with corresponding enhancement or reduction of the tip resistance, leading to variation of the AC phase shift towards 90° or 0°, respectively, depending on the surface charge.

### 6.4.2 FEM Simulations

FEM simulations (see details in Supporting Information 6.6.1), performed at the tip distances to be employed in the BM-SICM experiments, and obtained with high accuracy from experimental approach curves at zero net bias,[52] allowed the generation of membrane charge-tip current characteristics (at the extreme CV potentials) for the quantitative estimation of the cell membrane surface charge for subsequent experiments. Simulations were run for both low (Figure 6.3a) and high (Figure 6.3b) electrolyte conditions.

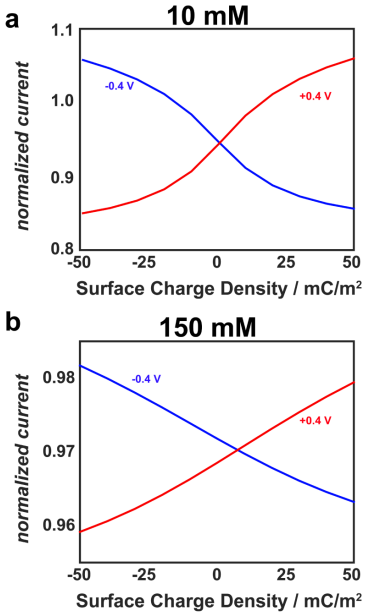


**Figure 6.3.** Working curve of normalised ionic current at a tip distance of **(a)** 30 nm above a charged interface in 10 mM electrolyte solution and **(b)** 40 nm above a charged interface in 150 mM electrolyte solution of varying surface charge density. The QRCE in the 90 nm radius pipette was biased +0.4 V (red) and -0.4 V (blue) with respect to that in bulk solution.

It can be seen that in the low electrolyte conditions, there is a much greater sensitivity to the surface charge of the substrate but that it is still possible, in media of high ionic strength, to observe the effects of varying surface charge on the expected ionic current at both extreme tip polarities over the range of surface charges considered here, opening up the possibility of surface charge mapping under physiological conditions. The results of these simulations provide working curves for further estimation of surface charge magnitudes on the cellular membranes during imaging and establish a quantitative footing for the technique.

### 6.4.3 Mapping Charge at Root Hair Cells: Proof-of-Concept Measurements

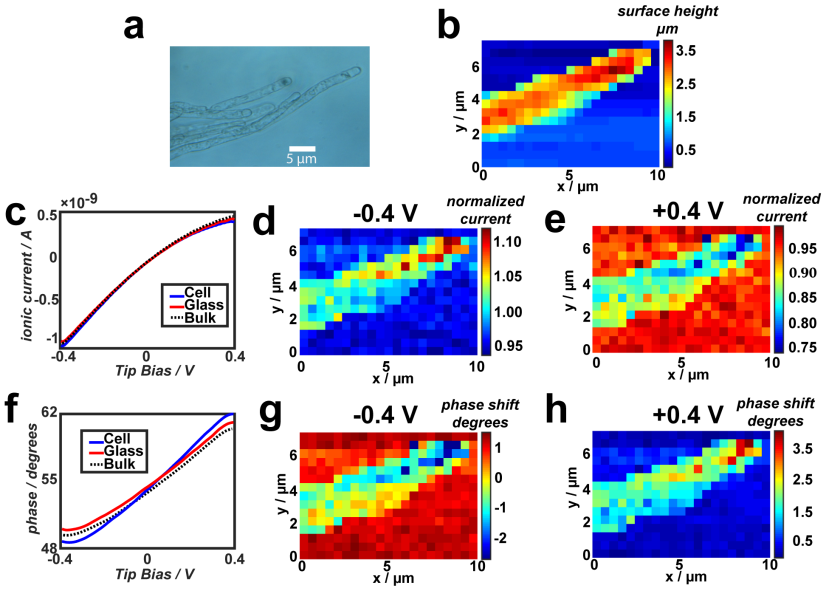


**Figure 6.4.** BM-SICM topographical and charge imaging on *zea mays* root hair cells. **a)** Optical microscope image of the cell sample on a glass slide substrate. **b)** Recorded topographical image with a 90 nm-radius glass nanopipette at 0 V mean bias and 10 mV harmonic oscillation at 270 Hz. The pixel pitch of the image is 500 nm and there is no processing or interpolation of data. **c)** Examples of acquired DC ionic current voltammograms near (tip 30 nm from) glass and cell surfaces (solid red and blue lines) compared to the response with the same nanopipette in bulk (dashed black line). Normalised (with respect to bulk values) DC ion current images at negative **(d)** and positive **(e)** tip biases. Corresponding AC phase shift voltammograms **(f)** and SICM images **(g-h)**.

To demonstrate the capabilities of BM-SICM to detect and map the surface charge of living cells, dynamic surface charge, and topographical, maps were first acquired on *zea mays* root hairs (see optical micrograph on Figure 6.4a) in 10 mM KCl solution (pH 6.5). Root hair cell walls comprise primarily of cellulose microfibrils and other polysaccharides such as pectin,[64] and protect the root hair from pressure effects, maintain cell shape as well as acting as a filter, in which surface charge is expected to play an important role.[20] A typical topographical image of a root cell tip, extracted from the absolute values of vertical piezoelectric positioner extension, from a series of approaches, is shown on Figure 6.4b. Note that there is no interpolation or other post-processing algorithms employed for these raw data. The lateral dimensions of the cell in this image correspond well with those from optical microscopy and reveal the cell height to be *ca.* 3 μm.

Typical nanopipette voltammetric responses, acquired during the image in Figure 6.3b with the probe near the cell, the glass substrate and in bulk, are each compared in Figure 6.4c. It can be seen that the bulk current-voltage (*I*-*V*) response is typical of ion current rectification of a negatively charged nanopipette with a higher conductance state (accumulation of cations at the nanopipette) at negative tip bias, and a lower conductance state (expulsion of cations) at positive tip bias resulting in a diminished current.[54,55,60,62] As can be seen, there are differences between each of these voltammograms, which are magnified at the most extreme potentials (+/- 0.4 V). The *I*-*V* response over the cell, exhibits stronger (magnified) rectification compared with the nanopipette in bulk solution and near a glass surface, an effect that is diagnostic of more negative surface charge on the cell surface.

The measured responses at the extremes of the potential scan (-0.4 V and 0.4 V tip bias) recorded at each pixel of the topographical image in Figure 6.4b, can be represented in a form of images, as shown in Figure 6.4d and e, respectively. Observations at negative tip bias (Figure 6.4d) evidence an enhanced current (with respect to bulk) above the root cell surface, which is indicative of the presence of a negative surface charge on the cell wall (as explained in Figure 6.2b),[20] most likely due to the presence of the polysaccharides, such as pectin. The glass surface at neutral pH also bears a slight negative charge caused by dissociation of silanol

groups (point of zero charge at glass or silica in aqueous electrolytes is in pH range 2 – 4).[63]

The AC ion current components, and especially phase shift, offer higher sensitivity towards surface charge detection in comparison to measured DC currents. This is evident from the voltammetric data in Figure 6.4f, which shows much more noticeable differences in the AC voltammetric phase response between the bulk solution, glass and cell surfaces as compared to the DC data in Figure 6.4c. Furthermore, the AC phase images in Figure 6.4g and h reveal greater contrast and better signal/noise between the cell surface and glass support.

A particularly interesting charge feature can be observed in the region at the tip of the root hair (right hand side top corner on images on Figure 6.4d–e and g–h), where the higher contrast (either larger change in the normalised current with respect to bulk, or larger phase shift) indicates enhanced negative surface charge in this region. The negative surface charge of the cell helps regulate the exchange of cations across it and the exclusion of anions.[20] Ion-selective microelectrode measurements have shown that there is enhanced calcium flux to the tip of root hairs[65] and our measurements indicate that the enhanced negative charge in this location may play a role in this relative enhancement of flux (in low–moderate electrolyte strengths).

It is important to consider whether there is any significant effect (or artefact) of the SICM tip on the ion distribution probed. For example, were the electric field at the nanopipette to induce the transport of cations across the cell membrane, the effects seen would be magnified at negative tip potentials but not at positive potentials, and one would therefore observe a different apparent charge at the extreme positive and negative potentials, which is not the case in practice. The electric field at the pipette tip is not expected to induce any significant ionic transport through the cellular membrane, as the membrane resistance (10-100 GΩ)[66,67] is a few orders of magnitude higher than the resistance of the tip-to-substrate gap at the point of closest approach (of order of 10-100 MΩ), ensuring reliable topography and surface charge measurements.

Comparing the normalised current at the two extreme potentials presented in Figure 6.4 to the simulated working curves (Figure 6.3a) one can estimate surface charge magnitudes on the cellular membrane (around -20 mC $m^{-2}$ for the root hair). The surface charge estimate for the root hair is within the range of average values estimated in previous work on ensembles of cells using other techniques,[68] giving confidence in our new approach. The charged feature at the tip of the root hair, which has not been seen previously, has a much higher charge value of around -50 mC $m^{-2}$.

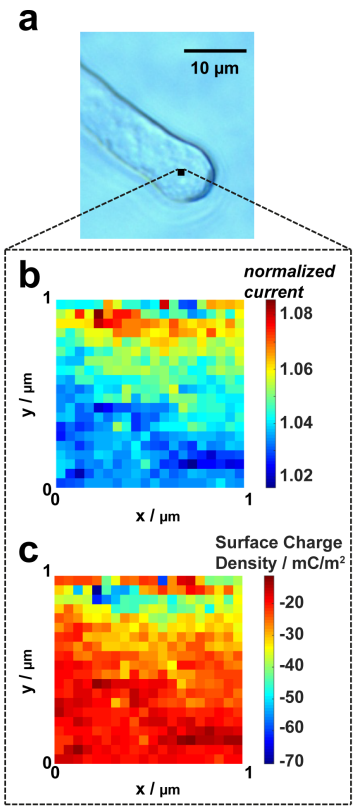


**Figure 6.5.** High-resolution surface charge map of a root hair tip with 50 nm pixel size. **a)** An optical image of the scanned root hair with the scanned region represented by a black square, **(b)** normalised current at -0.4 V tip bias with respect to bulk, and **(c)** map of surface charge in the region scanned based on FEM simulations**.**

Higher resolution BM-SICM images (1 µm × 1 µm area), acquired with a 40 nm diameter nanopipette on the tip region of the root cell (see Figure 6.5a), also evidenced significant surface charge heterogeneities at the cellular interface. Figure

6.5b depicts a typical normalised current map that was used for further quantification of charge magnitudes, aided by FEM simulations (details in Supporting Information 6.6.2). It can be seen from Figure 6.5c that the majority of the scanned region exhibited a surface charge of ca. -20 mC $m^{-2}$, similar to that observed in lower resolution images, but some regions of the high-resolution scan showed highly localised surface charges approaching -50 mC $m^{-2}$ – -60 mC $m^{-2,}$.

### 6.4.4 Surface Charge Mapping in Physiological Conditions

In many cases, the choice of medium for biological materials is rather limited, and many cell types need to be kept in physiological conditions (typically, electrolyte of high ionic strength buffered to pH 7.2) to maintain an appropriate osmotic pressure and electrical potential across the cellular membrane. Unlike the plant cells studied above, AbSc cells, do not exhibit a cell wall to protect the cell membrane from changes in osmotic pressure. As such, it is essential that they are maintained in media of ionic strength and composition similar to that of the extracellular conditions in which they would be present in the body; ionic strength of around 150 mM, containing predominantly NaCl (~144 mM) as well as essential nutrients for cell growth, buffered to pH 7.2 (see experimental section).

Whilst the ICR and SIR phenomena manifest most prominently at low electrolyte concentrations, ICR has also been observed in electrolytes of high ionic strength (100 mM and higher) if there is a sufficient charge on the nanopipette/nanopore walls and the probe opening size is sufficiently small.[62] It is therefore reasonable to expect that SIR would also be manifest under these conditions and that particular care would be needed when SICM experiments are performed over charged substrates, including cells, as topographical images could become convoluted with charge effects when using the classical SICM arrangement.[53]

We now explore whether BM-SICM can be used to probe the DDL, and hence surface charge, under physiological conditions, simultaneously with cell topography. Figure 6.6 shows typical results of SICM scans of an AbSc cell on a collagen support ($26 \times 26$ pixels with pixel size of 200 nm), with an optical image of the scanned area

presented in Figure 6.6a. These adipocyte cells were not fully matured and had a spindle shape, similar to that of preadipocyte cells[69,70]. As can be seen from the topographical data (Figure 6.6b), the section of the cell imaged appears as a reasonably flat structure of ~2 μm width and around 1 μm in height. The DC current images (Figures 6c-d) and AC phase images (Figures 6f-g) at opposite polarities (+/- 0.4 V) demonstrate that there is a very clear contrast between the positively charged collagen substrate and the living AbSc cell (viability tested as explained in experimental section). Thus, at -0.4 V tip bias, the DC current is higher over the cell than over collagen, whereas the phase shift is greater (more positive) over collagen than over the cell. This contrast is inverted, at positive tip bias (as expected, *vide supra*). However, the measured normalised DC currents at both polarities do not exceed bulk values (*i.e.* normalised DC currents are all < 1), in contrast to the behaviour in low electrolyte media (Figure 6.4). Moreover, at negative tip bias, the phase shift is always positive, but the magnitude is sensitive to the surface chemistry.

It is important to note that these data were collected using a relatively large tip diameter of around 180 nm. The effects we observe would become more significant with smaller tip diameters (closer tip-surface separations), relative to the size of the Debye length, but the clear observation that SIR effects are apparent under these conditions (moderate tip size and high ionic strength) opens up considerable prospects for high-resolution SICM charge mapping experiments, as demonstrated previously for the root hair cells.

An interesting feature of the cell is a linear charge feature along its length, which is evidenced at both tip polarities, but has a smaller contrast at negative bias. This charge heterogeneity extends along the central part of the cell, in a small topographical "valley" apparent from the line profile across the cell presented in Figure 6.6e. This charge feature is unlikely to be a topographical artefact as the width of the topographical valley is larger than 2 tip diameters and is not observed on the side of the cell where the slope is similar in magnitude to the walls of the valley. Furthermore, this feature is observed regardless of the nanopipette probe polarity (see line profile, Supporting Information 6.6.2, Figure 6.9) and was seen in several scans of different AbSc cells. As discussed below, this region is characterised

by high positive charge and could pinpoint the location of key proteins in the cell membrane, which are considered to mediate fatty acid uptake and other functions.[71-73] The mechanism of free fatty acid transport is the subject of debate and it has been suggested that it is mediated by a still to be identified membrane protein pump.[74] Other work indicates that fatty acid transporter proteins, which span the cell membrane are characterised by the presence of the amino terminus on the extracellular side of the membrane.[75,76] This would result in a net positive charge, as observed in some regions of the AbSc cells.

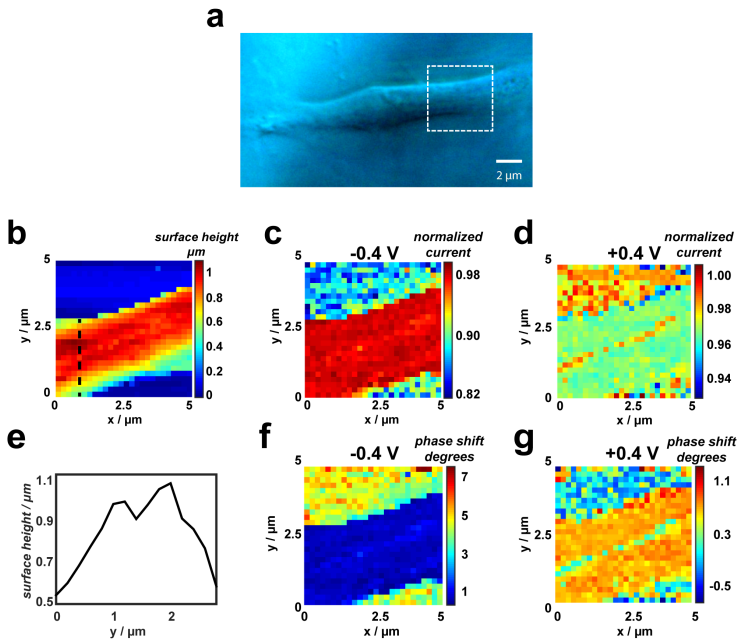


**Figure 6.6.** BM-SICM imaging of part of an adipocyte cell on a collagen support under physiological conditions (see text). **a)** Optical microscope image of the spindle shaped cell with the BM-SICM scan region indicated by white dashed lines. **b)** Topographical map, containing 26 by 26 pixels and corresponding normalised (with respect to bulk responses) DC ion current images at **(c)** negative (-0.4 V) and **(d)** positive (0.4 V) tip biases. Line profile along the black dotted line in b) shows the change in topography across the cell and reveals a trough feature in the cell surface morphology **(e)**. AC phase data at **(f)** -0.4 V and **(g)** 0.4 V reveal a strong contrast between the cell and collagen support.

For the AbSc cells in physiological conditions, comparison between theoretical and experimental results, at both positive and negative tip bias, suggests

a cell surface charge of about -15 mC $m^{-2}$ (Figure 6.3b), which is within the wide range of values quoted for other animal and plant cells, estimated using ensemble techniques.[68,77,78] The feature running along the centre of the cell has a positive charge of approximately 50 mC $m^{-2}$.

As noted above, the simulations in 150 mM electrolyte strength predict that the normalised current would not exceed 1 for the cell membrane surface charge range and tip-surface distances considered, as is seen experimentally (Figure 6.6). In contrast, at low ionic strength (10 mM) the effects of surface charge are manifested more strongly in the SICM current response. Depending on the tip potential, the normalised current is seen to result in current enhancements (or significantly diminished values) for high surface charges, as seen in the root hair data presented in Figure 4.

## 6.5 Conclusions

This work has demonstrated that SICM is a powerful probe for visualising simultaneously both the topography and surface charge at living cells in both low electrolyte and in physiological media. This work thus adds major new capability to SICM, which already rivals AFM for high-resolution cell topography imaging. The possibility of probing cell surface charge under physiological conditions, (where the double layer is compressed to small, sub-nm dimensions) is particularly noteworthy given that we employed relatively large pipette probes and tip/surface distances for much of the work. It has also been demonstrated that by reducing the size of the nanopipette opening employed, BM-SICM can become a tool for surface charge mapping with high spatial resolution. On the other hand, our work also raises some questions about the accuracy with which conventional SICM (with an applied bias) can be used to measure the true topography of cells, free from surface charge artefacts. The BM-SICM format that we describe neatly separates such effects by changing the applied bias and modulating the bias rather than the nanopipette position. This also provides a means of faster probe scanning at closer tip-substrate separations (higher spatial resolution).[79]

Our studies have highlighted the significant capabilities of BM-SICM for differentiating the surface charge of living cells from the support on which they are maintained, while also allowing for the identification of consistent heterogeneities in charge across individual cells in the case of both root hair cells and AbSc cells, where new charge features have been observed, which enhance understanding of the functioning of these cells. Importantly, the technique described is quantitative and amenable to detailed finite element method analysis. Data can thus be analysed to reveal surface charge values and 3D images of cell topography.

Ion conductance probes can be constructed with multiple channels,[80] and so in the future it may be possible to correlate surface charge with other properties, for example by sampling the cell for subsequent off-line analysis,[81] or by building spectroscopic functionality into SICM probes (*e.g.* tip enhanced Raman spectroscopy, near-field scanning optical microscopy, etc.).

## 6.6 Supporting Information

### 6.6.1 FEM Simulation Details

A representation of the 2D axisymmetric model (not to scale) used for FEM simulations in this work is depicted in Figure 6.7a together with typical transmission electron microscopy (TEM) images (Figure 6.7b and Figure 6.7c) from which dimensions of the nanopipette were extracted at a series of heights up the nanopipette. The bottom 1 mm of the nanopipette was simulated, immersed in a square domain (900 μm × 900 μm) of the axisymmetric geometry representing solution bulk. The model was constructed in Comsol Multiphysics (v4.4) using the "Transport of diluted species" and "Electrostatics" modules. The water and borosilicate glass were simulated using their respective dielectric constants (78 and 4.7, respectively). A constant electrostatic charge on the lowest 10 μm of the nanopipette walls was assumed to be -1.125 mC $m^{-2}$ as in previous work[52-55,60], whilst the charge on the substrate representing the cell or supporting substrate, was varied in between -50 mC $m^{-2}$ and 50 mC $m^{-2}$. The supporting electrolyte for the root hair simulations was 10 mM KCl whereas for the adipocytes the media used was assumed to be 150 mM NaCl, which was the primary component of the experimental

electrolyte for Adipocyte experiments. The potential was applied at the boundary at the top of the nanopipette with the furthermost right boundary of the bulk domain held at ground. The working distance for estimating the effects of surface charge on ionic current was chosen to be 40 nm for simulations in high ionic strength (150 mM) and 30 nm for simulations performed in low ionic strength (10 mM), based on approach curves from previous work in similar electrolyte conditions and similar probes.[2] The set of boundary conditions is summarized in Table 6.1.

**Table 6.1.** Summarised boundary conditions for the FEM model.

| **Boundary** | **Concentration condition** | **Potential/charge condition** |
|---|---|---|
| **B1** | $C_0$ = 150 mM | $V$ = +/- 0.4 V |
| **B2** | $J_i = 0$ | |
| **B3** | $C_0$ = 150 mM | $V = 0$ |
| **B4** | $J_i = 0$ | σ=-1.125 mC m$^{-2}$ |
| **B5** | $J_i = 0$ | $\sigma$ = varying |

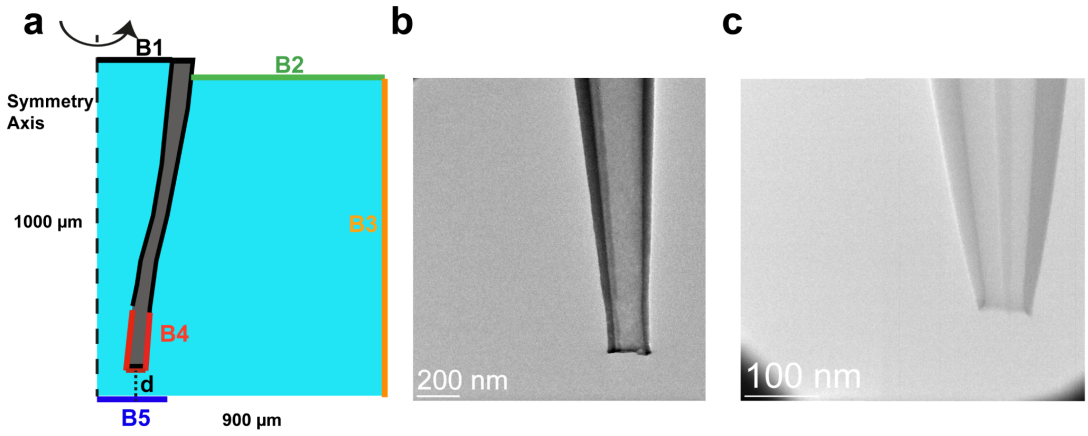


**Figure 6.7.** Not to scale schematic of the FEM simulation domain with a nanopipette positioned above a charged substrate **(a)**. Transmission electron micrograph of a typical borosilicate nanopipette **(b)** and quartz nanopipette **(c)** used in this work.

### 6.6.2. Working Curve for Quartz Nanopipette

FEM simulations were also performed of a 40 nm opening diameter nanopipette, positioned 15 nm above a charged substrate, in 10 mM electrolyte solution to mimic the conditions for high-resolution imaging. The surface charge applied to the substrate was varied between -10 mC/m$^2$ and -70 mC/m$^2$ and the expected current through the nanopipette calculated at an applied tip bias of -0.4 V, the extreme potential of the experimental potential sweep. These values were normalised to a bulk simulation where the nanopipette was positioned 3 µm from the substrate to generate a working curve of normalised current with surface charge, as shown in Figure 6.8. The simulations demonstrated that, by using smaller nanopipettes, the BM-SICM technique remained sensitive to surface charge variations and allowed for high-resolution surface charge mapping. The generated working curve could then be used to convert the normalised current recorded across the high-resolution root hair scan (Figure 6.5b) to a map of surface charge (Figure 6.5c).

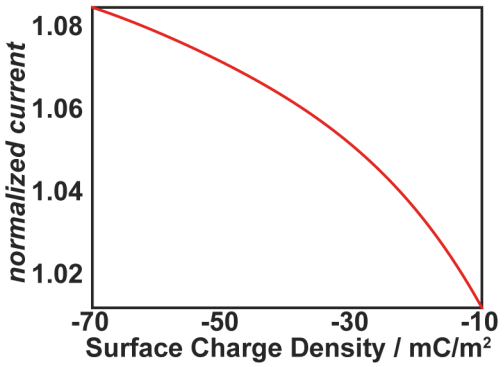


**Figure 6.8.** Working curve of varying surface charge of a substrate beneath a 40 nm diameter quartz nanopipette in 10 mM electrolyte solution, showing the effect on normalised ionic current through the nanopipette with respect to bulk at a tip bias of -0.4 V.

### 6.6.3. Adipocyte Cell Line Profiles

Line profiles are presented across one part of the heterogeneously charged feature along the black dashed line presented in Figure 6.6 of the main manuscript and

reveal a correlation between a valley on the topography map (Figure 6.6b) and the surface charge heterogeneity (Figure 6.9).

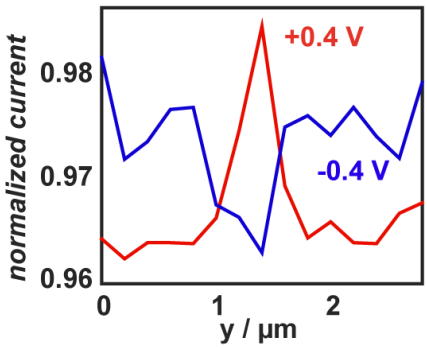


**Figure 6.9.** Line profiles of normalised current across the AbSc cell where a topographical (Figure 6.6d of manuscript) and surface charge feature was observed at positive tip bias (red) and negative tip bias (blue).

## 6.7 References


1. Trefalt, G.; Behrens, S. H.; Borkovec, M., *Langmuir* **2015**, *32*, 380-400.
2. Han, Y.; Wang, X.; Dai, H.; Li, S., *ACS Appl. Mater. Interfaces* **2012,** *4*, 4616-4622.
3. Oncsik, T.; Trefalt, G.; Csendes, Z.; Szilagyi, I.; Borkovec, M., *Langmuir* **2014,** *30*, 733-741.
4. Hellevang, H.; Miri, R.; Haile, B. G., *Cryst. Growth Des.* **2014,** *14*, 6451-6458.
5. Yanina, S. V.; Rosso, K. M., *Science* **2008,** *320*, 218-222.
6. Lan, W.-J.; Holden, D. A.; White, H. S., *J. Am. Chem. Soc.* **2011,** *133*, 13300-13303.
7. Guo, W.; Tian, Y.; Jiang, L., *Acc. Chem. Res.* **2013,** *46*, 2834-2846.
8. Armstrong, J. A.; Bernal, E. E. L. n.; Yaroshchuk, A.; Bruening, M. L., *Langmuir* **2013,** *29*, 10287-10296.
9. Cong, X.; Poyton, M. F.; Baxter, A. J.; Pullanchery, S.; Cremer, P. S., *J. Am. Chem. Soc.* **2015,** *137*, 7785-7792.
10. Asati, A.; Santra, S.; Kaittanis, C.; Perez, J. M., *ACS Nano* **2010,** *4*, 5321-5331.
11. Ghosh, P. S.; Kim, C.-K.; Han, G.; Forbes, N. S.; Rotello, V. M., *ACS Nano* **2008,** *2*, 2213-2218.

12. Zenobi, R., *Science* **2013,** *342*, 1243259.

13. Lesniak, A.; Salvati, A.; Santos-Martinez, M. J.; Radomski, M. W.; Dawson, K. A.; Åberg, C., *J. Am. Chem. Soc.* **2013,** *135*, 1438-1444.

14. Lee, K.-D.; Hong, K.; Papahadjopoulos, D., *Biochim. Biophys. Acta, Biomembr.* **1992,** *1103*, 185-197.

15. Christianson, H. C.; Svensson, K. J.; van Kuppevelt, T. H.; Li, J.-P.; Belting, M., *Proc. Natl. Acad. Sci. U. S. A.* **2013,** *110*, 17380-17385.

16. Shi, X.; Bi, Y.; Yang, W.; Guo, X.; Jiang, Y.; Wan, C.; Li, L.; Bai, Y.; Guo, J.; Wang, Y., *Nature* **2013,** *493*, 111-115.

17. Bakhti, M.; Snaidero, N.; Schneider, D.; Aggarwal, S.; Möbius, W.; Janshoff, A.; Eckhardt, M.; Nave, K.-A.; Simons, M., *Proc. Natl. Acad. Sci. U. S. A.* **2013,** *110*, 3143-3148.

18. Busscher, H. J.; van der Mei, H. C., *PLoS Pathog.* **2012,** *8*, e1002440-e1002440.

19. Dubiel, E. A.; Martin, Y.; Vermette, P., *Chem. Rev.* **2011,** *111*, 2900-2936.

20. Gregory, P. J., *Plant roots: growth, activity and interactions with the soil*. John Wiley & Sons: 2008.

21. Tedja, R.; Lim, M.; Amal, R.; Marquis, C., *ACS Nano* **2012,** *6*, 4083-4093.

22. Barisik, M.; Atalay, S.; Beskok, A.; Qian, S., *J. Phys. Chem. C* **2014,** *118*, 1836-1842.

23. Kim, S. T.; Saha, K.; Kim, C.; Rotello, V. M., *Acc. Chem. Res.* **2013,** *46*, 681-691.

24. Rivera-Gil, P.; Jimenez De Aberasturi, D.; Wulf, V.; Pelaz, B.; Del Pino, P.; Zhao, Y.; De La Fuente, J. M.; Ruiz De Larramendi, I.; Rojo, T.; Liang, X.-J., *Acc. Chem. Res.* **2012,** *46*, 743-749.

25. Haupt, A.; Campetelli, A.; Bonazzi, D.; Piel, M.; Chang, F.; Minc, N., *PLoS Biol.* **2014,** *12*, e1002029.

26. Wong, J. Y.; Langer, R.; Ingber, D. E., *Proc. Natl. Acad. Sci. U. S. A.* **1994,** *91*, 3201-3204.

27. Klenerman, D.; Korchev, Y. E.; Davis, S. J., *Curr. Opin. Chem. Biol.* **2011,** *15*, 696-703.

28. Bard, A. J.; Faulkner, L. R., *Electrochemical methods: fundamentals and applications*. Wiley New York: 1980; Vol. 2.

29. Henderson, E.; Haydon, P.; Sakaguchi, D., *Science* **1992,** *257*, 1944-1946.

30. Dammer, U.; Popescu, O.; Wagner, P.; Anselmetti, D.; Guntherodt, H.-J.; Misevic, G. N., *Science* **1995,** *267*, 1173-1175.

31. Raman, A.; Trigueros, S.; Cartagena, A.; Stevenson, A.; Susilo, M.; Nauman, E.; Contera, S. A., *Nat. Nanotechnol.* **2011,** *6*, 809-814.

32. Müller, D. J.; Dufrêne, Y. F., *Trends Cell. Biol.* **2011,** *21*, 461-469.

33. Alsteens, D.; Dupres, V.; Yunus, S.; Latgé, J.-P.; Heinisch, J. r. J.; Dufrêne, Y. F., *Langmuir* **2012,** *28*, 16738-16744.

34. Hillier, A. C.; Kim, S.; Bard, A. J., *J. Phys. Chem.* **1996,** *100*, 18808-18817.

35. Miyatani, T.; Horii, M.; Rosa, A.; Fujihira, M.; Marti, O., *Appl. Phys. Lett.* **1997,** *71*, 2632-2634.

36. Miyatani, T.; Okamoto, S.; Rosa, A.; Marti, O.; Fujihira, M., *Appl. Phys. A Mater. Sci. Process.* **1998,** *66*, S349-S352.

37. Manne, S.; Cleveland, J.; Gaub, H.; Stucky, G.; Hansma, P., *Langmuir* **1994,** *10*, 4409-4413.

38. Xu, S.; Arnsdorf, M. F., *Proc. Natl. Acad. Sci. U. S. A.* **1995,** *92*, 10384-10388.

39. Ahimou, F.; Denis, F. A.; Touhami, A.; Dufrêne, Y. F., *Langmuir* **2002,** *18*, 9937-9941.

40. Almonte, L.; Lopez‐Elvira, E.; Baró, A. M., *ChemPhysChem* **2014,** *15*, 2768-2773.

41. Sotres, J.; Baró, A., *Appl. Phys. Lett.* **2008,** *93*, 103903.

42. Sotres, J.; Baró, A., *Biophys. J.* **2010,** *98*, 1995-2004.

43. Korchev, Y.; Milovanovic, M.; Bashford, C.; Bennett, D.; Sviderskaya, E.; Vodyanoy, I.; Lab, M., *J. Microsc.* **1997,** *188*, 17-23.

44. Shevchuk, A. I.; Frolenkov, G. I.; Sánchez, D.; James, P. S.; Freedman, N.; Lab, M. J.; Jones, R.; Klenerman, D.; Korchev, Y. E., *Angew. Chem. Int. Ed.* **2006,** *118*, 2270-2274.

45. Happel, P.; Thatenhorst, D.; Dietzel, I. D., *Sensors* **2012,** *12*, 14983.

46. Rheinlaender, J.; Schaffer, T. E., *Soft Matter* **2013,** *9*, 3230-3236.

47. Hansma, P.; Drake, B.; Marti, O.; Gould, S.; Prater, C., *Science* **1989,** *243*, 641-643.

48. Chen, C. C.; Zhou, Y.; Baker, L. A., *Annu. Rev. Anal. Chem.* **2012,** *5*, 207-28.

49. Takahashi, Y.; Murakami, Y.; Nagamine, K.; Shiku, H.; Aoyagi, S.; Yasukawa, T.; Kanzaki, M.; Matsue, T., *Phys. Chem. Chem. Phys.* **2010,** *12*, 10012-10017.

50. Takahashi, Y.; Ito, K.; Wang, X.; Matsumae, Y.; Komaki, H.; Kumatani, A.; Ino, K.; Shiku, H.; Matsue, T., *Electrochemistry* **2014,** *82*, 331-334.

51. Shevchuk, A. I.; Gorelik, J.; Harding, S. E.; Lab, M. J.; Klenerman, D.; Korchev, Y. E., *Biophys. J.* **2001,** *81*, 1759-1764.

52. McKelvey, K.; Perry, D.; Byers, J. C.; Colburn, A. W.; Unwin, P. R., *Anal. Chem.* **2014,** *86*, 3639-46.

53. McKelvey, K.; Kinnear, S. L.; Perry, D.; Momotenko, D.; Unwin, P. R., *J. Am. Chem. Soc.* **2014,** *136*, 13735-13744.

54. Perry, D.; Al Botros, R.; Momotenko, D.; Kinnear, S. L.; Unwin, P. R., *ACS Nano* **2015,** *9*, 7266-76.

55. Sa, N.; Lan, W.-J.; Shi, W.; Baker, L. A., *ACS Nano* **2013,** *7*, 11272-11282.

56. Clarke, R. W.; Zhukov, A.; Richards, O.; Johnson, N.; Ostanin, V.; Klenerman, D., *J. Am. Chem. Soc.* **2013,** *135*, 322-9.

57. Gilroy, S.; Jones, D. L., *Trends Plant Sci.* **2000,** *5*, 56-60.

58. Chung, T.-H.; Wu, S.-H.; Yao, M.; Lu, C.-W.; Lin, Y.-S.; Hung, Y.; Mou, C.-Y.; Chen, Y.-C.; Huang, D.-M., *Biomaterials* **2007,** *28*, 2959-2966.

59. Strober, W., *Curr. Protoc. Immunol.* **2001**, A. 3B. 1-A. 3B. 2.

60. Momotenko, D.; Cortes-Salazar, F.; Josserand, J.; Liu, S.; Shao, Y.; Girault, H. H., *Phys. Chem. Chem. Phys.* **2011,** *13*, 5430-5440.

61. Siwy, Z.; Heins, E.; Harrell, C. C.; Kohli, P.; Martin, C. R., *J. Am. Chem. Soc.* **2004,** *126*, 10850-10851.

62. White, H. S.; Bund, A., *Langmuir* **2008,** *24*, 2212-2218.

63. Behrens, S. H.; Grier, D. G., *J. Chem. Phys* **2001,** *115*, 6716-6721.

64. Showalter, A. M., *The Plant Cell* **1993,** *5*, 9.

65. Jones, D. L.; Shaff, J. E.; Kochian, L. V., *Planta* **1995,** *197*, 672-680.

66. Sakmann, B.; Neher, E., *Annual review of physiology* **1984,** *46*, 455-472.

67. Jonas, E. A.; Knox, R. J.; Kaczmarek, L. K., *Neuron* **1997,** *19*, 7-13.

68. Kinraide, T. B.; Wang, P., *J. Exp. Bot.* **2010**, erq082.

69. Daya, S.; Loughlin, A. J.; MacQueen, H. A., *Differentiation* **2007,** *75*, 360-370.

70. Hemmrich, K.; Von Heimburg, D.; Cierpka, K.; Haydarlioglu, S.; Pallua, N., *Differentiation* **2005,** *73*, 28-35.

71. Harmon, C. M.; Abumrad, N. A., *J. Membr. Biol.* **1993,** *133*, 43-49.

72. Abumrad, N. A.; El-Maghrabi, M. R.; Amri, E.; Lopez, E.; Grimaldi, P., *J. Biol. Chem.* **1993,** *268*, 17665-17668.

73. Schneider, H.; Staudacher, S.; Poppelreuther, M.; Stremmel, W.; Ehehalt, R.; Füllekrug, J., *Arch. Biochem. Biophys.* **2014,** *546*, 8-18.

74. Kampf, J. P.; Parmley, D.; Kleinfeld, A. M., *Am. J. Physiol. Endocrind. Metab.* **2007,** *293*, E1207-E1214.

75. Lewis, S. E.; Listenberger, L. L.; Ory, D. S.; Schaffer, J. E., *J. Biol. Chem.* **2001,** *276*, 37042-37050.

76. Stahl, A., *Pflügers Archiv* **2004,** *447*, 722-727.

77. Rubenstein, D.; Yin, W.; Frame, M. D., *Biofluid Mechanics: An Introduction to Fluid Mechanics, Macrocirculation, and Microcirculation*. Academic Press: 2011.

78. Neu, B.; Meiselman, H. J., *Biophys. J.* **2002,** *83*, 2482-2490.

79. Rheinlaender, J.; Geisse, N. A.; Proksch, R.; Schäffer, T. E., *Langmuir* **2010,** *27*, 697-704.

80. Paulose Nadappuram, B.; McKelvey, K.; Byers, J. C.; Güell, A. G.; Colburn, A. W.; Lazenby, R. A.; Unwin, P. R., *Anal. Chem.* **2015**, *87*, 3566-3573.

81. Actis, P.; Maalouf, M. M.; Kim, H. J.; Lohith, A.; Vilozny, B.; Seger, R. A.; Pourmand, N., *ACS Nano* **2013,** *8*, 546-553.

# Chapter 7. Fast Nanoscale Surface Charge Mapping with Pulsed-Potential Scanning Ion Conductance Microscopy

The previous chapters have shown how the issues with convoluted surface charge and topography can be resolved through using a BM-SICM scheme with no fixed bias to avoid perturbing the DDL at charged interfaces including living cells imaged in physiological conditions. This chapter adapts the previous method to increase the image acquisition rate for faster imaging with more pixels. This is achieved through adopting a DC feedback approach, using the minimum bias that can still provide a robust feedback as well as using a pulsed potential mode which provides surface charge information an order of magnitude quicker than the CV approach used in earlier work. Consequently, it is possible to achieve surface charge maps with much higher pixel density of PC12 cells and quantitative surface charge information can be obtained using FEM simulations.

This chapter has been published as a technical note in *Analytical Chemistry*. All cell culturing and experiments were jointly performed with Ashley Page. All FEM simulations were performed by myself and manuscript preparation was jointly done.

# Fast Nanoscale Surface Charge Mapping with Pulsed-Potential Scanning Ion Conductance Microscopy

Ashley Page,[1,2,†] David Perry,[1,2,†] Philip Young[3], Daniel Mitchell[4], Bruno Frenguelli[3] and Patrick R. Unwin[1,*]

[1]Department of Chemistry, [2]MOAC Doctoral Training Centre, [3]School of Life Sciences and [4]Warwick Medical School, University of Warwick, Coventry, CV4 7AL, United Kingdom. †These authors contributed equally to this work

***Corresponding Author**

p.r.unwin@warwick.ac.uk

## 7.1 Abstract

A vast range of interfacial systems exhibit charge heterogeneities on the nanoscale. These differences in local surface charge density are challenging to visualise, but recent work has shown the scanning ion conductance microscope (SICM) to be a very promising tool to spatially resolve and map surface charge and topography via a hopping potential sweep technique with a single nanopipette probe, with harmonic modulation of a bias applied between a quasi-reference counter electrode in the nanopipette and bulk solution, coupled with lock-in detection. Although powerful, this is a relatively slow process, with limitations on resolution and the size of the images that can be collected. Herein, we demonstrate a new scanning regime for mapping surface charge and topography with SICM, which increases the data acquisition rate by an order of magnitude, and with the potential for further gains. Furthermore, the method is simplified, eliminating the need for bias modulation lock-in detection, by utilising a potential-pulse, chronoamperometric approach, with self-referencing (calibration) of the response at each pixel in an image. We demonstrate the application of this new method to both a model substrate and living PC12 cells under physiological (high ionic strength) conditions, where charge mapping is most difficult (small Debye length). This work contributes significantly to

the emergence of SICM as a multifunctional technique for simultaneously probing interfacial structure and other function with nanometre resolution.

## 7.2 Introduction

Scanning ion conductance microscopy (SICM) is a powerful technique for nanoscale non-contact imaging of surface topography[1,2] that finds particular application in the study of cellular systems,[3–6] where resolution has been extended to the individual protein level[7] and is comparable to atomic force microscopy (AFM).[8] SICM utilises a nanopipette filled with electrolyte to probe an interface that is also bathed in electrolyte. A bias is applied between a quasi-reference counter electrode (QRCE) in the nanopipette and one in bulk solution to generate an ionic current. Changes in the ionic current as the nanopipette approaches the substrate can be used to sense, and provide information about, the interface.

Recent developments have taken SICM beyond topography and shown that the current response may be inherently sensitive to other interfacial properties, most notably surface charge heterogeneities[9–11] and surface reactions.[12] Local changes in ionic conductivity near an interface affect the SICM current and can thus be mapped and analysed, for example, with finite element method (FEM) modelling.[13–15] All of these applications require careful consideration of the scanning routine used, particularly the applied potential bias, so that SICM provides unambiguous information on surface properties.

However, it has been shown that without careful experimental design, the topographical and surface charge data obtained with SICM can become convoluted, affecting the accuracy of these studies. To address this issue, surface charge mapping with SICM has been performed in a bias modulated (BM-) SICM[16] format that enables topography and surface charge to be resolved simultaneously without convolution.[10] In this regime the nanopipette is approached to the surface or interface of interest, with no net (time averaged) bias applied between the two QRCEs, just a small harmonic oscillation of the bias around 0 V. Importantly, this renders the SICM response relatively insensitive to surface charge, so that topography is mapped. Upon detection of the substrate (usually by a change of the

current phase), the bias is then swept between two extreme values and the SICM response becomes sensitive to surface charge. The surface charge is elucidated by comparing the voltammogram near the surface to one performed in bulk at each and every pixel in a self-referencing regime.

In this contribution, we introduce a new regime that significantly advances SICM topography-charge mapping, increasing the pixel acquisition rate by an order of magnitude (with scope for further gains), thereby allowing for imaging with a much higher pixel density. The method eliminates the modulation of the bias and replaces this with a minimal fixed bias that permits faster approach speeds for topographical imaging, while a pulse in the bias at the point of closest approach, as opposed to a voltammogram, allows faster acquisition of surface charge information. Voltage- switching has proved useful in the related technique of scanning electrochemical microscopy (SECM), for topography and activity imaging with a single solid nanoelectrode probe, but requires the use of two redox mediators in solution which may be somewhat restrictive.[17] FEM simulations allow for the quantification of the experimental data and show no loss of accuracy when compared to the previous potential-scanning regime.[10] The increase in pixel density afforded by this new approach reveals previously unseen charge heterogeneities in two substrates: an interrupted polystyrene film in high electrolyte concentration; and a neuron-like PC12 cell imaged in cell culture media. Thus, the reliable increase of the scanning speed improves the viability of SICM as a multifunctional technique for surface charge mapping on the nanoscale, and offers new control functions that could be applied to other SICM methods.

## 7.3 Materials and Methods

### 7.3.1 Solutions

Milli-Q reagent grade water (resistivity ca. 18.2 MΩ cm at 25°C) was used for all solutions. 50 mM KCl (Sigma-Aldrich) was used for the SICM charge maps of the interrupted polystyrene film on glass. PC12 cells were cultured and imaged in RPMI 1640 media containing 15% horse serum, 2.5% foetal calf serum, 5 mM glutamine, 100 U/mL penicillin and 100 µg/mL streptomycin (all Sigma Aldrich).

### 7.3.2 Nanopipettes and Electrodes

Nanopipettes were pulled from borosilicate glass capillaries (o.d. 1.2 mm, i.d. 0.69 mm, Harvard Apparatus) using a laser puller (P-2000, Sutter Instruments; pulling parameters: Line 1: Heat 330, Fil 3, Vel 30, Del 220, Pul -; Line 2: Heat 330, Fil 3, Vel 40, Del 180, Pul 120). The inner radius of the probe was measured using a JEOL 2000FX transmission electron microscope (TEM) to be 80 nm ± 15 nm. (see Supporting Information, Table 7.1 for experimental geometries of the two probes used). Two Ag/AgCl electrodes were used, one in the nanopipette and a second in bulk solution.

### 7.3.3 Substrates

Glass-bottomed Petri dishes with detachable coverslips (3512, WillcoWells) were used for both substrates. In the case of the polystyrene, the glass-bottom of the dish was dip-coated in a solution of polystyrene dissolved in chloroform (1 mg/mL) to ensure a heterogeneous substrate. The PC12 cells used were adherent to glass-bottomed petri dishes and so these were used as a support.

### 7.3.4 Cell Culturing Procedure

Adherent PC12 cells (ATCC-CRL-1721.1) were cultured in tissue culture flasks in the above-specified media until confluent, before trypsinisation and transfer to Petri dishes. They were allowed 72 hours to adhere to the glass substrate before imaging in fresh media.

### 7.3.5 Instrumentation

The basic instrumentation setup has been described in detail previously.[10] Briefly, the lateral movement of the probe was controlled using a two-axis piezoelectric positioning system with a range of 300 μm (Nano-BioS300, Mad City Labs, Inc.), while movement normal to the substrate was controlled using a more precise piezoelectric positioning stage of range 38 μm (P-753-3CD, Physik Instrumente). The

electrometer and current-voltage converter used were both made in-house, while user control of probe position, voltage output and data collection was via custom made programs in LabVIEW (2013, National Instruments) through an FPGA card (7852R, National Instruments).

### 7.3.6 Fast Charge Mapping SICM

All images presented herein were collected using a self-referencing scan hopping mode of SICM, with the regime for each pixel as follows (Figure 7.1a): (I) First, the probe was translated towards the surface at 6 μm/s with the QRCE in the probe biased at +20 mV vs. the QRCE in bulk. When the ionic current between the two electrodes had reduced by a chosen threshold value (giving a precise working distance, as calculated from FEM simulations, see below), the probe motion was halted before (II) a 50 ms pulse of the probe potential to -400 mV. After this pulse (III) the probe potential was returned to +20 mV and the probe was retracted either 1 μm or 2 μm for the polystyrene or PC12 cell samples, respectively (retract distance dependent on the height variation of the substrate, but sufficient to represent bulk solution as it was always well over 5 times the dimensions of the nanopipette opening) at 10 μm/s before (IV) a second 50 ms pulse in the bulk solution and (V) the probe was then moved to the next pixel. The current was monitored during the entire process at a rate of 2 kHz and the current-time (*I*-*t*) curve at the surface and the *I*-*t* curve in bulk were compared to extract surface charge information at each pixel.

### 7.3.7 FEM Simulations

A 2D axisymmetric model of the nanopipette in bulk solution and near a substrate was constructed in Comsol Multiphysics (v. 5.2) with the Transport of Diluted Species and Electrostatics modules. A schematic of the simulation domain and boundary conditions is presented in Supporting Information (Figure 7.5). The dimensions of the nanopipettes were extracted from TEM images of nanopipettes.[18]

To obtain working distances for experimental SICM measurements, simulations were performed at varying probe-substrate separation with an applied

probe bias of 20 mV (the experimental approach bias). Once the working distance, corresponding to the experimental feedback threshold was known, time-dependent simulations were performed at this separation distance with varying surface charge applied to the domain boundary below the nanopipette. Simulations were also performed with the nanopipette positioned in bulk solution and the near-surface values of the ionic current, with different applied surface charge, were normalised to those in bulk to elucidate surface charge from experimental maps. For all of these simulations the initial conditions used were obtained from steady-state simulations performed with the same conditions, except the tip bias was 20 mV (the approach bias).

## 7.4 Results and Discussion

### 7.4.1 Scanning Regime for Interfacial Charge Mapping

Previous work on SICM showed that the charge at an interface, particularly in low ionic strength electrolyte concentrations (<10 mM aqueous solution), can have a significant effect on the current response during the approach of the nanopipette probe towards a substrate surface.[9,10] This convolution of charge and topography becomes more significant as the potential difference between the two QRCEs is increased.[10] To overcome this problem, our previous work utilised a BM-SICM regime, which allowed topographical information to be extracted with no net bias and just a small harmonic perturbation, followed by the application of a linear scan of potential at each pixel to reveal the charge. However, the use of modulation-based SICM constrains the approach speed of the probe, depending on the time constant of the lock-in amplifier used and modulation frequency employed.[16] Herein, we make use of a direct current (DC) feedback mode to generate a feedback signal for essentially charge-insensitive topographical mapping. In this setup, a small bias (+20 mV at the probe electrode with respect to the QRCE in bulk solution) is applied to produce the ionic current for DC feedback (topographical mapping). It was possible to apply such a small bias, which generated a reasonable current magnitude, because the experiments were carried out in physiologically-relevant media, which has high ionic strength, and will be most relevant for future work, *e.g.*

for cell imaging. The choice of approach bias in these measurements is important and requires a theoretical consideration. The bias chosen will depend on the ionic strength of the imaging media and the size of the nanopipette, as well as the range of surface charges that are to be probed. The bias needs to be chosen such that it provides a robust feedback signal for tracking topography experimentally, but simulations (such as those reported herein) are also required to justify that under the imaging conditions, the surface charge of the substrate does not influence the nanopipette response. Upon approach to within a probe diameter of the substrate of interest, a decrease of the ionic current between the two QRCEs occurs[2] which is attributed to the increased access resistance near the nanopipette opening. This approach comfortably allows the mapping of topography at approach speeds of 5 μm/s and above (maximum not tested). The small applied bias, as discussed below, meant that there was little convolution of the topography and charge at the interface in relatively high electrolyte concentrations (≥50 mM), and the current response allowed for accurate topographical mapping (see below).

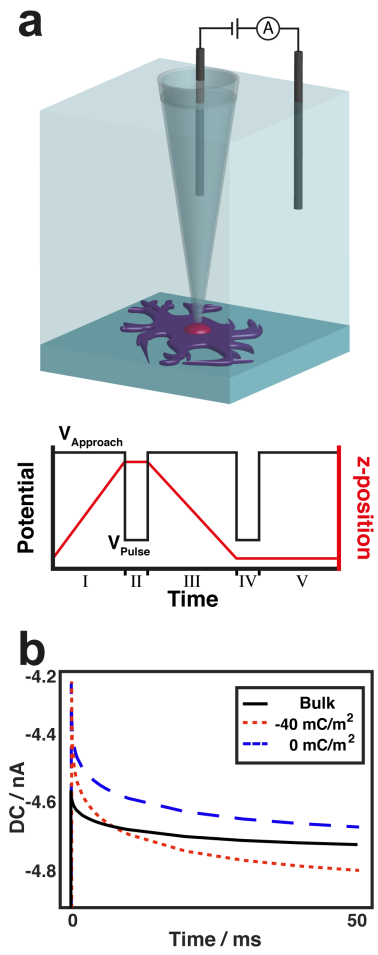


**Figure 7.1.** Setup for a high-speed charge mapping experiment. **a)** Schematic of basic SICM setup used for charge mapping, with a trace of z-position and potential at each hop in the scan hopping regime: (I) probe approaches the surface at +20 mV, (II) 50 ms pulse at -400 mV before (III) probe is retracted at +20 mV and (IV) a second pulse to -400 mV in bulk solution. (V) Probe is moved in the x or y direction to the next point. **b)** Simulated *I-t* curves of a probe in bulk (black line) and at a 15 nm separation from surfaces of neutral and negative charge (red and blue lines respectively).

As mentioned above, the extraction of interfacial charge information in previous work utilised the measurement of a cyclic voltammogram (CV) at both the surface and in bulk solution, considering the rectification of the current-voltage behaviour as a result of the diffuse double layer (DDL) at the tip and surface.[10,19,20] Typically the CV was obtained by sweeping the potential between –400 and +400 mV at a scan rate of 1 V/s - a total of 3.2 s of CV time per pixel (1.6 s at the surface and

1.6 s in bulk). Despite the wealth of information collected at each pixel in this regime (including potential-resolved current-space movies), surface charge was manifest in the current response mostly at large bias. In fact, in our previous work, the FEM simulations for the quantification of surface charge were only carried out at the extreme potentials of the CV, with an applied potential of -400 mV proving to be the most sensitive to variations in local interfacial charge.[10]

In this work, the time taken to collect interfacial charge information is significantly reduced by pulsing the probe bias from the approach potential (+20 mV) to -400 mV at the point of closest approach, and in bulk, in a self-referencing format (Figure 7.1a). To prove the potential pulse concept, current-time (*I*-*t*) transients were simulated in 50 mM KCl (Figure 7.1b). For the three simulated *I*-*t* curves shown, the initial conditions were obtained by first performing a steady-state simulation at the approach probe potential (+20 mV) before a subsequent time-dependent simulation with an applied bias of -400 mV, with different surface charges applied to the substrate. The simulations at 0 $mC/m^2$ and -40 $mC/m^2$ used a probe-substrate separation of 15 nm, which corresponded to the set point used during experiments, as obtained below. It is clear that the *I*-*t* response near the surface is different compared to the bulk solution, and that when the probe is near the surface, the charge has a significant influence on the response, validating the use of this new imaging methodology. In these conditions, a negatively charged surface caused an enhancement of the current while a neutral surface caused a diminution, when compared to the bulk response as explained in previous work.[10,19] Further simulations produced working curves of normalised current as a function of surface charge for each of the experimental conditions below. For the present work, 50 ms was taken as length of the experimental potential pulse, with the final few points of the surface *I*-*t* curve normalised with respect to the final few points of the bulk *I*-*t* curve at each pixel to produce spatially-resolved surface charge maps. The significant improvements to both the approach speed and interfacial charge collection time reduce the typical pixel acquisition rate for this technique from over 5 s to less than 0.5 s, markedly increasing the efficacy and potential applications of SICM for localised surface charge mapping. Clearly, however, there would be scope for further improvement in the experimental time in the future, since differences in the *I*-*t*

behaviour are apparent on a few ms timescale (Figure 7.1c), and it should be possible to use piezoelectric positioners with a faster response than are used herein.

### 7.4.2 Validation of the Technique with a Polystyrene Film on Glass

The high-speed approach was first validated experimentally using an incomplete polystyrene film on a glass substrate, such that there were pinholes in the polystyrene layer, exposing the glass below to the solution. The topography from a typical scan, collected in 50 mM KCl with a DC feedback threshold (decrease in current from bulk to the point of closest approach) of 15 pA, is shown in Figure 7.2a, demonstrating a highly heterogeneous film that varies in thickness from a few tens of nm in some areas to a few hundreds of nm in others. Pinholes in the film in which the glass is exposed are of variable size, with some clearly visible and others not resolved as well, as they are the same size or smaller than the probe opening (~150 nm). The resolution of traditional SICM measurements and surface charge measurements is typically observed to be of a similar order of magnitude to the nanopipette dimensions ($0.5\ r - 1.5\ r$)[1] where $r$ is the nanopipette opening radius and hence smaller nanopipettes would be required to resolve these features further.

The heterogeneities in the topography of the substrate are reproduced in the normalised current map (Figure 7.2b), obtained from the pulse procedure outlined above. Areas in which there is a large expanse of glass have normalised current values in the range 1.05-1.07 (yellow/white colouring) while areas of thick polystyrene have normalised current values below 1 (dark red/black colouring). Interestingly the intermediate areas of the scan largely have values between these two extremes (red colouring), which can be attributed to pinholes on a scale less than that of the probe diameter. This explanation of the intermediary values of normalised current in those areas of the scan where the film is very thin also explain the wide range of values seen in these regions. If we denote the area of the substrate that affects the current response during the potential pulse as the 'footprint' of the probe, then any value between the 'true glass' value of ~1.06 and the 'true polystyrene' value of ~0.99 could be obtained with differing percentages of glass and polystyrene in the footprint. A scan collected from a different sample in

which the polystyrene is more uniform is presented in the Supporting Information (Figure 7.6) for comparison, which instead mainly shows just two regions of different charge.

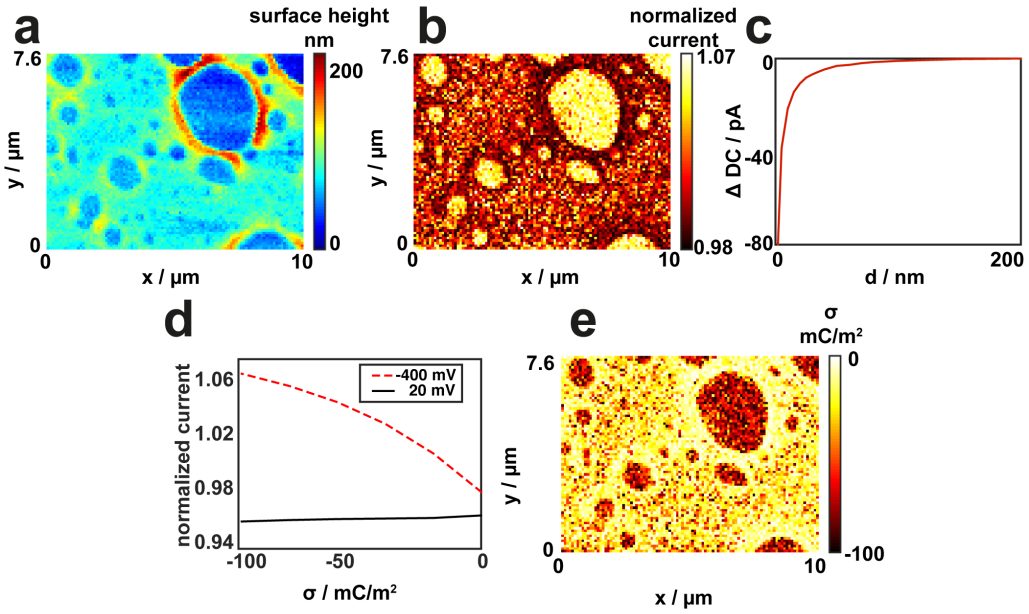


**Figure 7.2.** Simultaneous topography and quantified charge maps of an incomplete polystyrene film on a glass substrate. **a)** Topography image recorded with a ~70 nm radius nanopipette in a hopping regime using DC feedback. **b)** Normalised current (surface current divided by bulk current) map collected concurrently with the topography. **c)** FEM simulation of the change in DC as the probe approaches the surface, showing dependence of probe-substrate separation on set point. **d)** Simulated dependence of the normalised current on the charge at the surface, used to generate the quantified charge map in **(e)**.

An approach curve was simulated using the same probe geometry and electrolyte conditions as the experiment (Figure 7.2c) in order to extract the probe-substrate separation when a feedback threshold of 15 pA is used. From the approach curve, this value was found to be 15 nm, a separation that was then used for the time-dependent simulations at surfaces of differing charge density (Figure 7.2d). Note, that further increases in the feedback threshold used could improve the sensitivity to charge heterogeneities. The red curve demonstrates a strong dependence of the normalised current on the surface charge density when the QRCE

in the probe is biased at -400 mV, while at +20 mV (black curve) there is almost no effect of the surface charge on the normalised current, legitimising the use of this potential during the approach for topographical imaging. The combination of the normalised current map in Figure 7.2b with the calibration curve in Figure 7.2d produced the quantified charge map in Figure 7.2e. Areas in which the polystyrene film is complete have a charge density of 0 $mC/m^2$, the expected value given the neutrality of the polymer, while glass has a charge of about -60 $mC/m^2$, comfortably within the range of those values quoted in the literature.[19] Note, that the apparent surface charge in the glass regions is quite heterogeneous, most likely due to the heterogeneous distribution of the polymer film. For example, small patches of polystyrene are likely to be present within the predominantly glass regions. A typical scan collected using the bias modulation and CV approach in previous work is shown for comparison (Supporting Information, Figure 7.7). The range of current values is larger as a lower electrolyte concentration (10 mM) was used, but the local charges are similar. It should be noted that despite containing significantly fewer pixels it took more than twice as long to obtain that image than the main scan presented in Figure 7.2.

### 7.4.3 Surface Charge Mapping of Neuron-like PC12 Cells

Having validated the use of high-speed charge mapping with SICM on a model substrate, we then investigated whether the technique could also be used in higher ionic strength conditions (~150 mM, RPMI 1640 media, see Materials and Methods for composition) in which the width of the DDL would be significantly reduced.[21] Figure 7.3a shows an optical micrograph of a spontaneously differentiated neuron-like cell from the PC12 cell line, with the scan area, extending from the cell body along the length of a neurite, outlined by the dashed white square. The topographical data (Figure 7.3b), collected with a feedback threshold of 8 pA and a working distance of 30 nm (see approach curve, Figure 7.3c), show that the region of the cell imaged varies in height by ~2 μm, with the thickest area at the cell body and the thinnest area towards the furthest extension of the neurite. Patches of increased height, several hundred nanometres in prominence, are seen along the length of the

cell. The numbers on Figure 7.3b correspond to the experimental *I-t* curves in Figure 7.3f, and highlight differences in charge between regions of the neurite (1), the cell body (2) and the glass (3). All three of these curves are lower in magnitude than a typical experimental bulk *I-t* curve (shown in blue). The compression of the range of possible normalised currents arises as a result of the decrease in double layer thickness, meaning the effect of charge density on ionic transport to the probe is diminished. Nonetheless, it is important to note that despite a range of only 1.5% in the normalised current across the entire scan (see Supporting Information, Figure 7.8) the technique is still sensitive enough to quantify the charge density (Figures 7.3d,e).

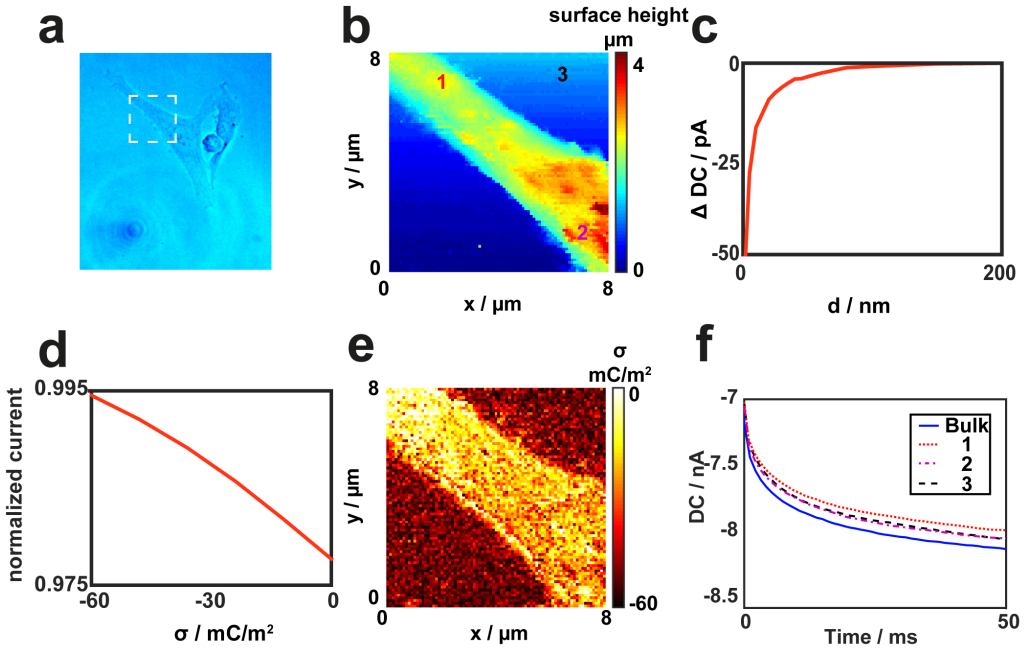


**Figure 7.3.** Simultaneous topography and charge maps of a PC12 neurite on a glass substrate. **a)** Optical image of the scanned cell, the white square showing the scan area. **b)** Topographical image of the neurite, collected concurrently with the quantified charge map **(e)**. **c)** FEM simulation of the change in DC as the probe approaches the surface at +20 mV, showing dependence of probe-substrate separation on set point. **d)** Simulated dependence of the normalised current on the charge at the surface, used to generate the quantified charge map in **(e)**. Experimental *I-t* curves at the points of the scan labelled in **(b)** are shown in **(f)**, along with a bulk *I-t* curve for comparison.

As would be expected, the glass carries a homogeneous negative charge (~-55 mC/$m^2$). While this value differs from that obtained from the polystyrene scan above, the two are not directly comparable as the surface charge of glass relies on the acid-base equilibrium of silanol groups (SiOH) at the interface, the termination of which is dependent on the pH of the solution used. The 50 mM KCl was ~pH 6.2 while the cell media was buffered to pH 7.2, as such a lesser proportion of the silanol groups would be protonated in the media and thus a higher charge density would be expected. However, a lower surface charge is apparent in Figure 7.2. These small differences in the data for glass between Figures 7.2e and 7.3e are likely attributable to small polystyrene features within the glass region, which cannot be resolved topographically, which would serve to reduce the total surface charge presented in the nanopipette footprint. Additionally, the surface charge of the glass in the PC12 study could be impacted by the presence of other molecules (nutrients, proteins, etc.) in the cell growth (imaging) media, which could adsorb on the glass and alter its surface properties. In contrast to the glass substrate, the charge density of the PC12 cell, though negative in polarity throughout, is highly heterogeneous. There is a gradient from the predominantly more negatively charged cell body (as highly charged as the glass in some areas, see Figure 7.3f *I-t* curve 2) to the end of the less highly charged neurite (Figure 7.3f, *I-t* curve 1), though patches of lower charge also appear along the length of the cell. These heterogeneities could arise as a result of protein or charged-lipid rafts in the cell membrane, and further correlative techniques could probe the cellular function of these charge differences.

## 7.5 Conclusions

The image quality of interfacial charge mapping using SICM has been greatly improved by using a new tip approach and potential control function which increases the pixel acquisition rate by an order of magnitude, compared to our recently introduced format. The reduction in the time taken to acquire a single pixel of data was achieved via two separate improvements. First, changing the type of feedback used when detecting the surface increased the approach speed of the

probe. Second, the time taken to extract charge information in a given hop was reduced to 100 ms when previously it was in excess of 3 s. The resulting increase in image quality allowed the visualisation of previously unseen features on the nanoscale, including ~100 nm defects in an interrupted polystyrene film and rafts of different charge at the surface of a neuron-like PC12 cell. It should be noted that these studies present negative to neutral charges, but that the protocol would also be sensitive to positive surface charges, with enhanced sensitivity to such surface charges possible through tuning the pulse bias. Additionally, these scans were collected using nanopipettes of ~80 nm radius and with a decrease in size of the probes used, the resolution, and thus the power, of this technique could be improved further still. It should also be possible to decrease the pulse time to a couple of ms and the approach speed with better piezoelectric positioners.

This work contributes to the rise of SICM as a multifunctional technique in this case, allowing surface charge to be mapped with a resolution and image quality approaching that of the topographical mapping for which it is most commonly used.

## 7.6 Supporting Information

### 7.6.1 Dimensions of Nanopipettes

Nanopipettes used in SICM experiments, discussed in the manuscript were characterised using transmission electron micrograph (TEM) images to obtain accurate dimensions for the use in finite element method (FEM) simulations. The dimensions extracted for these tips are presented in Table 7.1 with a TEM micrograph of one of the nanopipettes displayed in Figure 7.4.

**Table 7.1.** Dimensions of nanopipettes used for polystyrene and PC12 scans

| **Height nm** | **Polystyrene Experiments** | | **PC12 Experiments** | |
|---|---|---|---|---|
| | **Inner Radius nm** | **Outer Radius nm** | **Inner Radius nm** | **Outer Radius nm** |
| 0 | 94 | 121 | 70 | 82 |
| 100 | 97 | 123 | 77 | 94 |
| 200 | 102 | 126 | 83 | 98 |
| 300 | 105 | 132 | 87 | 103 |
| 400 | 118 | 145 | 90 | 110 |
| 500 | 127 | 160 | 93 | 165 |
| 1000 | 193 | 210 | 153 | 192 |
| 5000 | 433 | 527 | 340 | 520 |
| 10000 | 643 | 845 | 610 | 840 |
| 50000 | 2191 | 2750 | 1910 | 2400 |
| 100000 | 2932 | 3400 | 2907 | 3250 |
| 150000 | 4726 | 5800 | 4630 | 5620 |

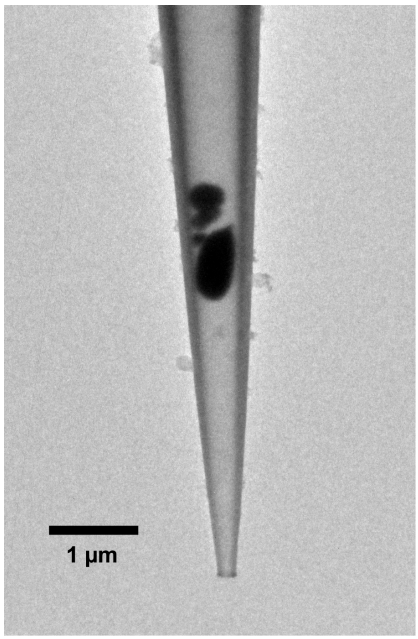


**Figure 7.4.** One of a series of TEM images of the nanopipette used for the PC12 cell experiments presented in the manuscript.

### 7.6.2 FEM simulations

FEM simulations were constructed and run in COMSOL 5.2 as outlined in the manuscript. A 2D axisymmetric domain of the nanopipette with dimensions extracted from TEM images was constructed. Simulations were either performed with 50 mM KCl in the nanopipette and bath solution or with a solution consisting of 103 mM NaCl, 23 mM $NaHCO_3$ and 5 mM KCl to mimic the main components of the RPMI 1640 media used as supporting electrolyte in PC12 cell experiments. The boundary conditions for all FEM simulations are displayed in Figure 7.5. The tip potential of either +20 mV or -400 mV was applied to the upper nanopipette boundary with the outer bath boundary held at ground. In each media, approach curves were run with an applied bias of +20 mV in order to calculate the working distance used experimentally for surface charge measurements. The charge applied to the nanopipette wall was -40 $mC/m^2$.

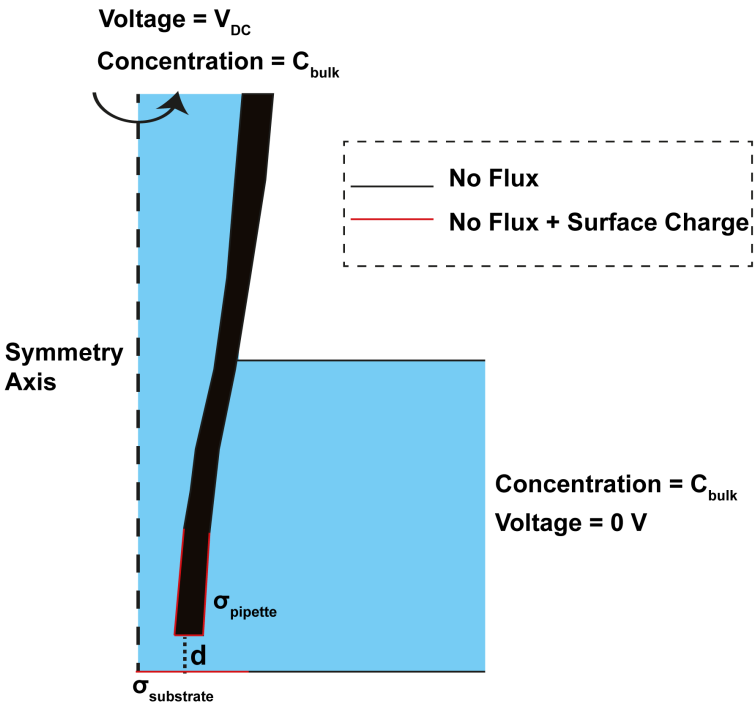


**Figure 7.5.** Schematic of 2D axisymmetric FEM simulation domain with applied boundary conditions depicted. Surface charge was applied to the lowest 10 µm of the inner and outer nanopipette walls. The surface charge on the boundary beneath the nanopipette was varied in order to calculate experimental surface charge values.

### 7.6.3 More Complete Polystyrene Scan

The SICM surface charge map of the polystyrene film presented in the manuscript suggested the presence of 3 regions, a uniform polystyrene region with a surface charge of 0 $mC/m^2$, a negatively charged glass region and an in-between region which is attributed to glass pinholes smaller than the SICM nanopipette footprint giving a surface charge consisting of glass and polystyrene regions. A second scan of a more complete region of polystyrene was performed and is depicted in Figure 7.6 where instead just two distinctly charged regions are observed over the glass pinholes and the polystyrene.

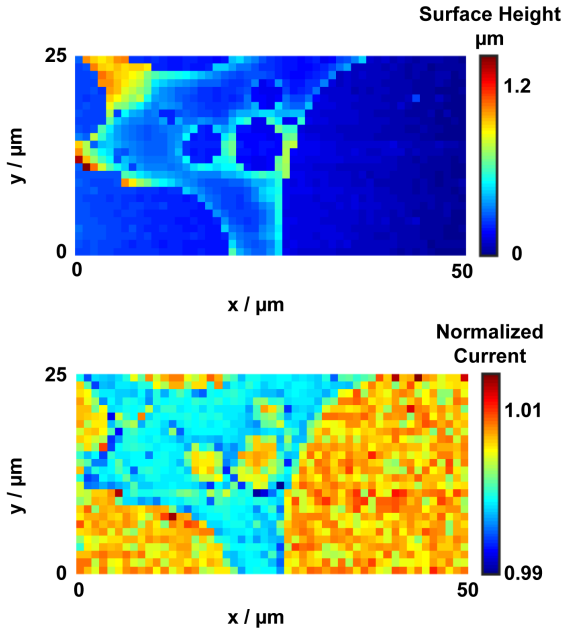


**Figure 7.6.** SICM topographical image **(a)** and normalised current map **(b)** of a more uniform region of polystyrene film on a glass support suggesting a uniform surface charge across the polystyrene film.

### 7.6.4 Previous Polystyrene Scan Data

A typical image collected in the previous scanning regime of bias modulated approach feedback and cyclic voltammogram charge extraction. Presented here for comparison of pixel density and image quality.

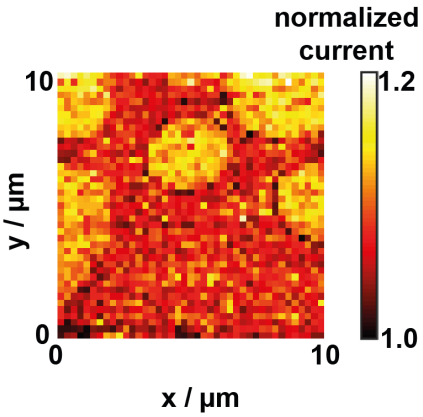


**Figure 7.7.** Typical surface charge map of an interrupted polystyrene film on a glass substrate collected using the previous bias modulation voltage-scanning regime. Adapted with permission from reference 10.

### 7.6.5 Raw PC12 Scan Data

Figure 7.3 of the manuscript presents a surface charge map and IT curves for a PC12 cell on a glass substrate. Figure 7.8 depicts the raw data used to obtain these surface charge values including the experimental map of normalised surface to bulk currents at the experimental working distance.

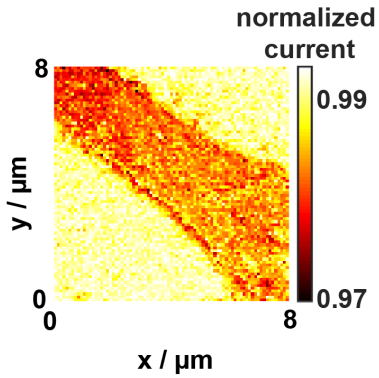


**Figure 7.8.** Normalised current map across the PC12 cell discussed in the manuscript, converted to estimated surface charge values presented in the map of Figure 7.3.

## 7.7 References

1. Chen, C.-C.; Zhou, Y.; Baker, L. a. *Annu. Rev. Anal. Chem.* **2012**, *5*, 207–228.
2. Hansma, P. K.; Drake, B.; Marti, O.; Gould, S. A.; Prater, C. B. *Science (80-. ).* **1989**, *243*, 641–643.

3. Korchev, Y. E.; Bashford, C. L.; Milovanovic, M.; Vodyanoy, I.; Lab, M. J. *Biophys. J.* **1997**, *73*, 653–658.
4. Novak, P.; Li, C.; Shevchuk, A. I.; Stepanyan, R.; Caldwell, M.; Hughes, S.; Smart, T. G.; Gorelik, J.; Ostanin, V. P.; Lab, M. J.; Moss, G. W. J.; Frolenkov, G. I.; Klenerman, D.; Korchev, Y. E. *Nat Meth* **2009**, *6*, 279–281.
5. Takahashi, Y.; Murakami, Y.; Nagamine, K.; Shiku, H.; Aoyagi, S.; Yasukawa, T.; Kanzaki, M.; Matsue, T. *Phys. Chem. Chem. Phys.* **2010**, *12*, 10012–10017.
6. Happel, P.; Thatenhorst, D.; Dietzel, I. D. *Sensors (Switzerland)* **2012**, *12*, 14983–15008.
7. Shevchuk, A. I.; Frolenkov, G. I.; Sanchez, D.; James, P. S.; Freedman, N.; Lab, M. J.; Jones, R.; Klenerman, D.; Korchev, Y. E. *Angew. Chemie - Int. Ed.* **2006**, *45*, 2212–2216.
8. Rheinlaender, J.; Geisse, N. A.; Proksch, R.; Schäffer, T. E. *Langmuir* **2011**, *27*, 697–704.
9. McKelvey, K.; Kinnear, S. L.; Perry, D.; Momotenko, D.; Unwin, P. R. *J. Am. Chem. Soc.* **2014**, *136*, 13735–13744.
10. Perry, D.; Al Botros, R.; Momotenko, D.; Kinnear, S. L.; Unwin, P. R. *ACS Nano* **2015**, *9*, 7266–7276.
11. Perry, D.; Paulose Nadappuram, B.; Momotenko, D.; Voyias, P. D.; Page, A.; Tripathi, G.; Frenguelli, B. G.; Unwin, P. R. *J. Am. Chem. Soc.* **2016**, *138*, 3152–3160.
12. Momotenko, D.; McKelvey, K.; Kang, M.; Meloni, G. N.; Unwin, P. R. *Anal. Chem.* **2016**, *88*, 2838–2846.
13. Korchev, Y. E.; Negulyaev, Y. a; Edwards, C. R.; Vodyanoy, I.; Lab, M. J. *Nat. Cell Biol.* **2000**, *2*, 616–619.
14. Zhou, Y.; Chen, C. C.; Baker, L. A. *Anal. Chem.* **2012**, *84*, 3003–3009.
15. Novak, P.; Gorelik, J.; Vivekananda, U.; Shevchuk, A.; Ermolyuk, Y.; Bailey, R.; Bushby, A.; Moss, G. J.; Rusakov, D.; Klenerman, D.; Kullmann, D. M.; Volynski, K.; Korchev, Y. *Neuron* **2013**, *79*, 1067–1077.
16. McKelvey, K.; Perry, D.; Byers, J. C.; Colburn, A. W.; Unwin, P. R. *Anal. Chem.* **2014**, *86*, 3639–3646.
17. Takahashi, Y.; Shevchuk, A. I.; Novak, P.; Babakinejad, B.; Macpherson, J.;

Unwin, P. R.; Shiku, H.; Gorelik, J.; Klenerman, D.; Korchev, Y. E.; Matsue, T. *Proc. Natl. Acad. Sci. USA*. **2012**, *109*, 11540–11545.

18. Perry, D.; Momotenko, D.; Lazenby, R. A.; Kang, M.; Unwin, P. R. *Anal. Chem.* **2016**, *88*, 5523-5530.
19. Sa, N.; Lan, W. J.; Shi, W.; Baker, L. A. *ACS Nano* **2013**, *7*, 11272–11282.
20. Sa, N.; Baker, L. A. *J. Am. Chem. Soc.* **2011**, *133*, 10398–10401.
21. Stumm, W.; Morgan, J. J. *Aquatic chemistry: chemical equilibria and rates in natural waters*, Third Edit.; John Wiley & Sons, 1996.

# Chapter 8. Electrochemical Control of Calcium Carbonate Crystallisation and Dissolution in Nanopipettes

Thus far, nanopipettes have been used in an SICM format in order to elucidate topographical and surface charge information about an interface. Another important use of nanopipettes is as sensors for a variety of analytes. Nanopipettes are capable of making resistive pulse measurements whereby changes in the current through the end of the nanopipette as an entity passes through it provides information about the entity's size, shape and translocation speed. In this chapter the nanopipette is used as a centre for driving crystal growth, using the bias between the QRCE inside and outside the nanopipette to control the local mixing of ions for either driving crystallisation or dissolution events. These processes can be tracked through changes in the ionic current and it provides a powerful platform for screening the effects of additives through how they affect the blocking transients. FEM simulations also allow for a better understanding of the mixing processes and growth kinetics to be established.

This chapter has been published as an article in *ChemElectrochem*. The experiments presented in this work were performed by Alexander S. Parker, although I have performed similar measurements for this, and similar, crystal systems. The FEM simulations presented were performed by myself and the manuscript was prepared by myself.

# Electrochemical Control of Calcium Carbonate Crystallization and Dissolution in Nanopipettes

David Perry,[1,2,†] Alexander S. Parker,[1,†] Ashley Page[1,2] and Patrick R. Unwin[1,*]

[1]Department of Chemistry and [2]MOAC Doctoral Training Centre, University of Warwick, Coventry, CV4 7AL, United Kingdom.† These authors contributed equally to this work

***Corresponding Author**

p.r.unwin@warwick.ac.uk

## 8.1 Abstract

Electrochemically-controlled nanopipettes are becoming increasingly versatile tools for a diverse range of sequencing, sizing and imaging applications. Herein, the use of nanopipettes to induce and monitor quantitatively crystallisation and dissolution in real time is considered, using $CaCO_3$ in aqueous solution as an exemplar system. The bias between a quasi-reference counter electrode (QRCE) in a nanopipette and a QRCE in a bulk solution, is used to mix (or de-mix) two different solutions by ion migration and drive either growth or dissolution depending on the polarity of the applied bias. Furthermore, Raman spectroscopy can be applied simultaneously to identify polymorphs formed at the end of the nanopipette. The technique is supported with a robust finite element method (FEM) model that allows the extraction of time-dependent saturation levels and mixing characteristics at the nanoscale. Moreover, modelling allows growth rates to be deduced from experimental ion current-time transients. The technique shows great promise as a tool for rapidly screening growth additives and inhibitors. Eight different additives (organic and inorganic) are considered and can quickly be put in rank order for efficacy of crystal growth rate inhibition.

## 8.2 Introduction

Nanopipettes, under electrochemical control, are increasingly becoming powerful tools for a host of analytical applications because of their ease of manufacture and low cost as well as their versatility, being adaptable to suit a wide range of different configurations. To date, applications of nanopipettes have included use as sensors for a variety of different analytes,[1, 2, 3, 4, 5] as well as tools for local delivery of molecules, achieved by varying the electric field at the end of the nanopipette to trap or release charged species.[6, 7, 8] Additionally they serve as powerful probes for electrochemical reaction, surface charge and topographical imaging[9, 10, 11, 12, 13] as well as other diverse applications, such as enabling the nanobiopsy of living cells[14] and electrospray analysis.[15]

Herein, nanopipettes are used as a reaction centre to study crystallisation events on the nanoscale, with the aim of measuring the initial rates of calcium carbonate, $CaCO_3$, growth and dissolution. With the versatile approach presented, multiple growth and dissolution events can be induced and monitored repetitively and reversibly (at will) on a rapid timescale. We selected $CaCO_3$ for study given its significance in many areas, from being one of the most abundant minerals on Earth,[16] to its use as a biomineral by organisms in the formation of eggshells, seashells, snail shells and skeletal matter.[17, 18] $CaCO_3$ is a significant component of coral reefs[19] and serves as a repository for carbon dioxide.[20] There is also great interest in understanding and preventing the formation of $CaCO_3$ limescale, especially through the use of additives.[21, 22, 23]

$CaCO_3$ crystallisation is achieved by filling a nanopipette with a bicarbonate solution (for example) and a quasi-reference counter electrode (QRCE) and applying a bias between this electrode and another QRCE, in a bulk solution of calcium chloride into which the nanopipette is placed. Changing the magnitude and polarity of the bias applied, gives control over the local mixing of $Ca^{2+}$ and $CO_3^{2-}$ ions at the end of the nanopipette, such that growth or dissolution of $CaCO_3$ can be driven. Simultaneously, the ionic current through the end of the nanopipette is sensitive to

these events and can be monitored with high time resolution. This approach builds on earlier work that considered the crystallisation of zinc phosphate in a nanopipette, showing that the current through the nanopipette was sensitive to growth events and that this process could be manipulated through alteration of the local electric field.[24] Our work develops and advances this methodology significantly and puts it on a quantitative footing. In particular, the use of FEM modelling, allows for an understanding of the mixing processes occurring at the end of the nanopipette and the analysis of the experimental growth (and dissolution) rates, which we are able to follow on a faster timescale. The growth process is typically complete within a few hundred ms. Moreover, the possibility of utilising Raman spectroscopy *in-situ* is briefly explored and it is shown that this can allow for further polymorphic identification of the $CaCO_3$ material that forms in the end of the nanopipette.

Finally, a key strength, and new feature, of the approach described in this work is that the effects of additives can readily be studied, on a fast timescale, from which a ranking of efficacy can be obtained. This capability could have a great impact as it provides a platform wherein nanopipettes could cheaply and robustly be used as a screening tool to discover, and assess, new additives very quickly.

## 8.3 Materials and Methods

### 8.3.1 Solutions

All solutions were made up using 18.2 MΩ cm water (Millipore Inc.) and chemicals used were purchased from Sigma Aldrich. The nanopipette contained 125 mM $NaHCO_3$ electrolyte solution for experiments and the bath contained 25 mM $CaCl_2$, unless stated otherwise. For inhibitor studies, maleic acid (MA) was added to the bath solution at concentrations ranging from 0.5 mM to 8 mM. Studies with other inhibitors were performed with concentrations of 8 mM added to a series of bath solutions. For all experiments, solutions were adjusted to pH 9.2.

### 8.3.2 Nanopipettes

Nanopipettes were fabricated using quartz glass capillaries with filaments (outer diameter 1.0 mm, inner diameter 0.5 mm, custom manufactured, Friedrich and Dimmock) using a laser puller (P-2000, Sutter Instruments; parameters of: Line 1: Heat 750, Fill 4, Vel 30, Del 150, Pull 80; Line 2: Heat 650, Fil 3, Vel 40, Del 135, Pull 150) to give a tip opening diameter of approximately 40-60 nm (determined accurately).[30]

### 8.3.3 Instrumentation

The electrometer and current-voltage converter used were home built, while the user control of voltage output and data collection was via custom made programs in LabVIEW (2013, National Instruments) through an FPGA card (7852R, National Instruments).

### 8.3.4 Bias Driven Crystallisation Experiments

Typical crystallisation experiments involved filling the nanopipette with $NaHCO_3$ solution, to serve as both supporting electrolyte and a source of $CO_3^{2-}$ ions (adjusted to pH 9.2 by addition of NaOH), along with a chloridised silver wire, which served as a QRCE. The nanopipette was immersed in a solution of $CaCl_2$ containing a second Ag/AgCl QRCE. To drive crystallisation, a negative bias was applied to the nanopipette QRCE relative to the bulk electrode. To unblock the nanopipette for subsequent experiments a positive bias (4 V) was applied. The open circuit potential was measured using a custom built high impedance voltage follower and was found to be -40 mV at the nanopipette QRCE with respect to the bulk QRCE. As this was considerably smaller than the blocking and unblocking biases applied in experiments and simulations (*vide infra*), all values for potential stated are uncorrected but this could be easily accounted for.

Each experimental run consisted of 25 blocking and unblocking events and all quoted blocking times, $\tau_{1/2}$, referred to herein, are measured from the time of the voltage switch to the time the current dropped to half its maximum value (open tip

current at the same potential). All experiments were performed at room temperature, measured to be 25 °C.

### 8.3.5 FEM Simulations

A 2D axisymmetric model of the nanopipette in bulk solution was constructed in Comsol Multiphysics (v. 5.2) with the Transport of Diluted Species and Electrostatics modules. The dimensions of the nanopipette were extracted from TEM images of nanopipettes and these were faithfully reproduced in the model so that the experimental geometry was mimicked precisely.[30] The equations and boundary conditions solved in the FEM simulations were as in previous work,[11, 30] and outlined in the manuscript but additionally with calcium carbonate speciation incorporated with parameters shown in Table 8.1.[45] Ionic transport is assumed to follow the classical Nernst-Planck relationship, where the flux $J_i$ of species, *i,* is given as:

$$J_i = -D_i \nabla c_i - z_i \frac{F}{RT} D_i c_i \nabla \phi \qquad (8.1)$$

and the Poisson equation describes the electrical potential $\phi$:

$$\nabla^2 \phi = -\frac{F}{\varepsilon \varepsilon_0} \sum_i z_i c_i \qquad (8.2)$$

where $c_i$ denotes the species concentration, while $D_i$, $z_i$, $F$, $R$, $T$, $\varepsilon$ and $\varepsilon_0$ specify constants: system diffusion coefficient of *i*, its charge number, the Faraday constant, gas constant, temperature, relative permittivity and vacuum permittivity, respectively.

The $CaCl_2$ concentration was set as 25 mM to the rightmost boundary of the bulk domain with the top of the nanopipette domain held at 125 mM $NaHCO_3$. The bias, $V_{DC}$, was applied to the bulk nanopipette domain and was usually -0.25 V for the study of crystal growth or 2 V for the study of subsequent unmixing. There was a no flux condition at the walls of the nanopipette and bulk domain boundary.

To extract growth rates, a FEM simulation was run with spherical particles of different radius in the nanopipette, positioned 5 µm from the nanopipette opening into the nanopipette. The percentage block off of current was compared to experimental transients to extract an estimated size for the crystal varying with time.

**Table 8.1** Calcium carbonate speciation parameters

| Eq | Reaction | pK |
|---|---|---|
| 8.3 | $CO_2 + H_2O \rightleftharpoons H_2CO_3$ | 1.466 |
| 8.4 | $H_2CO_3 \rightleftharpoons H^+ + HCO_3^-$ | 6.351 |
| 8.5 | $HCO_3^- \rightleftharpoons H^+ + CO_3^{2-}$ | 10.33 |
| 8.6 | $CaHCO_3^+ \rightleftharpoons Ca^{2+} + HCO_3^-$ | 1.015 |
| 8.7 | $CaCO_{3(aq)} \rightleftharpoons Ca^{2+} + CO_3^{2-}$ | 3.2 |
| 8.8 | $H_2O \rightleftharpoons OH^- + H^+$ | 13.997 |

### 8.3.6 Raman Spectroscopy

*In-situ* micro-Raman spectra were collected from a 10 µm long region at the end of a nanopipette that had undergone a blocking event, using a Raman microscope (Renishaw, UK) fitted with a Charge Coupled Device (CCD) detector and a 514.5 nm $Ar^+$ laser. A 20X lens was employed.

## 8.4 Results and Discussion

### 8.4.1 Growth of Calcium Carbonate in a Nanopipette Under Electrochemical Control

The principles of using a single barrelled nanopipette for the study of calcium carbonate nucleation and growth are depicted in Figure 8.1a and b. For most studies, the nanopipette was filled with 125 mM $NaHCO_3$ and placed in a bath of 25 mM $CaCl_2$ (both solutions fixed at pH 9.2) while applying a bias of 4 V to a QRCE in the

nanopipette with respect to the QRCE in bulk solution. In this state, a steady current was observed corresponding to an unblocked nanopipette. The tip potential was then switched to -0.25 V to drive $CO_3^{2-}$ (and $HCO_3^-$) ions down the nanopipette and $Ca^{2+}$ ions from the bath towards the tip (Figure 8.1a, counter ion flows not shown), leading to the nucleation and growth of $CaCO_3$ at the end of the tip (*vide infra*). The growth process restricts the ion flow, which can be monitored simultaneously via the ion conductance current. After the growth period, the tip potential was switched positive (4 V) and the $CaCO_3$ dissolves (Figure 8.1b).

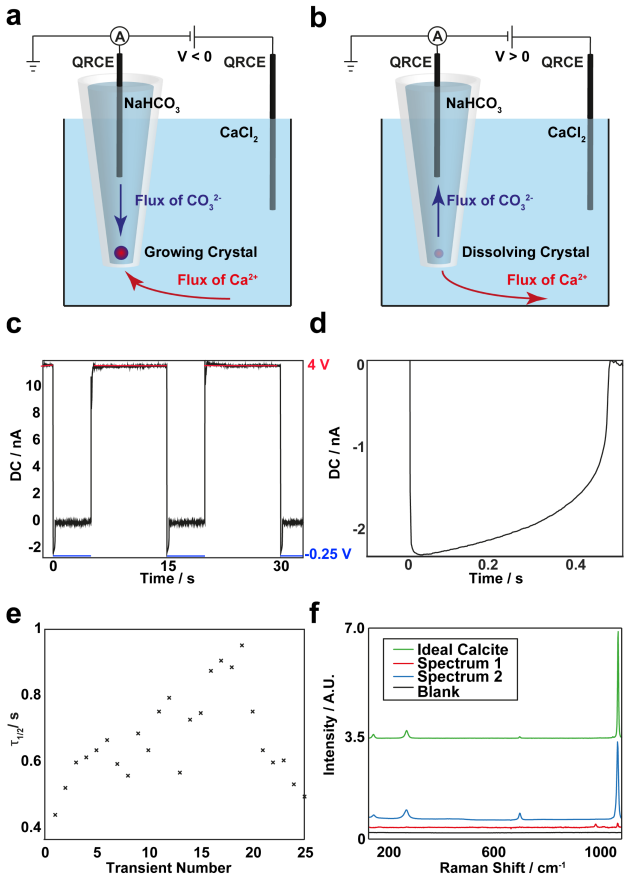


**Figure 8.1.** Schematic of the principles of precipitation in a nanopipette with growth occurring with negative tip bias, **(a)**, and dissolution promoted when the polarity is reversed, **(b). c)** Typical experimental blocking and unblocking events with blockages occurring with a tip bias of -0.25 V and unblocking at 4 V. **d)** Typical blocking transient with a blocking time, $\tau_{1/2}$, of about 400 ms. **e)** Variation of the blocking time, $\tau_{1/2}$, for an experimental run of 25 growth and dissolution events. **f)** Raman spectra obtained at different times during a long-time blocking measurement with the green line showing the simulated spectrum of calcite for comparison. The black

line shows the spectrum of the nanopipette immersed in solution before the polarity was switched to -0.25 V and the blocking event occurred. The red spectrum was collected over a period of 5 minutes (with the potential of -0.25 V still applied) after the blocking occurred and suggests at the presence of amorphous calcium carbonate. The final spectrum (blue) recorded 30 min later (-0.25 V potential still applied), shows the presence of calcite, indicating an ACC-calcite transformation.

Upon switching the bias to -0.25 V, to promote $CaCO_3$ growth, the ionic current initially has a value for an unblocked tip, but then begins to decrease, first gradually and then more rapidly with time, eventually approaching zero, corresponding to a blocked tip, as seen in Figure 8.1c and d. Upon switching the polarity of the bias, so that the QRCE potential in the tip was positive, the nanopipette can be seen to return to its open state, as evidenced by the large current flow in Figure 8.1c. It is interesting to note that the nanopipettes exhibit a rectified current-voltage response, evidenced by the open current values at 4 V and -0.25 V, respectively. This is attributed to the different solutions present in the nanopipette and bulk solution and the differing ion mobilities, although there could be an effect of the nanopipette surface charge as well. It can be also be seen that when the nanopipette is unblocked (at 4 V applied) the current appears to be less noisy than when the nanopipette is blocked. When the nanopipette becomes blocked, ion migration would no longer drive blockage and this could lead to dissolution of the particle. Once the particle has dissolved slightly, migration would switch back on and there would be subsequent regrowth. This repeated dissolution and regrowth process could manifest as noise.

Figure 8.1e depicts the time taken for 50 % blockage of the ionic current from the open state, $\tau_{1/2}$, from a run of 25 crystal growth (blocking) and unblocking events with the same nanopipette. It can be seen that although there is some variation in the blocking timescale, there is no overall trend and an average blocking time of around 660 $\pm$ 250 ms is observed. The variation in timescale is most likely due to slight changes in the position within the nanopipette where the nucleation and growth event occurs (*vide infra*), as well as the stochastic nature of nucleation. When performing these measurements, it is important to make sure that there is no

trace of the grown particle for subsequent events. Consequently, unblocking times of 10 s were used for these experiments.

A significant strength of the nanopipette technique is that it is amenable to combination with additional *in situ* characterisation techniques, although this was not the primary focus of this work. As an example, Raman spectroscopy was performed, focused on a 10 μm portion at the end of a nanopipette (and the surrounding solution), which confirmed that solid $CaCO_3$ was formed. Figure 8.1f shows typical Raman spectra obtained during and after a growth event carried out over a longer period. There were no noticeable peaks between 200 $cm^{-1}$ and 1000 $cm^{-1}$ over an acquisition time of 5 minutes when the QRCE inside the nanopipette was maintained at a positive bias (4 V) with respect to the QRCE in bulk solution, so that growth would be prevented. Upon switching the bias to -0.25 V, a second Raman spectrum (5 minutes acquisition time) was obtained (red line) with two peaks, one at 1085 $cm^{-1}$ and one at around 1000 $cm^{-1}$. The noticeable absence of a peak at 711 $cm^{-1}$ and the presence of that at 1085 $cm^{-1}$ suggests the formation of ACC.[25] Further, the peak at 1000 $cm^{-1}$ may be attributed to one of the metastable ACC polymorphs.[26] On a longer timescale (after 30 minutes), with the -0.25 V bias still applied, there was a phase transition to calcite evidenced by characteristic peaks[27] at 1085 $cm^{-1}$, 711 $cm^{-1}$ and the lattice peaks at 282 $cm^{-1}$ and 155 $cm^{-1}$, by comparison to the green trace of Figure 8.1f for calcite. These results indicate that the initial blocking of the nanopipette is likely to result from the formation of ACC, but that this eventually transforms to the more stable calcite polymorph of $CaCO_3$.[28, 29] For the timescale of the kinetic measurements herein, which occur on a timescale of 1 s and less, the nucleation, growth and dissolution processes relate to ACC. We wish to point out that although not explored in this work. The nanopipette-based technique is well suited to ambient TEM measurements[30] and it could be worth exploring cryo-TEM in the future for further characterisation of material formed.

The effect of varying the $Ca^{2+}$ concentration in the bath solution was also considered and it was found (Figure 8.2), that increasing the concentration of $Ca^{2+}$ initially present in solution (by adjusting the $CaCl_2$ concentration) resulted in a decrease in the timescale of the growth process. This is attributed to the lower saturation levels that would be achieved. Although not presented, the dissolution

rates were also quicker for lower Ca2+ concentrations for the same reason. Further, in experiments where the locations of the $CO_3^{2-}$ and $Ca^{2+}$ salts were switched ($Ca^{2+}$ solution in the nanopipette, $CO_3^{2-}$ in the bath), the polarity needed to drive crystallisation was reversed. Briefly, increasing the $CO_3^{2-}$ concentration resulted in shorter blocking times (data not presented).

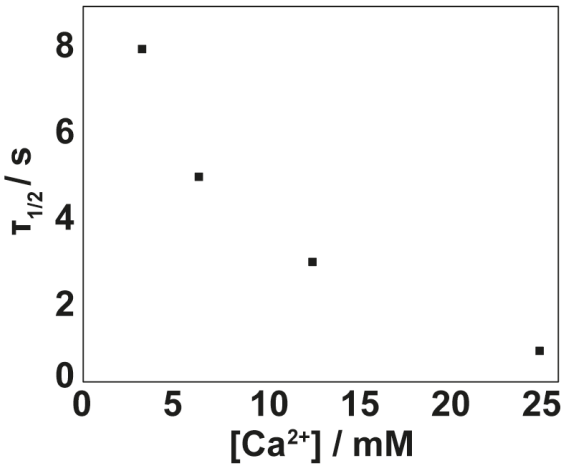


**Figure 8.2.** Effect of [$Ca^{2+}$] on the time required for calcium carbonate to block a nanopipette. Points are the average of 25 individual transients and the error bar is one standard deviation.

### 8.4.2 Mixing of $Ca^{2+}$ and $CO_3^{2-}$ in a Nanopipette

To aid understanding of the mixing and growth phenomena occurring in this system, FEM simulations of the mass transport processes due to the imposed electric field were performed with conditions similar to those that were mainly used for experiments, i.e. 125 mM $NaHCO_3$ in the nanopipette domain and 25 mM $CaCl_2$ in the bath solution (both pH 9.2, and with full speciation considered, as outlined in Table 1). The problem considered was generally similar to related nanopipette transport problems that are readily tackled with finite element method (FEM) modelling.[30, 31] A schematic of the simulation domain is depicted in Figure 8.3a.

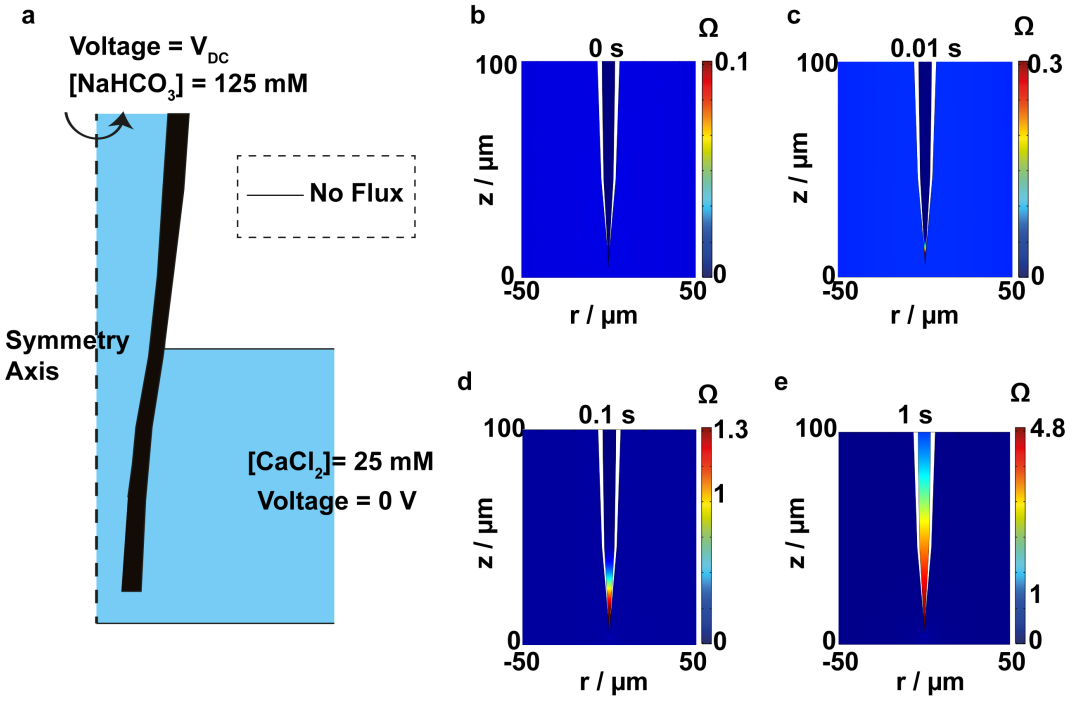


**Figure 8.3. a)** Schematic of FEM simulation domain used to study mixing. Simulations of the saturation level of calcium carbonate in solution, $\Omega$, at times ranging from 0 ms to 1000 ms, **(b-e)** following the application of a potential of -0.25 V to the QRCE in the nanopipette with respect to that in bulk solution.

Initially, a steady-state simulation was performed with a bias of 2 V applied to the upper boundary of the nanopipette domain. In experiments (see above), 4 V was applied in order to enhance the rate of unblocking, but it was difficult to obtain a converged solution for this condition with the computer power available. The simulation at 2 V was sufficient to illustrate the main effects with a positive QRCE potential in the tip. Using the steady-state solution for the concentration distribution with positive tip bias as the initial condition, a time-dependent simulation was then run, with the tip bias jumped to -0.25 V. Figures 8.3b-e depict the subsequent change in the saturation levels of $CaCO_3$ defined as:

$$\Omega = \sqrt{\frac{[Ca^{2+}]\times[CO_3^{2-}]}{K_S}} \qquad (8.9)$$

where $[Ca^{2+}]$ and $[CO_3^{2-}]$ are the concentrations of calcium and carbonate ions respectively and $K_S$ is the solubility product of calcium carbonate in water (defined in terms of concentration, rather than activity).

At the start of the simulation (before application of the driving bias), the highest value for $\Omega$ was calculated to be 0.05 and was located outside of the nanopipette. After 0.01 s with an applied bias of -0.25 V, a region at the end of the nanopipette with a higher saturation is distinguishable, with values of up to 0.3. By 0.1 s of electric-field driven mixing, the saturation level increases above 1, i.e. the solution is supersaturated (which would promote growth). After 1 s of mixing, a supersaturation of around 5 is achieved. Figure 8.4a shows how the maximum supersaturation, $\Omega_{max}$, across the simulation domain varies with time. The increase in $\Omega$ is dramatic initially, but the rate of increase gradually tails off with time. As typical blocking events lasted between 400 ms and 800 ms under these conditions, the supersaturation levels achieved were typically in the range of 3 — 5.

It is interesting to note that while the supersaturation levels change throughout the 1 s of mixing, the ionic current remains constant, after the first 0.1 ms, as shown in Figure 8.4b. This finding is important because it means that any change in current (experimentally) on longer timescales can be assigned to blockage of the nanopipette due to crystal growth, and the current can be used to estimate growth rates (*vide infra*).

Simulations also enabled us to elucidate the position at which growth was most likely to occur. Figure 8.4c shows the location of $\Omega_{max}$ within the nanopipette, measured from the nanopipette opening. When the solution was first supersaturated, time ~40 ms, this position was around 5 μm into the nanopipette, making this the most likely position for initial nucleation and growth to occur. Up to a time of about 300 ms, after applying the growth driving potential, this position increased to about 12 μm into the nanopipette, before settling at around 6 μm from the tip end at longer times.

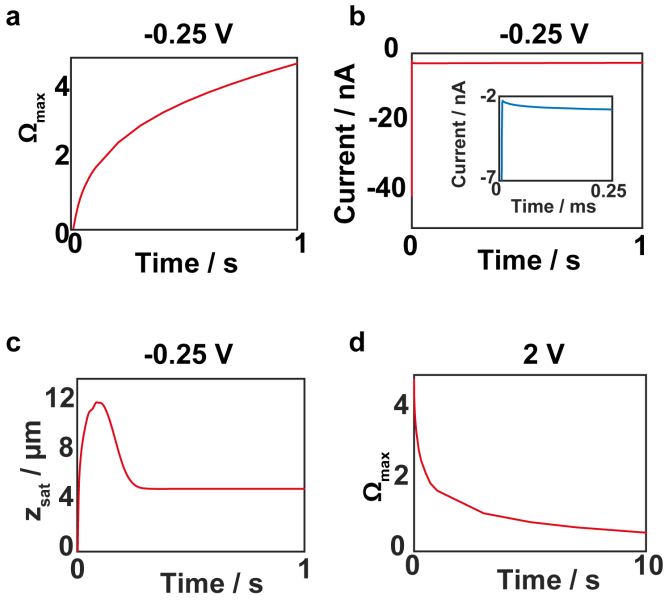


**Figure 8.4. a)** Maximum saturation (sampling the whole simulation domain), $\Omega_{max}$, as a function of time following the switch in the QRCE potential in the nanopipette from 2 V to -0.25 V, with respect to that in bulk solution. **b)** The simulated ionic current at a tip bias of -0.25 V can be seen to stabilise within 0.25 ms after switching the potential, inset shown with zoom to short times. **c)** Position of maximum saturation level, $Z_{sat}$, within the nanopipette (measured from the nanopipette end into the nanopipette body) as a function of time (applied potential -0.25 V). Upon switching the tip bias to be 2 V, after 600 ms of mixing at -0.25 V, the saturation can be seen to decrease rapidly with time **(d).**

Simulations also provided justification of the time required for sufficient de-mixing of solutions, before recording the response for subsequent growth events. Figure 8.4d shows how the maximum value of saturation decreases when a bias of 2 V was applied after 600 ms of initial mixing. These results evidence a time of around 4 s for the saturation level to drop back below 1. This would be expected to be quicker with a higher applied bias, as used experimentally, due to the stronger electric field.[32, 33] In the experiments, an unblocking period of 10 s was used, and the fact that there was little difference between the initial blocking transient, and those that followed

(*e.g.* Figure 8.1c), is good evidence that this was sufficient time to clear the tip and reset similar starting conditions between growth events.

### 8.4.3 Quantifying Growth Rates in a Nanopipette

FEM simulations described above, predicted a position of around 5 μm above the nanopipette opening as the most likely location for the growth of calcium carbonate. Further FEM simulations enabled us to determine how the size of the growth product, modelled as a spherical particle, as has been observed for ACC in other work,[26] would affect the ion current. As an illustrative example, the simulation was used to analyse the experimental growth transient, presented in Figure 8.5a, which is representative. Simulations were performed with increasing particle size, radius, *r* (see Experimental section) and the corresponding effect on the ionic current is observed in Figure 8.5b. It can be seen that the initial growth of the particle results in a small but measurable blockage of the ionic current. As the particle becomes larger, and so approaches closer to the walls of the nanopipette, the resistance increases and there is a sharp fall in the current that can pass around the growing sphere. This helps to explain the shape of the experimental transient, which typically presents a slower initial decay of the current before a sharp decrease to 0 (Figure 8.5a).

By combining the data of Figure 8.5a and b, a plot of predicted particle radius with time can be obtained and is presented in Figure 8.5c. It can be seen that there is an initially high rate of linear (radial) growth, with the radius changing at a rate approaching 12 nm/ms until the particle size reaches a radius of around 300 nm and then the growth rate tails off. Note that the times presented in Figure 8.5 are from the point of greatest (tip open) current and do not include the initial mixing time after jumping the potential, to attain a supersaturated solution (~ 50 ms).

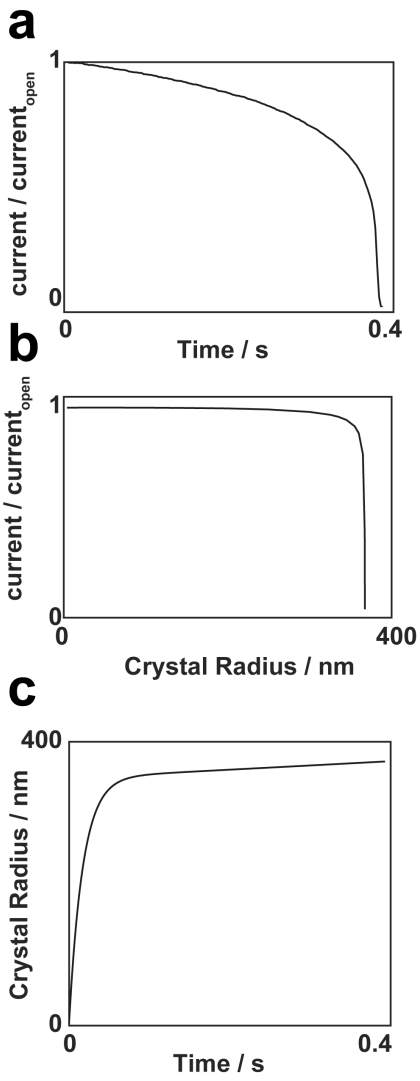


**Figure 8.5. a)** Typical experimental blocking event showing how the ion conductance current (normalised by the open, maximum value) decreases with time due to blocking by $CaCO_3$ growth**. b)** FEM simulation of the current-time response with a growing sphere in a nanopipette (at a height of 5 μm into the nanopipette). By combining the simulation results in **(b)** with the experimental data in **(a)**, the radius of the growing particle in a blocking event, with time can be estimated **(c)**.

To determine whether the observed blocking times were reasonable, the timescale for nanopipette blocking can be compared to that expected for the flux of material to an isolated growing spherical $CaCO_3$ particle. For growth due to a flux, *j*, the rate of change in volume *V*, with *t* is given by:

$$\frac{dV}{dt} = 4\pi r^2 \frac{dr}{dt} = j\frac{4\pi r^2}{\rho} \quad (8.10)$$

where $r$ is the radius of the particle and $\rho$ is the molar density of $CaCO_3$.
For a flux controlled by diffusion (maximum possible rate):

$$j = \frac{D\sqrt{K_S}(\Omega - 1)}{r} \quad (8.11)$$

where $D$ is the diffusion coefficient of $Ca^{2+}$ and $CO_3^{2-}$ (assumed equal for this simple treatment). Combining equations 8.10 and 8.11 and integrating gives an expression for a growing spherical particle with time as:

$$r^2 = \frac{4D\sqrt{K_S}(\Omega - 1)}{\rho} t \quad (8.12)$$

Using a value for $D$ of $8.5 \times 10^{-6}$ $cm^2/s$,[34] $\rho$ as 0.027 mol $cm^{-3}$ [35] and $K_S$ as $4 \times 10^{-7}$ mol $cm^{-3}$ [36], together with $\Omega$ taken to be varying with time as per $\Omega_{max}$ from Figure 8.4a, this yielded an extent of growth of around 200 nm over the timescales at which blocking events were observed, a similar magnitude to the growth rates extracted from the above analysis. The transients do not strictly fit to eq. 8.12 because of the complex time-dependent geometry and mass-transport (diffusion and migration) to a growing nanoparticle (assumed to be spherical for simplicity) in a nanopipette, but this simple analysis highlights that the process is fast and close to mass-transport controlled.

### 8.4.4 The Effect of Applied Bias on Blocking Rates

The effect of changing the applied bias was briefly explored. Growth experiments were performed with varying tip bias between -1.2 V and -0.001 V, and $\tau_{1/2}$ values extracted (4V bias applied between each growth event, as above). It can be seen from Figure 8.6a that increasing negative bias from -0.001 V to -0.4 V, resulted in smaller values for $\tau_{1/2}$ *i.e.*, faster $CaCO_3$ growth rates. However, more negative biases, beyond -0.4 V, did not result in shorter blockage times.

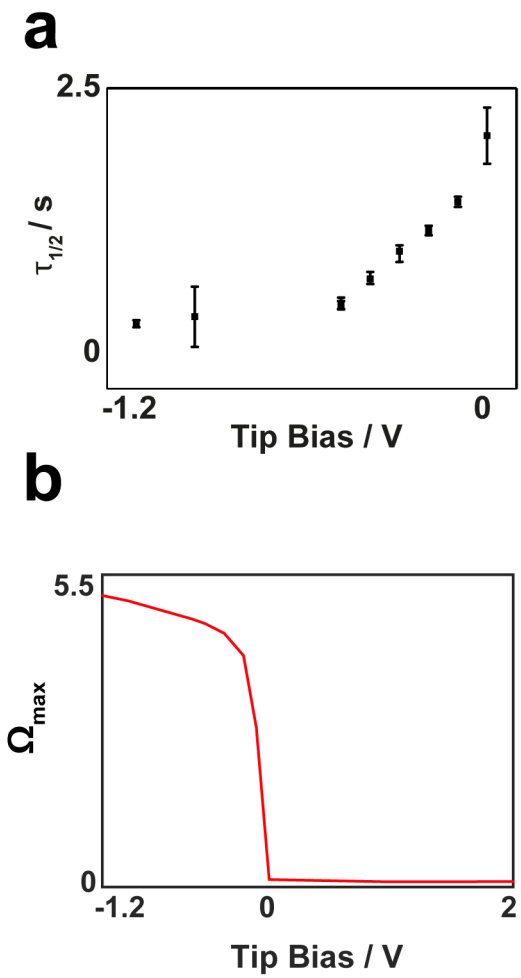


**Figure 8.6. a)** Experimental effect of varying the tip bias on the blocking time. As the bias is decreased below -600 mV **b)** FEM simulations reveal how the maximum saturation level, $\Omega_{max}$, varies with the tip bias. Data relate to a time of 1 s after the bias application, a similar duration to the experiments.

Simulations performed at similar tip biases revealed that the achieved saturation levels (after 1s, as illustrative) followed a similar trend to the experimental blocking times, as shown in Figure 8.6b. There is a relatively sharp transition (increase) in saturation level in the nanopipette tip between 0 V and -0.4 V, but at more negative bias, the saturation level does not increase appreciably. Comparison of experiment and theory over the range of applied bias confirms that local supersaturation in the tip is the driving force for crystallisation and provides insights on how the driving force may be controlled via the bias. It is however interesting to note that when there is no bias applied, the solution does eventually

become locally supersaturated, because of the effects of diffusion alone and so crystal growth and blockage is possible under these conditions. This agrees with experiments performed with no net bias where the nanopipettes were observed to block.

### 8.4.5 Effect of Additives

There is great interest in assessing the impact of additives on $CaCO_3$ formation, particularly in relation to scaling,[25, 37, 38, 39, 40] and, as such, novel methods of assessing and being able to compare the effects of additive are very valuable. The nanopipette method offers a robust platform to quickly assess and rank such growth inhibitors. Maleic acid (MA), which exists as the dianion under typical $CaCO_3$ growth conditions (herein at pH 9.2), is one such growth inhibitor that has been studied and shown to be effective for both dissolution and growth inhibition of calcite.[41, 42] The mechanism of the inhibitory action of MA has been debated, with one hypothesis being that it acts as a chelating agent, binding to $Ca^{2+}$ ions to desupersaturate solutions.[43, 44] The alternative mode of action is that MA acts on the calcite surface.[42] Experimental runs of 25 growth (and unblocking) events, were performed as outlined above at each of a series of MA concentrations present in the bath solution. The same nanopipette was used and the bath simply changed. This eliminates error from small changes in the nanopipette geometry and highlights how hundreds of quantitative growth measurements can be made quickly, making this a powerful screening methodology.

Figure 8.7a shows typical ion conductance current-time transients for different concentrations of MA (up to 8 mM) in the bath solution. It can be seen that increasing the concentration of MA in solution results in significantly longer times required for full blocking of the nanopipette, with the blocking time ($CaCO_3$ growth rate) being one to two orders of magnitude longer in the presence of 8 mM MA than without. Figure 8.7b suggests a strong effect of MA concentration on the mean value of $\tau_{1/2}$. Furthermore, through careful design of the initial experimental concentrations, it is possible to obtain some mechanistic information about the MA mode of action. Specifically, were MA solely acting as a chelating agent, 8 mM MA

would (at most) desupersaturate the bath solution by 8 mM of $Ca^{2+}$ ions. An experimental run was thus performed with 17 mM $CaCl_2$ present in the bath solution. This experiment yielded a value for $\tau_{1/2}$ of 2.1 ± 0.1 as compared to the value of $\tau_{1/2}$ with 8 mM MA of around 16 s. Thus, MA does not act solely as a $Ca^{2+}$ chelation agent, but has significant surface effects, consistent with AFM measurements of calcite growth in the presence of MA.[42]

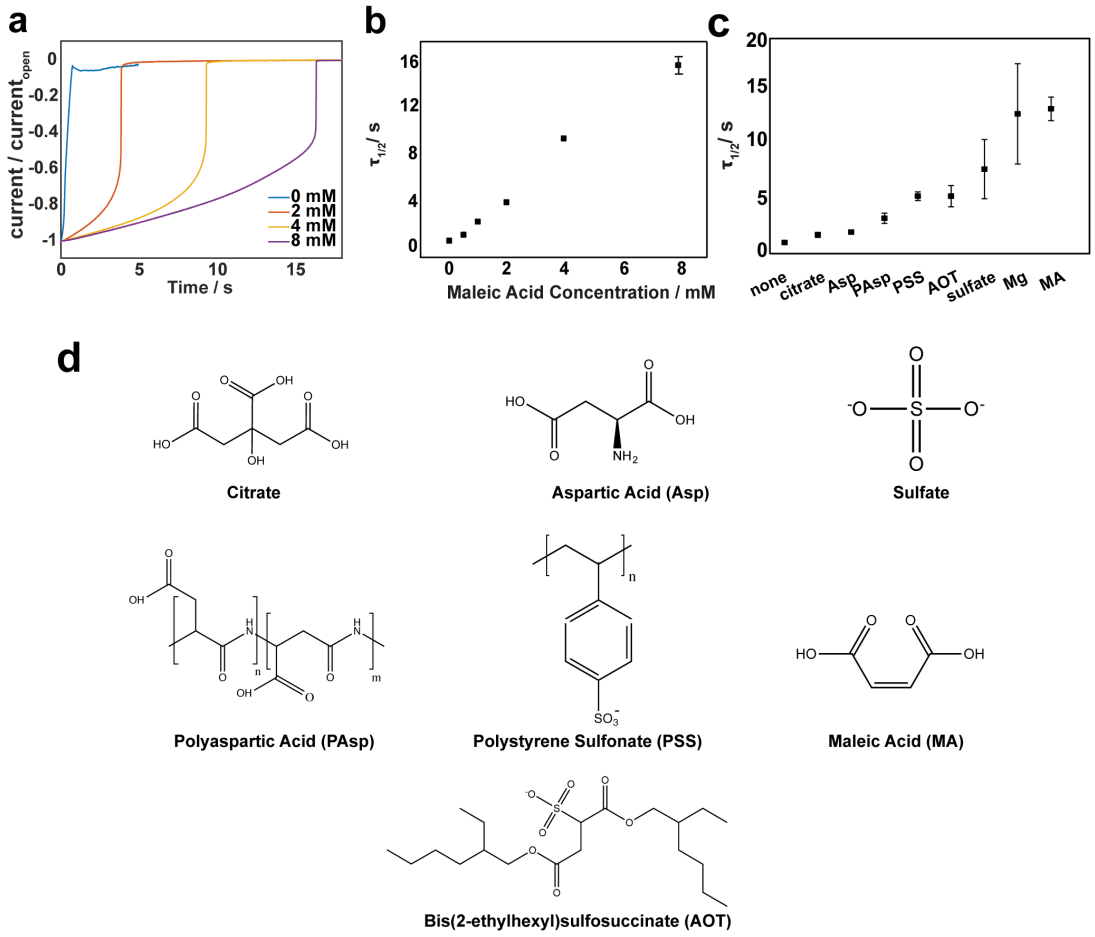


**Figure 8.7. a)** Example current-time transients with different concentrations of the additive, MA as indicated. **b)** Summary plot of mean values of $\tau_{1/2}$ for 25 runs in each case, with the error bars representing the standard error of the mean. **c**) Mean blockage time over a run of 25 growth events for each of the different additives. **d)** Structures of tested additives.

To highlight the application of this technique for fast additive screening, several different known growth inhibitors were incorporated into the nanopipette bath

solution to observe the subsequent effect on crystallisation times. These were citrate, aspartic acid (Asp), polyaspartic acid (PAsp), polystyrene sulfonate (PSS), bis(2-ethylhexyl)sulfosuccinate (AOT), sulfate and magnesium all of which are known to have some effect on $CaCO_3$ crystallisation and whose structures are presented in Figure 8.7d .[25] The addition of 8 mM each of these different additives to a set of baths allowed their efficacy for crystal growth inhibition to be rapidly screened. The resulting average blockings time are summarised in Figure 8.7c and the trend – for the same additives - is consistent with bulk studies,[25] although the nanopipette method reveals the additive effect much more quickly. This methodology paves the way for the rapid screening of crystal growth and dissolution additives.

## 8.5 Conclusions

Nanopipettes, under bias control, provide a powerful, robust and quantitative platform for the electrochemical (conductimetric) monitoring of crystal growth events on the nanoscale. By tuning the bias applied between a QRCE in a nanopipette and one positioned outside in a bath solution, crystal formation can be driven at the end of a nanopipette, and the corresponding current-time response can be used to extract growth kinetics. The deposit can be removed subsequently by reversing the polarity of the applied bias and the system is reset to perform the next growth experiment. The power of this technique is increased further through combination with other methods, most notably Raman spectroscopy, which can provide diagnostic information about the product formed *in-situ*. We further anticipate that other complementary techniques such as cryo-TEM could also be incorporated in future work. The studies herein relate to the nucleation and growth of amorphous calcium carbonate, which is an important precursor involved in the formation of other $CaCO_3$ polymorphs.

The approach described has been supported by a detailed FEM model, which provides key information about the mixing times needed for product formation as well as the supersaturation levels achievable. Furthermore, the effect of varying the applied bias has been explored, combining experimental and simulation results, to

reveal how the technique can be used optimally to drive and control crystallisation events.

Finally, the power of this technique in the study of additives has been highlighted. Maleic acid has been revealed as a potent inhibitor of $CaCO_3$ growth, which has a strong concentration-dose response, and the method has been employed to produce a rank order of additive efficacy. As the search for effective crystal growth additives is challenging and somewhat time consuming with conventional batch methods, the nanopipette format is particularly attractive and opens up important new possibilities for rapid screening.

## 8.6 References


1. Fu, Y.; Tokuhisa, H.; Baker, L. A., *Chem. Commun.* **2009**, 4877-4879.
2. Actis, P.; Mak, A. C.; Pourmand, N., *Bioanal. Rev.* **2010,** *1*, 177-185.
3. Byers, J. C.; Paulose Nadappuram, B.; Perry, D.; McKelvey, K.; Colburn, A. W.; Unwin, P. R., *Anal. Chem.* **2015,** *87*, 10450-10456.
4. Edwards, M. A.; German, S. R.; Dick, J. E.; Bard, A. J.; White, H. S., *ACS Nano* **2015,** *9*, 12274-12282.
5. Holden, D. A.; Watkins, J. J.; White, H. S., *Langmuir* **2012,** *28*, 7572-7577.
6. Bruckbauer, A.; James, P.; Zhou, D.; Yoon, J. W.; Excell, D.; Korchev, Y.; Jones, R.; Klenerman, D., *Biophys. J.* **2007,** *93*, 3120-3131.
7. Bruckbauer, A.; Ying, L.; Rothery, A. M.; Zhou, D.; Shevchuk, A. I.; Abell, C.; Korchev, Y. E.; Klenerman, D., *J. Am. Chem. Soc.* **2002,** *124*, 8810-8811.
8. Ivanov, A. P.; Actis, P.; Jönsson, P.; Klenerman, D.; Korchev, Y.; Edel, J. B., *ACS Nano* **2015,** *9*, 3587-3595.
9. Ebejer, N.; Güell, A. G.; Lai, S. C.; McKelvey, K.; Snowden, M. E.; Unwin, P. R., *Annu. Rev. Anal. Chem.* **2013,** *6*, 329-351.
10. Perry, D.; Al Botros, R.; Momotenko, D.; Kinnear, S. L.; Unwin, P. R., *ACS Nano* **2015,** *9*, 7266-7276.
11. Perry, D.; Paulose Nadappuram, B.; Momotenko, D.; Voyias, P. D.; Page, A.; Tripathi, G.; Frenguelli, B. G.; Unwin, P. R., *J. Am. Chem. Soc.* **2016,** *138*, 3152-3160.

12. Li, Q.; Xie, S.; Liang, Z.; Meng, X.; Liu, S.; Girault, H. H.; Shao, Y., *Angew. Chem. Int. Ed.* **2009,** *48*, 8010-8013.

13. Kranz, C., *Analyst* **2014,** *139*, 336-352.

14. Actis, P.; Maalouf, M. M.; Kim, H. J.; Lohith, A.; Vilozny, B.; Seger, R. A.; Pourmand, N., *ACS Nano* **2013,** *8*, 546-553.

15. Yuill, E. M.; Shi, W.; Poehlman, J.; Baker, L. A., *Anal. Chem.* **2015,** *87*, 11182-11186.

16. Heath, C. R.; Leadbeater, B. C. S.; Callow, M. E., *J. Appl. Phycol. 7*, 367-380.

17. Wang, S.-S.; Xu, A.-W., *Cryst. Growth Des.* **2013,** *13*, 1937-1942.

18. Rodríguez-Navarro, A. B.; Marie, P.; Nys, Y.; Hincke, M. T.; Gautron, J., *J. Struct. Biol.* **2015,** *190*, 291-303.

19. Miyazaki, Y.; Reimer, J. D., *ZooKeys* **2015**, 1.

20. Lackner, K. S., *Science* **2003,** *300*, 1677-1678.

21. Matveenko, B. R. S. a. L. P. R. a. I. A., *IOP Conference Series: Earth and Environmental Science* **2015,** *27*, 012042.

22. Butler, M. F.; Glaser, N.; Weaver, A. C.; Kirkland, M.; Heppenstall-Butler, M., *Cryst. Growth Des.* **2006,** *6*, 781-794.

23. Tribello, G. A.; Liew, C.; Parrinello, M., *J. Phys. Chem. B* **2009,** *113*, 7081-7085.

24. Vilozny, B.; Actis, P.; Seger, R. A.; Pourmand, N., *ACS Nano* **2011,** *5*, 3191-3197.

25. Ihli, J.; Kim, Y.-Y.; Noel, E. H.; Meldrum, F. C., *Adv. Funct. Mater.* **2013,** *23*, 1575-1585.

26. Tlili, M. M.; Amor, M. B.; Gabrielli, C.; Joiret, S.; Maurin, G.; Rousseau, P., *J. Raman Spectrosc.* **2002,** *33*, 10-16.

27. Behrens, G.; Kuhn, L. T.; Ubic, R.; Heuer, A. H., *Spectrosc. Lett.* **1995,** *28*, 983-995.

28. Nielsen, M. H.; Aloni, S.; De Yoreo, J. J., *Science* **2014,** *345*, 1158-1162.

29. Bots, P.; Benning, L. G.; Rodriguez-Blanco, J.-D.; Roncal-Herrero, T.; Shaw, S., *Cryst. Growth Des.* **2012,** *12*, 3806-3814.

30. Perry, D.; Momotenko, D.; Lazenby, R. A.; Kang, M.; Unwin, P. R., *Anal. Chem.* **2016,** *88*, 5523–5530.

31. Ying, L.; White, S. S.; Bruckbauer, A.; Meadows, L.; Korchev, Y. E.; Klenerman, D., *Biophys. J.* **2004,** *86*, 1018-1027.

32. Morris, C. A.; Friedman, A. K.; Baker, L. A., *Analyst* **2010,** *135*, 2190-2202.

33. Clarke, R. W.; White, S. S.; Zhou, D.; Ying, L.; Klenerman, D., *Angew. Chem. Int. Ed.* **2005,** *44*, 3747-3750.

34. Haynes, W. M., *CRC handbook of chemistry and physics*. CRC press: 2014.

35. Ihli, J.; Wong, W. C.; Noel, E. H.; Kim, Y.-Y.; Kulak, A. N.; Christenson, H. K.; Duer, M. J.; Meldrum, F. C., *Nat. Commun.* **2014,** *5*.

36. Brečević, L.; Nielsen, A. E., *J. Crys. Growth* **1989,** *98*, 504-510.

37. Hamza, S. M.; Hamdona, S. K., *J. Chem. Soc. Faradat T.* **1992,** *88*, 2713-2716.

38. Amjad, Z., *Mineral scale formation and inhibition*. Springer Science & Business Media: 2013.

39. Sancho-Tomás, M.; Fermani, S.; Durán-Olivencia, M. A.; Otálora, F.; Gómez-Morales, J.; Falini, G.; García-Ruiz, J., *Cryst. Growth Des.* **2013,** *13*, 3884-3891.

40. Bracco, J. N.; Grantham, M. C.; Stack, A. G., *Cryst. Growth Des.* **2012,** *12*, 3540-3548.

41. Amjad, Z.; Koutsoukos, P. G., *Desalination* **2014,** *335*, 55-63.

42. Dobson, P. S.; Bindley, L. A.; Macpherson, J. V.; Unwin, P. R., *ChemPhysChem* **2006,** *7*, 1019-1021.

43. Changa, D., *J. Am. Oil Chem. Soc.* **1983,** *60*, 618-622.

44. Kumar, T.; Vishwanatham, S.; Kundu, S., *J. Petrol. Sci. Eng.* **2010,** *71*, 1-7.

45. Nadappuram, B. P.; McKelvey, K.; Al Botros, R.; Colburn, A. W.; Unwin, P. R., *Anal. Chem.* **2013,** *85*, 8070-8074.

# Chapter 9. Summary

SICM is an increasingly powerful member of the SPM family, serving as a robust tool for mapping local topography of substrates, most notably living cells. The technique relies on using changes in the ion conductance signal upon approach to a substrate as a means of sensing the surface, allowing it to track, and scan, across it. The work presented in this thesis greatly extends the capabilities of SICM beyond topographical mapping, local delivery and conductance measurements, which have been the primary applications to date.

Chapter 2 presents one of the first studies that highlighted the exciting possibility of using SICM, with DM feedback, to probe and map surface charge across a sample. This was demonstrated for two different substrates and was shown to be consistent with what would be expected based on FEM simulations. Most significantly this study raised questions about whether traditional SICM experiments, and the topographical data produced from them, can be considered accurate, as the topographical data could easily become convoluted by surface charge effects under a range of imaging conditions, low ionic strength, small probe dimensions, etc.

BM-SICM, described in chapter 3, intends to provide a more robust feedback method for SICM. This novel feedback type involves applying a small harmonic oscillation between the two SICM QRCEs in order to generate an AC signal that can be used for sensing the substrate, and which can be used for feedback for topographical mapping. In contrast to most SICM studies, which require a significant bias applied to produce an ionic current for feedback signal, the harmonic oscillation used here can be applied about 0 V. The technique holds several advantages over DM-SICM, removing the physical oscillation of the probe which could perturb the sample and which could limit probe-substrate separation distances. Additionally, the range of oscillation frequencies accessible is beyond that achievable with DM-SICM, which is limited by the resonant frequency of the piezo positioners used for probe positioning.

The possibility of convolution between surface charge and topography raised in chapter 2 is addressed in chapter 4 where it is shown that through using a BM-SICM it is possible to track surface topography free from surface charge effects with

no net bias applied before then obtaining surface charge information through tuning the bias between the QRCEs. The AC phase component of the AC signal is shown to be particularly sensitive to the surface charge and the scan regime demonstrated here allows for dynamic maps to be generated with surface charge maps produced at a wide range of biases.

Whilst FEM simulations had provided validation for the surface charge mapping with SICM in previous chapters, the models used lacked quantification because of insufficient knowledge about the nanopipette characteristics itself. In SICM studies, and, more generally, any studies that use nanopipette probes, there is no consistency with how nanopipettes are characterised. Chapter 5 attempts to rectify this, employing TEM for obtaining accurate nanopipette dimensions in a way not possible with other techniques. Then, using FEM simulations of the nanopipette probe geometry, it is possible to obtain surface charge properties for the nanopipette material through matching the current-voltage properties between experiment and simulation. Finally, with a fully characterised probe it is then possible to perform quantifiable surface charge mapping with SICM. The work presented in this chapter aims to provide a robust platform for future studies whereby nanopipettes and their response can be consistently and accurately modelled after experiments for a truer understanding of the underlying system.

The first studies using SICM for charge mapping of living cells are presented in Chapter 6 and with knowledge of the nanopipette probes, it becomes possible to obtain quantitative information about the surface charge of the cellular interface. This is demonstrated for root hair cells, in low ionic conditions but more significantly, this work shows the exciting possibility for mapping surface charge heterogeneities on the cell membrane of mammalian cells in physiological conditions. This is significant as living cells will often require a specific media to maintain viability, which often equates to a high ionic strength. Under these conditions, it is assumed the DDL is too compressed to have an influence on the SICM response, but this study shows this is not the case, and that more care needs to be taken, and surface charge effects considered more vigorously, when designing SICM experiments.

Modulation techniques in SPM experiments, allow for a more robust scanning platform than simply using the ionic current as the feedback signal, as they

are less susceptible to drift effects, and noise, through locking into the current response at a specific frequency. However, these approaches can limit the image acquisition rates possible in SICM. Chapter 7 aims to improve the surface charge mapping image acquisition rate. Chapter 4 showed how minimising the bias between the QRCEs was essential for minimising convolution of surface charge and topography. In this chapter, a small bias is applied to allow for a faster feedback response, whilst still minimising convolution of surface charge and topography. Demonstrated for inert and living systems, this approach to surface charge mapping, which also utilises a short (<50 ms) pulse of the voltage to become sensitive to surface charge allows for maps with over ten times as many pixels as the previous studies to be obtained with lower scan times.

Finally, another use for the nanopipette probe itself is explored in chapter 8, where it is possible to locally drive the formation of crystals in the end of the nanopipette through applying a bias to mix together ions from the nanopipette and bath solution. The resulting crystal growth causes an obstruction to the nanopipette, resulting in a drop off in the ionic current and when reversed, the bias can be used to instead drive the dissolution of the formed solid. This provides a powerful platform for studying growth additives whose effect on the resulting blocking transient measured in the nanopipette can be evaluated to gauge the efficacy of the additive.

In summary, this thesis has helped position SICM as a powerful tool for multifunctional imaging, capable of performing surface charge measurements of living and inert interfaces. The utilisation of SICM, with innovative scan regimes, could help to answer fundamental questions about the role of spatial heterogeneities in surface charge in systems such as living cells. In order to achieve these aims, a multi-microscopy approach will become increasingly essential, whereby other techniques, such as confocal microscopy, will provide complimentary information to the surface charge measurements that can help relate the charge differences to specific function. SICM is increasingly being shown to be an important and capable technique, with interest in the technique increasing at pace despite slow beginnings. It is only now that its potential as a powerful, multifunctional SPM technique is beginning to be realised and fulfilled and it is likely that the future will see its prominence increase further.